

# Thesis Report

## Ganymede: A Frozen Enigma

Exploring possible internal density distributions  
through gravitational potential field variations

*March 20th, 2019*

**Max van Strien - 4006240**

Delft University of Technology





# Thesis Report

## Ganymede: A Frozen Enigma

Exploring possible internal density distributions through gravitational potential field variations

March 20th, 2019

by

Max van Strien - 4006240

to obtain the degree of Master of Science  
at the Delft University of Technology,  
to be defended publicly on Friday March 22, 2019 at 10:00 AM.



Student number:	4006240
Project duration:	April 23, 2018 – March 22, 2019
Thesis committee:	Dr. ir. W. van der Wal, TU Delft, chair
	Dr. ir. B. Root, TU Delft, supervisor
	Dr. ir. D. Dirkx, TU Delft, supervisor
	Dr. P.G. Ditmar, TU Delft

*This thesis is confidential and cannot be made public until March 21, 2019.*

An electronic version of this thesis is available at <http://repository.tudelft.nl/>.



# ABSTRACT

In 2022, ESA plans to launch the JUICE (JUperiter ICy moons Explorer) mission which will spend at least three years making detailed observations of Jupiter and three of its largest moons, Ganymede, Callisto and Europa. These moons are currently a hot topic within the science community as their interiors might include oceans consisting of liquid water. These oceans could provide life, but at the moment little is known about the exact composition and structure of these interiors. Only Earth based observations and a few fly-by's have been performed to measure the characteristics of these moons. The JUICE mission will provide more detailed information on the moons through fly-by's. This thesis research will focus on Ganymede as JUICE will be the first human-developed satellite to orbit this moon.

Ganymede stands out as a potential scientific target due to several specific reasons; the most remarkable being it's intrinsic magnetic field. Only two other solid bodies within the Solar System generate such a magnetic dipole field (Earth and Mercury). The complex interactions of this magnetic field with Jupiter's magnetic field are unique and could provide a lot of new knowledge when studied. Measurements from Galileo and the Hubble space telescope suggest that a subsurface layer of (saline) water is present within the moons interior. Saline water could be a good conductor of electricity, generating the magnetic field. The magnetic field of Ganymede could also point towards a complex core, which is another possibility for the generation of this field. It could be that the core of Ganymede consists of liquid, iron rich elements which generate and maintain this magnetic field.

Unfortunately, current models of the gravitational potential field and the interior of Ganymede are still uncertain. A precise gravitational model of Ganymede could provide a lot of information about this interior. An orbiter or in-situ probes are required to achieve high precision gravitational potential field models. JUICE is expected to obtain a model of Ganymede's gravitational potential field of at least degree and order 15. This thesis will provide insight in how different possible internal density distributions of Ganymede influence the gravitational potential field of the moon. This way, when JUICE obtains more information on the gravitational potential field of Ganymede, variations within this field can directly be utilized to determine what interior aspects could cause these variations.

From 44 billion 1D homogeneous models considered during this research, only 260 adhered to current known characteristics of Ganymede. Certain elements and water phases are present in all models: a pure iron or iron-sulfide core, a silicon mantle, an ice VI layer together with an liquid ocean and a outer crust consisting of Ice  $I_h$ . Dependent on the exact layer thicknesses within a model, intermediate ice phases, ice III and V, can also be present. Layer correlations between the 260 models were analyzed and fourteen models were selected for further research.

These models were combined with different boundary and density variations to obtain different 3D heterogeneous models. Gravitational potential simulations for spherical harmonics coefficients up to order/degree 48 were performed. It was found that several relations exist between gravitational potential field data and internal density distributions within Ganymede. If one can effectively correct gravitational potential field signals for measurable components within Ganymede's interior, several sets of internal structures emerge. Furthermore, taking into account the established limitations and correlations between layers, the gradient of the gravitational signal power over spherical harmonics degree can be directly related to the thickness of an interiors ocean. Several distinguishable models show that the presence of ice III, and to a lesser extent ice V, increase the gravitational signal power of a model. When combined with the correlations found between internal layers during this research, one could even establish an accurate first order approximate of Ganymede's internal composition. These results, together with measurements performed by JUICE, will provide numerous new insights on Ganymede's frozen enigma.



# PREFACE

It has been quite a journey. The past decade has been an amazing experience and I would not have had it any other way. Competitive sports, an active social life including a full-time board year and the coaching of rowing crews has been a large part of my student career. This resulted in a bumpy start on my path to become an Aerospace Engineer. After catching up on the initial backlog, I really began to enjoy my studies. After starting my masters degree in space exploration, I could finally broaden my horizon with respect to current research on space related topics. This really sparked my interest and also resulted in an amazing internship at SRON Netherlands Institute for Space Research, where I learned a lot about micro kinetic inductance detectors and other aspects of space engineering. My journey as a student ends here, after a thesis research of which I enjoyed every single moment. I am grateful for the opportunities that were handed to me and will never forget the amazing people that I have met and the things that I have learned.

This journey would not have been possible without some people close to me. First of all I want to thank my parents for everything they have done for me. All your support and understanding throughout the years made it possible for me to develop as an individual and allowed me to follow my dreams. I will never forget this and hope that one day I can return the favor. Another person I want to thank is my sister Tess. Even though sometimes I am way to busy, I want you to know that I will always be there for you, as you are for me. A lot of appreciation also goes to my aunt, Karin, for letting me stay at her place during my internship period and for all the crazy and fun times we had together. Thank you for listening to me when I most needed it. Last but not least, my grandmother for all the nice dinners at her place, these are always a welcome change of scenery from the busy life in Delft.

My supervisors, Bart and Dominic, thank you for all your patience, knowledge and commitment throughout the last year. I am really happy with the thesis subject you made available to me and could not have wished for better supervision.

Finally, I want to thank everyone that I got to know during my years as a student, without you this journey would not have been the same.

*Max van Strien - 4006240  
Delft, March 2019*



# CONTENTS

<b>Abstract</b>	<b>iii</b>
<b>List of Figures</b>	<b>xi</b>
<b>List of Tables</b>	<b>xv</b>
<b>List of Symbols</b>	<b>xvii</b>
<b>Abbreviations</b>	<b>xix</b>
<b>1 Ganymede: A Frozen Enigma</b>	<b>1</b>
1.1 Previous Discoveries . . . . .	1
1.1.1 Differentiation . . . . .	2
1.1.2 Surface Features . . . . .	2
1.1.3 Magnetic Field . . . . .	4
1.1.4 Gravitational Coefficients . . . . .	5
1.1.5 Global Layers . . . . .	5
1.1.6 Local Density Variations . . . . .	6
1.1.7 Known Characteristics . . . . .	8
1.2 JUPITER ICy moons Explorer . . . . .	8
1.2.1 Instruments . . . . .	8
1.2.2 Objectives . . . . .	9
1.2.3 Measuring Gravity effects . . . . .	9
1.2.4 Expectations from ESA for JUICE . . . . .	10
1.3 Knowledge gaps . . . . .	11
1.4 Research question . . . . .	11
1.5 Structure of the report . . . . .	12
<b>2 Homogeneous 1D Modeling</b>	<b>13</b>
2.1 Main Considerations . . . . .	13
2.2 Model Requirements . . . . .	14
2.2.1 Mass . . . . .	15
2.2.2 Moment of Inertia Factor . . . . .	15
2.2.3 Gravitational and Pressure Distributions . . . . .	16
2.2.4 Ice Phases . . . . .	16
2.3 Implementation . . . . .	17
2.3.1 Modules . . . . .	18
2.3.2 Data Processing . . . . .	18
<b>3 Heterogeneous 3D Modeling</b>	<b>21</b>
3.1 Topography . . . . .	21
3.2 Crustal Models . . . . .	22
3.2.1 Thickness Variations Through Albedo . . . . .	22
3.2.2 Isostasy . . . . .	23
3.2.3 Combined Crust Model . . . . .	24
3.3 Internal Boundary Variations . . . . .	25
3.4 Pockets and Diapirs . . . . .	26
3.5 Implementation . . . . .	26
3.5.1 Modules . . . . .	27
3.5.2 Data Processing . . . . .	27

<b>4</b>	<b>Gravitational Potential Simulations</b>	<b>31</b>
4.1	Input Models . . . . .	31
4.2	Output of Simulations . . . . .	32
4.2.1	Gravitational Potential Field . . . . .	32
4.2.2	Outlining. . . . .	35
4.2.3	Gravity Model Coefficients . . . . .	37
4.3	Methodology Synopsis . . . . .	38
<b>5</b>	<b>Verification and Validation</b>	<b>39</b>
5.1	Homogeneous 1D Models. . . . .	39
5.1.1	Mass . . . . .	39
5.1.2	Moment of Inertia Factor . . . . .	40
5.1.3	Pressure and Gravity Profiles. . . . .	40
5.1.4	Ice Phases . . . . .	41
5.1.5	Homogeneous Model Simulations: Fixing a Boundary Layer. . . . .	42
5.2	Heterogeneous 3D Models . . . . .	43
5.2.1	Finding Boundaries . . . . .	43
5.2.2	Topography . . . . .	44
5.2.3	Crustal Variations . . . . .	45
5.2.4	Internal Boundary Variations . . . . .	50
5.2.5	Pockets and Diapirs . . . . .	51
5.2.6	Implementation of the Global Spherical Harmonics Package . . . . .	52
<b>6</b>	<b>Results</b>	<b>55</b>
6.1	Homogeneous 1D Models. . . . .	55
6.1.1	Initial Simulation . . . . .	55
6.1.2	Main Simulations . . . . .	56
6.1.3	Layer Correlations . . . . .	57
6.1.4	Worlds of Interest . . . . .	60
6.1.5	Results Synopsis I . . . . .	67
6.2	Heterogeneous 3D Models . . . . .	69
6.2.1	Global Worlds . . . . .	69
6.2.2	Individual Anomalies . . . . .	74
6.2.3	Results Synopsis II . . . . .	77
<b>7</b>	<b>Discussion</b>	<b>79</b>
7.1	Homogeneous 1D Models. . . . .	79
7.1.1	Ice $I_h$ layer Correlations . . . . .	79
7.1.2	Ocean layer Correlations. . . . .	81
7.1.3	Ice III layer Correlations . . . . .	82
7.1.4	Relations with respect to the ice V, VI, mantle and core layers . . . . .	83
7.1.5	Main 1D Homogeneous Model Findings . . . . .	84
7.2	Heterogeneous 3D Models . . . . .	84
7.2.1	Global Worlds . . . . .	84
7.2.2	Individual Anomalies . . . . .	87
7.2.3	Main 3D Homogeneous Model Findings . . . . .	90
<b>8</b>	<b>Conclusions</b>	<b>91</b>
8.1	Layer Correlations . . . . .	92
8.2	Selected Homogeneous Models. . . . .	92
8.3	Anomaly limitations . . . . .	93
8.3.1	Isostasy . . . . .	93
8.3.2	Pockets. . . . .	93
8.4	Degree Variance Findings . . . . .	93
8.5	Concluding Remarks . . . . .	94

---

<b>9 Recommendations</b>	<b>95</b>
<b>Bibliography</b>	<b>97</b>
<b>A Appendix A - Vance's Interior Models</b>	<b>101</b>
<b>B Appendix B - Spherical Harmonics</b>	<b>103</b>
B.1 Spherical bodies . . . . .	103
B.2 Zonal Spherical Harmonics . . . . .	104
B.2.1 $J_2$ effect, main distortion . . . . .	104
B.2.2 Higher order zonal terms . . . . .	105
B.3 Sectoral and Tesseral Spherical Harmonics . . . . .	106
B.3.1 Normalizing the geopotential coefficients . . . . .	108
B.3.2 Modeling Density Variations . . . . .	108
<b>C Appendix C - Full Correlation Figures</b>	<b>109</b>



# LIST OF FIGURES

1.1	Image of Ganymede taken by the Voyager 1 spacecraft [46]. . . . .	3
1.2	Higher resolution image of Ganymede taken by the Voyager 1 spacecraft, which shows the difference between the cratered and grooved terrain types [46]. . . . .	3
1.3	Image of Ganymede taken by the Voyager 2 spacecraft [47]. . . . .	4
1.4	Higher resolution Voyager 2 image of Ganymede which shows grooved terrain (the bright strip) created by a fault [47]. . . . .	4
1.5	The effect of the thermal runaway over time on the interior of Ganymede, it shows that the initially frozen ice I and III layers undergo melting and form an internal ocean. The eccentricity of Ganymede's orbit over time in is given in (a), which is expected to drop when orbital resonance occurs. . . . .	6
1.6	How the Earth's gravity is influenced by its shape/interior. . . . .	7
1.7	Some examples of anomalies which could be present in an icy body [55]. . . . .	7
1.8	The motion of the satellite and the ground station during signal travel time for two-way Doppler measurements[26]. . . . .	10
1.9	ESA's schematic view of the strategy to characterise Ganymede's crust and liquid layer by using different techniques. [12] . . . . .	11
2.1	Ganymede's exterior as observed by different previous missions. . . . .	14
2.2	A possible representation of Ganymede's interior models, which include all considered layers. It is possible that certain models do not include all these layers, but only a selection. The thickness of the layers in the picture is not necessarily a good representation of the layers within the final selected models. These are chosen for illustration purposes. . . . .	14
2.3	The used phase transitions for fresh and saline water [54]. . . . .	17
2.4	Block diagram for the algorithm which determines the 1D homogeneous models. . . . .	18
2.5	An example of a world which is adherent with all set requirements. Generated by the 1D homogeneous model generator. It is named Aqva I due to its large ocean. . . . .	19
3.1	The point control network of Ganymede, circle sizes are proportional to coordinate errors. The color variation indicates the height in kilometers above the best-fit sphere (2632.63 km) [59]. . . . .	21
3.2	The topography of Ganymede with respect to a reference spheroid, resulting from the selected point control network [59]. . . . .	22
3.3	A cylindrical map of Ganymede [59], the two different types of terrain are clearly visible. Latitude varies between -90 and 90 degrees and longitude varies between 0 and 360 degrees. . . . .	23
3.4	Pratt's hypothesis (left) and Airy's hypothesis (right). Colors are not related to the albedo variations. . . . .	24
3.5	The provided topographic height maps. Towards the right these maps get larger topographic variations and towards the bottom the maps are more smoothed. Currently no value for latitude and longitude is included. This can be determined for each boundary interaction individually. . . . .	25
3.6	Block diagram for the algorithm which determines the 3D heterogeneous models. . . . .	27
3.7	The topography, Crust-L, L-VI, VI-M and M-C interfaces (top to bottom) of Aqva I when varied up to 20 km with respect to the reference sphere. Boundary variations are to scale and are located at depths corresponding to Aqva I's layers. . . . .	29
3.8	Several boundary interfaces located at different depths. Boundary variations are enhanced for illustration purposes. Layers depths are not related to any possible models. . . . .	29
4.1	An example of a set of boundary and density .gmt input files. . . . .	31
4.2	The gravitational potential field (SHbounds 0-48) for Aqva I including topography. . . . .	32
4.3	The gravitational potential field (SHbounds 0-15) for Aqva I including topography. . . . .	33

4.4	The gravitational potential field variations (SHbounds 2-48, excluding $C_{2,0}$ effect and Ganymede's tidal bulge) for Aqva I including topography. . . . .	34
4.5	The gravitational potential field variations (SHbounds 2-48, excluding $C_{2,0}$ ) for Aqva I including topography, 50 % Pratt compensation and topographic reduction. . . . .	35
4.6	Mapping of Ganymede using six different thresholds. . . . .	36
4.7	Original 40m threshold outline. . . . .	36
4.8	New 40m threshold outline with less detail. . . . .	36
4.9	The same gravitational potential field output for Aqva I including topography as Figure 4.4, but now with a zero-lining. . . . .	37
4.10	The uncertainties which will be used to determine which results could theoretically be measurable. . . . .	38
5.1	The expected gravitational potential and pressure profile within Ganymede [49]. The three different curves are for a pure iron core (bold curve), 50% iron 50 % FeS and 100 % FeS core (light curve). . . . .	41
5.2	The gravitational potential (g) and pressure (p) profiles determined by the algorithm for Spes I. This is performed on a model with a pure iron core and thus adheres to the bold curves in Figure 5.1. The solid lines represent the integrations performed from the surface to the core of Ganymede. The dotted lines the integration from the core to the surface. . . . .	41
5.3	Temperature profiles resulting from the simulations for viable models with a non saline ocean and an expected core density. . . . .	42
5.4	Layers thicknesses within the allowable models from the initial simulation. The ice VI layer has been fixed to the known radius of Ganymede. . . . .	43
5.5	Same simulation but now with the ocean layer fixed to the known radius of Ganymede. . . . .	43
5.6	The topography of Ganymede with respect to a reference spheroid, resulting from the selected point control network [59]. . . . .	44
5.7	The height variations in km resulting from the gmt file of the topography boundary interface. . . . .	45
5.8	A cylindrical map of Ganymede [59] based on its surface including albedo variances. Latitude varies between -90 and 90 degrees and longitude varies between 0 and 360 degrees. . . . .	46
5.9	The height variations within the crust of the model considered during this section. The algorithm was programmed to vary the thickness between 75 and 55 kilometers. A longitudinal phase shift of 180 degrees with respect to Figure 5.8 was performed such that the .gmt file corresponds to the input files of the GSHP. . . . .	46
5.10	The height variations within the crust of the model due to 100% Airy compensation. . . . .	47
5.11	The height variations within the crust of the model due to 25% Airy compensation. . . . .	48
5.12	The density variations within the crust of the model due to 100% Pratt compensation. . . . .	49
5.13	The density variations within the crust of the model due to 25% Pratt compensation. . . . .	49
5.14	The topographic map used to vary the model's ocean floor. . . . .	50
5.15	The ocean floor thickness variations. These vary between -20 and +20 kilometers with respect to the reference sphere at -825 km. . . . .	51
5.16	Pixel size distribution due to equidistant scaling. . . . .	52
6.1	Layers thicknesses within the allowable models from the initial analysis using the settings provided in Table 6.1. These are 1D homogeneous models with a non-saline ocean and a core density of $7.030 \text{ g/cm}^3$ . . . . .	56
6.2	Layers thicknesses within the possible 1D homogeneous models of Ganymede resulting from the main simulations using the settings provided in Table 6.2. The ice VI layer has been fixed to the known radius of Ganymede. . . . .	57
6.3	The color indicators for the different model sets which were analyzed during the first part of the thesis research. Low core density = $5.150 \text{ g/cm}^3$ , expected = $7.030 \text{ g/cm}^3$ and high = $8.000 \text{ g/cm}^3$ . The salinity percentages are mass percentages. . . . .	58
6.4	The correlations between the different layer thicknesses of the models that passed all requirements. Colors are scaled with respect to the different model sets as provided in Figure 6.3. . . . .	59
6.5	The temperature profile for Spes I. . . . .	60
6.6	The temperature profile for Spes II. . . . .	61
6.7	The temperature profile for Spes III. . . . .	61

6.8	The temperature profile for Spes IV. . . . .	62
6.9	The temperature profile for Gelo I. . . . .	62
6.10	The temperature profile for Gelo II. . . . .	63
6.11	The temperature profile for Aqva I. . . . .	63
6.12	The temperature profile for Aqva II. . . . .	64
6.13	The temperature profile for Aqva III. . . . .	64
6.14	The temperature profile for Aqva IV. . . . .	65
6.15	The temperature profile for Aqva V. . . . .	65
6.16	The temperature profile for Libra I. . . . .	66
6.17	The temperature profile for Libra II. . . . .	66
6.18	The temperature profile for Libra III. . . . .	67
6.19	Degree variances of the 14 selected worlds with all heterogeneous anomalies included except isostatic compensation. Degree 2-48, 500 km above sphere. Uncertainties are based on JUICE's instrument performance [4]. . . . .	70
6.20	The gravitational potential field of Spes I including all heterogeneous anomalies except isostatic compensation. Degree 2-48 (no $C_{2,0}$ ), 500 km above sphere. . . . .	70
6.21	Degree variances of the 14 selected worlds with all heterogeneous anomalies included except the topography. 50% compensation, degree 2-48, 500 km above sphere. Uncertainties are based on JUICE's instrument performance [4]. . . . .	71
6.22	The gravitational potential field of Spes I including all heterogeneous anomalies except the topography. 50% compensation, degree 2-48 (no $C_{2,0}$ ), 500 km above spheroid. . . . .	71
6.23	Degree variances of the 14 selected worlds with all heterogeneous anomalies included except the topography and isostatic compensation. Degree 2-48, 500 km above sphere. Uncertainties are based on JUICE's instrument performance [4]. . . . .	72
6.24	The gravitational potential field of Spes I including all heterogeneous anomalies except the topography and isostatic compensation. Degree 2-48 (no $C_{2,0}$ ), 500 km above spheroid. . . . .	73
6.25	Degree variances of the 14 selected worlds with internal boundary variations and pockets included. Degree 2-48, 500 km above sphere. Uncertainties are based on JUICE's instrument performance [4]. . . . .	73
6.26	Degree variances of the 14 selected worlds with only the different internal boundary variations included. Degree 2-48, 500 km above sphere. Uncertainties are based on JUICE's instrument performance [4]. . . . .	74
6.27	Signal power of all the different anomalies for Gelo I. Degree 2-48, 500 km above sphere. Uncertainties are based on JUICE's instrument performance [4]. . . . .	75
6.28	Signal power of all the different anomalies for Spes I. Degree 2-48, 500 km above sphere. Uncertainties are based on JUICE's instrument performance [4]. . . . .	76
6.29	Signal power of all the different anomalies for Aqva II. Degree 2-48, 500 km above sphere. Uncertainties are based on JUICE's instrument performance [4]. . . . .	77
7.1	Correlation between the ice III and crust layers with the model set color-scale. . . . .	79
7.2	Correlation between the ice V and crust layers with the model set color-scale. . . . .	79
7.3	The used phase transitions for sweet and saline water [54]. . . . .	80
7.4	Correlation between the ice VI and ocean layers with an ice $I_h$ color-scale. . . . .	80
7.5	Correlation between the mantle and core layers with an ice $I_h$ color-scale. . . . .	80
7.6	Correlation between the mantle and VI layers with an ocean color-scale. . . . .	81
7.7	Correlation between the core and ocean layers with the model set color-scale. . . . .	81
7.8	Correlation between the ice III and ocean layers with the model set color-scale. . . . .	82
7.9	Correlation between the ice V and ocean layers with the model set color-scale. . . . .	82
7.10	Correlation between the ice III and ice V layers with the model set color-scale. . . . .	82
7.11	Correlation between the ice III and ice VI layers with the model set color-scale. . . . .	83
7.12	Correlation between the ice III and mantle layers with the model set color-scale. . . . .	83
7.13	Correlation between the ice VI and mantle layers with an ice V color-scale. . . . .	83
7.14	Correlation between the mantle and core layers with an ice VI color-scale. . . . .	83
7.15	Degree variances of the 14 selected worlds with all heterogeneous anomalies included except isostatic compensation. Degree 2-48, 500 km above sphere. Uncertainties are based on JUICE's instrument performance [4]. . . . .	85

7.16 Degree variances of the 14 selected worlds with only the different internal boundary variations included. Degree 2-48, 500 km above sphere. Uncertainties are based on JUICE's instrument performance [4]. . . . .	87
7.17 Signal power of boundary variations for Gelo I. Degree 2-48, 500 km above sphere. Uncertainties are based on JUICE's instrument performance [4]. . . . .	88
7.18 Signal power of boundary variations for Spes I. Degree 2-48, 500 km above sphere. Uncertainties are based on JUICE's instrument performance [4]. . . . .	88
7.19 Signal power of boundary variations for Aqva II. Degree 2-48, 500 km above sphere. Uncertainties are based on JUICE's instrument performance [4]. . . . .	89
A.1 The results using the models from Vance et al [54]. Interiors are provided for varying mass fractions of salinity and bottom melting temperatures of the ice $I_h$ layer (The temperatures between 250 and 270K are chosen as lower boundary conditions as these correspond to the phase diagram of ice I over the range of temperatures for a homogeneous solid mix of water which contains magnesium sulfate, see Figure 2.3. Zero values indicate that a layer is not present and dashed values indicate that salinity is too low to allow for the presence of a liquid layer. $q_b$ is the heat flux used for the thermal profile in $mW/m^2$ that corresponds to the equilibrium ice $I_h$ thickness. S/Si is the Sulfur to Silicon mass fraction which is consistent with the interior structure.	101
B.1 Cartesian and spherical coordinate systems. . . . .	103
B.2 The gravitational potential due to the $J_2$ effect as function of latitude and longitude [29]. . . . .	105
B.3 First six degrees of zonal harmonics. . . . .	106
B.4 First five degrees of sectoral harmonics. . . . .	107
B.5 Some tesseral harmonics. . . . .	107
B.6 An overview of the different harmonics, their influence on the gravitational potential field model and the corresponding coefficients. The S coefficients are used for negative orders and the C coefficients for positive orders [23]. . . . .	108
C.1 The correlation between the different layers of the models that passed all requirements, colors scaled with respect to the models mass [kg]. . . . .	110
C.2 The correlation between the different layers of the models that passed all requirements, colors scaled with respect to the models moment of inertia factor [-]. . . . .	111
C.3 The correlation between the different layers of the models that passed all requirements, colors scaled with respect to the ice $I_h$ layer thickness [km]. . . . .	112
C.4 The correlation between the different layers of the models that passed all requirements, colors scaled with respect to the Ocean layer thickness [km]. . . . .	113
C.5 The correlation between the different layers of the models that passed all requirements, colors scaled with respect to the ice III layer thickness [km]. . . . .	114
C.6 The correlation between the different layers of the models that passed all requirements, colors scaled with respect to the ice V layer thickness [km]. . . . .	115
C.7 The correlation between the different layers of the models that passed all requirements, colors scaled with respect to the ice VI layer thickness [km]. . . . .	116
C.8 The correlation between the different layers of the models that passed all requirements, colors scaled with respect to the mantle thickness [km]. . . . .	117
C.9 The correlation between the different layers of the models that passed all requirements, colors scaled with respect to core thickness [km]. . . . .	118
C.10 The correlation between the different layers of the models that passed all requirements, colors scaled with respect to the models core pressure [Pa]. . . . .	119

# LIST OF TABLES

1.1	The measured gravity coefficients of the two Galileo fly-by's. $\mu$ is the correlation coefficient [1]. . . . .	5
1.2	Characteristics of interest for Ganymede. . . . .	8
2.1	An overview of the layers found in the models. . . . .	13
2.2	Measured characteristics of Ganymede. . . . .	14
3.1	The data used for the different boundary interactions. . . . .	26
5.1	The models used to verify the mass determination part of the algorithm. . . . .	39
5.2	The masses of the individual shells and the total models. These are obtained by applying Equations 5.1 and 5.2 with the densities and thicknesses of each shell. . . . .	40
5.3	The moment of inertia of each individual shell and the total models. These are obtained by applying Equations 2.7 - 2.10 with the densities and thicknesses of each shell provided in Tables 2.1 and 5.1. The MoI factors are based on an average model MoI based on Equation 2.9, a mean density of $1.936 \text{ g/cm}^3$ and the GM and radius measurements of Galileo [1]. . . . .	40
5.4	The boundary depths with corresponding layer numbers of Aqva I. Density gaps between boundaries are also provided. . . . .	43
5.5	Pockets locations and column densities. . . . .	52
5.6	Pockets characteristics analytically determined by Equations 5.15 - 5.18. . . . .	52
6.1	Initial simulation step-size and values per layer. [54] . . . . .	55
6.2	Full scale simulation step-size and limits per layer [54]. . . . .	57
6.3	The known characteristics of each selected world presented in this section. The main feature on which each world has been selected has been provided and the corresponding layers are highlighted for clarity. . . . .	68
7.1	The maximum Pratt compensation percentages based on the different crust thicknesses of the generated models. . . . .	86



# LIST OF SYMBOLS

$a$	Acceleration	$[\frac{m}{s^2}]$
$\mathbf{a}$	Acceleration vector	$[\frac{m}{s^2}]$
$A$	Bond albedo	[-]
$\mathbf{B}$	Body Fixed Frame	[-]
$c$	Speed of light	299792458 $[\frac{m}{s}]$
$C_{n,m}$	Tesseral harmonic coefficient	[-]
$\bar{C}_{n,m}$	Normalized tesseral harmonic coefficient	[-]
$C_V$	Volume Square column	$[m^3]$
$d$	Depth	$[km]$
$D$	Compensation depth	$[m]$
$D$	Diameter (Section 5.2.5)	$[m]$
$\Delta g_F$	Final gravitational potential field variations	$[\frac{m^2}{s^2}]$
$\Delta \rho$	Density gap	$[\frac{g}{cm^3}]$
$\Delta$	Laplace operator	[-]
$\delta_{0m}$	Kronecker symbol	[-]
$f$	Function	[-]
$g$	Gravitational potential	$[\frac{m^2}{s^2}]$
$g_b$	Topographic reduction	$[\frac{m^2}{s^2}]$
$g(\lambda)$	Normal gravity correction	$[\frac{m^2}{s^2}]$
$\bar{g}_{obs}$	Observed gravitational acceleration	$[\frac{m^2}{s^2}]$
$\delta g_r$	Main shape corrections	$[\frac{m^2}{s^2}]$
$G$	Gravitational constant	$6.67408 \cdot 10^{-11} [\frac{m^3}{s^2 kg}]$
$h$	Height	$[m]$
$I$	Moment of Inertia	$[kgm^2]$
$J_{n,m}$	Zonal harmonic constant	[-]
$K$	Kaula constant	[-]
$\lambda$	Longitude	$[deg]$
$\lambda_s$	Amount of longitudinal steps	[-]
$m$	Order of spherical harmonics	[-]
$M$	Mass	$[kg]$
$\mu$	Gravitational parameter (Appendix B)	$[\frac{m^3}{s^2}]$
$\mu$	Correlation coefficient	[-]
$n$	Degree of spherical harmonics	[-]
$\nabla$	Gradient	[-]
$P$	Pressure	$[Pa]$
$P_S$	Pixel size	$[m]$
$P_{n,m}$	Legendre polynomial function	[-]
$\partial$	Partial derivative	[-]
$\phi$	Latitude	$[deg]$
$\Phi$	Perturbation of the gravitational potential energy	$[\frac{m^2}{s^2}]$
$r$	(Radial) distance	$[m]$
$\mathbf{r}$	Position vector	$[m]$
$\dot{r}$	Velocity	$[\frac{m}{s}]$
$\ddot{\vec{r}}_g$	Acceleration of JUICE	$[\frac{m}{s^2}]$
$\ddot{\vec{r}}_{geo}$	Geopotential acceleration	$[\frac{m}{s^2}]$

$R$	Radius	[m]
$R_S$	Radial Scale	[m]
$\rho$	Density	$[\frac{kg}{m^3}]$
$\rho$	Residual (Section 1.2.3)	[-]
$\dot{\rho}$	Range rate	$[\frac{m}{s}]$
$s$	Position	[m]
$S_{n,m}$	Sectoral harmonic coefficient	[-]
$\bar{S}_{n,m}$	Normalized sectoral harmonic coefficient	[-]
$\sigma_n$	Degree variance	[-]
$\mathbf{r}$	Position vector	[m]
$t$	Time	[s]
$T$	Temperature	[K]
$t_c$	Count time interval	[s]
$\tau_d$	Downlink light time	[s]
$\tau_u$	Uplink light time	[s]
$\theta$	Azimuthal angle	[rad]
$\Theta$	Moment of inertia factor	[-]
$U$	Gravitational potential energy	$[\frac{m^2}{s^2}]$
$V$	Gravitational potential energy	$[\frac{m^2}{s^2}]$
$V_q$	Volume Square	$[m^3]$
$x$	Distance from plane defined by $z$ and $y$ axis	[m]
$y$	Distance from plane defined by $z$ and $x$ axis	[m]
$z$	Distance from plane defined by $x$ and $y$ axis	[m]

# ABBREVIATIONS

1D	One dimensional
3D	Three dimensional
3GM	Gravity and Geophysics of Jupiter and Galilean Moons
EPSC	European Planetary Science Congress
ESA	European Space Agency
Fe	Iron
FeS	Iron-Sulfide
GALA	Ganymede Laser Altimeter
gmt	Gene Matrix Transposed
GSHP	Global Spherical Harmonics Package
H <sub>2</sub> O	Water
HST	Hubble Space Telescope
J-MAG	A Magnetometer for JUICE
JANUS	Camera System
JUICE	Jupiter Icy Moons Explorer
MAJIS	Moons and Jupiter Imaging Spectrometer
MgSO <sub>4</sub>	Magnesium-sulfate
MoI	Moment Of Inertia
PCN	Point Control Network
RIME	Radar for Icy Moons Exploration
RK4	Runge-Kutta 4
wt%	Weight percentage



# GANYMEDE: A FROZEN ENIGMA

In 2022, ESA plans to launch the JUICE (JUperiter ICy moons Explorer) mission which will spend at least three years making detailed observations of Jupiter and three of its largest moons: Ganymede, Callisto and Europa [10]. These moons are currently a hot topic within the science community as their interiors are expected to include oceans consisting of liquid water [45] [18]. These oceans could harbor life [11]. Currently little is known about the exact composition and structure of these interiors as there only have been remote observations and a few fly-by's. The JUICE mission will provide more detailed information on the moons. This thesis research will be focused on Ganymede as JUICE will be the first human-developed satellite to orbit this moon. It will provide insight on how different possible internal density distributions of Ganymede influence the gravitational potential field of the moon. Variations of the gravitational potential field measured by JUICE can then directly be utilized to determine from which internal aspects these originate.

Ganymede is one of Jupiter's 70 moons and the largest of the four Galilean satellites. It is the most massive and largest moon within the Solar system and is the largest body without a substantial atmosphere [9] [12]. Ganymede stands out as a potential scientific target due to several specific reasons. The most remarkable being its intrinsic magnetic field [41]. Only two other solid bodies within the Solar System generate such a magnetic dipole field; Earth and Mercury. The complex interactions of Ganymede's magnetic field with Jupiter's magnetic field are unique and could provide a lot of new knowledge when studied [12]. Measurements from Galileo and the Hubble space telescope [39] suggest that a subsurface layer of (saline) water is most likely present within the moons interior. If present and saline, this water could be a good conductor of electricity, generating the magnetic field. It is expected that the internal ocean of Ganymede will consist of more water than all surface water on Earth combined [9].

The size of Ganymede, combined with its mass and inertia factor, suggests that the interior of the moon is fully differentiated and consists of both ices and higher density layers [50] [1]. The magnetic field of Ganymede could point towards a complex core, which is another possibility for the generation of this field. It could thus be that the core of Ganymede consists of liquid iron-rich elements which generate and maintain this magnetic field [1] [17] [43]. The surface of the moon includes both cratered and very old terrain, together with areas that are younger and consist of a lot of grooves and ridges [46] [47]. This could indicate that there was tectonic activity within Ganymede or that icy volcanism was present in the past to form these younger areas. [12] As liquid water will be present within Ganymede, other questions that remain are how habitable the moon could be. Are biosignatures present on Ganymede and what are the exact elements that are present on the moon? Are elements, like carbon and oxygen, present such that the moon could support life? [9] [12]

This chapter will provide the reader with an introduction on Ganymede and what has been discovered about this icy moon in Section 1.1. It provides insight in the JUICE mission and its goals in Section 1.2. From this information the current, most important, knowledge gaps were determined, which are discussed in Section 1.3. These form a foundation for the research question and objective, around which this thesis research is based. These are discussed in Section 1.4. Finally, the chapter concludes with an overview of the global structure of this report in Section 1.5.

## 1.1. PREVIOUS DISCOVERIES

Early theories and observations on Ganymedes interior date back to the 60's and 70's. Photometric, (mass) spectrometric and polarimetric studies of minor planets and satellites from Earth determined several aspects for the Galilean moons. It was determined which elements are present in the moons, in what percentual quantities these are present and the approximate size of the bodies. From these characteristics it could be concluded that the densities for the Jovian satellites vary from Moon-like (Io) to ice-like (Ganymede/Callisto) [56] [20] [13] [24]. The results of these studies did include large uncertainties as these were purely based on

observations made from the Earth's surface, but could be used as a foundation for further investigation of the different possibilities for the interiors of icy moons.

In the mid 70's, a new method was developed with a higher observation precision: occultation. This method observes a body while it passes in front of another celestial object [34]. This provided more precise information about the density of the Galilean satellites. The outer two satellites consist of a lower density material as the inner satellites and thus would at least be partly made out of ices/water. Radar observations of Ganymede indicated that the surface of this Jovian moon is rougher than the surfaces of Mars/Venus/Mercury [8]. This became apparent due to Ganymede reflecting power from the entire disk instead of just from its centre, which is the case for a smooth body. This brought up the debate if the surface of Ganymede could perhaps consist of rocks and/or minerals, as an icy surface usually reflects like a smooth body.

### 1.1.1. DIFFERENTIATION

It was demonstrated [24] that the internal structures of Jupiter's Galilean satellites could have been extensively molten due to radioactive decay within the satellites. For icy bodies, he showed that large objects above 900 km in radius should contain molten and differentiated interiors. This is based on the steady-state balance between heat liberation within the objects interior and the net flux conducted to the surface [24]. Jupiter's satellites have surface temperatures which suggest these have been extensively molten in the past. The interior of larger bodies would consist of a relatively thin ice crust and a deep liquid mantle. The center of the object would be composed of hydrous silicates and iron oxides and thus would have a 'muddy' consistency. If the object was ever completely molten, the surface will be made up by mostly water ice [24].

In 1979 it was suggested [31] that due to the low melting temperature of ice in combination with different heating processes, early melting may have been extensive on Ganymede. The following heating processes were considered:

- **Impact/Accretional heating:** Warming up of a body due to forces and shocks applied to it by external objects which collide with the body.
- **Tidal heating:** The conversion of tidal energy to heat due to friction, which usually is subsurface friction for icy-moons.
- **Radiogenic heating:** The thermal energy released as a result of spontaneous nuclear disintegrations. In the Earth, the major isotopes concerned today are of the elements uranium, thorium, and potassium.

Taking these suggestions into account leads to an interior which consists of an icy lithosphere, this is the outer-most shell of a body. For a body that undergoes significant amounts of melting, this is the solid-state ice crust overlying a liquid-water mantle. The models used [31] predict that large amounts of melting occurred during the evolution of a homogeneously-accreted body. Therefore, the present state of the interior of Ganymede is expected to be largely liquid. Due to large amounts of melting, the ice and silicate components within the moon are rapidly segregated. This results in the current interior of Ganymede to consist of a silicate core surrounded by a liquid-water mantle.

Early theories [33], [30], [15] suggested that tidal heating would be of influence on the evolution of natural satellites orbiting a dominant body. Resonance between different bodies can force eccentricities on the orbits of the bodies. For the Jovian satellites Io, Europa and Ganymede this is an 1:2:4 ratio. During each orbit of Ganymede, Europa orbits twice and Io orbits four times around Jupiter. When the tides induced by the host body are huge, as for Jupiter [33], these forced eccentricities cause a large amount of tidal dissipation within the natural satellites. This heats up the interior of the satellites as these undergo a 'deforming' effect. Io is an extreme example and is the only Jovian moon which shows present day activity on its surface due to these forced eccentricities [18]. The heat induced by this effect can cause the melting of icy interiors, creating internal oceans. The combination of these tides and eccentricities can cause currents within an internal ocean [5]. These currents in turn will generate heat due to tidal dissipation within the body through friction of the liquid layer with the adjacent solid interior layers[53].

### 1.1.2. SURFACE FEATURES

In 1979, Voyager 1 and Voyager 2 were the first space missions to observe the outer solar system from a close distance with different instruments [46] [47]. This resulted in new information about the outer planets and

the natural satellites which orbit these planets.

Voyager 1 was the first to observe the Jupiter system from a close proximity [46]. From these observations new knowledge was obtained about the natural satellites orbiting Jupiter. The Galilean satellites of Jupiter have vastly different surfaces. Volcanism dominates the surface of Io and complex tectonics affect Ganymede's and Europa's surfaces. Callisto shows huge impact features and flattened remnants.



Figure 1.1: Image of Ganymede taken by the Voyager 1 spacecraft [46].



Figure 1.2: Higher resolution image of Ganymede taken by the Voyager 1 spacecraft, which shows the difference between the cratered and grooved terrain types [46].

Complex stripes with an approximately equal width that are brighter than the other parts of its surface were observed on Ganymede. These stripes occur in several different patterns at different locations on Ganymede's surface (like in the bottom-left corner of Figure 1.1). Higher resolution pictures showed that the surface of Ganymede consists of two different types of terrain. Figure 1.2 clearly depicts cratered and grooved sections of terrain. The latter originates from the complex strips which have already been discussed. It shows darker, cratered terrain and lighter, grooved terrain. The overall crater density on the grooved terrain was observed to be only one-tenth of the crater density on the cratered terrain. This indicates that the grooved terrain is younger than the cratered terrain, which could mean that resurfacing occurred at several locations on Ganymede's surface. The grooves are generally curved and include sharp bends, which means that it is most unlikely that these are formed by strike-slip tectonics. There seems to be no major-relief on Ganymede, such as large mountainous landforms or basins. This is probably because Ganymede has a muddy interior [24]. This induces creep within its icy crust reducing large forms of relief [19].

Voyager 2 [47] provided data about the Jovian system which proved to be a great addition to the Voyager 1 images. New observations of Ganymede were made, resulting in better insights about the natural satellite.



Figure 1.3: Image of Ganymede taken by the Voyager 2 spacecraft [47].



Figure 1.4: Higher resolution Voyager 2 image of Ganymede which shows grooved terrain (the bright strip) created by a fault [47].

It observed the other hemisphere of Ganymede, complimenting the previous observations of Voyager 1. Consisting of the same type of regions as the first hemisphere, Figure 1.3 depicts the second hemisphere. A large dark circular feature is present (top middle) together with the light grooved terrain and darker cratered terrain. The resolution is three times better as the resolution of Voyager 1. Therefore, a larger variety of complex forms within the grooved terrains can be observed. Large transform faults were found, which are represented by bright strips on the surface of Ganymede (Figure 1.4). Some of the craters are cut through by these fault systems. This suggests that Ganymede's surface is partly formed by expansion and spreading of the crust.

This data suggests that Ganymede had an active crust in its early history, during which the younger grooved terrain replaced the older cratered terrain. Viscous flow under the surface has reduced the relief of both moderate and large topographic anomalies (craters and basins). [46]. Most features on Ganymede's surface were at least partly formed by spreading of the crust or local expansion [47]. It was determined that Ganymede is composed of approximately 60% rock and 40% ice, with a mean density of  $1.940 \text{ g/cm}^3$  [1].

In 1981 new models for the interiors of the Galilean satellites were proposed. The appearance of Ganymede's surface, observed by the Voyagers, is considered evidence that the outer layers underwent ice-rock differentiation. Therefore, these models consist of an ice outer layer which surrounds an undifferentiated ice-silicate shell. The silicates from the outer layer have migrated to the center of the model and formed a rocky core due to gravitational instabilities [40]. Previous discussed models [31] of Ganymede consist of a solid silicate core surrounded by water or ice mantles. Radiogenic heating and accretional heating are the main physical processes considered responsible for the separation of water/ice from rock inside the moon. The new models show that sub-solidus convection in a homogeneous ice-silicate mixture can counter radiogenic heat. This prevents the melting of ice inside the moon [40] [37]. It is unlikely that the ice melted during a later period in time as a radio-active heat source degrades over time. Accretional heating can only melt the outer layers of the moon, causing differentiation of ice and silicates.

### 1.1.3. MAGNETIC FIELD

From 1991 onwards, a lot of new information has been generated on the Jovian system. The Galileo satellite has provided the largest contribution as other missions (like JUNO, Ulysses and Cassini-Huygens) consisted of brief flyby's. Galileo performed several fly-by's of Ganymede, providing new theories for possible interiors.

The Doppler shift of radio signals from Galileo showed that Ganymede is strongly differentiated. It includes a dense core, which is surrounded by a thick shell of ice [41]. It was observed that Ganymede has a magnetic field which is aligned approximately anti-parallel to Jupiter's magnetic field. Therefore, Ganymede's core probably consists of an outer silicate mantle which surrounds a liquid inner core of iron or iron-sulphide [41]. The core might include sulphide, as adequate convection is required within the core to sustain a dynamo. Concentrations of sulfur can drive compositional convection [17]. This liquid inner core could generate the

magnetic field through dynamo action. The dynamo theory describes the process through which a rotating, convecting and electrically conducting fluid can maintain a magnetic field over astronomical time scales. Other options for the presence of the magnetic field, remnant magnetization or magneto-convection, are unlikely [41].

An electrically conducting fluid has to be present in the body to generate the magnetic field. In the case of Ganymede there are two possible regions in which this could occur; an ocean of salty water at the bottom of the satellite's ice shell or a metallic inner core. A salty ocean could only generate the magnetic field if large velocities within the fluid are present. This however seems improbable as the size of the convective motions within this ocean should then be  $10^4$  times larger as the motions within Earth's core. The velocities required exceed the velocities predicted by Kolmogorov scaling, which represent the smallest scales in turbulent flow by several orders in magnitude [41]. Therefore, a liquid metallic core is most likely required to generate Ganymede's magnetic field. It thus seems most probable that Ganymede's interior consists of an inner metallic core surrounded by an outer silicate mantle. The inner core will most likely consist of liquid iron, but probably will include traces of sulfur [1] [17] and might even include hydrogen [43]. The metallic core most likely consists of a density between  $8.000 \text{ g/cm}^3$  (iron) and  $5.150 \text{ g/cm}^3$  (iron-sulfide). [1] [17] [54].

#### 1.1.4. GRAVITATIONAL COEFFICIENTS

The Galileo spacecraft provided measurements on Ganymede's overall density and spherical harmonics  $J_2$  and  $C_{22}$  of its gravitational field. From this data it could be concluded that the interior of Ganymede is differentiated into a core and a mantle [1].

The Galileo spacecraft passed Ganymede twice. These encounters targeted the optimization of gravitational field data using radio Doppler measurements. The first encounter would pass Ganymede near its equator, where the measurements are sensitive to  $C_{22}$ . The second encounter would pass near one of Ganymede's poles, where the measurements are sensitive to  $J_2$ . The obtained coefficients (Table 1.1) are slightly correlated and can still vary with respect to the obtained values. The coefficients are assumed hydrostatic, hence the fluids within Ganymede are at rest or the flow velocity is constant over time. Thus external forces are balanced by a pressure gradient force.

Table 1.1: The measured gravity coefficients of the two Galileo fly-by's.  $\mu$  is the correlation coefficient [1].

	Encounter 1	Encounter 2
$J_2$	$(126.0 \pm 6.0) \times 10^{-6}$	$(127.8 \pm 3.0) \times 10^{-6}$
$C_{22}$	$(37.8 \pm 1.8) \times 10^{-6}$	$(38.3 \pm 1.0) \times 10^{-6}$
$\mu$	0.7399	0.5870

The moment of inertia of Ganymede was determined using these coefficients and its known rotational parameter [1]. The axial moment of inertia factor was too low, 0.3105, for an interior which consists of a constant density. A lower inertia means that the body's interior gets more concentrated towards its centre. The inertia was even amongst the smallest for any planet/satellite within the Solar system. Thus the interior of Ganymede is strongly differentiated.

#### 1.1.5. GLOBAL LAYERS

Half of Ganymede's surface is old and shows no signs of volcanic activity and/or melting. The other half has resurfaced long after heavy bombardment occurred. Detailed interior structures of Ganymede are determined by considering its thermal evolution and the coupled orbital evolution of Ganymede.

The orbits of the Jovian Galilean moons have evolved through different orbital resonance phases [45] [18]. Passage through eccentricity-pumping resonance could lead to the resurfacing of Ganymede, impacting its interior due to thermal runaway (Figure 1.5). This occurs in situations where an increase in temperature changes conditions which again causes an increase in temperature, often leading to a destructive result. It is a type of uncontrolled positive feedback and conditions should be quite specific for this to occur.

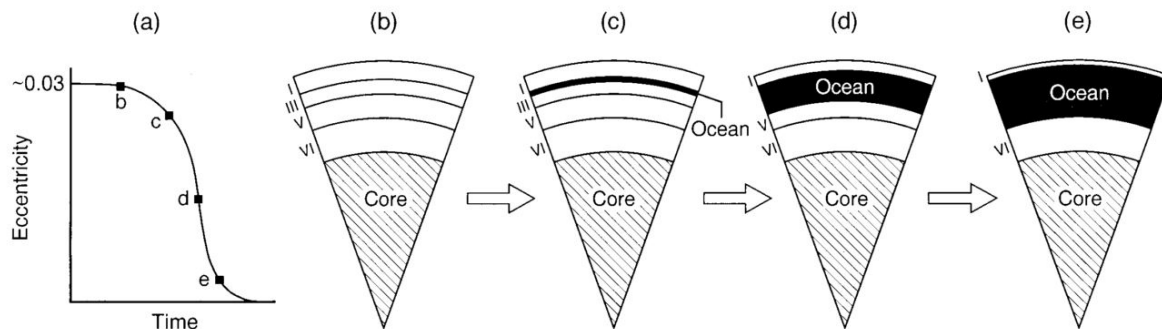


Figure 1.5: The effect of the thermal runaway over time on the interior of Ganymede, it shows that the initially frozen ice I and III layers undergo melting and form an internal ocean. The eccentricity of Ganymede's orbit over time is given in (a), which is expected to drop when orbital resonance occurs.

Figure 1.5 depicts how the ice layers evolve through thermal runaway. The inner ice I and III layers melt due to heating and form an internal ocean. The outer ice I and inner ice VI layers remain solid. This is due to the outer layer remaining at low temperatures and the higher melting point for Ice VI, which not reached for the inner layer.

#### INTERIORS INCLUDING SALINE OCEANS

It is a possibility that saline oceans exist within Ganymede's interior [54]. Pressures up to 1.2 GPa occur at the water-rock interface, resulting in ice I, V and VI layers sandwiching the ocean [50] [1] [22]. Salinity will influence the thickness of these ice layers as it alters the thermoclines of water [54]. Observations of the auroral ovals occurring on Ganymede with the Hubble Space Telescope (HST) point out that a saline subsurface ocean could exist within its interior [39].

The influence of salinity within the internal oceans on the interior structure of Ganymede was assessed [54]. Phase-equilibrium data was used to predict the freezing of water ice in the presence of magnesium-sulfate [58]. Combined with the thermal profiles in Ganymede's interior, the thicknesses of the ocean and ice layers (I, III, V and VI [50]) can be determined. The models use the total mass of Ganymede, its moment of inertia and assume a liquid core. The results for all different considerations can be found in Figure A.1.

The iron core- and silicon mantle radii are restricted by the known density structure of Ganymede, together with the determined layer thicknesses in the overlaying material [54]. For the lowest of boundary temperatures, the ocean should be at least 10 wt% (weight contents) saline for a liquid layer to occur. Otherwise, it would freeze. In this case, the interior structure of Ganymede shall include only a thin liquid layer (31 km) surrounded by frozen layers of ice. Increasing the bottom melting temperature of the  $I_h$  layer increases the thickness of the liquid inner layer for an equal wt%. For a constant bottom melting temperature, a more saline ocean layer will be thicker. As salinity decreases the melting point of water, a larger liquid state is present at lower temperatures.

The models of Vance et al [54] conclude that the interior of Ganymede consists of an outer ice  $I_h$  layer which is 13-148 km thick. Beneath this ice  $I_h$  the liquid layer can be found, varying from 31-753 km thickness. When the bottom melting temperature is low, Ice III, V and VI layers exist below the ocean with a thickness up to 52, 155 and 447 km respectively. However, when salinity and boundary temperatures increase, the Ice III and V layers will melt entirely (first ice III, then ice V). In the most extreme case, a layer of only 130km of frozen Ice VI remains. Below the ice VI layer a silicon mantle and iron core complete the interior model of Ganymede. No liquid layer exists below the high pressure ice layers, this is due to the increasing pressure with depth and because high pressure ices occur at higher temperatures [21]. The boundary layer between the ocean and high pressure ices probably consist of a slushy, snowy mixture of liquid and ices.

#### 1.1.6. LOCAL DENSITY VARIATIONS

Local geometric density variations are present within celestial bodies. For a rocky body like Earth, a lot about such anomalies is already known. Mountains, ocean trenches, lakes (and other types of large reservoirs),

internal mass distributions, tides, hollow caves and/or large buildings in cities are all examples. The approximate size of the effect on Earth's gravitational acceleration due to these anomalies is given in Figure 1.6. When the anomalies decrease in size, a higher degree and order spherical harmonics model is required to properly determine the effects of the anomaly on the gravitational potential field. More information on the spherical harmonics representation can be found in Appendix B.

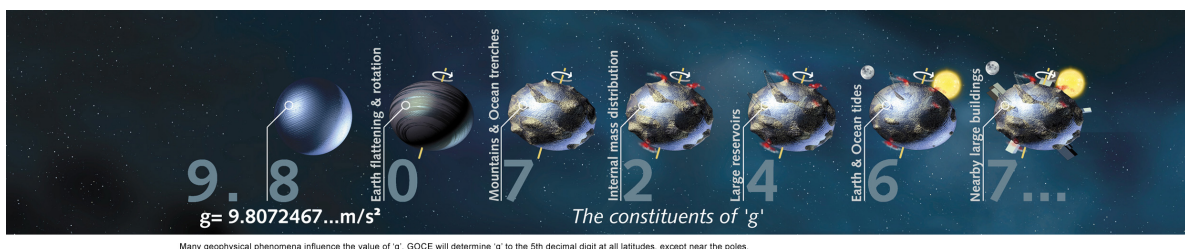


Figure 1.6: How the Earth's gravity is influenced by its shape/interior<sup>1</sup>.

The internal dynamics of icy celestial bodies are different than that of rocky planets. There is less information available on the icy body dynamics as extensive in-situ research has been performed on the Earth. This research has provided large amounts of knowledge about rocky planet interiors and dynamics. From theories about internal structures of icy bodies and the physics of water, several different anomalies arise that could be present in icy bodies. These could influence the gravitational potential field of such a body. Several of these are depicted in Figure 1.7.

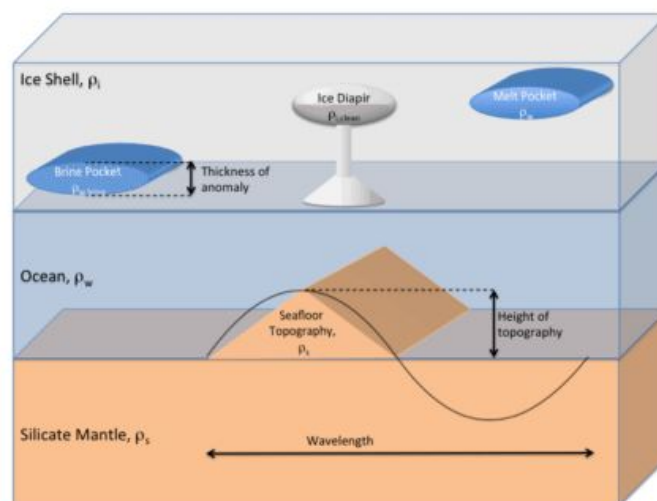


Figure 1.7: Some examples of anomalies which could be present in an icy body [55].

Several anomalies are the same as for rocky planets. Depending on the icy bodies crust thickness, mountains and/or basins may be present at the surface. Next to general internal mass distributions, more specific anomalies could occur within the ice layers of icy bodies [55] [32]. Melt pockets could be present, which are local spots where ice has molten and formed a pocket filled with liquid water. Another form of such a melt pocket, a brine pocket (a pocket filled with a saline liquid), could occur when salts are present in the icy body.

As the possibility exists that the interior includes a liquid (water) layer between the mantle and crust, several new anomalies could arise. The ice crust has a lower density than the liquid layer below. Therefore the crust 'floats' on the liquid layer and resurfacing events could occur. Thickness variations of the crust could thus be present. The presence of a mixed ice/liquid 'slush' at certain locations at the boundary between the

<sup>1</sup>How is the Earth's gravitational acceleration influenced by its shape/interior: <https://earthzine.org/2007/10/29/esas-earth-observation-programmes-advancing-earth-science-through-new-sensing-technology/comment-page-1/>, [cited 12-04-2018]

ice and liquid layers could influence local density. These anomalies could both affect the gravitational potential field of Ganymede. The interactions between the crust and ocean layers could induce ice diapirs within the crust. These are local liquid intrusions resulting from the liquid layer. The tides within the liquid layer are of importance and could occur both locally and globally. Warm ice convection and hydrothermal plumes in the subsurface ocean could influence the gravitational potential field. Finally, the thicknesses and consistencies of the core, mantle, liquid and ice layers will influence the gravitational potential field of the icy body.

Finally, a mass or mass deficiency at the surface will naturally be compensated by an inverse mass anomaly beneath the surface. Hence beneath a mountain-chain a less dense area is present or underneath deep valleys high density areas occur. These attributes are examples of isostasy. This is a theory which requires a celestial bodies surface layer (lithosphere) to be rigid and to float on, or in, the layer beneath it (asthenosphere).

### 1.1.7. KNOWN CHARACTERISTICS

Discussed observations result in some important characteristics of Ganymede, these have been listed in Table 1.2.

Table 1.2: Characteristics of interest for Ganymede.

	Value	Uncertainty
Radius [km]	2634.1 [44]	0.3 [44]
Mass [ $10^{23}$ kg]	1.4817 [44] [1]	0.0002 [1]
Inertia Factor [-]	0.3105 [44] [1] [54]	0.0028 [44] [1] [54]
Core Pressure [GPa]	~10 [49] [54]	2 [49] [54]

These characteristics and uncertainties provide some restrictions on Ganymede's internal composition. The low MoI factor (Section 1.1.4) already suggests that the interior of Ganymede should be strongly differentiated. Thus, Ganymede is likely to consist of a dense core (and mantle) surrounded by less dense layers like ice and water. The uncertainty of the core pressure is substantial as currently the exact internal dynamics of Ganymede are unknown.

## 1.2. JUPITER ICY MOONS EXPLORER

To obtain more information about Ganymede, ESA will send JUICE in 2022 to perform more detailed measurements by orbiting this moon. JUICE will perform investigations of Jupiter and its system including its inter-relations. A particular emphasis has been put on Ganymede as a planetary body, potential habitat and on its magnetic and plasma interactions with the surrounding environment. Ganymede, Europa and Callisto are all believed to harbor internal oceans and are different with regard to internal dynamics, structure and formation. Therefore observing these moons will extensively contribute to the understanding of the habitability of icy worlds. More knowledge will be gained on the history of the Jovian system, which will provide insights in how gas giants and their satellites are formed and evolve<sup>2</sup>.

It will take JUICE 7.6 years to reach the Jovian system. Once in-situ, it will start the second phase of the mission in which the satellite will observe Jupiter, the inner Jupiter system and Ganymede/Callisto/Europa through fly-by's. This phase will take about 2.5 years. When completed, JUICE will transfer to an orbit around Ganymede. It will orbit Ganymede in two different ways. Initially in an elliptical orbit, followed by a low altitude circular orbit at 500km height. <sup>3</sup> [12].

### 1.2.1. INSTRUMENTS

JUICE hosts eleven different instruments of which several are of relevance to this thesis. These are listed below<sup>4</sup> [12].

1. 3GM - A radio science package. A X/Ka transponder and an ultra stable oscillator are used to study Ganymede's gravitational potential field up to order 15 or higher [12]. These measurements can be

<sup>2</sup>JUICE's science objectives: <http://sci.esa.int/juice/50068-science-objectives/> [cited 12-04-18]

<sup>3</sup>JUICE mission scenario and operations: <http://sci.esa.int/juice/50074-scenario-operations/> [cited 12-04-18]

<sup>4</sup>JUICE's science payload: <http://sci.esa.int/juice/50073-science-payload/> [cited 12-04-18]

compared to the spherical harmonics coefficients resulting from this research. This could provide better estimates of Ganymede's internal structure.

2. JANUS - An optical camera system. Utilized to study the morphology of the moons. It will provide a better understanding on Ganymede's topography. This can be beneficial for this research as it is one of the anomalies considered.
3. MAJIS - A spectrometer which can characterize the ices and minerals on the surfaces of the icy moons. This information can be used to confirm the consistency of Ganymede's ice crust. It could also provide new knowledge on resurfacing events.
4. GALA - A laser altimeter which will study the topography and morphology of the icy moon surfaces and the tidal deformation of Ganymede. These measurements can be used for the same purposes as those of JANUS.
5. RIME - A radar which will study the subsurface structure of the icy moons up to 9 kilometer depth. This instrument could detect shallow pockets and other anomalies present within Ganymede's ice shell. If the shell is thin it could also detect the internal ocean.
6. J-MAG - A magnetometer which will study the subsurface oceans of the icy moons and the interaction between the magnetic fields of Jupiter and Ganymede. It could provide information on the consistency and thickness of Ganymede's internal ocean and Ganymede's core since these both are related to its magnetic field.

### 1.2.2. OBJECTIVES

Several instruments on JUICE aim to look into how the composition of Ganymede affects the particles near the moons surface. For example the magnetic field interactions between Jupiter and Ganymede influence aurora's on both bodies. Other instruments will investigate the outer layers of the moon's exosphere. This will provide a better understanding of which elements these layers consist and if these have an effect on the orbiting spacecraft.

The measurements performed by Galileo on Ganymede's ocean salinity were not conclusive due to the magnetic field interactions of Jupiter and Ganymede. A lot of questions remain considering the internal ocean. Therefore, one of the main objectives of JUICE will be to gain a better understanding on the ocean's depth, size and composition. More information will be obtained on the thicknesses of the different layers within the moons interior, including its core and the complexity of the core. This will reveal if, and how, it could generate and sustain Ganymede's magnetic field. The observations provided by the instruments listed above will all be key to obtain this goal.

Stereo imaging and laser altimetry will determine what geological processes formed Ganymede's surface. Radar will be able to penetrate the subsurface up to 9 kilometers, obtaining a minimal thickness of the crust. If the crust is thin, it could also detect an internal ocean. High resolution observations will be made of several areas to obtain a more detailed understanding of the local geology. A better estimation of Ganymede's surface composition could lead to information on how habitable the moon could be. [9] [12].

### 1.2.3. MEASURING GRAVITY EFFECTS

JUICE will measure Ganymede's gravitational potential field up to at least an order and degree 15. The 3GM instrument will use radio tracking to provide information on the static gravity field, rotational state and tidal deformation of Ganymede. JUICE will use two-way Doppler tracking, which is obtained by integrating Doppler counts over a time interval  $t_c$ . Doppler tracking is based on the exchange of photons between a ground tracking station and a distant spacecraft [25].

In two-way Doppler tracking, the ground station transmits a signal to the spacecraft. In turn the spacecraft tracks the phase of the uplink signal and generates a phase coherent downlink signal. The ground station then compares the received frequency with the initial transponded frequency to obtain a frequency shift. Then, the measured range-rate is modeled as the difference between the two-way ranges at the start and end of the time-interval. Thus for a single measurement four light-time iterations are required. This is depicted in Figure 1.8.

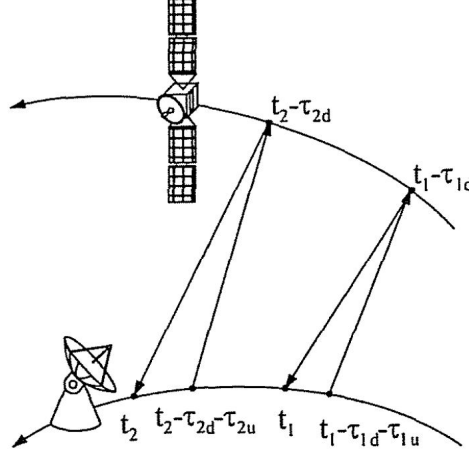


Figure 1.8: The motion of the satellite and the ground station during signal travel time for two-way Doppler measurements[26].

In Figure 1.8  $t_2$  is the end of the time-interval and  $t_1 (= t_2 - t_c)$  the beginning of the count interval start. The associated carrier signal was transponded by the satellite at  $t_2 - \tau_{2u}$ . The ground station transmitted it at time  $t_2 - \tau_{2u} - \tau_{2d}$ . In a similar way, the signal at  $t_1$  was sent by the satellite at time  $t_1 - \tau_{1u}$  and the ground station broadcasted at time  $t_1 - \tau_{1u} - \tau_{1d}$ . Then the average range rate measurement can be determined using Equation 1.1[26].

$$\vec{\rho}(t) = \frac{c}{2} \frac{(\tau_{2u} + \tau_{2d}) - (\tau_{1d} + \tau_{1u})}{t_c} = \frac{1}{2} \frac{(\rho_{2u} + \rho_{2d}) - (\rho_{1d} + \rho_{1u})}{t_c} \quad (1.1)$$

Where the individual range rates involved are given by  $\rho_i = c\tau_i$ .  $\tau_{id}$  are the downlink light times and  $\tau_{iu}$  are the uplink light times. The 3GM instrument will provide range-rates for the JUICE mission. These can be used to determine the geopotential forces which Ganymede exerts on JUICE. This is done using Equation 1.2.

$$\vec{f}_g = \vec{\nabla} V = \vec{\nabla} \left[ \frac{\mu}{r} \left( \sum_{n=0}^{\infty} \sum_{m=0}^{\infty} \left( \frac{R}{r} \right)^n \bar{P}_{n,m}(\sin(\phi)) [\bar{C}_{n,m} \cos(m\lambda) + \bar{S}_{n,m} \sin(m\lambda)] \right) \right]^B \quad (1.2)$$

Equation 1.2 is the classical description of the gravity field potential for a celestial body. More background theory on this equation and spherical harmonics can be found in Appendix B.  $C_{n,m}$  and  $S_{n,m}$  are the tesseral and sectoral components of the spherical harmonics representation. An estimation of these values and the orbit of JUICE will be used during the calculations.  $\vec{f}_g$  is the acceleration of JUICE,  $V$  the gravitational potential,  $\phi$  the polar angle measured from the positive z-axis to the radial. Furthermore  $\lambda$  is the longitude,  $R$  the radius of the body,  $n$  the degree considered,  $m$  the order,  $\mu$  the gravitational parameter and  $P_{n,m}$  the associated Legendre function.

Models for other forces of influence, like third body perturbations, should be included to obtain proper estimates of the gravitational potential. 3GM has an accuracy of 1-3  $\mu\text{m/s}$  for the range-rate. It will exploit the X and Ka bands at 7.2-8.4 Ghz and 32.5-34 GHz respectively [12]. Altimetry will be used to determine the extent to which topography affects the gravity field and if it is well compensated.

#### 1.2.4. EXPECTATIONS FROM ESA FOR JUICE

Figure 1.9 depicts how the different measurements and their uncertainties will result in a thickness range for the crust and ocean of Ganymede. These measurements will be provided by JUICE.

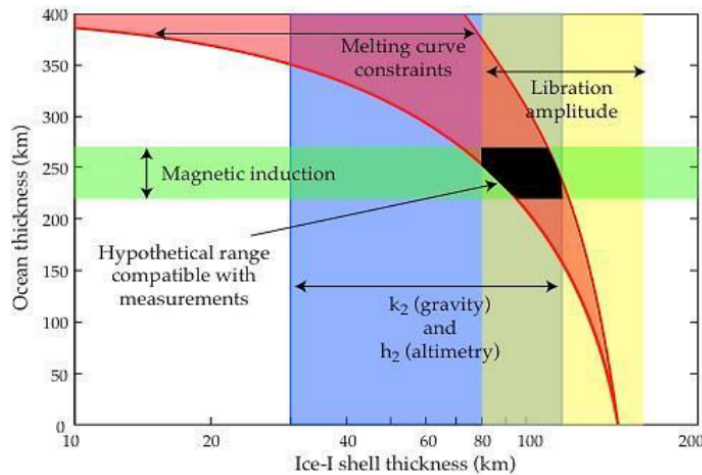


Figure 1.9: ESA's schematic view of the strategy to characterise Ganymede's crust and liquid layer by using different techniques. [12]

The black area indicates the hypothetical range resulting from the combination of all measurement uncertainties. The uncertainty of the Love numbers  $h_2$  and  $k_2$  are due to the ambiguity of the rigidity of ice I. The libration amplitude depends on the density contrast between the ice I and ocean layers. Magnetic induction signals will vary based on the electrical conductivity of the ocean. In Figure 1.9 error bars have been exaggerated.

### 1.3. KNOWLEDGE GAPS

Currently the understanding about Ganymede is limited by the Galileo mission, which only passed Ganymede 5 times during fly-by's. This providing the most in depth information up until today. Hence, a lot of interesting questions remain with respect to the exact composition of the moons interior including [12];

1. How does the interior of Ganymede generate its magnetic field?
2. Is liquid water present within the interior of Ganymede?
3. Of which elements do the differentiated layers within Ganymede's interior consist?
4. How thick are the layers within the interior of Ganymede?
5. What type of density variations are present within the layers of the interior?

A precise gravitational model of Ganymede could provide information about the moon's interior. Currently only  $C_{2,0}$  and  $C_{2,2}$  are available. An orbiter or in-situ probes are required to achieve high-precision gravitational potential field models. This will change as JUICE is planned to orbit around Ganymede.

### 1.4. RESEARCH QUESTION

JUICE will provide an excessive amount of new information on Ganymede. New research can be performed to better understand the knowledge obtained by this mission. Therefore the research question of this thesis is formulated as follows:

#### ***What can JUICE's gravitational potential field measurements provide about Ganymede's interior?***

Three sub-questions were phrased to gain a better understanding about the different important aspects required to answer the research question.

- What are possible 1D homogeneous interior models for Ganymede?
  1. *What H<sub>2</sub>O phases are present and how can JUICE distinguish these?*
  2. *In what way are individual layer thicknesses correlated with respect to each other?*
  3. *How can these correlations be used to better analyze JUICE's measurements?*
  4. *How are layer thicknesses restricted to known observations of Ganymede?*
- What are possible 3D heterogeneous interior models for Ganymede?
  1. *Which heterogeneous variations are expected and measurable by JUICE?*

2. *What degree of spherical harmonics is required to model these heterogeneous models?*

- How is the gravitational potential field of Ganymede affected by the different heterogeneous models?
  1. *How do different 1D worlds affect variations within the gravitational potential field?*
  2. *How do local variations within a single homogeneous world affect the gravitational potential field?*
  3. *Is it possible to distinguish different worlds with the expected accuracy of JUICE?*

When all above questions are answered, one can find the research objective. This states:

**Determining the effects of expected density variations within Ganymede's interior on its gravitational potential field, as observable by JUICE.**

To obtain a better time-management for the project, as time is limited, the research objective has been split up into several sub-goals:

1. Homogeneous 1D modeling of Ganymede
2. Heterogeneous 3D modeling of Ganymede
3. Gravitational potential simulations.

Where each sub-goal will include a methodology, implementation, verification, analysis and reporting part. These sub-goals are the foundation for the three main pillars of which the project consists.



These three main pillars will return on various points within the report to provide the reader with an overview of the thesis research. Each of the next three chapters of this report will be based on one of the pillars.

## 1.5. STRUCTURE OF THE REPORT

The next part of this report, Chapter 2, will show how the 1D homogeneous models are generated and implemented. It also provides the different requirements that the different models should adhere to. The 3D heterogeneous models and their variations are elaborated on in Chapter 3. Chapter 4 completes the methodology and discusses the modeling of the gravitational potential field variations using the determined interior models of Ganymede. Verification and validation will follow in Chapter 5 to determine that the algorithm and all of its modules work as intended. Results of the research are provided in Chapter 6 and these results will be discussed in Chapter 7. Finally, conclusions and recommendations which are based on the outcome of the research are given Chapter 8.

## HOMOGENEOUS 1D MODELING

Chapter 1 already discussed the findings and thoughts of experts on the internal structure of Ganymede. To determine which type of interiors are possible, taking into account current knowledge, an extensive set of simulations has to be performed. The methods behind these simulations and how the interiors of the models will be structured are discussed in this chapter. Section 2.1 discusses the main considerations behind the determination of the homogeneous 1D models of Ganymede. The different requirements for these models are provided in Section 2.2. Finally, the implementation of the different theories is provided in Section 2.3.

### 2.1. MAIN CONSIDERATIONS

Several theories exist behind the interior models of Ganymede (see Section 1.1.5). However, most recent models follow a common thread. These consist of an inner Fe/FeS core, which is surrounded by a mantle of silicon. Outer layers of several ice phases are present, including a liquid water ocean. This ocean could be saline due to the presence of magnesium-sulfate ( $H_2O - MgSO_4$ ). During the first part of this research, it is assumed that the interior of the moon consists of uniform spherically symmetrical layers. These all consist of a single element with a coherent density (hence 1D homogeneous layers). Due to the pressure and temperature ranges within the models, probably ice  $I_h$ , III, V and VI phases are present within Ganymede. These ice phases adhere to the known thermoclines for  $H_2O$ , which can be found in Figure 2.3. A brief discussion is included on the different layers in Table 2.1. Possible densities for each layer are also provided.

Oceans with wt0, 3, 5 and 10% salinity are considered [54]. This is equal to densities of 0.937, 1.047, 1.08 and 1.163 g/cm<sup>3</sup> respectively. These densities are based on a water density of 0.997 g/cm<sup>3</sup> and a MgSO<sub>4</sub> density of 2.66 g/cm<sup>3</sup>. The core density will also be varied, it can consist of 5.150 g/cm<sup>3</sup> (highest expected FeS percentage), 7.030 g/cm<sup>3</sup> (expected) and 8.000 g/cm<sup>3</sup> (pure Fe) [54] [3] [41] [22] [17]. This results in 4 different ocean salinities per core density, thus in total 12 model sets are analyzed.

Table 2.1: An overview of the layers found in the models.

Layer	Density [g/cm <sup>3</sup> ]	Description
Ice $I_h$	0.937	A hexagonal form of common ice. Almost all ice in Earth's biosphere is ice $I_h$ , except for a small amount of ice $I_c$ that is present in the upper atmosphere.
Liquid	0.997-1.163	The liquid water layer which can include different percentages of magnesium-sulfide. The density range is based on a salinity mass percentage of 0 - 10%.
Ice III	1.166	A form of solid matter which consists of tetragonal crystalline ice. It is formed by cooling liquid water to 250 K at 300 MPa. It is the least dense of the high-pressure water phases.
Ice V	1.267	Formed by cooling water to 253 K at 500 MPa. Most complicated structure of all the phases.
Ice VI	1.360	Formed from liquid water at 1.1 GPa by lowering its temperature to 270 K. It consists of tetragonal crystals.
Mantle	3.250	The mantle of Ganymede consists of silicon [54]. It is fully differentiated from the water phase layers.
Core	5.150-8.000	Ganymede's core consists of iron-sulfide or pure iron. The lower density is based on the maximum possible amount of sulfide [55]. The upper density on pure iron.

Temperatures within the models are not low enough for ice II to form. Ice IV is a metastable form of ice which

is not expected to occur within the moons interior. When considering the logical order in which the water phases occur with respect to pressure, a model as depicted in Figure 2.2 is obtained. The liquid layer can only occur between the ice  $I_h$  and the higher pressure ice phases [28] [51]. This is based on the phase stability of water. Models without a liquid layer will not be considered during this thesis research as it is unlikely that Ganymede is completely frozen [39] [54].



Figure 2.1: Ganymede's exterior as observed by different previous missions.

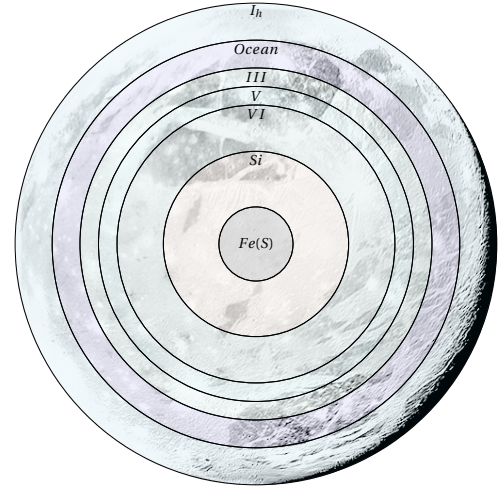


Figure 2.2: A possible representation of Ganymede's interior models, which include all considered layers. It is possible that certain models do not include all these layers, but only a selection. The thickness of the layers in the picture is not necessarily a good representation of the layers within the final selected models.

These are chosen for illustration purposes.

To learn more about layer thicknesses, correlations between layers and present elements within Ganymede, all possible 1D homogeneous layer combinations should be found. Models will be selected if these adhere to all requirements based on current knowledge on Ganymede.

## 2.2. MODEL REQUIREMENTS

Several requirements have been derived from information that has been acquired about Ganymede. This section of the report will provide these requirements and how these can be compared to the simulated models. These aspects of Ganymede and their uncertainties are once again provided in Table 2.2.

Table 2.2: Measured characteristics of Ganymede.

	Value	Uncertainty
Radius [km]	2634.1 [44]	0.3 [44]
Mass [ $10^{23}$ kg]	1.4817 [44] [1]	0.0002 [1]
Inertia Factor [-]	0.3105 [44] [1] [54]	0.0028 [44] [1] [54]
Core Pressure [GPa]	~10 [49] [54]	In the order of GPa [49] [54]

The uncertainty of the core pressure is substantial as currently the exact internal dynamics of Ganymede are unknown. However, it can be used to determine if the models are realistic and do not result in unexpected core pressures. The radius will be rounded to the nearest integer, 2634 km, as its value will be used in different loops. Therefore the uncertainty of the radius will not be considered. This will not have a large impact on the results as the lowest considered resolution of layer thickness is 10 km. Internal (hydrostatic) pressure and temperature distributions can also be determined for the models. Together with the known thermoclines of  $H_2O$ , it can be checked if the model's generated layers can exist at these pressures and temperatures. This is discussed in section 2.2.4.

The uncertainties will decrease significantly after JUICE arrives at Ganymede [12]. It will provide a better estimation for the requirements as it will perform in-situ measurements. The possible theoretical internal models can then be further narrowed down. This can be done using the models resulting from this research

as a foundation.

The generated models initially consist of layer thicknesses and densities. These cannot directly be compared to the requirements provided in Table 2.2. Sections 2.2.1-2.2.4 discuss how this data can be used to calculate the desired characteristics for each model. Then, the generated models can be compared to the requirements.

### 2.2.1. MASS

The density and thickness of the spherical shells within each generated model are known. Using this information, it can be determined if the model adheres to the different requirements. The mass of each shell can be calculated by using the fundamental principle to obtain the mass of a sphere provided in Equation 2.1 [49].

$$\frac{dM}{dr} = 4\pi r^2 \rho \quad (2.1)$$

Where  $\frac{dM}{dr}$  is the variation of mass with respect to the radius,  $\rho$  is the density of the material and  $r$  is the distance to the spheres centre. Each shell has a symmetrical shape with a continuous density. Thus Equation 2.1 can be integrated between the inner and outer radius for each individual shell. This results in Equation 2.2.

$$M_{shell} = \frac{4}{3}\pi r_{out}^3 \rho_{shell} - \frac{4}{3}\pi r_{in}^3 \rho_{shell} \quad (2.2)$$

In Equation 2.2  $M_{shell}$  represents the mass of each individual shell.  $\rho_{shell}$  is the density of the shell and  $r_{out}$  and  $r_{in}$  are the outer and inner distances of the shell to the center of the model. Equation 2.2 can be simplified to obtain Equation 2.3.

$$M_{shell} = \frac{4}{3}\pi \rho_{shell} (r_{out}^3 - r_{in}^3) \quad (2.3)$$

Then, the individual shell masses can be added to obtain the mass of the entire model as depicted in Equation 2.4.

$$M_{Model} = \sum_{i=1}^n M_{shell}(i) \quad (2.4)$$

In this summation  $n$  represents the total amount of shells and  $i$  indicates the shell considered,  $M_{Model}$  is the mass of the entire model. The total mass will then be compared to the determined mass of Ganymede, which is provided in Table 2.2. If  $M_{Model}$  has a value between the determined mass  $\pm$  the uncertainty of this mass, then the considered model will be accepted in terms of mass.

### 2.2.2. MOMENT OF INERTIA FACTOR

It will be verified if the model has an internal mass distribution which corresponds to the determined mass distribution of Ganymede. This can be done by comparing the inertia factor of the model to the measured inertia factor (Table 2.2). The moment of inertia factor is a dimensionless quantity that characterizes the radial distribution of mass inside a celestial body. It provides the amount of differentiation within a body, where a lower factor indicates a larger density difference throughout the model [1]. To obtain the inertia factor, the moment of inertia of a shell is determined. This is done using Equation 2.5. This simply subtracts the moment of inertia of an inner sphere from the moment of inertia of an outer sphere.

$$I_{shell} = \frac{2}{5} M_{shell} (r_{out}^2 - r_{in}^2) \quad (2.5)$$

Where  $I_{shell}$  is used to represent the moment of inertia of the considered shell in  $\text{kgm}^2$ . The mass of each shell is already known as a function of density. Equation 2.3 can then be substituted into Equation 2.5 to obtain the moment of inertia as a function of density (Equation 2.6).

$$I_{shell} = \frac{2}{5} \frac{4}{3} \pi \rho_{shell} (r_{out}^2 - r_{in}^2) (r_{out}^3 - r_{in}^3) \quad (2.6)$$

Or when expanded, this results into Equation 2.7.

$$I_{shell} = \frac{8}{15} \pi \rho_{shell} (r_{out}^5 - r_{in}^3 r_{out}^2 - r_{out}^3 r_{in}^2 + r_{in}^5) \quad (2.7)$$

Then, the total moment of inertia of the model can be determined by adding all individual shell moments of inertia. This is done through Equation 2.8.

$$I_{Model} = \sum_{i=1}^n I_{shell}(i) \quad (2.8)$$

The moment of inertia factor of the model can be determined by dividing the calculated total moment of inertia by the 'average' moment of inertia (Equation 2.10). This average can be calculated using Equation 2.9 and the average density of the model. Equation 2.9 is derived from Equation 2.7 with  $r_{in} = 0$ . The average density has been determined through the GM and radius measurements of Galileo [1]. When this measured mass is divided by the radius, a mean density value of  $1.936 \text{ g/m}^3$  is obtained.

$$I_{Av} = \frac{8}{15} \pi \rho_{shell} r_{out}^5 \quad (2.9) \quad \Theta_{Model} = \frac{I_{Model}}{I_{Av}} \quad (2.10)$$

With  $I_{Av}$  representing the 'average' moment of inertia of the sphere and  $\Theta_{Model}$  the moment of inertia factor of the model. It is checked if the calculated moment of inertia factor is within the limits of the known moment of inertia factor of Ganymede (Table 2.2, value  $\pm$  uncertainty). If so, the model is accepted in terms of moment of inertia factor.

### 2.2.3. GRAVITATIONAL AND PRESSURE DISTRIBUTIONS

It is important to consider the variation of the gravitational potential and the hydrostatic pressure throughout the layers of the model. These are considered as the gravitational potential affects the hydrostatic pressure. This in turn influences the water and ice phases as will be discussed in Section 2.2.4. The variation of gravitational potential and pressure within a sphere are given by Equation 2.11 and Equation 2.12 respectively [49] [50]. It is assumed that models are spherically symmetrical and in thermal and mechanical equilibrium. Hence internal heat sources and dynamic interactions within and between layers have not been accounted for.

$$\frac{dg}{dr} = 4\pi G\rho - 2\frac{g}{r} \quad (2.11)$$

$$\frac{dP}{dr} = -\rho g \quad (2.12)$$

In these Equations  $G$  represents the gravitational constant ( $6.67408 \times 10^{-11} \text{ kg}^{-2}\text{m}^2\text{N}$ ),  $g$  the gravitational potential.  $p$  is the pressure at location  $r$  in a sphere with respect to its centre. The density is known for each layer of the model and the location  $r$  will change by 1 km per step.

#### RUNGE-KUTTA PROPAGATION

As both parameters vary with depth, a fourth order Runge-Kutta integrator (RK4) will be utilized to determine the gravitational potential and pressure throughout the model. This method uses an initial state vector containing the pressure (neglectable [49], Equation 2.13) and the gravitational potential at the surface of the model. This gravitational potential can be calculated using Equation 2.14.

$$P_0 = 0 \quad (2.13) \quad g_0 = \frac{GM_{Model}}{R_{Model}^2} \quad (2.14)$$

Where  $R_{Model}$  represents the radius of the model and  $g_0$  the gravitational potential at the surface of the model.

### 2.2.4. ICE PHASES

Now that the pressure distribution within the model has been determined, the pressures and temperatures at the different layer interfaces are considered. It can be checked if the pressure at each boundary is coherent with the ice phase present at that boundary. This is done using the known thermoclines for  $\text{H}_2\text{O}$ . These are provided in Figure 2.3 [54] for different phases and salinities (due to  $\text{MgSO}_4$ ).

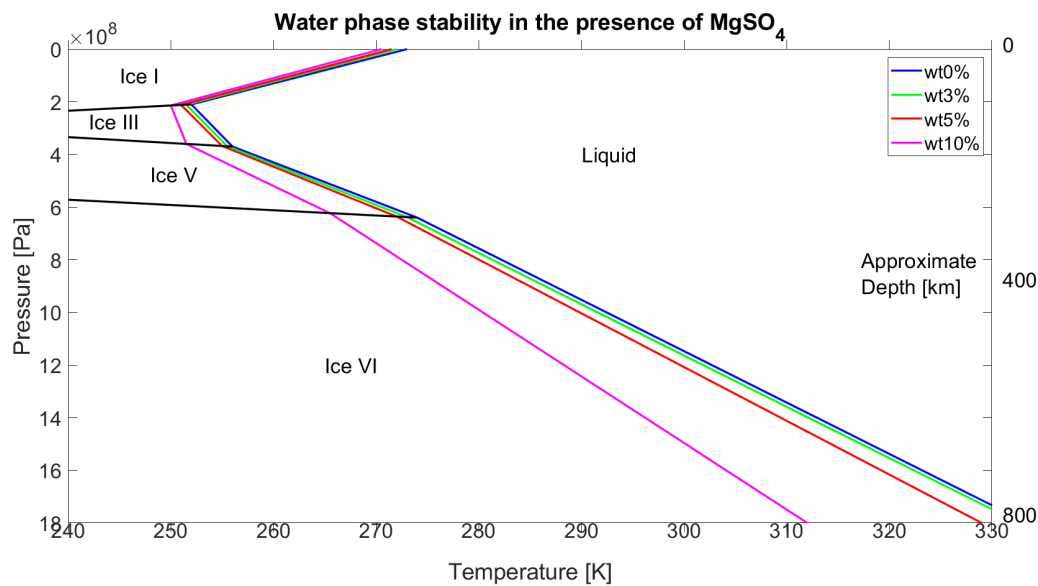


Figure 2.3: The used phase transitions for fresh and saline water [54].

In Figure 2.3 the weight contents (wt%'s) of  $\text{MgSO}_4$  indicate the salinity of the water. The black and colored lines represent the pressures and temperatures at which phase transitions occur. Depth is provided at the right hand side of the figure. These depths are a rough approximation and can slightly vary for models consisting of different layers due to density variations. It does however give an indication of how deep the phases are located.

The pressure profiles of the models, based on Equation 2.12, will be compared to Figure 2.3. The model will be considered viable for internal layer phases and local pressures if these correspond with the phase stability of water. Temperatures at the different boundaries will then be considered. Internal heat generation is not accounted for during this thesis research [49] [50] [54]. Therefore 1D-steady-state temperature profiles are sub-adiabatic, with an exception for low pressures (<200 MPa) [54] [22]. Therefore viable models are limited to increasing temperature profiles for increasing pressure.

## 2.3. IMPLEMENTATION



Matlab<sup>®</sup> was utilized to create an algorithm which implements the theory of the 1D homogeneous models. Selected models should adhere to the requirements provided in Table 2.2 and the layer order depicted in Figure 2.2. Figure 2.4 provides the structure of the algorithm, which consists of different modules. Several of these modules determine aspects of the model and immediately check if that part of the model is compliant with set requirements. If the model is within requirement uncertainties (Table 2.2), it will be considered 'OK'. The algorithm then moves on to the next aspect and requirement. In the case that a model is not confirm requirements, it gets a 'NOK' and the algorithm continues with the next iteration. Data is only saved if the model passes all modules.

These simulations will use a 'clock' approach. A clock can digitally be represented as [hh : mm : ss]. When the seconds have completed a full cycle, 60 seconds, the minutes increase by a single step value, 1 minute. The seconds reset to their initial value, zero, and start over. In turn, when the minutes have completed a full cycle, 60 minutes, the hours increase by a single step value, 1 hour. In the mean time the seconds will have completed 60 cycles.

This part of the research will use a similar approach, or in digital representation: [I<sub>h</sub> : L : III : V : M : C]. Where L is the liquid layer, M the mantle, C the core and the others the ice layers. First the inner most layer

thickness, the core, will be varied between its lowest and highest values. Once this cycle is finished, the layer on top of the previous layer, in this case the mantle, will increase by a single step-size. Then, the core will again be varied between its lowest and highest values. This process is repeated for all layers, until the outer most layer (ice  $I_h$ ) has completed a full cycle.

#### Inputs:

For this part of the code to be executed, several inputs should be provided. These are given in the list below.

- Densities of the layers [ $\text{g}/\text{cm}^3$ ], Table 2.1.
- Radius of the body [km], Table 2.2.
- Layer ranges [km], defined by user per layer.  
Format: [Initial thickness; Step thickness; Final thickness]

#### Outputs:

The output of this algorithm consists of models which adhere to all set requirements. This data only varies radially. For each individual model the following data is indexed:

- Layer Boundaries [km].
- Layer Densities [ $\text{g}/\text{cm}^3$ ].
- Mass [kg].
- Moment of Inertia Factor [-].
- Pressure Profile [Pa].
- Gravitational Acceleration Profile [ $\text{m}/\text{s}^2$ ].
- Temperature Profile [K].

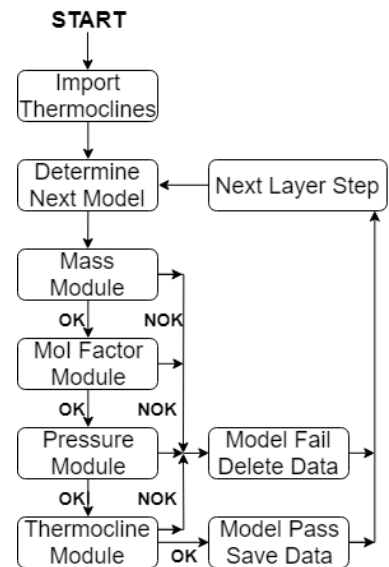


Figure 2.4: Block diagram for the algorithm which determines the 1D homogeneous models.

### 2.3.1. MODULES

The mass module follows the theory provided in Section 2.2.1 to determine the mass of the model considered. It calculates the mass based on the layer thicknesses and the densities of the layers. The moment of inertia module uses the same input variables, together with the theory discussed in Section 2.2.2, to obtain the moment of inertia factor. Both the pressure and gravitational acceleration profiles as a function of depth are determined in the pressure module. This module is based on Section 2.2.3 and again uses the layer thicknesses and densities as inputs. The pressure profiles are compared to the thermoclines of water (Figure 2.3) in the thermocline module. The temperature profiles are also determined in this module, based on Section 2.2.4.

### 2.3.2. DATA PROCESSING

First the layers correlations between all the models that are within requirement uncertainties will be considered. Each layer is compared to all other layers and it is inspected if these are related. This will result in a 7x7 grid with correlation data. This data will also be compared to the different set requirements to observe how these affect behavior.

From the models which adhere to all set requirements, several will be selected for further examination. This is done due to time limitations since analyzing these models into further detail is time expensive. The models are selected such that end members are considered and all possible variations of Ganymede's interior are included. This selection is based on the layer correlations. An example of such a model is Aqva I, which is provided in Figure 2.5.

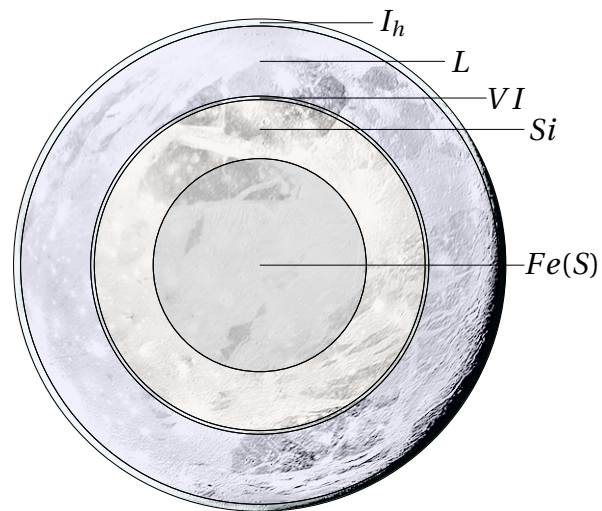


Figure 2.5: An example of a world which is adherent with all set requirements. Generated by the 1D homogeneous model generator. It is named Aqva I due to its large ocean.

Several models like Aqva I will form the foundation for the 3D heterogeneous variations. These will be discussed in Chapter 3.



## HETEROGENEOUS 3D MODELING

When all possible 1D homogeneous layer models of Ganymede have been determined, local density and boundary variations will be considered. A combination of the homogeneous models with the local variations can then be used to determine possible gravitational potential field variations for Ganymede. This will be elaborated on in Chapter 4. This chapter introduces and discusses the different expected anomalies within Ganymede in Sections 3.1-3.4. It concludes with the implementation of the theories in Section 3.5.

### 3.1. TOPOGRAPHY

The first and most apparent anomaly is Ganymede's topography. The variation of surface height with respect to a perfect sphere will have a large influence on the gravitational potential field measured by JUICE. Therefore it is important that the topography should be modeled accurately.

As a result of images taken of Ganymede by the Voyager and Galileo missions, the height variation of the topography of Ganymede could roughly be determined. In total 213 images have been used to determine a 3D geodetic point control network for Ganymede [59]. This network provides a global shape of Ganymede, from which an estimate of its topography can be determined. For 97 percent (1 sigma) of the control points, the height accuracy is better than 5.0 km [59]. All outliers with an uncertainty higher than 15 km have been removed. The point control network is depicted in Figure 3.1

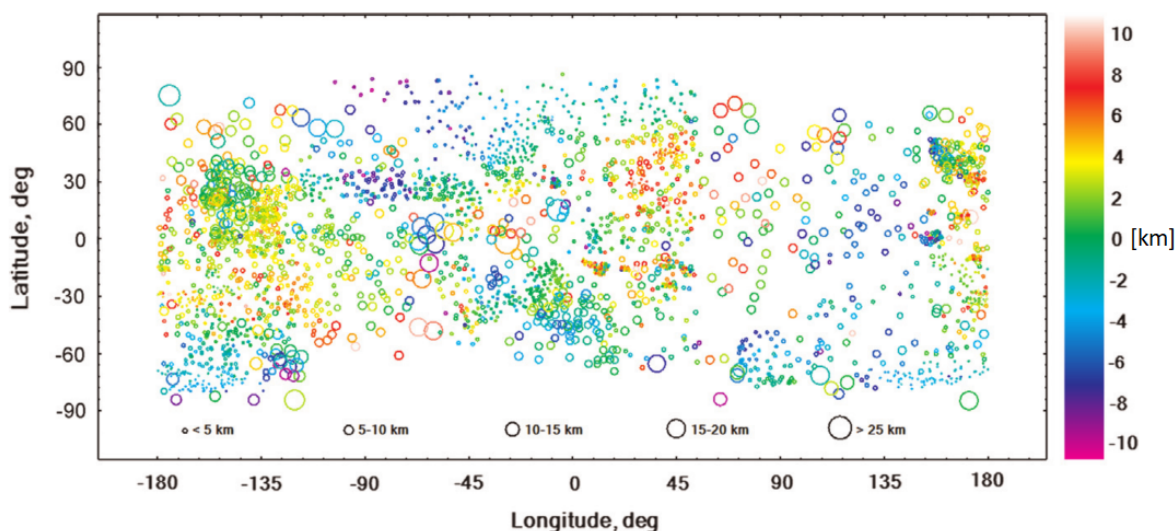


Figure 3.1: The point control network of Ganymede, circle sizes are proportional to coordinate errors. The color variation indicates the height in kilometers above the best-fit sphere (2632.63 km) [59].

The point control network in Figure 3.1 has to be processed. It then can be used for the gravitational potential field simulations. The raw data is imported and converted. The topography resulting from the point control network is given in Figure 3.2. Note that the height is not on an 1:1 scale with respect to the real case. However, the height variations provided in Figure 3.1 are present in Figure 3.2 at the corresponding longitudes and latitudes.

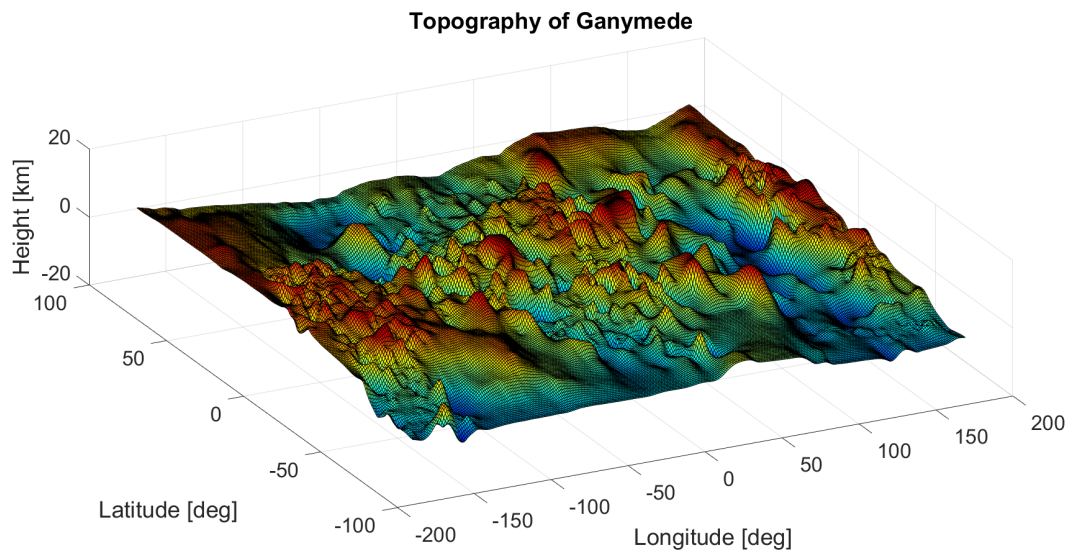


Figure 3.2: The topography of Ganymede with respect to a reference spheroid, resulting from the selected point control network [59].

Figure 3.2 shows that the topography of Ganymede consists of lower and higher regions. As the topography is a visible and measurable entity, it can be corrected for in gravitational potential field models. Once JUICE arrives at Ganymede, it will perform measurements on the moons topography with an altitude resolution of 10 cm [12]. This is a huge improvement on the current PCN model. This new topographic model can be used to improve the accuracy of the gravitational potential models resulting from this research. Therefore the current uncertainties in the PCN network will not have a negative impact on the results of this thesis.

## 3.2. CRUSTAL MODELS

Next, models that account for boundary and density variations within Ganymede's crust are considered. Several theories will be discussed during this section. Based on these, also a combined crust model will be determined.

### 3.2.1. THICKNESS VARIATIONS THROUGH ALBEDO

Ganymede's surface consists of several interesting features. It was observed that two different main types of terrain are present; darker, cratered terrain and lighter, grooved terrain (Section 1.1.2). The lighter grooved terrain is younger and has resurfaced multiple times due to the overall crater density being only one-tenth of that of the dark terrain [46] [47]. This could affect the local crust thickness. The crust below the younger and lighter terrain is likely thinner than below the older and darker terrain.

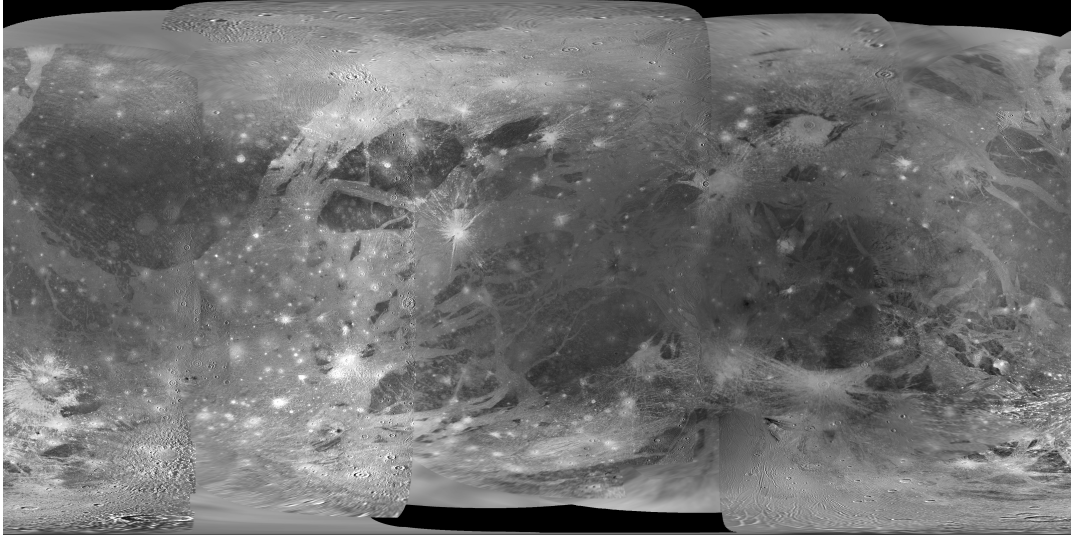


Figure 3.3: A cylindrical map of Ganymede [59], the two different types of terrain are clearly visible. Latitude varies between -90 and 90 degrees and longitude varies between 0 and 360 degrees.

To account for these variations, the crustal thickness can be varied based on the local albedo of the surface. This will be done with respect to the crusts bottom boundary, using a maximum variation and a scale between 1 and 0. The lightest terrain, with the highest albedo, is represented by 1. The darkest terrain, with the lowest albedo, by 0. The values between these extremes will be scaled based on the gray-scale of the cylindrical height resolution map of Ganymede, which is depicted in Figure 3.3. This has been created together with the point control network [59].

### 3.2.2. ISOSTASY

Other crust layer variations could be due to isostasy. A mass or mass deficiency at the surface of a body will be naturally compensated by an inverse mass anomaly beneath the surface. The depth below which all pressures are hydrostatic is known as the compensation depth. From this depth onwards the weight of imaginary vertical columns with the same cross-section should be equal [14]. Two different methods will be used to model isostasy.

#### Airy's Hypothesis [Boundary Variations]

In this hypothesis the layers, upper ( $\rho_u$ ) and substratum ( $\rho_s$ ), are assumed to have constant densities. The isostatic compensation follows from the depths of the root for individual virtual columns, this is shown in the right of Figure 3.4. A mountain with height  $h_1$  will have a root  $r_1$ , which can be determined by Equation 3.1. Features beneath sea level (at depth  $d$ ) would have an anti-root  $r_2$  as determined by Equation 3.2[14].

$$r_1 = \frac{h_1 \rho_u}{\rho_s - \rho_u} \quad (3.1)$$

$$r_2 = \frac{d(\rho_u - \rho_w)}{\rho_s - \rho_u} \quad (3.2)$$

Where  $\rho_w$  represents the density of a fluid within the feature beneath sea-level. Equations 3.1 and 3.2 can be applied to the crust (upper) and the mantle (substratum) of a celestial body, as the crust-mantle boundary is embedded in the lithosphere.

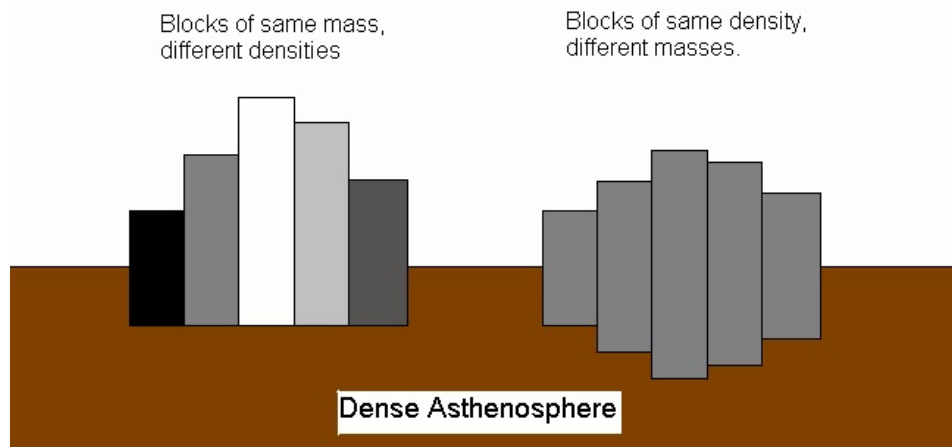


Figure 3.4: Pratt's hypothesis (left) and Airy's hypothesis (right)<sup>1</sup>. Colors are not related to the albedo variations.

Airy isostasy will encounter some problems for icy moons. The density difference between the ice  $I_h$  and ocean layers can be relatively small, 0.937 and 0.997 g/cm<sup>3</sup> respectively. Therefore this theory will result in large variations of the bottom boundary of Ganymede's crust. Since the compensation cannot exceed the crust and ocean layer thickness, only low Airy compensation amounts are possible for a large amount of models.

#### Pratt's Hypothesis [Density Variations]

Another way of modeling isostasy is to keep the base of the upper layer at a constant depth. Densities are varied for each individual column, as depicted in the left part of Figure 3.4. Taking the base of the upper layer as the compensation depth and determining the masses above this level results in Equations 3.3 and 3.4 for mountains and oceans respectively [14].

$$\rho_1 = \rho_u \left( \frac{D}{h_1 + D} \right) \quad (3.3) \quad \rho_d = \frac{\rho_u D - \rho_w d}{D - d} \quad (3.4)$$

Where  $\rho_1$  is the density of the upper layer beneath a mountain of height  $h_1$ .  $\rho_u$  is the density of the upper layer beneath land at sea level.  $D$  represents the compensation depth and  $d$  is the depth of liquids within the ocean.

Airy and Pratt isostasy can be present in different quantities and the amount of compensation varies per body. For example, on Earth large scale masses follow Airy isostasy [57] whereas small scale masses adhere to topographic reduction (more on this in Section 4.2.1). Isostatic behavior on ice like bodies as Ganymede is not yet known. Therefore the entire range of compensation rates is considered during this research, as long as these do not result in model errors. This will be modeled as a percentage of compensation. Equations 3.1 - 3.4 are considered as 100% compensation. Lower percentages of compensation are determined by simply downscaling the full compensation effect (multiplication of  $h_1$  and  $d$  by percentage/100). Pratt compensation will be limited by the crust density, which should be representative for ice. Airy compensation by the thickness of the ocean and crust layers.

#### 3.2.3. COMBINED CRUST MODEL

The albedo and isostasy theories are very different. It is hard to determine which combination can be a best estimation for the crustal model of Ganymede. The three theories will be examined individually, together with a combined crustal model which is a combination of the albedo boundary variations and Pratt isostasy. Airy isostasy is not included as it also affects the lower boundary of the crust and will encounter problems for ice moons. The combined model will first scale the bottom boundary of the crust layer, followed by the density variations within the layer.

<sup>1</sup>Isostasy theories: <http://large.stanford.edu/courses/2007/ph210/pan2/>, [cited 31-07-2018]

### 3.3. INTERNAL BOUNDARY VARIATIONS

Simulated models will consist of different phases and elements in several layers. Boundary interactions are present, like an ocean floor- and mantle topography. Liquid/ice slushes can be present at the boundaries of the liquid layer. Internal pressures and temperatures differ locally for a heterogeneous model, thus variations within the ice phase boundaries can be present. To observe the gravitational potential effects of the variations between the different boundaries, these will be considered during this thesis research.

The internal boundary variations will be based on topographic height maps. These have been generated using software created by Ir. Robin Thor [52]. Dr. Ir. Bart Root provided 16 different topographic variations which were determined using this software. The different maps vary in smoothness and local variation and are depicted in Figure 3.5.

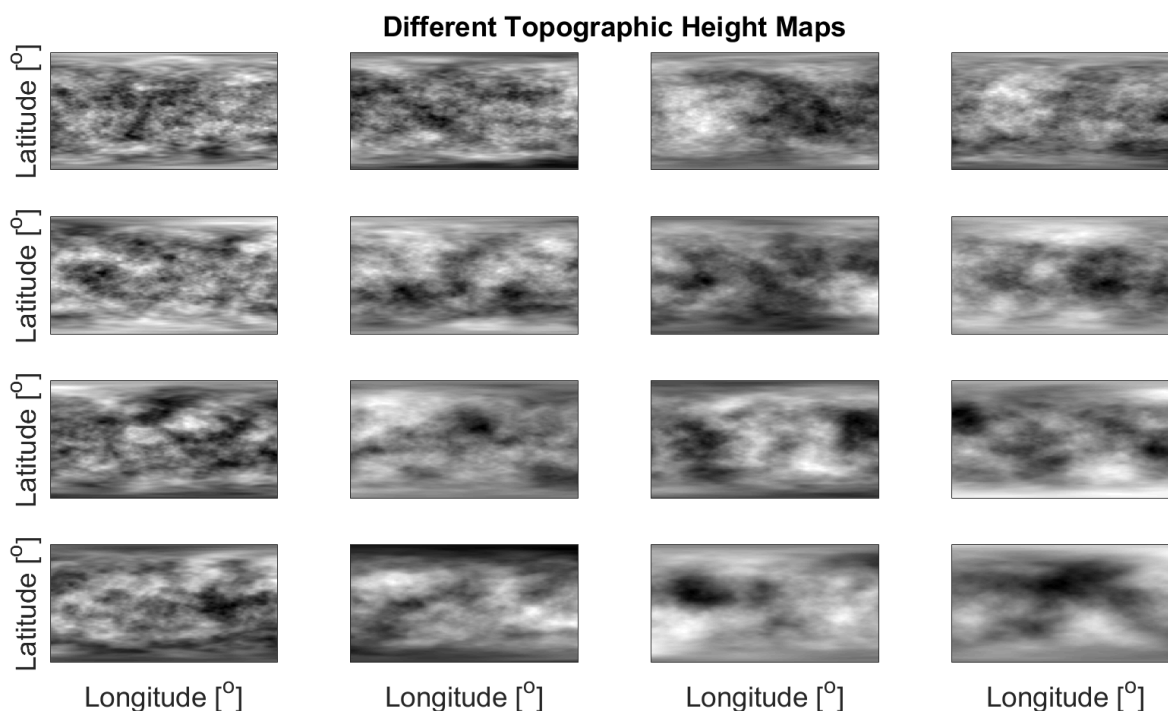


Figure 3.5: The provided topographic height maps. Towards the right these maps get larger topographic variations and towards the bottom the maps are more smoothed. Currently no value for latitude and longitude is included. This can be determined for each boundary interaction individually.

These maps are not yet scaled and vary between 1 (black) and -1 (white). Therefore these will be scaled with respect to a maximum height value which can be determined by the user. The maps have no exact longitudinal/latitudinal orientation, but this will be included whilst the boundary interactions between the different layers are generated.

Different topographic maps will be utilized for each boundary such that these will not result in similar gravitational field patterns. If all boundaries used an equal map, this could induce aliasing. Each different boundary interaction will thus select a different map; these are divided as provided in Table 3.1. Figure 3.5 is considered as a [4,4] matrix where the first integer indicates the horizontal position. The second integer provides the vertical position starting at 1. The density differences between the layers are given, assuming all layers are present within a model. These are based on Table 2.1. The density range at the ocean floor boundary is due to the variation of salinity. The range at the mantle-core interface is due to the different core densities considered. A bigger density difference, at a similar depth, will have a larger impact on the gravitational potential signal.

Table 3.1: The data used for the different boundary interactions.

Boundary	Topography	$\Delta\rho$ [ $\text{g}/\text{cm}^3$ ]
Ocean Floor	[2,2]	0.027 - 0.169
Ice III Bottom	[3,2]	0.101
Ice V Bottom	[2,3]	0.093
Ice-Mantle	[1,3]	1.89
Mantle-Core	[3,1]	1.9 - 4.75

For each boundary the selected topography will be scaled using the maximum height variation with respect to the original spherical boundary. The maximum height value should not exceed the thickness of one of the adjoining layers as it otherwise will interact with a multitude of layers. This results in a longitudinal/lateral height variation map of the boundary with respect to the original spherical boundary considered.

### 3.4. POCKETS AND DIAPIRS

Finally, it should be considered how much influence density pockets and diapirs within the crust have on the gravitational potential field. Brine and melt pockets are considered. In general, large stones are not located within the ice crust (except for fresh meteorites) as these would slowly sink through the crust due to their mass. If measurable, pockets at different depths within the crust will be considered. Pockets are assumed to be cubical and will be modeled using an assumed density, radius and longitudinal/latitudinal position. Diapirs are simply generated as pockets which are very close to the crust-ocean boundary, These are less visible as the other pockets, as these are located at the deepest possible location.

Recent models of Ganymede include crusts of 13-148 km thickness [54]. The variation of pocket depth will increase with crust thickness. Diapirs are located at the bottom of the crust and thus their depth depends solely on the crust thickness of the model considered. Furthermore, sizes of these anomalies are expected to be on a large-scale (>10 km) [55]. To gain a better understanding on the behavior of these anomalies on the gravitational potential field, also smaller sizes will be examined.

### 3.5. IMPLEMENTATION



Again Matlab<sup>®</sup> was used to implement the theory. This part of the code induces heterogeneous variations on the models selected in Chapter 2. To optimize for simulation time, the algorithm is able to follow two paths as indicated in Figure 3.6. Inputs and outputs are provided in an equal format for both paths.

**Blue Path:** If the user desires to run multiple variations on a single model, the algorithm will follow the blue path in Figure 3.6. For each module it will check if it is selected and will perform the required determinations if necessary.

**Red Path:** For a single variation, the algorithm will follow the red path in Figure 3.6. It does not consider other modules, which decreases simulation time significantly.

**Inputs:**

The inputs for this algorithm can consist of the following data, depending on which modules are selected. If relevant, the module for which the input is required will be stated.

- All outputs of the code discussed in Section 2.3.
- User selection of modules.
- PCN data map [Topography Module].
- Gray-scale albedo map [Crustal Variations].
- Pratt and Airy compensation % [Crustal Variations].
- Topographic height maps [Boundary Variations].
- Pockets sizes and densities [Pocket/Diapir Modules]

**Outputs:**

An existing package will perform the gravitational potential simulations. It is known as the Global Spherical Harmonics Package (GSHP) and will be thoroughly discussed in Chapter 4. However, models which will be considered by this package are required to have a specific structure. Gene Matrix Transposed files (.gmt files) are required. These consist of several columns, which represent different variables. Each row describes a data set. For the GSHP the first column represents the longitudinal position and the second column the latitudinal position. Two sets of .gmt files will be used. In one set the third column represents the height with respect to the spherical surface of Ganymede in km. The other set provides the density between the previous and next layer in  $\text{g/cm}^3$ .

Hence, the output of this part of the code consists of .gmt files which represent the heterogeneously varied model. These are both boundary and density files, which can be used for further processing by the GSHP.

**3.5.1. MODULES**

The topography module converts the PCN data to height variations in .gmt format, as discussed in Section 3.1. Its output is a single boundary .gmt file of the models outer layer. The crustal variations module consists of three parts. It can vary the crust thickness as a function of albedo and/or it can induce Airy and Pratt isostasy on the crust. These theories were elaborated on in Section 3.2. It uses a gray-scale map of Ganymede's surface and the density and boundary files as input. Based on user preferences, its output is a boundary and/or density .gmt file of the crust-water interface and crust respectively. Up to five boundary variation modules can be selected. These are based on the L-III, III-V, V-VI, VI-M and M-C interfaces for models which include all ice layers. Here the L represents the liquid layer, M the mantle, C the core and the other abbreviations the ice layers. If an ice layer is non-existent, the algorithm neglects that layer. All boundary variation modules use a similar theory, discussed in Section 3.3. These modules need height maps as a function of longitude, latitude and maximum height together with the depth of the considered layer as inputs. The output consist of a boundary .gmt file of the interface considered including the variation due to the height map. Finally, the pocket and diapir modules use the theory from Section 3.4 to add density variations to the density .gmt file of the crust. Required inputs are pocket density, depth and size.

**3.5.2. DATA PROCESSING**

The algorithm discussed in this section was used to obtain several sets of models. These can be divided in two main groups:

- Different 1D homogeneous models, which include several of the heterogeneous variations based on a similar user input. These will be used to compare differences within the gravitational potential field due to models with different internal layers.
- A single 1D homogeneous model with heterogeneous variations. Both single and multiple variations are scaled to observe the effects on the gravitational potential field. This can be achieved by changing

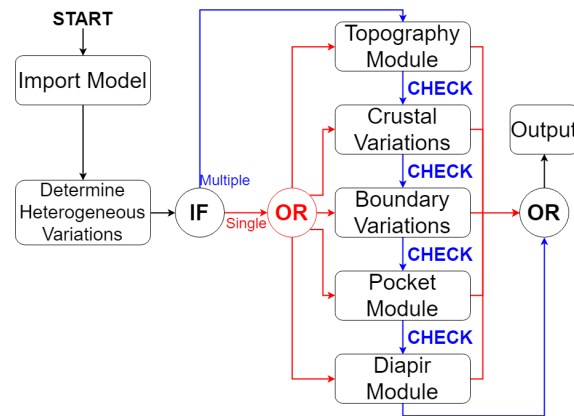


Figure 3.6: Block diagram for the algorithm which determines the 3D heterogeneous models.

the scaling height of a boundary map, by increasing pockets sizes etc.

The gravitational potential field simulations, which are discussed in Chapter 4, use these models as an input. Two examples of boundary variations are provided on the following page. The first example shows expected height variation values [55] and shows how small these variations are with respect to radius. These are based on boundary interfaces of Aqva I and are provided in Figure 3.7. From top to bottom these are the topography, Crust-L, L-VI, VI-M and M-C interfaces. These consist of a maximum height variation of 20 kilometers with respect to the reference sphere. Height variations and layer thicknesses are to scale in Figure 3.7.

The second example is included to illustrate the behavior of these boundary interfaces in more detail. The height variations are increased to 300 km. Figure 3.8 shows these exaggerated boundary variations located at random depths within Ganymede's radius. These are thus not the layers within a possible model, but simply layers which are spaced such that the boundaries do not overlap.

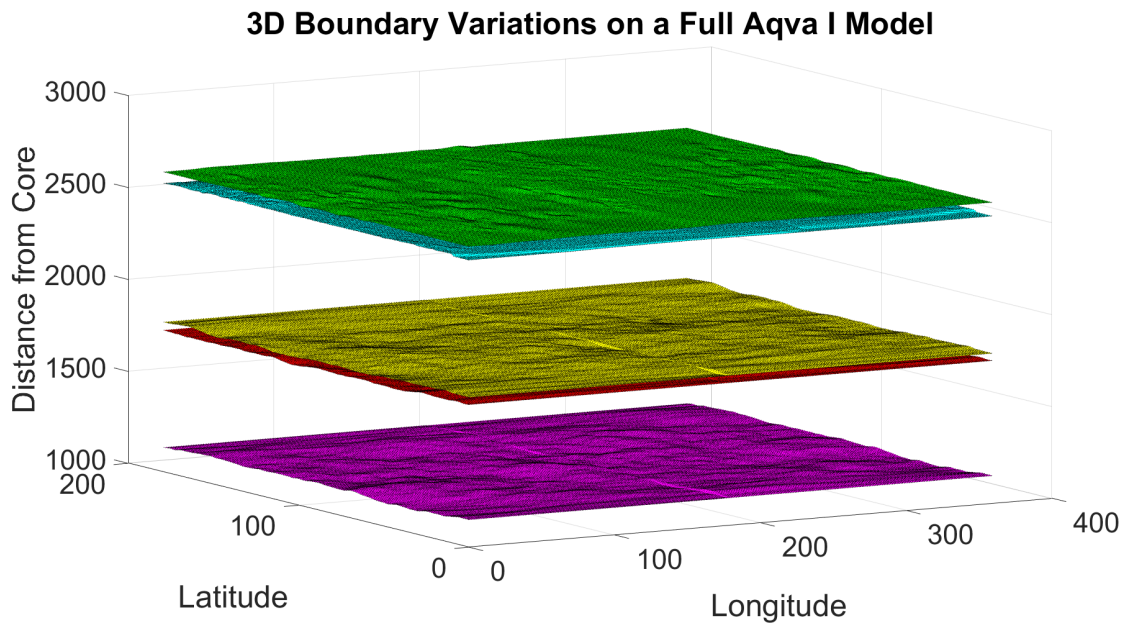


Figure 3.7: The topography, Crust-L, L-VI, VI-M and M-C interfaces (top to bottom) of Aqva I when varied up to 20 km with respect to the reference sphere. Boundary variations are to scale and are located at depths corresponding to Aqva I's layers.

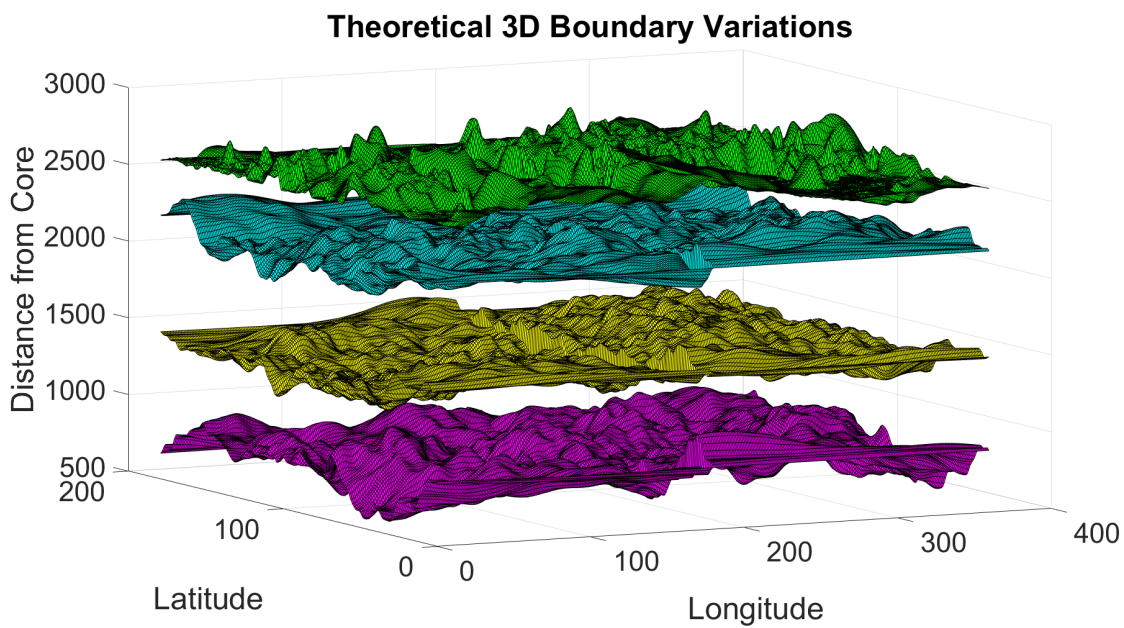
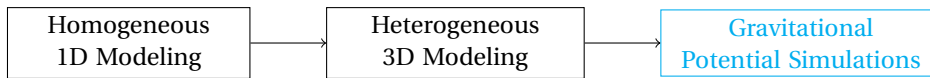


Figure 3.8: Several boundary interfaces located at different depths. Boundary variations are enhanced for illustration purposes. Layers depths are not related to any possible models.



# GRAVITATIONAL POTENTIAL SIMULATIONS

The interior models of Ganymede have been simulated and selected. Relations between these different internal mass distributions and possible gravitational potential fields still have to be obtained. A package which achieves this was created and elaborately tested by Dr. Ir. Bart Root during his PhD thesis [38]. This package, the Global Spherical Harmonics Package, has been made available for the remainder of this thesis research. It uses the spherical harmonics representation to generate gravitational potential fields and coefficients. More information on spherical harmonics can be found in Appendix B.



This chapter discusses the input models required for, and the main functioning of, this package in Section 4.1. The relevant outputs of the package are presented in Section 4.2.

## 4.1. INPUT MODELS

As discussed in Section 3.5, the input models of the GSHP should consist of two sets of .gmt files. These files consist of three columns representing the longitude, latitude and local height or density between boundaries. Considering computation times for increasing resolution, the resolution of the longitude and latitude of the input models has been set to 1 degree. This resolution results in fast computation times which do not limit research capability. As only the first 15 coefficients of the gravitational potential field will be measured by JUICE [12] this resolution will not influence the simulation results in a negative manner.

The longitude varies between 0.5 and 359.5 degrees. Latitudes between 89.5 and -89.5 degrees. The latitude will decrease by 1 resolution step after a full set of longitudes has been considered. This results in a grid of  $360 \times 180 = 64800$  positions for a resolution of 1 degree. The .gmt files will thus have a size of  $64800 \times 3$  cells.

First, a set of files is required in which the third column represents the height value of the boundary with respect to the spherical surface of Ganymede ( $R_G = 2634.1$  km), where the direction towards the centre is considered negative. Each boundary is represented by a separate .gmt file. It is important that the maximum layer thickness should not exceed 100 kilometers as the package tends to diverge for higher degrees and orders of spherical harmonics for large layer thicknesses [38]. Hence, multiple layers can be present between two boundaries. This will increase simulations length due to the larger amount of layers, but improves the reliability of the results significantly.

The second type of .gmt files consists of a third column which indicates the value of the material density which is present between the previous and the next boundaries in  $\text{g/cm}^3$ . Each density field between two boundaries is again represented by an individual .gmt file. Figure 4.1 provides a visual representation of a set of these .gmt files. The model in this figure consists of 8 boundaries (including boundary 8, which is located at the centre of the core) and 7 density files, located between these boundaries.

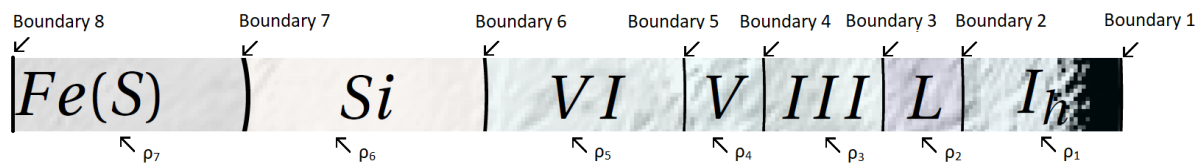


Figure 4.1: An example of a set of boundary and density .gmt input files.

The setup of the .gmt files provides an elegant method of implementing variations at boundaries and between layers. These values can easily be varied locally and additional layers can simply be added by including an extra density and boundary .gmt file. Chapter 3 provided in which way the different anomalies can be modeled based on height and density variations for different longitude and latitude. The gravitational potential simulations will be performed 500 kilometers above the surface of the models. This is the orbit height of JUICE when it is in proximity of Ganymede. The GSHP will be executed for spherical harmonics coefficients up to order/degree 48. This is based on the uncertainties of the 3GM instrument onboard of JUICE, which will perform the gravitational potential field measurements. These were determined up to an degree and order 48 [4] and are discussed in Section 4.2.3.

## 4.2. OUTPUT OF SIMULATIONS

Values for the gravitational potential field together with its coefficients can be obtained from the different 3D heterogeneous input models. Both variables will be measured by JUICE. Hence the determined models of Ganymede can provide a better understanding between JUICE's measurements and possible internal density distributions within Ganymede.

*Before the results of this research are presented, a simple homogeneous 1D model of Ganymede has been used for visualization and verification purposes. These are not the final results of this thesis research and are purely included to provide the reader with a complete explanation on the subject. This model can be considered to be purely 1 dimensional and homogeneous unless stated otherwise. It consists of 75 km ice  $I_h$ , a 750 km wt10% ocean, 39 km ice  $V$ , a 630 km mantle and a 1140 km FeS core. The model has passed all the requirements discussed in Section 2.2 and thus is considered a possible configuration for Ganymede's internal structure. It is similar to models from literature [54] and was briefly considered in Figure 2.5. It will be referred to as **Aqva I**.*

### 4.2.1. GRAVITATIONAL POTENTIAL FIELD

During this section, Aqva I will be combined with a topography that is based on the PCN discussed in Section 3.1. When running the GSHP for this model, the gravitational potential field variations due to Ganymede's topography in Figure 4.2 are obtained. These are purely due to Ganymede's topography and it is the full gravitational potential field of the model consisting of coefficients 0-48. The gravitational potential is the work per unit of mass that is required to displace an object from a reference point to a specified point. The GSHP plotting tool was designed to be used on Earth and thus utilizes the coast-lines of this body. These are not relevant for the current research and were thus removed.

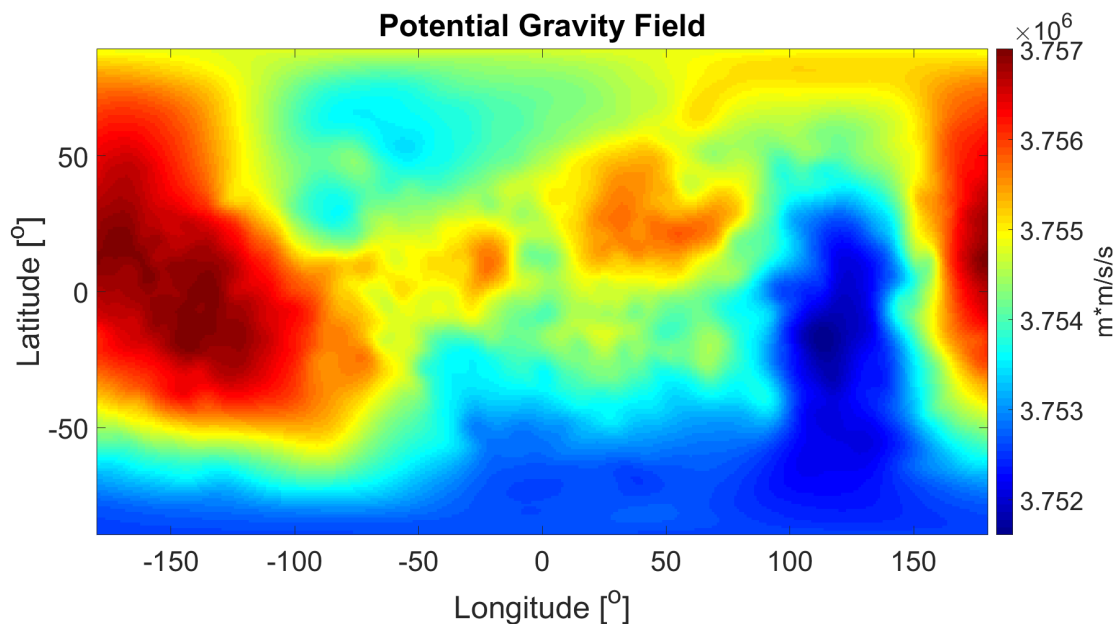


Figure 4.2: The gravitational potential field (SHbounds 0-48) for Aqva I including topography.

In Figure 4.2, the gravitational potential field variations in  $\text{m}^2/\text{s}^2$  can be observed as a function of longitude and latitude 500 kilometers above the models surface. The measurements provided by JUICE will be up to an order and degree 15. Figure 4.3 depicts the gravitational potential field up to this order and degree.

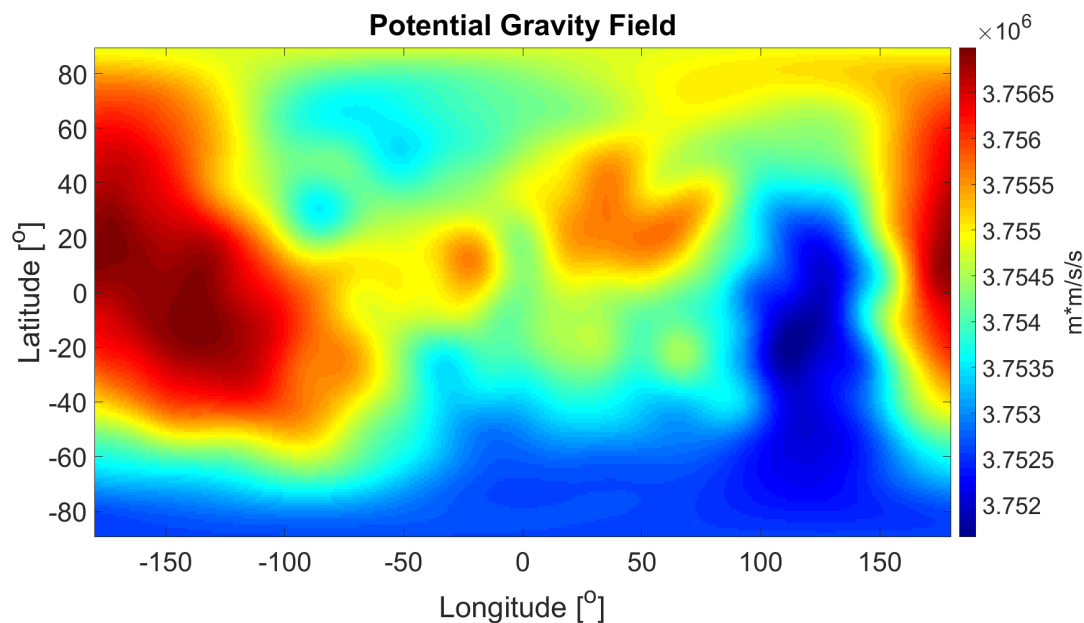


Figure 4.3: The gravitational potential field (SHbounds 0-15) for Aqva I including topography.

Both figures provide a similar gravitational potential field. However, more local variations are present within Figure 4.2 due to the higher orders and degrees included. When compared to Ganymede's topography (Figure 3.2) it is observed that above excess masses, the gravitational potential is slightly higher (red areas). Above mass deficits, the gravitational potential is slightly lower (blue areas).

#### MAIN SHAPE CORRECTIONS

The final models considered during Chapter 6 will be more complex as these include several different boundary and density variations as discussed in Chapter 3. Therefore these models will be inspected in several ways. This enhances understanding on how Ganymede's interior could influence its gravitational potential field. Therefore several important corrections used in geodesy and geophysics will be briefly discussed.

The next potential field has been simulated for coefficients 2-48 (but without the  $J_2$  coefficient [2,0] and  $C_{2,2}$  coefficient due to Ganymede's tidal bulge [7]) to correct for the elliptical shape of Ganymede. Hence the  $C_0$ ,  $C_{1,m}$ ,  $C_{2,0}$  and  $C_{2,2}$  coefficients are equal to zero. This increases visibility of the variations within the field.

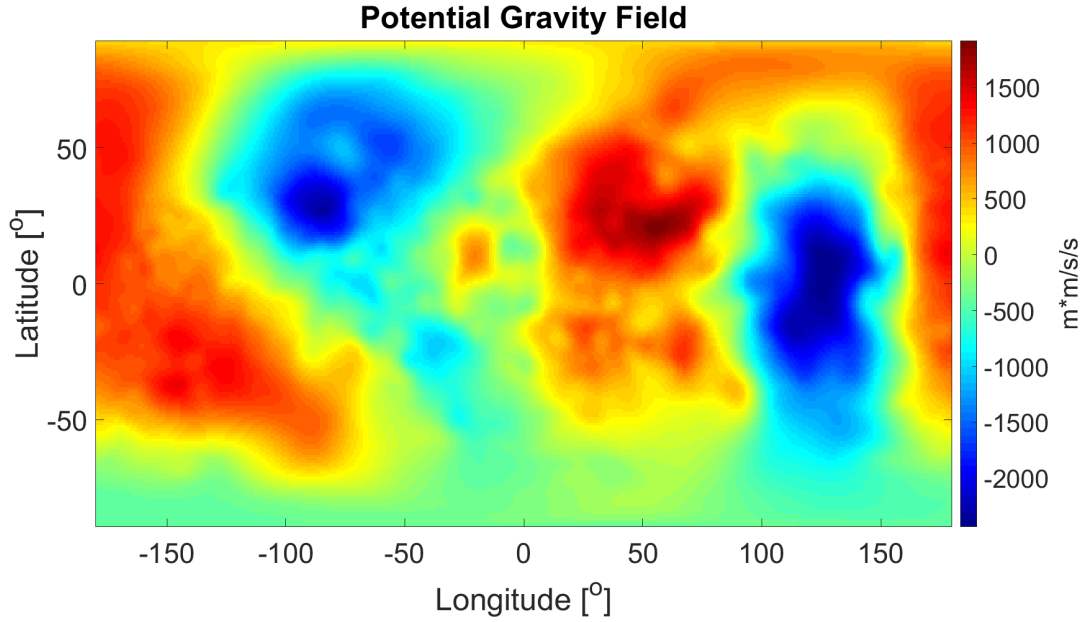


Figure 4.4: The gravitational potential field variations (SHbounds 2-48, excluding  $C_{2,0}$  effect and Ganymede's tidal bulge) for Aqva I including topography.

Local variations stand out more. The gravitational potential field can be converted to gravitational accelerations through Equation 4.1. Including the main shape corrections the gravitational acceleration is given by Equation 4.2

$$\bar{g}_{obs} = -\nabla V \quad (4.1) \quad \Delta g_F = |\bar{g}_{obs}| - g(\lambda) + \delta g_r \quad (4.2)$$

Where  $V$  is the gravitational potential field in  $m^2/s^2$ ,  $\bar{g}_{obs}$  the gravitational acceleration in  $m/s^2$  and  $g(\lambda)$  are normal gravity corrections. In this case these are due to the  $J_2$  effect and Ganymede's tidal bulge.  $\delta g_r$  is the main shape correction. These corrections are given by Equations 4.3 and 4.4.

$$\delta g_r = 2 \frac{GM}{R_3} h \quad (4.3) \quad g(\lambda) \approx g_{C_{2,0}} + g_{C_{2,2}} \quad (4.4)$$

$G$  is the gravitational constant,  $M$  the mass of the body considered,  $R$  the radius of the body and  $h$  the distance of the observer with respect to the bodies centre.

#### TOPOGRAPHIC REDUCTION

The topographic height variations are measurable by JUICE and could thus be corrected for. This would result in a gravitational potential field of a full interior model, but without its topography dominating it. This adjustment to a gravitational potential field is known as topographic reduction. As isostatic effects can be included in the model, high compensation values can result in a flip (higher=lower and vice versa) of the gravitational potential field. This can be observed in Figure 4.5

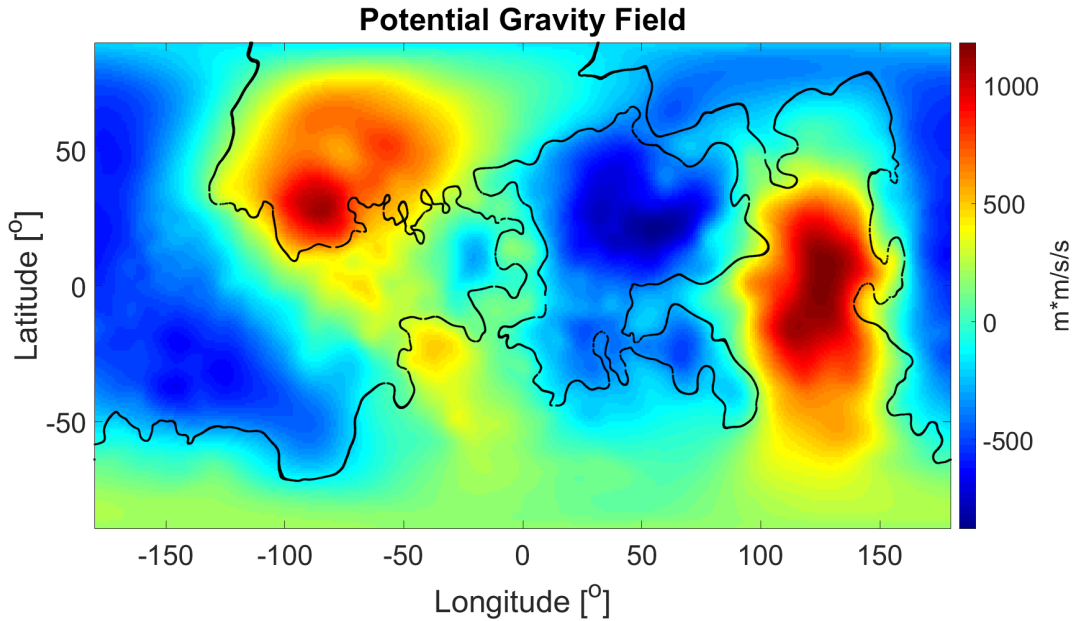


Figure 4.5: The gravitational potential field variations (SHbounds 2-48, excluding  $C_{2,0}$ ) for Aqva I including topography, 50 % Pratt compensation and topographic reduction.

The gravitational accelerations are now determined by Equation 4.5.

$$\Delta g_F = |\bar{g}_{obs}| - g(\lambda) + \delta g_r - \delta g_b \quad (4.5)$$

With  $\delta g_b$ , the topographic reduction. This correction is based on topographic height variations and the crustal density [38]. Through modeling the gravitational potential fields and by applying the corrections, variations can be observed between different models. The effect of these corrections on each individual world will also be simulated. This information can provide new insights about the relations between Ganymede's interior and its gravitational potential field.

#### 4.2.2. OUTLINING

For a better depiction of Ganymede's gravitational potential field, it could be convenient to add a reference outlining to the gravitational potential figures. For Earth these lines are typically located at the coastal regions. Ganymede does not have oceans at its surface. A different approach of finding a proper reference outlining should be considered. Ganymede's topography model is based on points located above and below a reference spheroid. Hence, a clear area exists where the topography values will be close to zero.

To obtain such a zero-lining for Ganymede, several height thresholds are considered. All points of the topography value matrix that are within a threshold value with respect to the topographic zero level will be marked as black dots. As the matrix consists of a large amount of values, a collection of these dots will form a line if the density of points is dense enough. Figure 4.6 provides the zero-lining of Ganymede for six different thresholds; 1, 5, 10, 20, 30 and 40 meters of height.

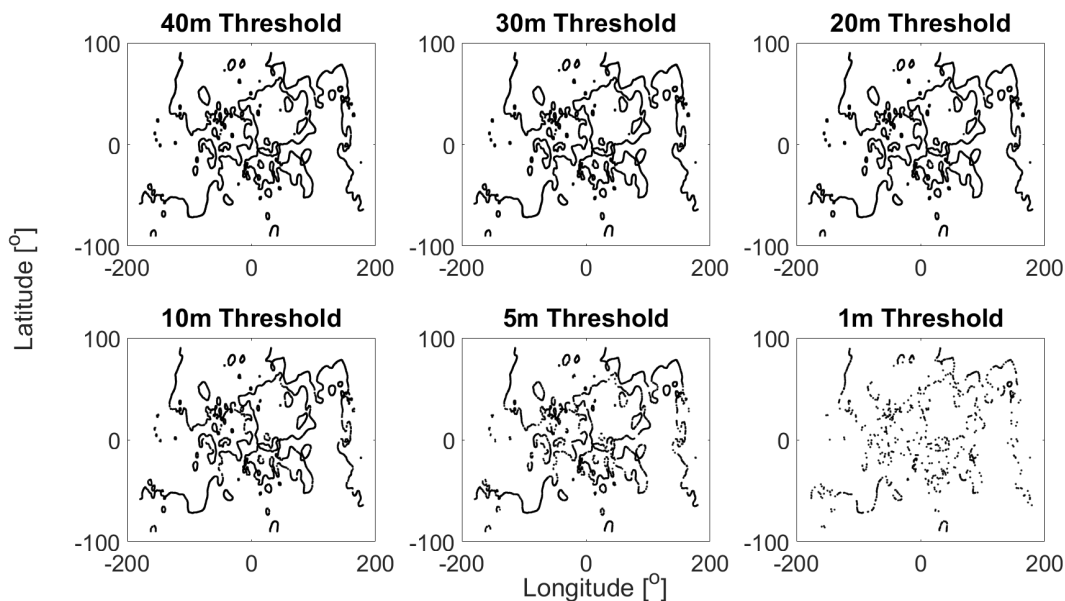


Figure 4.6: Mapping of Ganymede using six different thresholds.

From Figure 4.6 it becomes clear that the lower thresholds are not sufficient to obtain a zero-lining of Ganymede. This is especially true when the figures are presented in high resolution, the outlinings then become more sparse. From 20 meters and upwards a proper zero-lining of Ganymede is obtained. To include the best quality outlining during this research, the 40 meter threshold will be used. This still results in a proper outline. Higher thresholds take a lot of time to simulate and result in blurry, thick outlines with an unnecessary amount of detail. The main focus of the figures should be on the gravitational potential values and not on the outlining.

This rough 40m threshold outlining still includes a lot of unnecessary details. For reasons stated previously, some of these details will be removed. This was a tedious process as it had to be done manually. It was a worthwhile investment as the outlining only has to be generated once. The difference between these outlines is depicted in Figures 4.7 and 4.8.

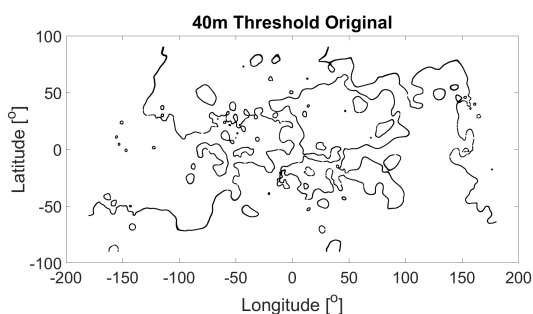


Figure 4.7: Original 40m threshold outline.

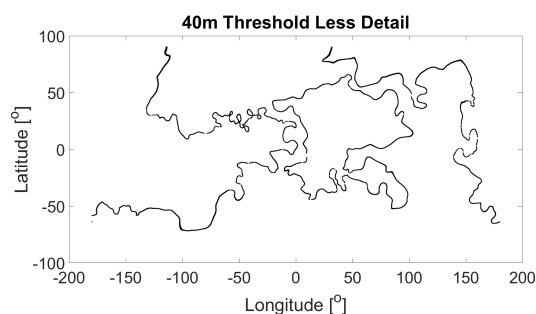


Figure 4.8: New 40m threshold outline with less detail.

The outline provided in Figure 4.8 will approximately follow the average potential values (green/cyan) of Figure 4.4. At these potential field values the topography will be close to zero kilometers with respect to the reference sphere. Both the outline and potential field are provided in Figure 4.9.

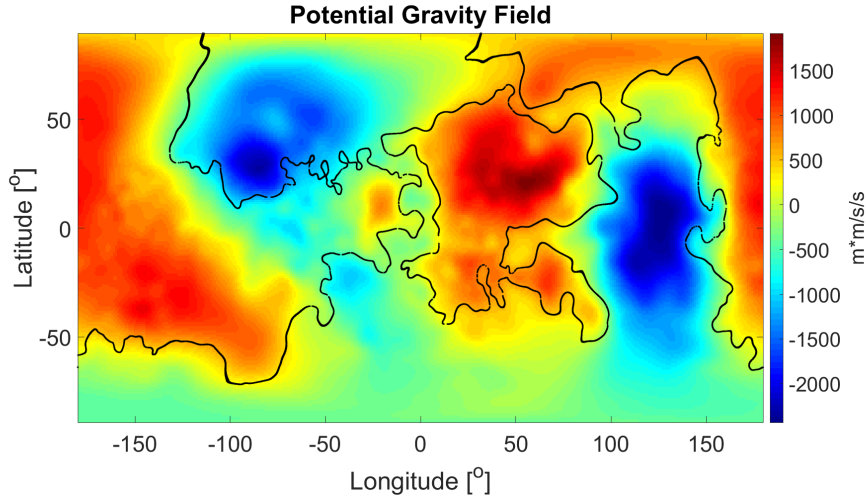


Figure 4.9: The same gravitational potential field output for Aqva I including topography as Figure 4.4, but now with a zero-lining.

The determined outline neatly follows the expected paths and coincides with the gravitational potential field. This outline will be added to all gravitational potential figures in the results and discussion chapters.

### 4.2.3. GRAVITY MODEL COEFFICIENTS

The GSHP provides the spherical harmonics coefficients of the individual models as an output. The variation of these coefficients can be determined for all worlds, anomalies and formal uncertainties. These can be compared to obtain a better insight in the effect of each of the gravitational potential field measurements.

From the coefficients the degree variance for each spherical harmonic degree can be derived. Degree variance models are power laws which describe the decay of the gravitational potential field signal in spectral representation. These reflect the observable variations in a set of spherical harmonics coefficients [36]. In this way the gravitational potential field signals of the different generated 3D heterogeneous models can be compared. This is done by using the sectoral and tesseral coefficients of the model, which are generated by the GSHP. This method can provide insight in the decay of the gravitational potential signal strength for increasing harmonic degree [48]. The degree variance of a model is calculated through Equation 4.6 [35].

$$\sigma_n = \sum_{m=0}^n C_{nm}^2 + S_{nm}^2 \quad (4.6)$$

Where  $\sigma_n$  is the degree variance at spherical harmonics degree  $n$ .  $m$  is the current spherical harmonics order,  $C_{nm}$  are the tesseral coefficients and  $S_{nm}$  are the sectoral coefficients.

### UNCERTAINTIES

Next to the degree variances of the different simulated models, it is important to know what can be detected by the measuring instrument. The current attainable performances of 3GM based on the latest trajectory kernels and the removal of dynamic noise induced by propellant slushing will be used [4]. These were presented at the European Planetary Science Congress 2018 in Berlin, Germany. An estimation of the accuracies at which it is possible to recover the gravitational potential field of Ganymede was provided. These uncertainties are depicted in Figure 4.10.

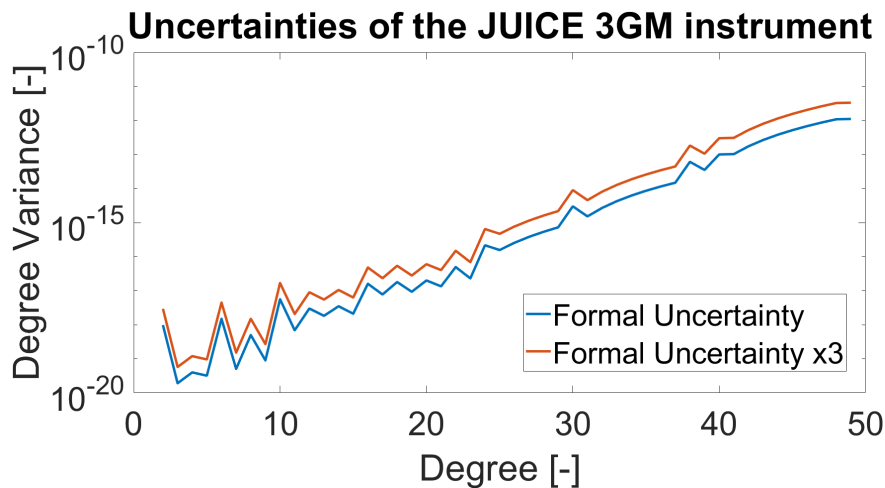
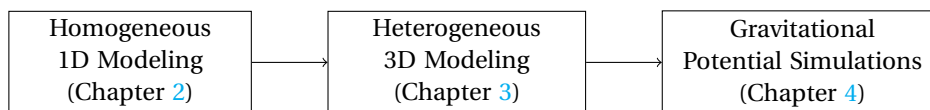


Figure 4.10: The uncertainties which will be used to determine which results could theoretically be measurable<sup>1</sup>.

Figure 4.10 provides all uncertainties up to a spherical harmonics degree of 48. The y-axis uses a logarithmic scale and both the formal uncertainty and three times the formal uncertainty have been included for completeness.

### 4.3. METHODOLOGY SYNOPSIS



Chapter 2 provided background theories which form the foundation for generating the 1D homogeneous models. The different layers and corresponding densities were introduced in Section 2.1, together with the twelve sets of models that will be considered. These sets are based on varying densities within the ocean and core layers. Several requirements were introduced in Table 2.2, based on current knowledge of Ganymede, to which the generated models should adhere. It was shown how these desired characteristics can be calculated for each generated model in Sections 2.2.1-2.2.4. Section 2.3 elaborated on the implementation of the theories provided in Chapter 2 and provided how the data resulting from these simulations will be processed.

Chapter 3 introduced local density and boundary variations which can occur within Ganymede's internal structure in Sections 3.1-3.4. The implementation of these different variations and adding them to the 1D homogeneous models from Chapter 2 was elaborated on in Section 3.5.

The Global Spherical Harmonics Package, which will be utilized to determine the gravitational potential fields of the models generated in Chapter 3, was discussed in Chapter 4. The input format of the package was introduced in Section 4.1 and its outputs in Section 4.2. Section 4.2.1 provided an explanation on gravitational potential field outputs and how these can be corrected, which enhances understanding of the results. Finally, the gravitational potential field model coefficients resulting from the GSHP and their degree variances have been discussed in Section 4.2.3.

All theories and methods to perform the desired research have now been provided. Chapter 5 will dive into the verification and validation of the different algorithms and modules. The final results of this research are presented in Chapter 6.

<sup>1</sup>European Planetary Science Congress 2018 Poster Presentations: [https://www.epsc2018.eu/information/general\\_information.html](https://www.epsc2018.eu/information/general_information.html), [cited 27-01-2019]

## VERIFICATION AND VALIDATION

It is important that the algorithm created to generate the models works as intended. Therefore the modules of the final algorithm have been verified and where possible validated. Section 5.1 provides the verification and validation of the 1D homogeneous model generators. All aspects involved in generating the 3D heterogeneous models are verified in Section 5.2.

### 5.1. HOMOGENEOUS 1D MODELS

To verify that the algorithm which determines the 1D homogeneous models works correctly, the results of the different modules have been checked. This is done by comparing results to known characteristics of Ganymede and by analytically checking if the output of certain parts of the algorithm work as intended.

#### 5.1.1. MASS

Equations 2.3 and 2.4 determine the mass of the model based on the layer thicknesses and densities of the layers that are provided as input. For convenience, these are provided again in Equations 5.1 and 5.2.

$$M_{shell} = \frac{4}{3}\pi\rho_{shell}(r_{out}^3 - r_{in}^3) \quad (5.1) \quad M_{Model} = \sum_{i=1}^n M_{shell}(i) \quad (5.2)$$

This part of the algorithm will be checked by analytically applying these equations and comparing these to numerical results. Another important consideration is that Ganymede consists of a mass of approximately  $1.4817 \cdot 10^{23}$  kg [44]. The input for this test will be three models which passed the mass check and these are referred to as Aqva I, Spes I and Gelo I. These models consist of varying internal structures which are provided in Table 5.1. The densities from Table 2.1 are also utilized, except for the ocean and core densities as these vary per model.

Table 5.1: The models used to verify the mass determination part of the algorithm.

	<b>Gelo I</b>	<b>Spes I</b>	<b>Aqva I</b>
Ice I <sub>h</sub> [km]	150	125	75
Ocean [km]	30	250	750
Ice III [km]	70	0	0
Ice V [km]	140	40	0
Ice VI [km]	414	379	39
Mantle [km]	1270	1210	630
Core [km]	560	630	1140
Ocean Density [g/cm <sup>3</sup> ]	0.997	1.047	1.163
Core Density [g/cm <sup>3</sup> ]	8.000	8.000	5.150

The mass of these models will first be determined analytically. Equation 5.1 provides several mass values for the individual shells, which add up to the total mass of each model. This data is all provided in Table 5.2, the values of the individual shells are rounded for a better visualization. This was not the case during the calculations which provided the final model masses.

Table 5.2: The masses of the individual shells and the total models. These are obtained by applying Equations 5.1 and 5.2 with the densities and thicknesses of each shell.

	<b>Gelo I</b>	<b>Spes I</b>	<b>Aqva I</b>
Ice $I_h$ [ $10^{23}$ kg]	0.116	0.0973	0.0595
Ocean [ $10^{23}$ kg]	0.0229	0.187	0.528
Ice III [ $10^{23}$ kg]	0.0600	0.000	0.000
Ice V [ $10^{23}$ kg]	0.119	0.0319	0.000
Ice VI [ $10^{23}$ kg]	0.295	0.268	0.0214
Mantle [ $10^{23}$ kg]	0.810	0.814	0.553
Core [ $10^{23}$ kg]	0.0589	0.838	0.320
<b>Total [<math>10^{23}</math> kg]</b>	<b>1.4819</b>	<b>1.4817</b>	<b>1.4818</b>

When applying the algorithm to determine the mass of these three models, this results in three equal model masses. Except for rounding differences, the masses of the shells are also exactly similar. Each of the model masses is within the mass requirement set in Table 2.2. Therefore this part of the algorithm can be considered verified.

### 5.1.2. MOMENT OF INERTIA FACTOR

This section verifies that the algorithm works correctly for the moment of inertia (MoI) factor. The same three models are considered as during the mass verification; Gelo I, Spes I and Aqva I (Table 5.1). Equations 2.7 - 2.10 are applied analytically and will be compared to the results of the algorithm. The equations have been depicted once more in Equations 5.3 - 5.6.

$$I_{shell} = \frac{8}{15} \pi \rho_{shell} (r_{out}^5 - r_{in}^3 r_{out}^2 - r_{out}^3 r_{in}^2 + r_{in}^5) \quad I_{Model} = \sum_{i=1}^n I_{shell}(i) \quad (5.4)$$

$$I_{Av} = \frac{8}{15} \pi \rho_{shell} r_{out}^5 \quad \Theta_{Model} = \frac{I_{Model}}{I_{Av}} \quad (5.5)$$

The moments of inertia for the individual shells and the total models are provided in Table 5.3

Table 5.3: The moment of inertia of each individual shell and the total models. These are obtained by applying Equations 2.7 - 2.10 with the densities and thicknesses of each shell provided in Tables 2.1 and 5.1. The MoI factors are based on an average model MoI based on Equation 2.9, a mean density of  $1.936 \text{ g/cm}^3$  and the GM and radius measurements of Galileo [1].

	<b>Gelo I</b>	<b>Spes I</b>	<b>Aqva I</b>
Ice $I_h$ [ $10^{35} \text{ kgm}^2$ ]	0.0355	0.0250	0.00928
Ocean [ $10^{35} \text{ kgm}^2$ ]	0.00136	0.0892	0.692
Ice III [ $10^{35} \text{ kgm}^2$ ]	0.00813	0.000	0.000
Ice V [ $10^{35} \text{ kgm}^2$ ]	0.0309	0.00229	0.000
Ice VI [ $10^{35} \text{ kgm}^2$ ]	0.199	0.165	0.00119
Mantle [ $10^{35} \text{ kgm}^2$ ]	0.984	0.973	0.406
Core [ $10^{35} \text{ kgm}^2$ ]	0.00738	0.0133	0.166
<b>Total [<math>10^{35} \text{ kgm}^2</math>]</b>	<b>1.2660</b>	<b>1.2676</b>	<b>1.2743</b>
<b>MoI Factor [-]</b>	<b>0.3078</b>	<b>0.3083</b>	<b>0.3099</b>

Table 5.3 provides the analytically determined moment of inertia aspects for each model. The MoI factors are based on an average model MoI based on Equation 2.9, a mean density of  $1.936 \text{ g/cm}^3$  and the GM and radius measurements of Galileo [1]. This results in an average moment of inertia of  $4.1124 \cdot 10^{35} \text{ kgm}^2$ . When these values are compared to the outputs of the algorithm, the data is equal except for rounding differences. When compared to Table 2.2, each model is within the requirements set for the MoI factor. Hence the algorithm is considered verified regarding the MoI factor.

### 5.1.3. PRESSURE AND GRAVITY PROFILES

To obtain a proper hydrostatic pressure profile of Ganymede's interior, a profile of the gravitational potential is required (Equation 2.12). When applying the fundamental principles as discussed in Section 2.2.3, the profiles should primarily look as depicted in Figure 5.1 [49].

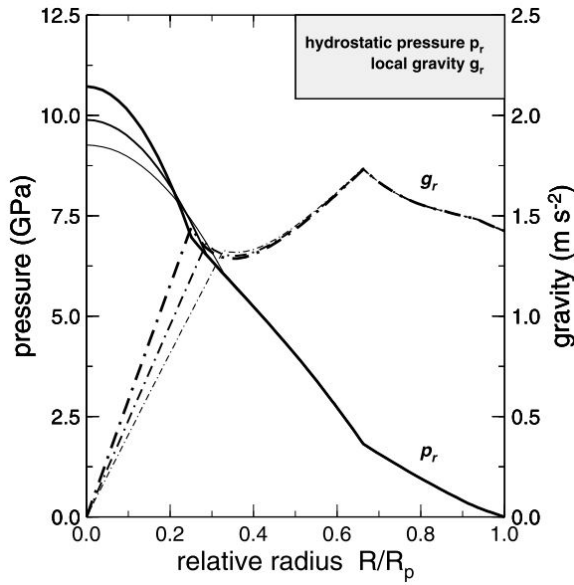


Figure 5.1: The expected gravitational potential and pressure profile within Ganymede [49]. The three different curves are for a pure iron core (bold curve), 50% iron 50% FeS and 100% FeS core (light curve).

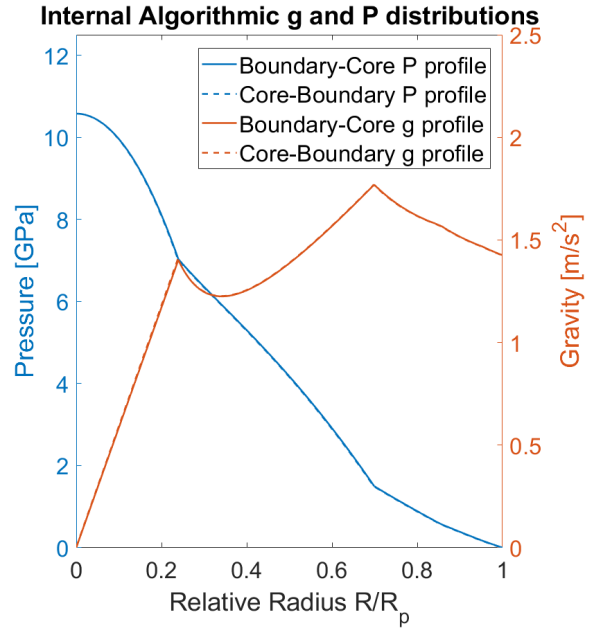


Figure 5.2: The gravitational potential ( $g$ ) and pressure ( $p$ ) profiles determined by the algorithm for Spes I. This is performed on a model with a pure iron core and thus adheres to the bold curves in Figure 5.1. The solid lines represent the integrations performed from the surface to the core of Ganymede. The dotted lines the integration from the core to the surface.

To be certain that the Runge-Kutta integrator works as intended for the provided inputs, the pressure and gravitational acceleration from the surface to the core and from the core back to the surface are determined. If the integrator is implemented correctly these two separate lines should coincide, this seems the case in Figure 5.2. The gravitational potential at Ganymede's surface is determined by using Equation 2.14 and the mass and radius of Ganymede, which were provided in Section 5.1.1. Substituting all values results in a gravitational potential of  $1.426 \text{ m/s}^2$  at Ganymede's surface. When initializing the integration at the surface with  $p = 0 \text{ GPa}$  and  $g = 1.426 \text{ m/s}^2$ , the resulting pressure and gravitational potential at the core are  $p = 10.58 \text{ GPa}$  and  $g = 0.00671 \text{ m/s}^2$ . When used as initial values for the integration from the core to the surface, the distributions follow the same profile and have final values of  $p = 0.005287 \text{ GPa}$  and  $g = 1.425 \text{ m/s}^2$ . Diverging errors are only 0.05% for the pressure and 0.07% for the gravitational potential. As the core pressure uncertainty is multiple times larger (Table 2.2), these uncertainties will not impact the results of the simulations. These do have to be taken into account when considering the ice phase diagrams in Section 5.1.4

The boundary conditions used for the integrator will be the pressure and gravitational potential at the surface of Ganymede, as these are both known. The pressure can be assumed to be equal to 0 Pa [49]. The results of the algorithm for Spes I (Table 5.1) can be found in Figure 5.2. The pressure and gravity distributions throughout Ganymede's interior follow an identical profile as literature [49]. The layer thicknesses and densities of the models from literature were not provided, hence the exact values within the profiles cannot be compared. However, internal structures based on similar internal density distributions and layers were considered. Hence the overall profiles from literature and the algorithm should be similar. This clearly is true for Figures 5.1 and 5.2. Hence it can be concluded that the gravity and pressure profile generator within the algorithm works correctly.

#### 5.1.4. ICE PHASES

Finally, if the considered model passes all previous requirements, it will be compared to Figure 2.3. This is done by checking if the pressure determined (as discussed in Section 5.1.3) at the start of each  $\text{H}_2\text{O}$  phase boundary corresponds to the pressure in Figure 2.3. Slight divergences exist within the pressure determinations, which were provided in Section 5.1.3. In the generated models densities of layers are constant over depth, whereas these typically would slightly increase [54]. Therefore an offset of 2% is allowed to prevent

false negative selections.

Next, the temperatures resulting from the boundary pressures and location within Figure 2.3 are considered. The temperature profile for each model should increase with depth as the 1D-steady-state temperature profiles are sub-adiabatic [54] [22]. The thermoclines provided in Figure 2.3 follow directly from previous research [54] and will be correct. The temperature profiles of viable models with a non-saline ocean and an expected core density have been provided in Figure 5.3. This is done to check if the calculated pressures of the models are located at the boundary interfaces between phases and if the temperature profiles of the models are sub-adiabatic.

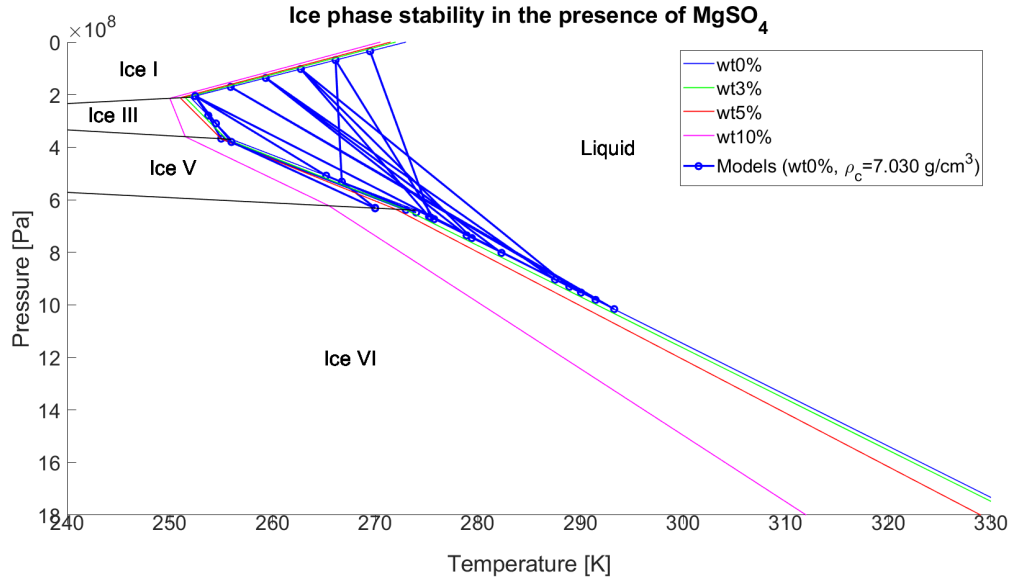


Figure 5.3: Temperature profiles resulting from the simulations for viable models with a non saline ocean and an expected core density.

Figure 5.3 provides the temperature profiles of all viable models with a fresh water ocean and core density of  $7.030 \text{ g/cm}^3$ . Only the interactions between the  $\text{H}_2\text{O}$  phase layers were considered (hence not the mantle/core temperature). The boundary pressures, indicated by dots, are all located on boundary interfaces. These interface are the black lines and blue lines for models with a fresh water ocean. The temperatures for the ice and liquid layers increase for increasing pressure. Therefore, the algorithm works correctly when considering internal pressures, temperatures and ice phases. The important aspect of the temperature profiles are the boundary temperatures and their relative size. For illustration purposes these boundary temperatures have been connected linearly.

### 5.1.5. HOMOGENEOUS MODEL SIMULATIONS: FIXING A BOUNDARY LAYER

As briefly mentioned in Section 2.1, during the main simulations the ice VI layer thickness will be determined based on the radius of Ganymede and the other layer thicknesses. This will reduce simulation times, but it should be checked if this does not manipulate the results in a negative manner. Therefore, two small test-runs were performed to see if this is the case. One run includes a fixed ice VI layer, whereas the other run has a fixed the ocean layer using the same method. The results are provided in Figures 5.4 and 5.5.

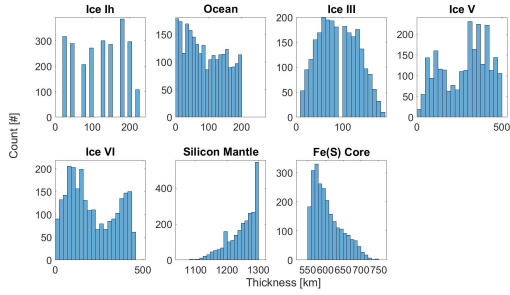


Figure 5.4: Layers thicknesses within the allowable models from the initial simulation. The ice VI layer has been fixed to the known radius of Ganymede.

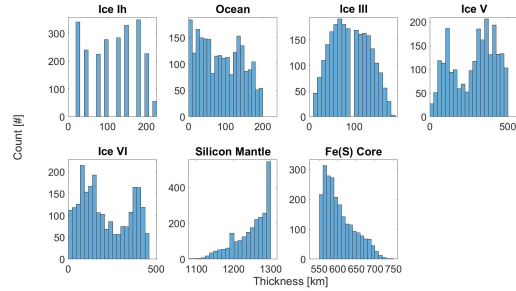


Figure 5.5: Same simulation but now with the ocean layer fixed to the known radius of Ganymede.

These figures provide the layer thicknesses within the generated models which adhere to the requirements. Small variations are expected in the ocean and ice VI layers as the radius of Ganymede equals 2634 kilometers and thus several models will have a slightly different layer thickness distribution. All layers in this verification use a step-size of 10 km, except for the topography. This layer uses a step-size of 25 km due to time constraints. Therefore the layer which is fixed will always include the last 4 or 9 kilometers of Ganymede's radius. This could result in slight shifts within the layer thickness distributions, but this will not influence the results of this research in a negative way (as it can only decrease step-size). Overall, the simulations result in similar models and thus the algorithm works correctly when fixing a single layer to Ganymede's radius.

## 5.2. HETEROGENEOUS 3D MODELS

Next to the determination of the 1D homogeneous models of Ganymede, the modules which generate the local boundary and density variations should be verified. Two steps are executed within these codes. The proper boundary interface should be selected, which can vary based on the anomaly considered. This is discussed in Section 5.2.1. Next, the height or density of the boundary should be varied as intended. This part of the modules is discussed per anomaly in Sections 5.2.2 - 5.2.5. The GSHP has already been extensively been verified [38], but its implementation will briefly be considered in Section 5.2.6.

### 5.2.1. FINDING BOUNDARIES

All modules have to find the correct boundary interface before these can be varied. This part of the algorithm should work with different boundary depths and minimum layer thicknesses (Section 4.1). Aqva I is considered during this section. Its boundaries correspond to the layers provided in Table 5.4 and are based on a nominal layer thickness of 100 km. A single layer only consists of a single type of element or phase, therefore layers can be less thick around the boundary interfaces. This is true for Aqva I's crust, which is only 75 km thick. Hence the ice  $I_h$  - ocean boundary in Table 5.4 is the second layer and the third layer will be located at 175 km depth. The ocean - ice VI boundary occurs 7 layers ( $6 \times 100 \text{ km} + 1 \times 50 \text{ km} = 650 \text{ km}$ ) below this third layer. The boundary depths in Table 5.4 are determined by adding the layer thicknesses in Table 5.1. Density gaps between boundaries are provided, these were discussed in Section 3.3.

Table 5.4: The boundary depths with corresponding layer numbers of Aqva I. Density gaps between boundaries are also provided.

<i>Aqva I</i>	Boundary Depth [km]	Layer [#]	Density Gap [g/cm <sup>3</sup> ]
Topography	0	1	0.937
Ice $I_h$ - ocean	75	2	0.226
Ocean - ice VI	825	10	0.197
Ice VI - mantle	864	11	1.83
Mantle - core	1494	18	1.9

The GSHP uses boundary and density .gmt files as an input, consisting of three columns (Section 4.1). The .gmt files will therefore be indexed based on the layers present within the models. For Aqva I, 30 boundary layers and 29 density layers are present. The size of the .gmt files was discussed in Section 4.1 and is equal to 64800x3 cells. The boundary .gmt files will be indexed in a 64800x90 (3x30) matrix and the density .gmt files in a 64800x87 (3x29) matrix for Aqva I.

The algorithm will be verified using the topography and the mantle - core interfaces as these are the first and last boundaries which the code should find. The code will use the density of the layers to find at which depths boundaries occur. Then, based on the density of the bottom layer, it will determine which boundary is present. Therefore absent boundaries within a model will not affect the functioning of the script. Finally, the algorithm will determine which column in the .gmt matrices should be varied, by multiplying the found layer number by 3. This is due to the longitude and latitude column which are included for each layer.

The algorithm provides the layer number at which the selected anomaly occurs. For the topography of Aqva I this indeed result in a 1, or the first occurring layer. When considering the mantle-core boundary it provides an 18. These are the layers which were provided in Table 5.4 and thus this part of the script can be considered verified.

### 5.2.2. TOPOGRAPHY

The topography of Ganymede, which consists of lower and higher regions, is depicted in Figure 3.2. The Figure is provided again in Figure 5.6 for convenience. This topography can be compared to the variances within the boundary .gmt file of the corresponding layer. The topography of the PCN network should vary between approximately  $\pm 10$  km [59]. The heights within the .gmt file vary between -11.8960 and 9.2879 km. As the exact heights of the PCN are not specified within literature, an exact match cannot be considered. However, the values resulting from the .gmt file seem to adhere to the minimum and maximum values of the PCN.

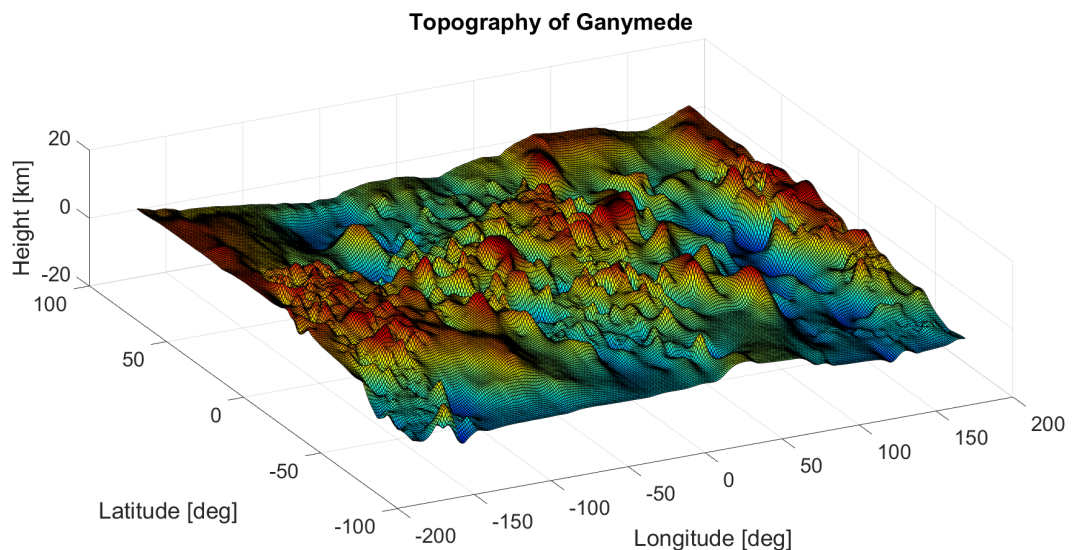


Figure 5.6: The topography of Ganymede with respect to a reference spheroid, resulting from the selected point control network [59].

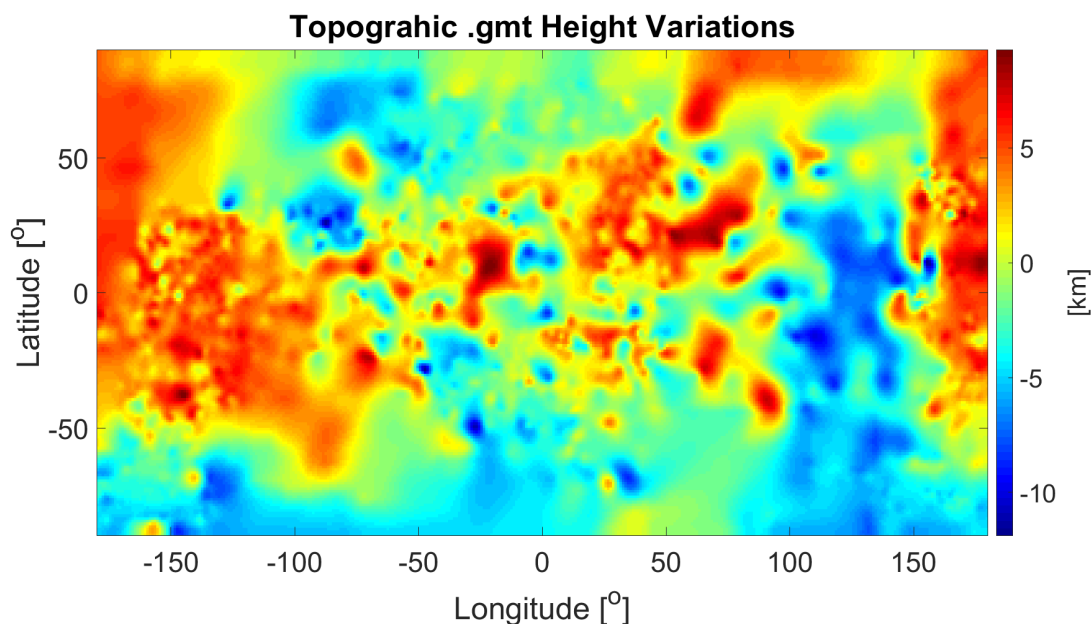


Figure 5.7: The height variations in km resulting from the gmt file of the topography boundary interface.

Another check will be performed on this part of the code. The topography in Figure 5.6 consists of a mass surplus at -180:-150 degrees longitude, -50:50 degrees latitude. A mass deficit is present at 100:150 degrees longitude and -90:-40 degrees latitude. The .gmt file can be inspected at these locations to check if the heights correspond to these variances. For the mass surplus region heights between 3.0337 and 6.6076 km are found and for the mass deficit region heights between -7.5597 and -4.1276 km are present. Finally, the .gmt boundary file as a function of longitude and latitude has been depicted in Figure 5.7. This figure shows that the height variations within the topography of the PCN have been successfully converted to the .gmt boundary file. The height surpluses and deficits are present at the same longitudes/latitudes as Figure 5.6 and vary between the discussed maximum and minimum values. This part of the code is thus considered verified.

### 5.2.3. CRUSTAL VARIATIONS

The three individual crustal variation theories will now be considered. First the thickness variations through albedo are verified, followed by the verification of the isostasy theories.

#### THICKNESS VARIATIONS THROUGH ALBEDO

The crustal thickness variations are based on the albedo of Ganymede's surface. These variations are based on Figure 3.3, which is again depicted in this section as Figure 5.8.

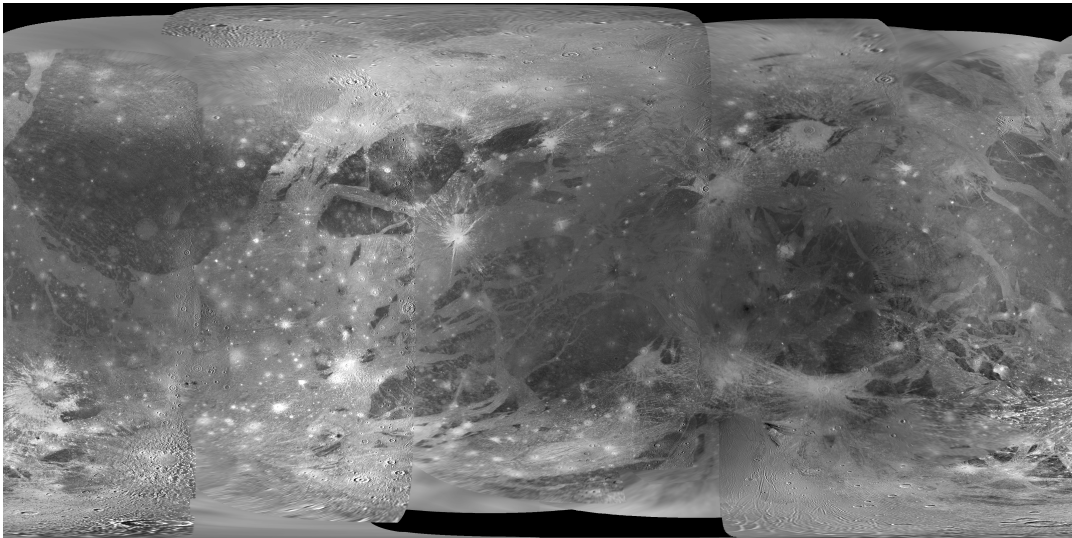


Figure 5.8: A cylindrical map of Ganymede [59] based on its surface including albedo variances. Latitude varies between -90 and 90 degrees and longitude varies between 0 and 360 degrees.

The map of Figure 5.8 has to be converted to a height variation map which is aligned with the longitudes and latitudes used in the GSHP. Again Aqva I is used as the input model, it has a crustal thickness of 75 km and the crustal variations only decrease crust thickness. Thus the lower boundary for the albedo thickness variation has to occur at -75 km (75 km depth with respect to the models surface). Next, the algorithm needs a maximum crust thickness variation difference. For this example it is set to 20 km (approximately the size which is expected [55]) and thus the minimum thickness of the crust should become 55 km. The algorithm should shift the longitudes and latitudes in Figure 5.8 such that these correspond to the input models of the GSHP. The .gmt file for the 20 km crustal thickness variations of Aqva I is provided in Figure 5.9.

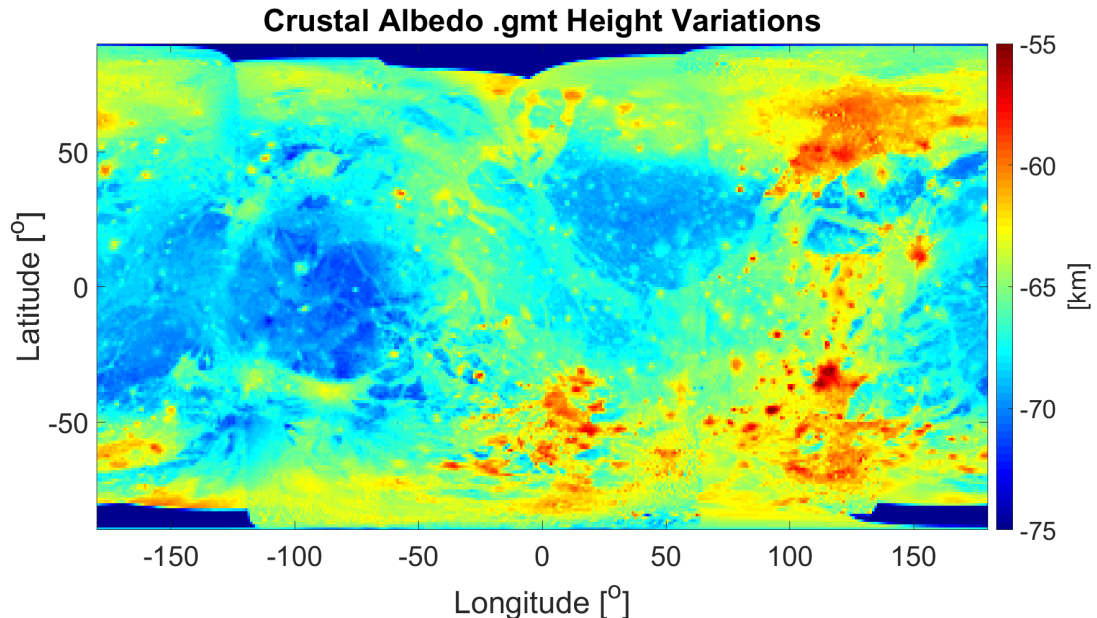


Figure 5.9: The height variations within the crust of the model considered during this section. The algorithm was programmed to vary the thickness between 75 and 55 kilometers. A longitudinal phase shift of 180 degrees with respect to Figure 5.8 was performed such that the .gmt file corresponds to the input files of the GSHP.

The .gmt boundary layer in Figure 5.9 is located at depths between 55 and 75 km. The figure shows distance below the models surface as negative values. A longitudinal phase shift of 180 degrees with respect to Figure 5.8 was performed such that the .gmt file corresponds to the input files of the GSHP. The height differences

(Figure 5.9) at each longitude/latitude adhere to the albedo of Ganymede's crust (Figure 5.8). The darker, low albedo regions, should result in a thicker crust (Section 3.2). For example the large dark area located at [180:270, -50:50] ([lon,lat]) in Figure 5.8 results in a thick crust at [-180:-90, -50:50] in Figure 5.9 (note the longitudinal phase shift). Therefore this part of the code should work as intended.

#### AIRY ISOSTASY

The next crustal variations which will be verified are due to Airy compensation. This theory adheres to Equations 3.1 and 3.2 and can be verified analytically. First it will be considered if the algorithm adheres to the theory provided in Section 3.2.2. Then, the scaling of the compensation is taken into account and if this works as intended. Again Aqva I is used as the input model and recall that the PCN topography varies between heights of -11.8960 and 9.2879 km (Section 5.2.2). Equations 3.1 and 3.2 are restated in Equations 5.7 and 5.8 can be applied with a crustal density of  $0.937 \text{ g/cm}^3$  and an ocean density of  $1.163 \text{ g/cm}^3$ .

$$r_1 = \frac{h_1 \rho_u}{\rho_s - \rho_u} \quad (5.7) \quad r_2 = \frac{d(\rho_u - \rho_w)}{\rho_s - \rho_u} \quad (5.8)$$

For a surface peak of 9.2879 km this results in a root of -38.51 km and a trench of -11.8960 results in a root of 49.32 km. When considering a boundary at 75 km depth, this results in a variance between -25.68 and -113.51 km. Figure 5.10 depicts the crustal variations due to full (100%) Airy compensation resulting from the .gmt boundary file.

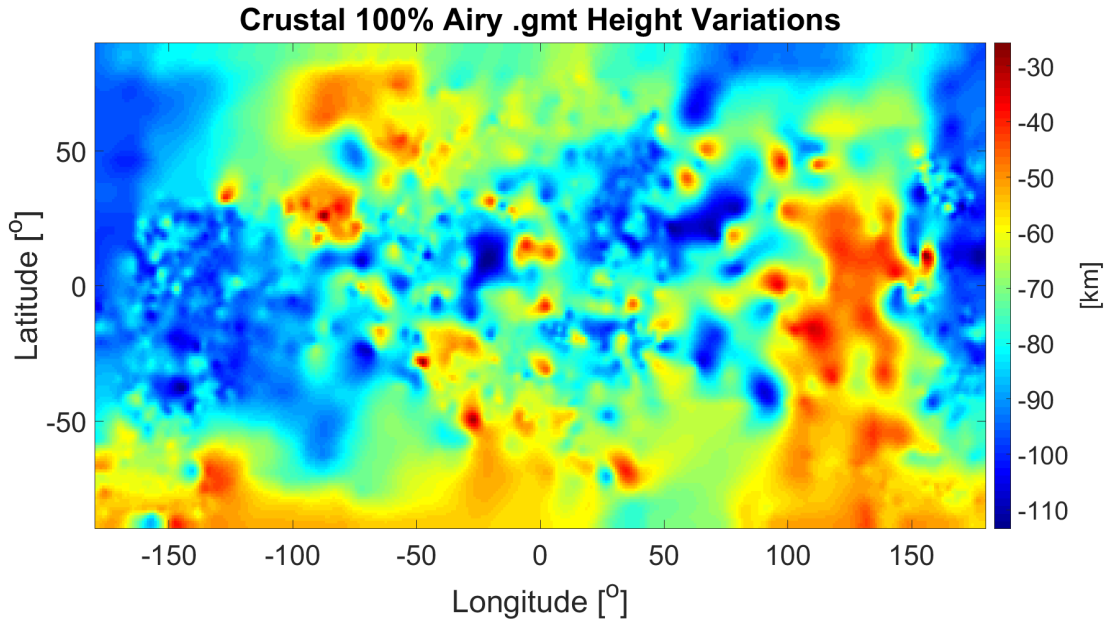


Figure 5.10: The height variations within the crust of the model due to 100% Airy compensation.

The height variances in Figure 5.10 adhere to the analytically determined maximum and minimum height. When compared to Figure 5.7, it is clear that a mass surplus at the surface will be compensated by a negative 'downward' root as the density of the crust is lower as the density of the ocean. A mass deficit at the surface will be compensated by a positive 'upward' root.

$$r_1 = \frac{\frac{1}{4} h_1 \rho_u}{\rho_s - \rho_u} \quad (5.9) \quad r_2 = \frac{\frac{1}{4} d(\rho_u - \rho_w)}{\rho_s - \rho_u} \quad (5.10)$$

25% Airy compensation will now be considered to verify that scaling of the compensation works as intended. Equations 5.7 and 5.8 can then be rewritten as Equations 5.9 and 5.10. The height of the boundaries then varies between -9.63 and 12.33 km. At 75 km depth this will thus be between -62.67 and -84.63 km. Figure 5.11 shows the variations for 25% Airy compensation resulting from the .gmt boundary file.

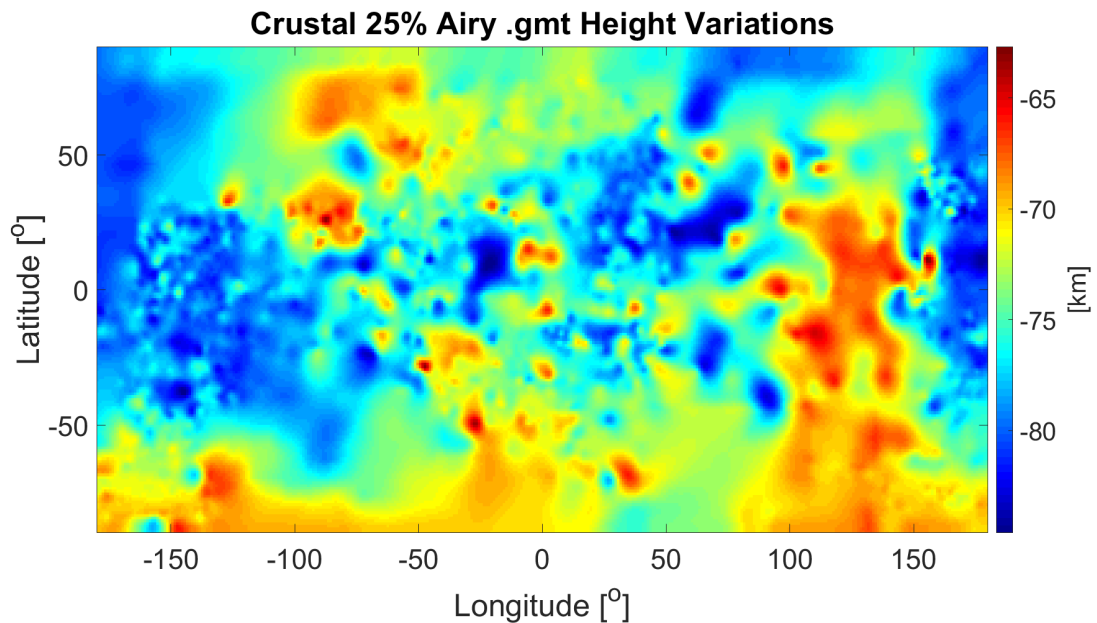


Figure 5.11: The height variations within the crust of the model due to 25% Airy compensation.

Figure 5.11 follows the same pattern as Figure 5.10, but varies only a fourth of the 100% compensation case. Since an equal topography was used and the maximum and minimum values follow the analytically computed range, this part of the algorithm is considered verified.

Due to the low density difference between the crust and ocean layers, Airy compensation can result in large roots. Limitations with respect to these roots and the layer thicknesses will be discussed thoroughly in Chapter 7. In this example 100% Airy compensation is multiple times larger as the albedo model (-113:-26 km and -75:-55 km). However, the 25% Airy compensation model is of similar size as the albedo model (-85:-63 km and -75:-55 km). Airy compensation can vary down and upwards, whereas the albedo model only varies upward. Therefore the variance average is located at different values even though both methods are based on the crust-ocean interface at 75 km depth.

#### PRATT ISOSTASY

Pratt compensation varies the density between two boundaries based on Equations 3.3 and 3.4, restated in Equations 5.11 and 5.12.

$$\rho_1 = \rho_u \left( \frac{D}{h_1 + D} \right) \quad (5.11) \quad \rho_d = \frac{\rho_u D - \rho_w d}{D - d} \quad (5.12)$$

Aqva I is again used as the reference model and due to its crustal thickness the compensation depth is equal to 75 km. Densities of the crust and ocean are again 0.937 g/cm<sup>3</sup> and 1.163 g/cm<sup>3</sup> respectively. The PCN topography, with height variations between -11.8960 and 9.2879 km (Section 5.2.2), is still considered. When analytically solving Equations 3.3 and 3.4 with the provided values for 100% Pratt compensation, values of 0.834 g/cm<sup>3</sup> for a peak of 9.2879 km and 1.114 g/cm<sup>3</sup> for a trench at -11.8960 km are found. Figure 5.12 provides the density variations within the .gmt density file due to 100% Pratt compensation.

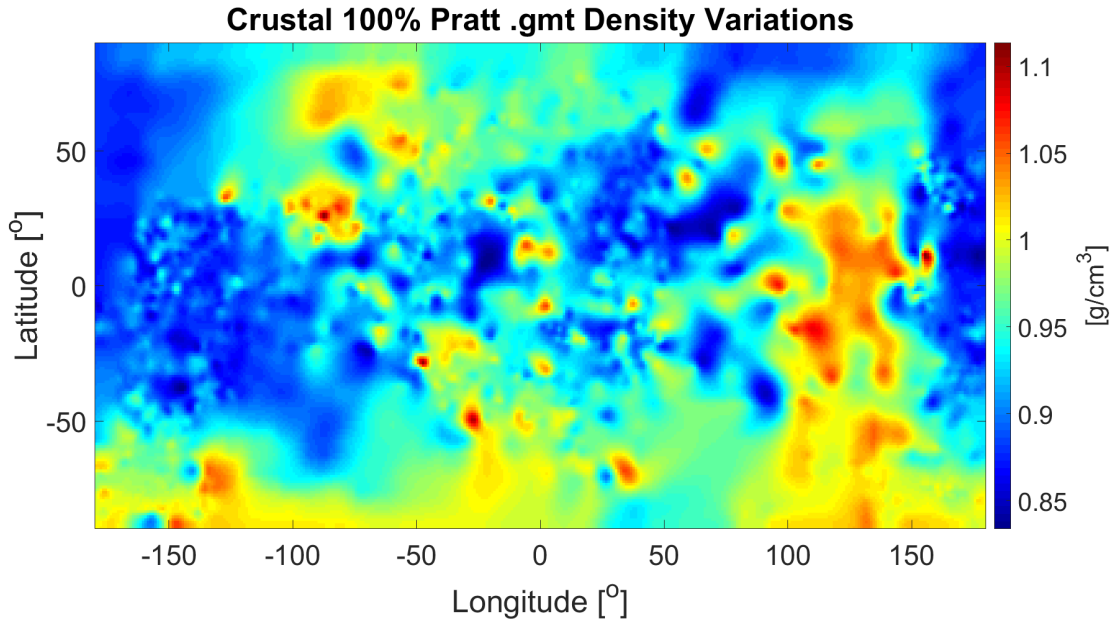


Figure 5.12: The density variations within the crust of the model due to 100% Pratt compensation.

The global structure of Figure 5.12 is similar to those of Figures 5.10 and 5.11, but local distributions of compensations tend to slightly vary due to the different theoretical approaches. The densities in Figure 5.12 adhere to the calculated values of  $0.834 \text{ g/cm}^3$  and  $1.114 \text{ g/cm}^3$ . A mass surplus at the surface will result in a lower density within the model's crust and a mass deficit is compensated by a higher density with the crust (Figures 5.7 and 5.12). Hence the theory provided in Section 3.2.2 is applied correctly. The Pratt compensation should be scalable and therefore also a model with 25% Pratt compensation is considered in Figure 5.13.

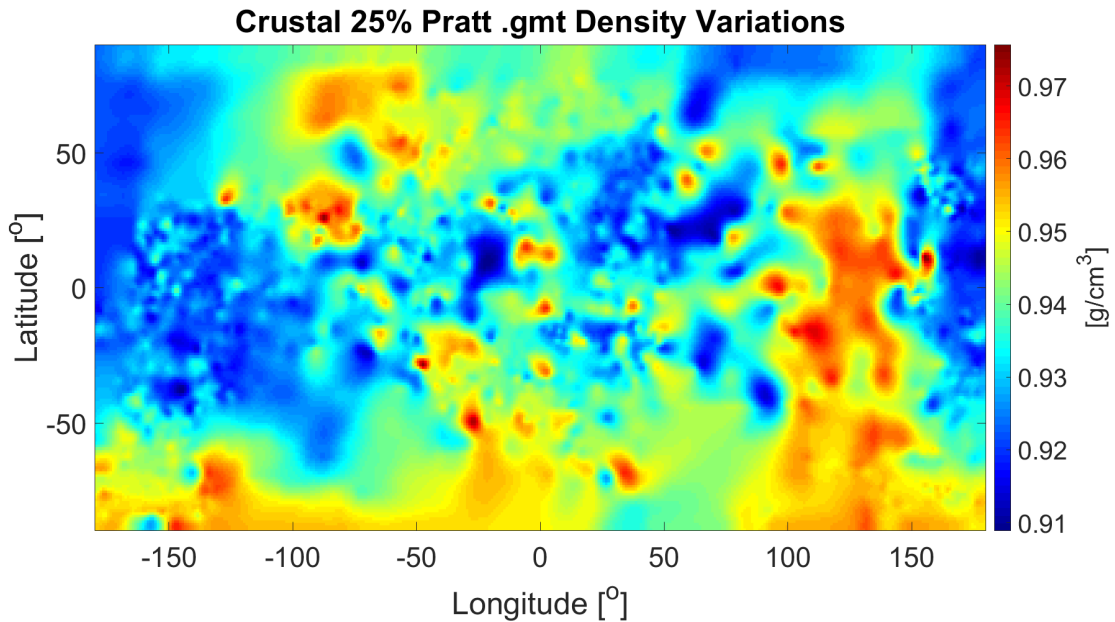


Figure 5.13: The density variations within the crust of the model due to 25% Pratt compensation.

The original density of the crust is equal to  $0.937 \text{ g/cm}^3$ . For 25% Pratt Equations 3.3 and 3.4 are given by:

$$\rho_1 = \rho_u \left( \frac{D}{\frac{1}{4}h_1 + D} \right) \quad (5.13)$$

$$\rho_d = \frac{\rho_u D - \rho_w \frac{1}{4}d}{D - \frac{1}{4}d} \quad (5.14)$$

When substituting the provided values in Equations 5.13 and 5.14, density values of 0.976 and 0.909 g/cm<sup>3</sup> are obtained for height variations between -11.8960 and 9.2879 km respectively. These are the density values which can be found in Figure 5.13. Hence, the last crustal variation type has been verified. The module which implements all these variations is thus also considered verified.

When applying the Pratt model, densities should be monitored to observe if these adhere to water phases within the crust. In extreme cases densities could vary up to the point that these represent rocks in stead of ice. This behavior will be discussed in Chapter 7 for the models resulting from this research.

#### 5.2.4. INTERNAL BOUNDARY VARIATIONS

The internal boundaries all use a different topography as discussed in Section 3.3, but are simulated in an identical manner. Therefore a single boundary will be considered; the ocean floor. Figure 5.14 provides the topographic map used to vary the ocean floor. The longitudes and latitudes are chosen such that these are compliant with the input format of the GSHP, but heights still have to be scaled.

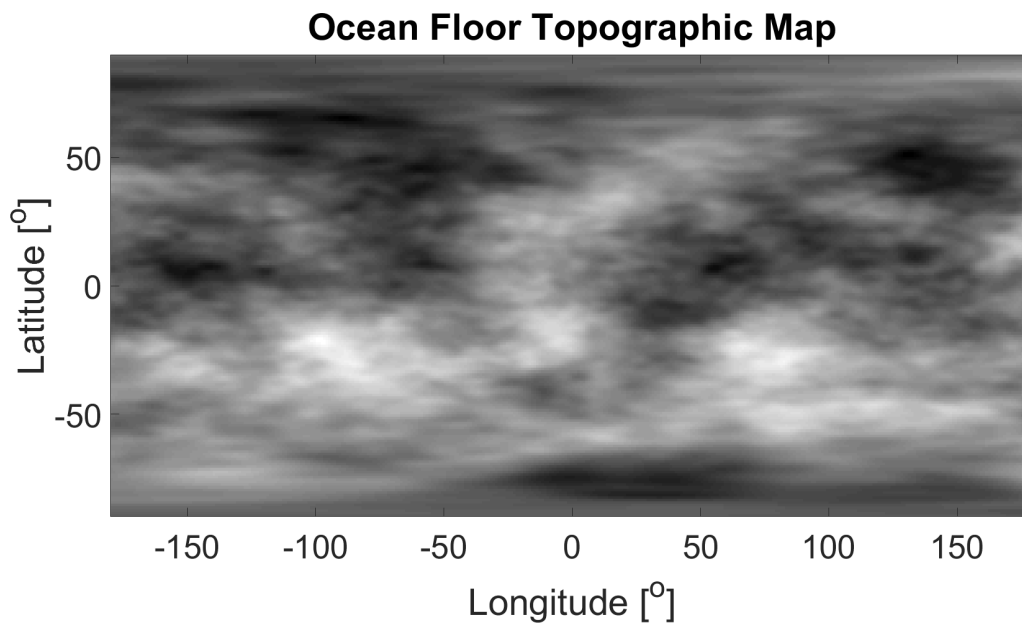


Figure 5.14: The topographic map used to vary the model's ocean floor.

Aqva I is again considered, its ocean floor is located at 825 km depth (Table 5.4). For the example in this section a ocean floor variation of  $\pm 20$  km is applied as is similar to the values expected by literature [55]. The boundary should thus vary between -805 and -845 km depth and adhere to the topography depicted in Figure 5.14. The ocean floor .gmt boundary height variations resulting from the algorithm are given in Figure 5.15.

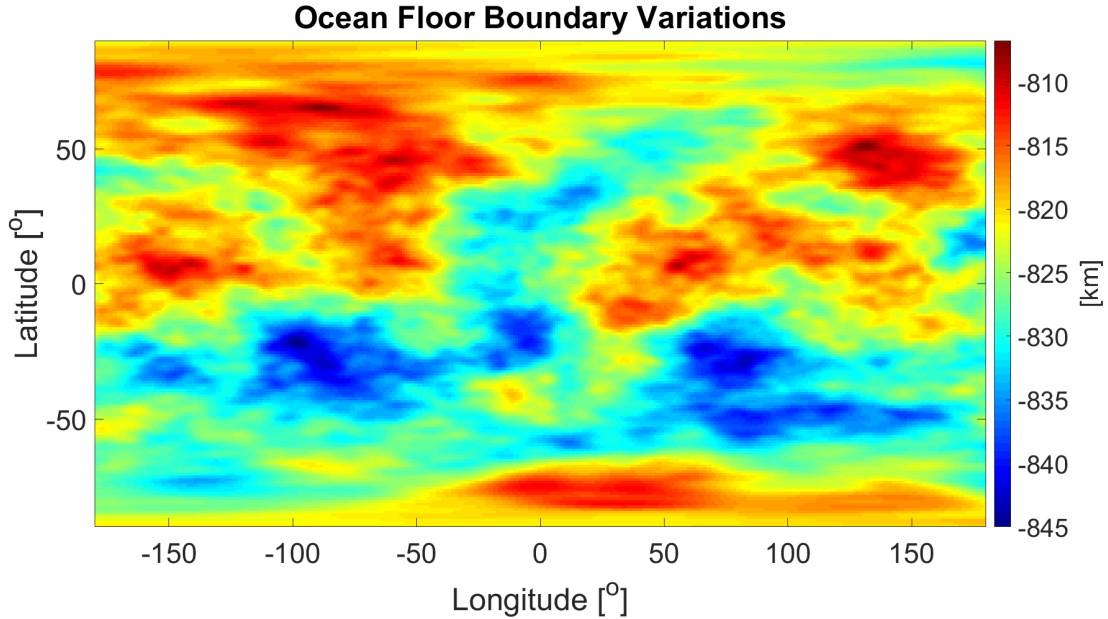


Figure 5.15: The ocean floor thickness variations. These vary between -20 and +20 kilometers with respect to the reference sphere at -825 km.

Figure 5.15 follows the topography of Figure 5.14 and as intended it varies between -805 and -845 km depth. Therefore this part of the algorithm can be considered verified.

### 5.2.5. POCKETS AND DIAPIRS

The last anomalies to be verified are pockets and diapirs. These will all be simulated using the same part of the algorithm and thus can be verified simultaneously. During this section Aqva I is again considered as input model. It now includes 10 pockets, which have been generated within the crust of the model. Unfortunately the depth variation of pockets is limited to individual layer thicknesses. Small layer sizes increase simulation times significantly and these are thus limited to 100 km for the current models. Therefore pockets can only be varied in height with steps of 100 km without adding additional layers. The effect of pockets within the crust can be measured and will be included within this thesis research. The pockets consist of brine with a density of  $1.15 \text{ g/cm}^3$  and have a radius of 5 km.

As the grid considered by the GSHP is equidistant, pixel size will vary with latitude [38]. Pockets are programmed to vary the density of a pixel and pixel sizes will decrease near the poles due to this scaling. Therefore pockets of equal radius will show a more apparent signal near the poles and a lower signal near the equator. To check if the pixel scaling is working correctly, these will be analytically verified through Equations 5.15 and 5.16.

$$R_S = \sqrt{|R_G^2 - (R_G(\phi/\phi_0))^2|} \quad (5.15) \quad P_S = 2\pi R_S/\lambda_s \quad (5.16)$$

Where  $R_S$  is the radial scale at latitude  $\phi$ ,  $R_G$  is Ganymede's radius and  $\phi_0$  is the latitude at -89.5 degree. At the equator of the model  $R_S = R_G$ .  $P_S$  is the pixel size and  $\lambda_s$  is the amount of steps within the longitude vector. In this case the resolution equals 1 degree (Section 4.1) and thus  $\lambda_s$  is 360 degrees. Equations 5.15 and 5.16 provide the pixel size distribution provided in Figure 5.16. Table 5.5 provides the pixel locations and the column densities resulting from the algorithm.

Table 5.5: Pockets locations and column densities.

Pocket #	Longitude [deg]	Latitude [deg]	Column Density [g/cm <sup>3</sup> ]
1	199.5	84.5	0.9507
2	116.5	65.5	0.9399
3	31.5	46.5	0.9389
4	306.5	28.5	0.9385
5	222.5	9.5	0.9384
6	137.5	-9.5	0.9384
7	53.5	-28.5	0.9385
8	328.5	-46.5	0.9388
9	244.5	-65.5	0.9398
10	159.5	-84.5	0.9483

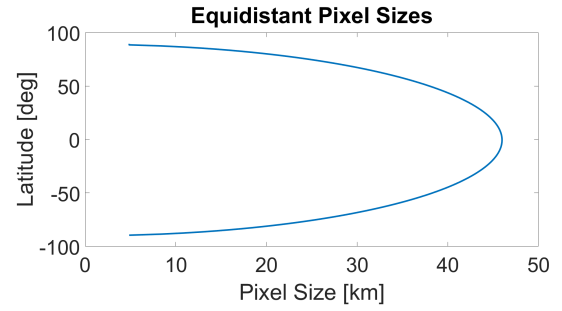


Figure 5.16: Pixel size distribution due to equidistant scaling.

The locations in Table 5.5 will be used during the remainder of this thesis research. This is done such that different models can be optimally compared. The volume of a cubical pocket is determined by Equation 5.17, that of a column with pixel size  $P_S$  by Equation 5.18.

$$V_q = D^3 \quad (5.17) \quad C_V = P_S^2 h \quad (5.18)$$

Where  $V_q$  is the volume of a cube,  $D$  the diameter of the cube,  $C_V$  the volume of a square column with pixel size  $P_S$  and height  $h$ . Equations 5.17 and 5.18 can be used to determine the effect of the pockets density on the column density through volume (Equation 5.19).

$$C_d = (\rho_{Ih} C_V + (\rho_p - C_{d0}) V_p) / C_V \quad (5.19)$$

$C_d$  is the new column density due to the pocket,  $\rho_{Ih}$  is the density of ice  $I_h$  and  $\rho_p$  the density of the pocket. Analytically solving Equations 5.15 - 5.19 for a pocket near the Equator (pocket 5) and for a pocket near one of the poles (pocket 1), results in the values provided in Table 5.6.

Table 5.6: Pockets characteristics analytically determined by Equations 5.15 - 5.18.

Pocket #	Longitude [deg]	Latitude [deg]	Volume [km <sup>3</sup> ]	Pixel Size [km]	Column Height [km]	Column Volume [km <sup>3</sup> ]	Column Density [g/cm <sup>3</sup> ]
1	199.5	84.5	1000	15.151	75	16216.46	0.9506
5	222.5	9.5	1000	45.697	75	156616.19	.9384

The density values of the pockets at the pole and equator resulting from the algorithm (Table 5.5) agree with the analytically determined values in Table 5.6. The density of pocket 1 is off 0.0001 g/cm<sup>3</sup>, but this is only a small offset and due to rounding errors in the analytical calculations. Therefore the pocket and diapir generator can be assumed to function properly.

### 5.2.6. IMPLEMENTATION OF THE GLOBAL SPHERICAL HARMONICS PACKAGE

The GSHP has already been extensively verified [38] and is assumed to work as intended. However, it should be checked if it is implemented correctly. The gravitational acceleration at Ganymede's surface can be determined by using the known mass and radius of Ganymede (Table 2.2), together with Newton's law of universal acceleration. The result is a gravitational attraction of 1.43 m/s<sup>2</sup> [1]. The gravitational potential can be converted to a gravitational acceleration using Equation 5.20 [6].

$$a = \frac{V \mathbf{r}}{r^2} \quad (5.20) \quad a_z = \frac{V}{r_g} \quad (5.21)$$

Where  $\mathbf{r}$  is a position vector in m,  $V$  is the gravitational potential in m<sup>2</sup>/s<sup>2</sup>,  $a$  is the gravitational acceleration in m/s<sup>2</sup> and  $r$  is the radius of the body in m. When considering the radial gravitational acceleration, the loca-

tion vector in Equation 5.20 becomes equal to Ganymede's radius  $r_g$ . and it can be rewritten as Equation 5.21 at Ganymede's surface. Here  $a_z$  is the gravitational acceleration in z-direction.

Aqva I, the 1D homogeneous model which was introduced in Section 4.2, is again considered, but now as a purely spherical body. Its full gravitational potential field should then obtain a singular value, from which the known gravitational acceleration at Ganymede's surface can be calculated. From Equation 5.21 and the average value of  $3.754 \cdot 10^6 \text{ m}^2/\text{s}^2$  which results from the GSHP for a spherical Aqva I, a value of  $1.43 \text{ m/s}^2$  for the gravitational acceleration of the model is found. Hence, the gravitational potential simulations work as intended.

It has been verified that all modules of the algorithm are in agreement with the methods discussed in Chapters 2 - 4. The results generated by the algorithm will be provided in Chapter 6 and are more thoroughly discussed in Chapter 7.



# 6

## RESULTS

The results of the thesis research are presented during this chapter. Section 6.1 provides the results of interest regarding the 1D homogeneous model simulations. The outcomes regarding the 3D heterogeneous models and the gravitational potential field simulations are presented in Section 6.2. All results have been provided with a brief explanation. A more in depth discussion on the important findings and how these could be interpreted can be found in Chapter 7.

### 6.1. HOMOGENEOUS 1D MODELS

First, the possible radial layer thicknesses within Ganymede are determined. The variations of, and correlations between, these layers will be inspected to gain a better understanding of Ganymede's internal structure. Based on these interactions, several models will be selected as an input for the second and third pillars of this thesis research in Section 6.2.

#### 6.1.1. INITIAL SIMULATION

Based on varying layer thicknesses, the number of possible models with 7 layers can be huge. An initial simulation with a relatively large step-size of 25 km was performed to converge on the lower and upper values of the individual layers. Hence an educated estimate for the thickness per layer is determined to avoid unnecessary iterations. This will reduce simulation times significantly as less models are considered during the main simulation (Section 6.1.2), which uses a smaller step-size. The models provided in section 1.1.5 were used as a rough baseline to determine the layer thicknesses used in the initial simulation.

The initial simulation will use the values and step-sizes provided in Table 6.1. The lowest values will be fixed to 0 to make sure models with absent layers will be included. The mantle and core already consist of loosely bounded lower values. This is due to the highly differentiated interior of Ganymede [54]. This cannot be due to the different H<sub>2</sub>O phase densities as these do not differ enough in density.

The densities used in the simulation can be found in Table 6.1, these are based on literature [49] [54] [50] [1]. This initial simulation includes the most likely core density [54] and a non saline ocean. For upcoming simulations, in which the core and ocean densities are varied, the outcome of this initial estimate will be used as a baseline. These results will be analyzed to check if any possible models could be missing within these values. It is assumed that densities remain constant over depth whereas these typically would rise slightly due to pressure differences. Models resulting from this thesis were compared to models using varying densities over depth [54]. This assumption did not result in unacceptable variations within the models.

Table 6.1: Initial simulation step-size and values per layer. [54]

	<b>Lowest Value [km]</b>	<b>Step-size [km]</b>	<b>Highest Value [km]</b>	<b>Density [g/cm<sup>3</sup>]</b>
Ice I <sub>h</sub>	0	25	1000	0.937
Liquid	0	25	1000	0.997
Ice III	0	25	1000	1.166
Ice V	0	25	1000	1.267
Ice VI	-	-	-	1.360
Mantle	400	25	1400	3.250
Core	300	25	1500	7.030

The ice VI layer does not include values and a step-size because the algorithm limits the total thickness of the layers to Ganymede's known radius (Table 2.2, rounded to km). If the model exceeds this radius, it is not

considered. The ice VI layer thickness will be equal to the difference between the known radius of Ganymede minus the total thickness of all the other layers, as long as the radius of Ganymede is not already exceeded by the thicknesses of the other layers.

Based on the models which fulfill all the requirements provided in Section 2.2, the lowest and highest values of the layers will be reduced. These new values will be used as a starting point for the main simulations. The initial simulation upper and lower layer values, as provided in Table 6.1, are depicted in Figure 6.1 as the x-axis limits. This simulation was performed on the models with an wt0% ocean and a  $7.030 \text{ g/cm}^3$  core density.

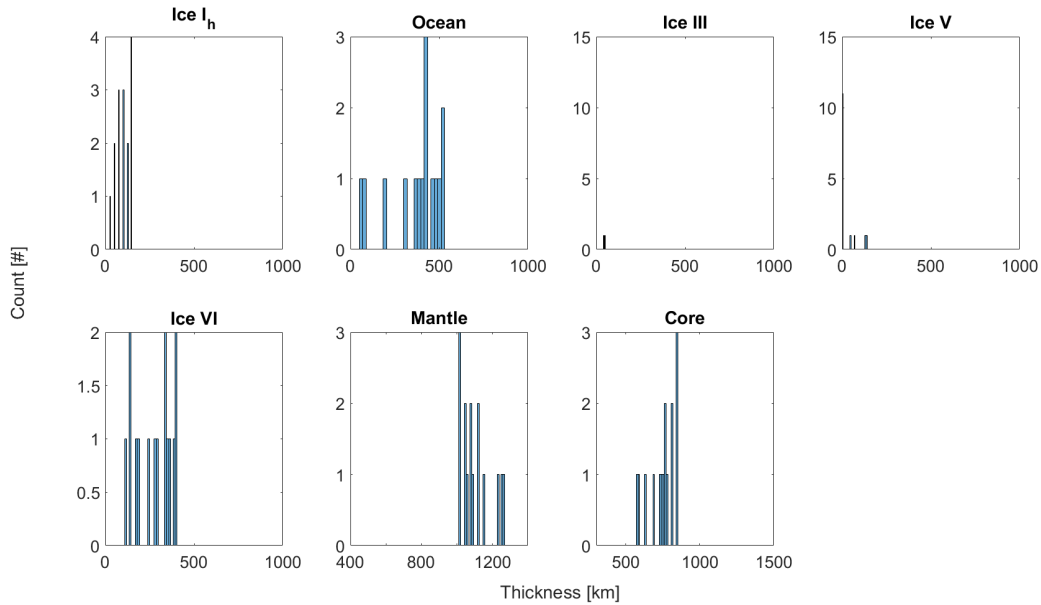


Figure 6.1: Layers thicknesses within the allowable models from the initial analysis using the settings provided in Table 6.1. These are 1D homogeneous models with a non-saline ocean and a core density of  $7.030 \text{ g/cm}^3$

The layer thicknesses of all models that are within the uncertainties of Table 2.2 have been depicted in Figure 6.1. Models are not possible for different layer thickness ranges, hence the thickness variations can be reduced significantly.

Several other aspects are considered for the estimation of the upper and lower layer thickness values of the main simulations. Higher salinity within an ocean will result in less freezing and a higher density core results in more low density elements, or a smaller core, due to a constant moment of inertia factor. Hence model layer thicknesses will vary slightly for different ocean and core densities. This is monitored through statistics, as in Figure 6.1. After each simulation a similar figure is generated, the lowest and/or highest values of a layer will be extended if these limit the simulation.

### 6.1.2. MAIN SIMULATIONS

For the main simulations step-sizes are significantly reduced to 10 km per layer. Only the outer crust remains at 25 km as otherwise simulation times would increase significantly. An overview of the full range of values to obtain all possible models can be found in Table 6.2. The different considered liquid and core densities, as discussed in Section 2.1, are included.

Table 6.2: Full scale simulation step-size and limits per layer [54].

	Lowest Value [km]	Stepsize [km]	Highest Value [km]	Density [g/cm <sup>3</sup> ]
<i>Ice<sub>Ih</sub></i>	25	25	250	0.937
<i>Liquid</i>	0	10	900	0.937, 1.047, 1.080, 1.163
<i>Ice III</i>	0	10	200	1.166
<i>Ice V</i>	0	10	200	1.267
<i>Ice VI</i>	-	-	-	1.360
<i>Mantle</i>	400	10	1400	3.250
<i>Core</i>	400	10	1300	5.150, 7.030, 8.000

Hence with the settings as provided in Table 6.2,  $12 * 10 * 21^2 * 101 * 91^2 \approx 44$  billion different models will be considered using the 7-layer setup as depicted in Figure 2.2. From the 44 billion combinations only 260 models are compliant with all requirements discussed in Section 2.2. The different layer thicknesses of the models have been depicted in Figure 6.2, these results include all different ocean and core densities. The x-axis limits correspond to the lowest and highest layer thickness values as provided in Table 6.2.

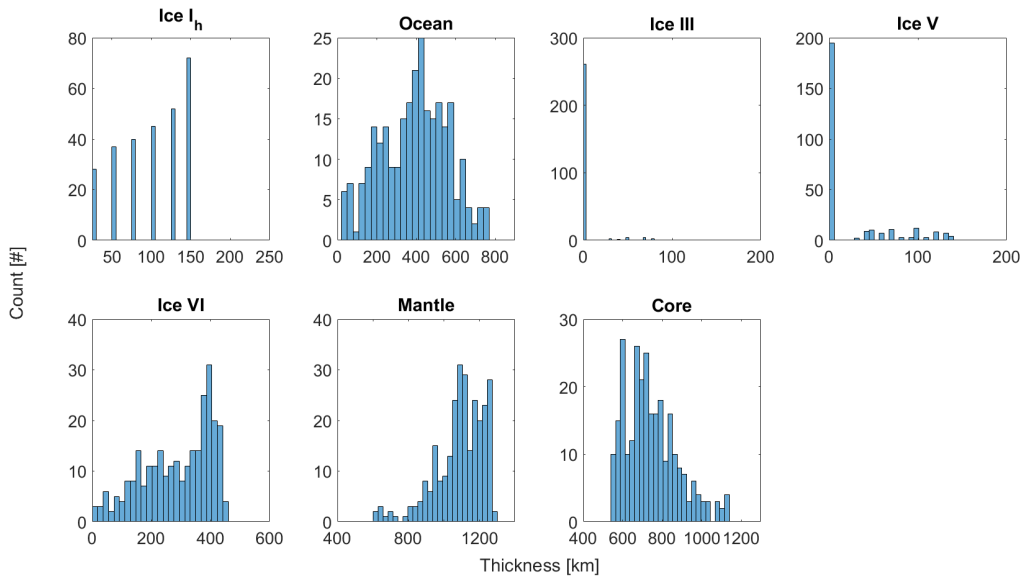


Figure 6.2: Layers thicknesses within the possible 1D homogeneous models of Ganymede resulting from the main simulations using the settings provided in Table 6.2. The ice VI layer has been fixed to the known radius of Ganymede.

Figure 6.2 shows that the model layer thicknesses are within the lowest and highest values provided in Table 6.2. Crusts cannot exceed a thickness of 150 km and models including ice III and ice V are rare. If ice III is present, this layer is thin. The mantle and core layers almost have an inverse distribution and the ice VI layer seems to roughly share the same distribution as the core. Furthermore, most models host an ocean of 200-600 km thickness. Due to these behaviors, it is likely that several correlations between layers are present.

These models were further examined to determine the worlds which will be used as a foundation for the 3D heterogeneous models. To efficiently achieve this, the correlations between all layers have been analyzed. It will be examined which layers are coherent with- and/or dependent on the other layers. The main results of these correlations are presented in Section 6.1.3.

### 6.1.3. LAYER CORRELATIONS

To obtain a comprehensive overview and a better understanding on the interactions between the layers and the requirements, the correlations between all layers have been depicted in several figures. In this section, the correlation plots have been color-scaled with respect to the twelve different model sets. The specified colors for the different sets are provided in Figure 6.3.

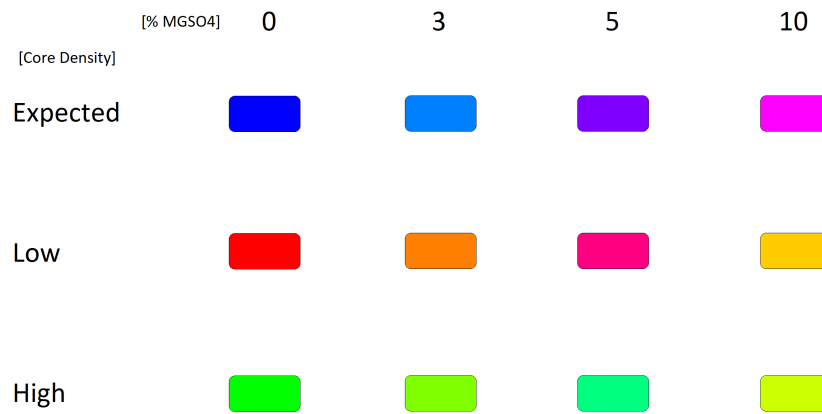


Figure 6.3: The color indicators for the different model sets which were analyzed during the first part of the thesis research. Low core density =  $5.150 \text{ g/cm}^3$ , expected =  $7.030 \text{ g/cm}^3$  and high =  $8.000 \text{ g/cm}^3$ . The salinity percentages are mass percentages.

One full correlation dataset has been depicted in this section, in Appendix C several similar datasets are provided. These are color scaled based on the requirements and layers to see how these influence the models selected. If important behavior is observed within these datasets, the individual plots will be given and discussed in Chapter 7. Figure 6.4 depicts the correlations between all the different layers masked by the color of the datasets (Figure 6.3). Several interesting dependencies between certain layers are present and these will be discussed in Section 7.1.

Correlation between the different layers [km]

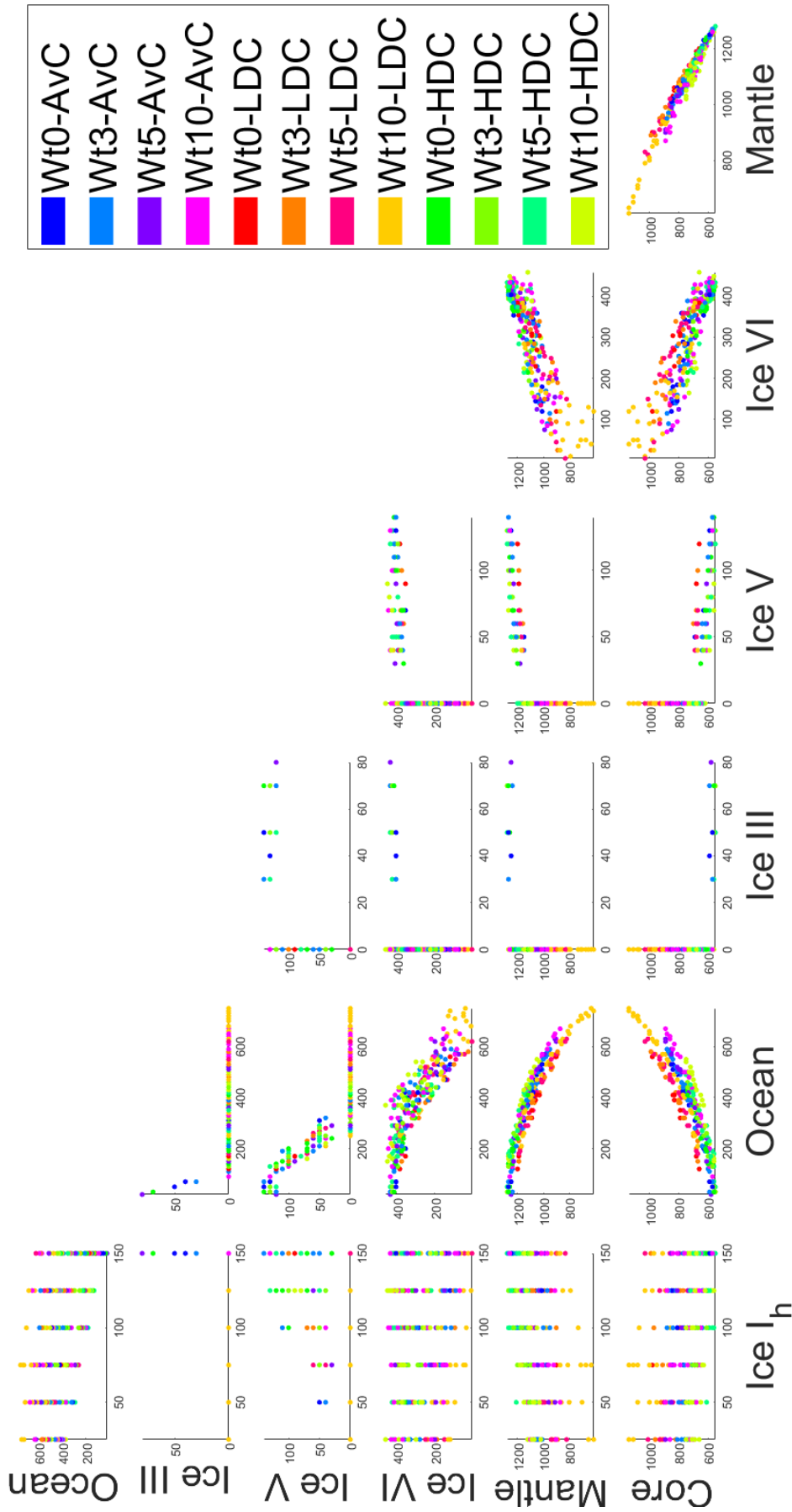


Figure 6.4: The correlations between the different layer thicknesses of the models that passed all requirements. Colors are scaled with respect to the different model sets as provided in Figure 6.3.

#### 6.1.4. WORLDS OF INTEREST

Time does not allow to analyze all 260 models into more detail. Therefore, several different 1D homogeneous models for Ganymede have been selected from the full dataset. This selection, based on the previously provided correlation plots, represents the entire variety of all models.

This section presents these worlds and gives a brief overview in Table 6.3, which provides all the information known about each world. Note that the layers within all the figures of the worlds are to scale and thus give a first visual representation on how the global interiors of the models are distributed. Temperature profiles are included to confirm that all models adhere to the temperature and pressure requirements.

Fourteen models were selected to account for all possible layer variations within Ganymede. Even though all models vary with respect to interior, these can be divided into four different groups and were named accordingly. These are as follows:

- **Spes I-IV** - These are the models which lie within ESA's hypothetical range [12]. Ice V is typically included and the ocean and crust layers are limited by Figure 1.9.
- **Gelo I-II** - Models which include ice III, V and VI. Thin oceans with a maximum thickness of 30 km. Large mantles and small cores are included.
- **Aqva I-V** - These worlds all host oceans with a thickness of 560 km or larger. This can result in configurations consisting of large cores and small mantles.
- **Libra I-III** - More 'balanced' worlds. Typically a mix between oceans of approximately 400 km and ice VI layers between 300 and 450 km. In contradiction to the Spes worlds, these models do not include ice V.

#### Spes I

One of the worlds that lies within ESA's hypothetical range (Figure 1.9) and that has been mentioned during Chapter 5. It consists of an 125 km ice  $I_h$  crust and an 250 km thick ocean with a salinity of wt3%. No ice III is present, but the model does include 40 km ice V and 379 km ice VI. A high density pure iron core with a 630 km radius is present together with a mantle of 1210 km thickness.

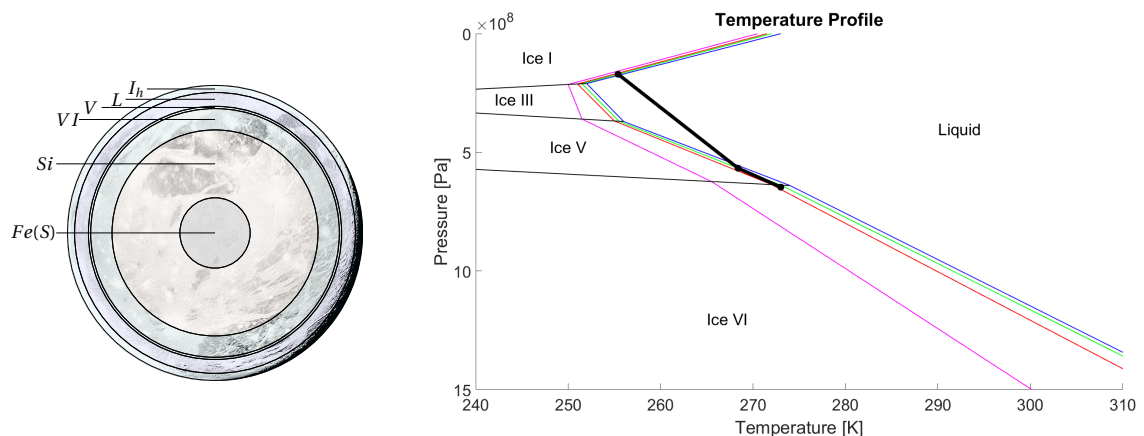


Figure 6.5: The temperature profile for Spes I.

### Spes II

Another model which is within ESA's hypothetical range. The layers differ slightly, but mainly are coherent with the layers within Spes I. Its crust and ocean (wt5%) are slightly thinner, 100 and 220 km respectively. 70 km ice V and 414 km ice VI are present, which is more as for Spes I. This model hosts a mantle of 1240 km and a high density pure iron core of 590 km thickness.

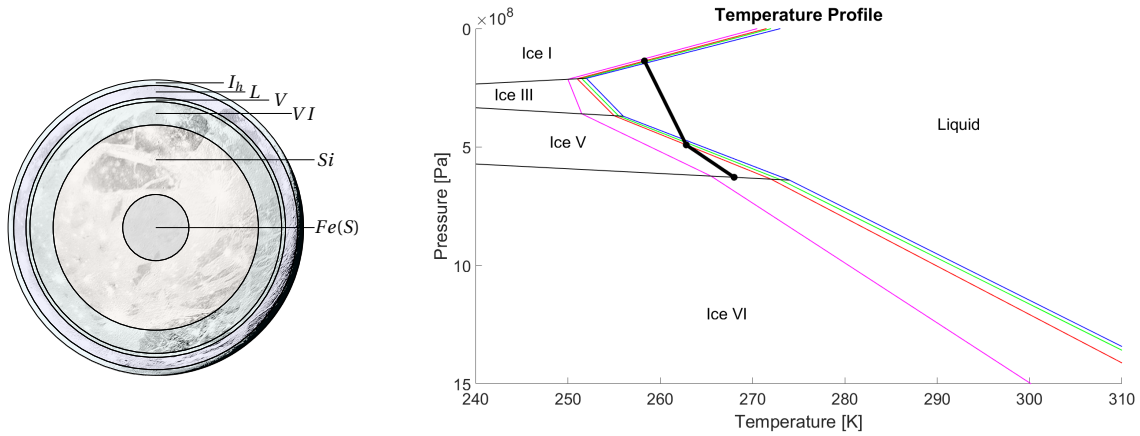


Figure 6.6: The temperature profile for Spes II.

### Spes III

The third selected model within ESA's hypothetical range. Whereas the previous models host high density iron cores, this model includes a low density iron-sulfate core. It consists of a wt5% ocean which is the thickest of the Spes worlds; 270 km. The crust is 75 km thick and ice V and VI are present in layers of 50 and 389 km. 1170 km of silicon is present within its mantle.

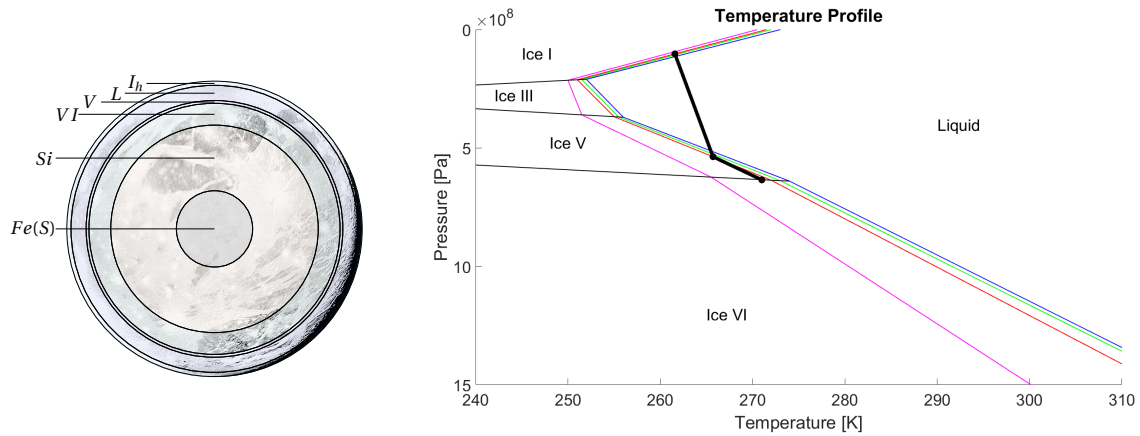


Figure 6.7: The temperature profile for Spes III.

### Spes IV

The final model which is selected based on ESA's hypothetical range. This model includes an average 610 km iron-sulfide core and an ocean of 240 with wt10% salinity. Ice V and VI are present with thicknesses of 40 and 434 km. The core is surrounded by a 1210 km mantle and the models crust has a thickness of 100 km.

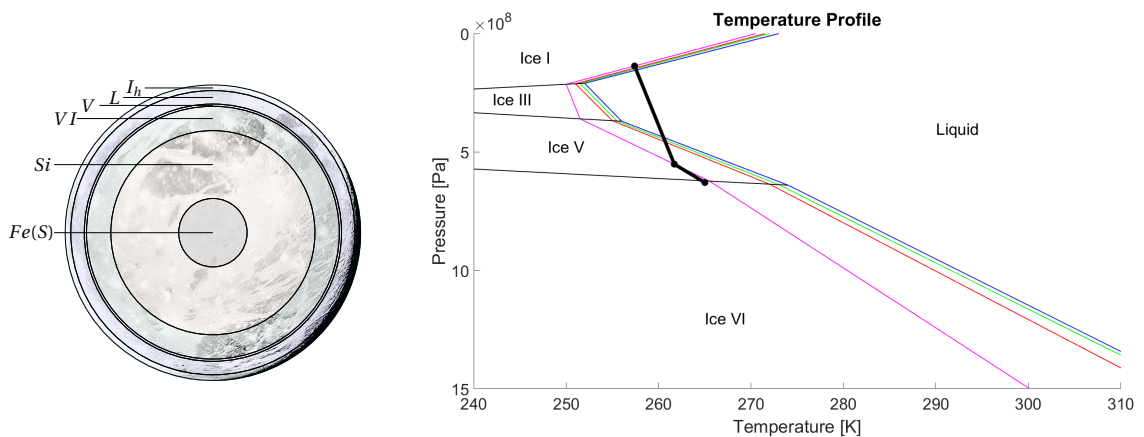


Figure 6.8: The temperature profile for Spes IV.

### Gelo I

Another model that has been mentioned during Chapter 5. A relatively frozen world, consisting of a thick outer crust of 150 km and only a thin ocean of 30 km. It has the thickest layer of ice V (140 km), the largest mantle (1270 km) and smallest core (560 km) of the selected models. It hosts a fresh water ocean and a high density core of pure iron. Its thermal profile almost aligns with the thermocline of fresh water, illustrating this is an end member with respect to present amounts of ice.

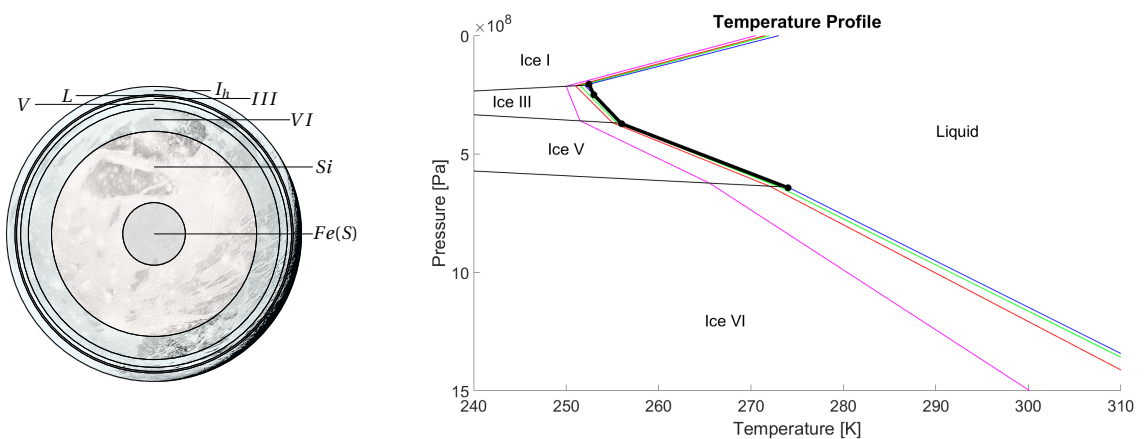


Figure 6.9: The temperature profile for Gelo I.

**Gelo II**

The second considered world consisting of a lot of ice. This world has the thickest ice III layer, 80 kilometers, of the 260 models which passed all requirements. It hosts the thinnest ocean of all the models; 20 kilometers. It's core and mantle are similar to those of Gelo I (580 and 1250 km respectively). It has an average iron-sulfide core and a wt5% ocean.

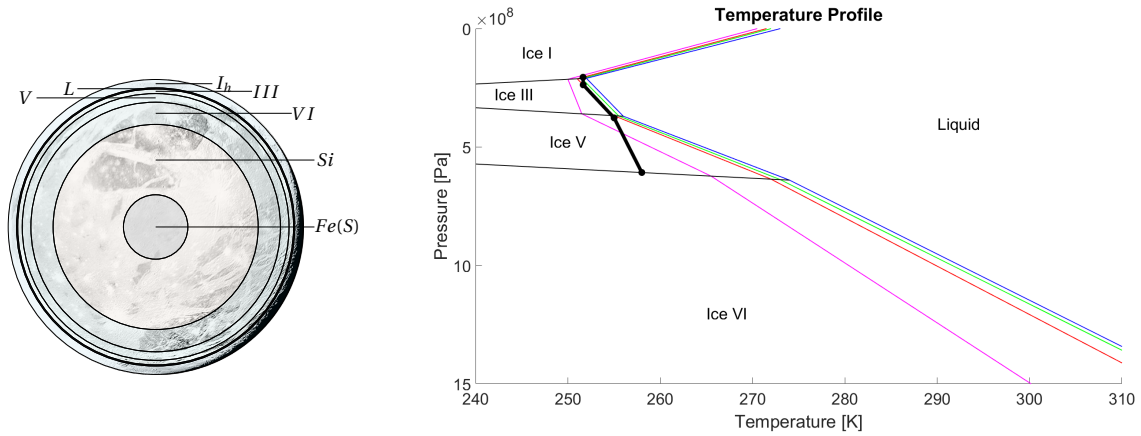


Figure 6.10: The temperature profile for Gelo II.

**Aqva I**

Aqva I has already been mentioned multiple times. This model has the largest ocean possible based on current requirements. Sandwiched by a crust of 75 km and an ice VI layer of 39 km, this ocean has a thickness of 750 km. No ice III or V is present. The mantle and core sizes are almost flipped with respect to the Gelo worlds. The largest core is included in this model; 1140 km. The ocean has a salinity of wt10% and the core is low density. Note for all Aqva worlds the huge jump within the temperature profiles due to these thick oceans.

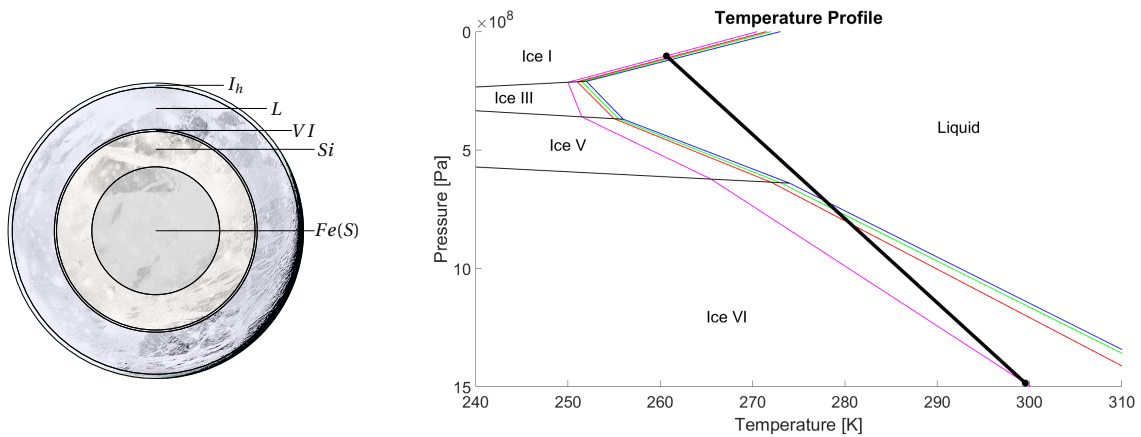


Figure 6.11: The temperature profile for Aqva I.

### Aqva II

Another world defined by its huge ocean. Similar to Aqva I, but this world has a thinner crust (25 km) and includes more ice VI (119 km). The smallest mantle (610 km) is included within this model and its core is the same size as Aqva I's (1140 km). Aqva II has a wt10% ocean of 740 km, a stronger angle of thermocline as Aqva I and a low density iron-sulfide core.

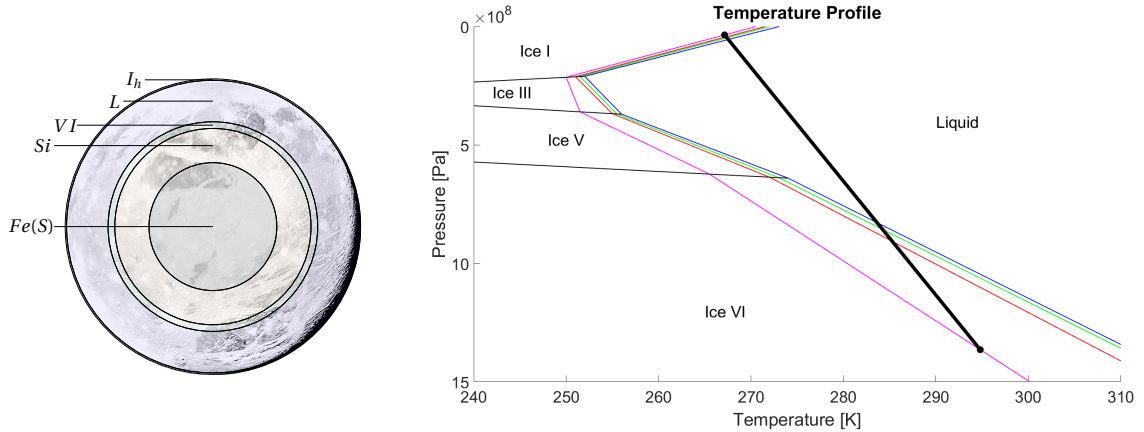


Figure 6.12: The temperature profile for Aqva II.

### Aqva III

A model with a slightly thinner ocean as the previous two models. Aqva III hosts an ocean of 620 km thickness. It has a thick crust (150 km), a mantle of 830 km and the thinnest ice VI layer of all the models; only 4 km. No ice III and V are present, making this the model with the least high pressure ice phases. It has a wt5% salinity ocean and a low density 830 km iron-sulfide core.

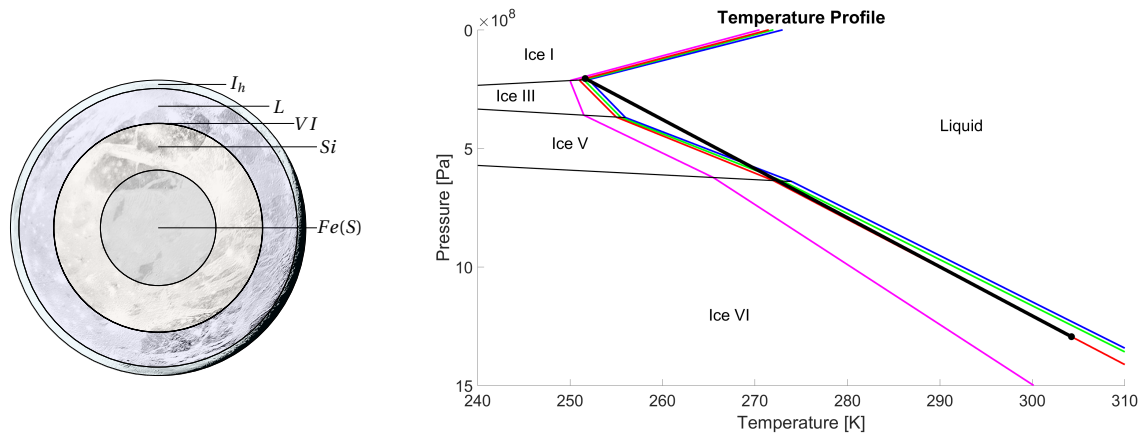


Figure 6.13: The temperature profile for Aqva III.

**Aqva IV**

Aqva IV still has a large ocean, but is already less extreme as the previous Aqva models. Its ocean is 570 km thick and its mantle and core thicknesses engage more typical values (960 km and 860 km). 50 km of ice  $I_h$  is present within its crust and 194 km ice VI around its mantle. It hosts a wt3% ocean and an average density core.

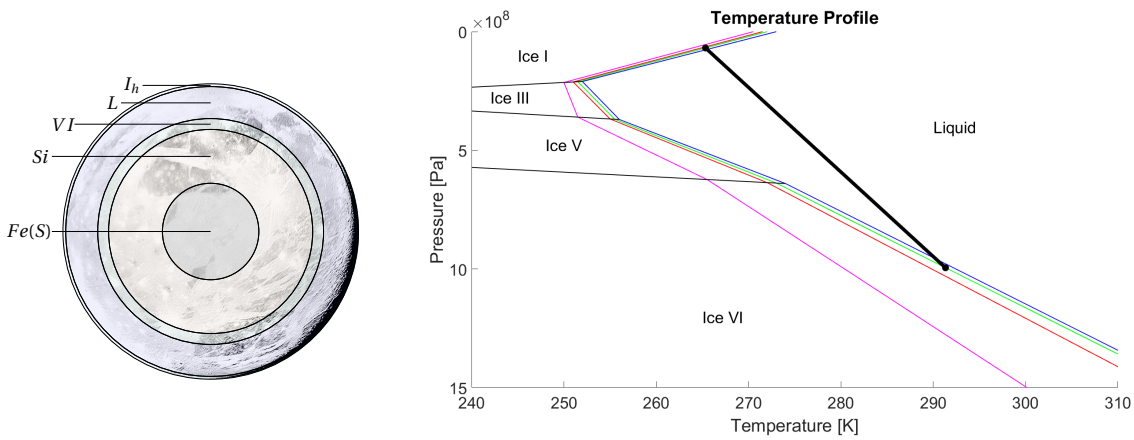


Figure 6.14: The temperature profile for Aqva IV.

**Aqva V**

The final oceanic world. It hosts the smallest ocean of the Aqva worlds (560 km), but no salinity is induced within this ocean. A 75 km crust and 119 km of ice VI are included. It was selected for its mantle/core ratio (900/980 km) and has a low density iron-sulfide core.

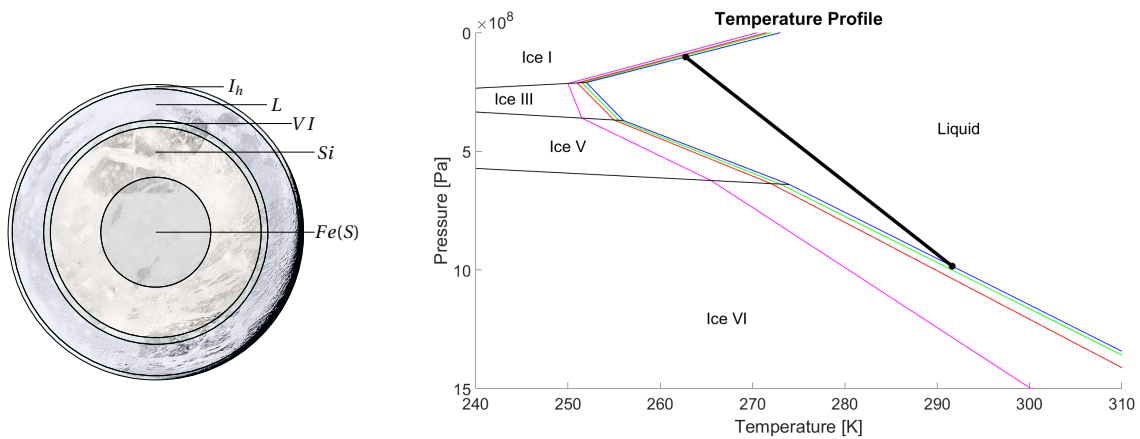


Figure 6.15: The temperature profile for Aqva V.

### Libra I

The first of the more balanced model group. These worlds are defined by a lack of ice III and V and a thick layer of ice VI (344 km for this model). A mantle of 1080 km is present. It includes a fresh water ocean of 400 km, a crust of 50 km and an average iron-sulfide density core.

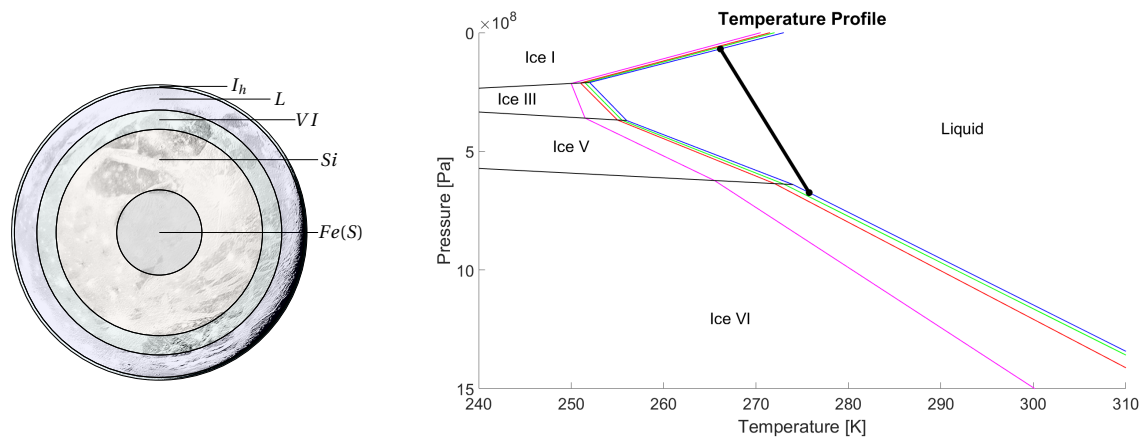


Figure 6.16: The temperature profile for Libra I.

### Libra II

This is the world which hosts the thickest layer of ice VI; 459 km is present. It has a thin 25 km crust and a highly saline wt10% ocean of 370 km thickness. A high density, pure iron, core of 660 km is included together with a mantle of 1120 km thickness. Almost no temperature variations are included within this models thermal profile.

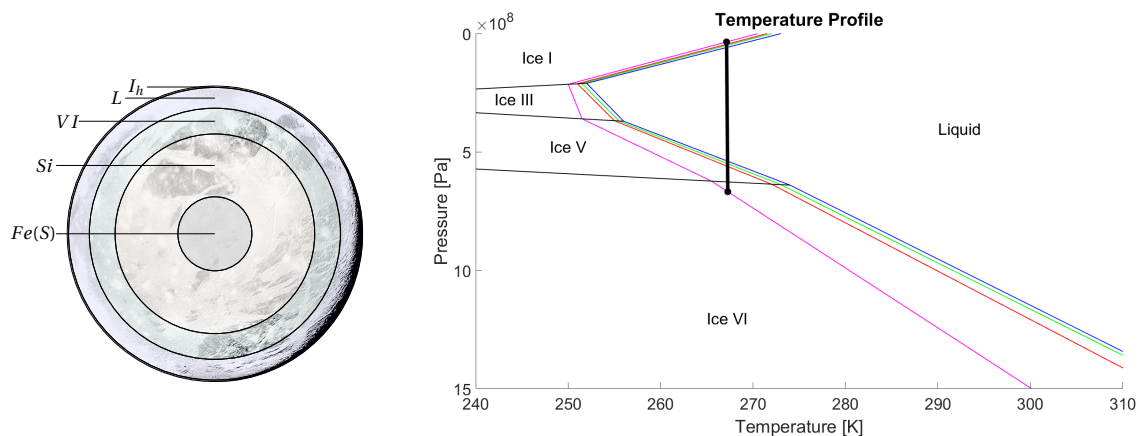


Figure 6.17: The temperature profile for Libra II.

### Libra III

The final selected world. It has a less thick ice VI layer as the previous two Libra worlds (284 km), but has the thickest crust (100 km) and smallest mantle (1070 km). Its wt3% ocean is 380 kilometers thick and the model has a low density iron-sulfide core of 800 km.

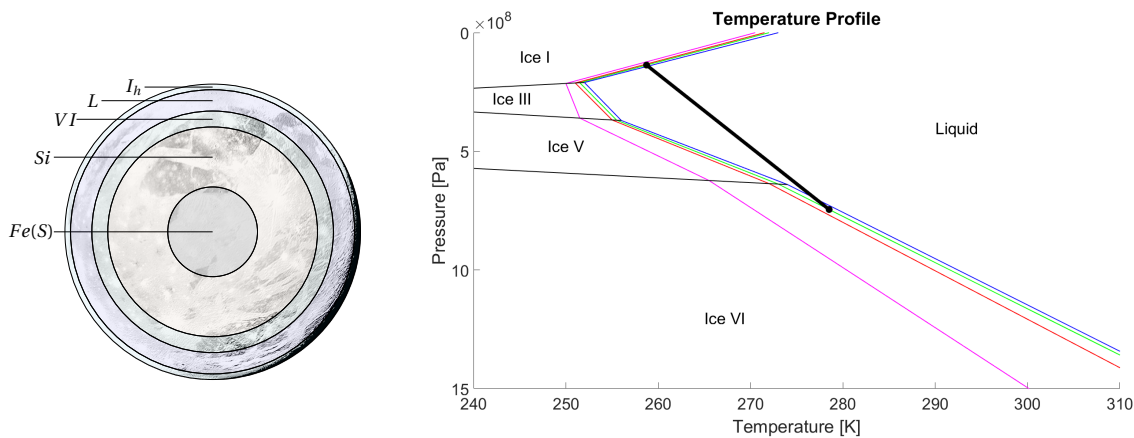


Figure 6.18: The temperature profile for Libra III.

#### 6.1.5. RESULTS SYNOPSIS I

From 44 billion models considered during this research, only 260 adhered to the requirements discussed in Section 2.2. Based on the correlations between the layers of the models, provided in Figure 6.4, fourteen models were selected. The characteristics of these selected models have been summarized in Table 6.3. These models have been grouped into four distinct sets, each with their own characteristics:

- **Spes I-IV** - Ocean and crust layers are limited by Figure 1.9 and Ice V is included.
- **Gelo I-II** - Models which include ice III, V, VI, thin oceans, large mantles and small cores.
- **Aqva I-V** - Models which include ice VI, large oceans, small mantles and large cores.
- **Libra I-III** - More 'balanced' worlds, but with a thick ice VI layer and no ice V.

Table 6.3 includes the main feature of each model. The important factors on which the models have been selected are highlighted. The mass, MoI factor and core pressure are also provided. When these are compared to Table 2.2, all models adhere to the mass, MoI and core pressure requirements. Table 6.3 can be used to compare the layer thicknesses between the models as these are all included. Ocean salinities are also given.

These fourteen selected models will be used as a foundation for the next part of this thesis research. The anomalies discussed in Chapter 3 will be included within these interiors. Then, the Global Spherical Harmonics Package will be utilized to determine the gravitational potential field differences between the models.

Table 6.3: The known characteristics of each selected world presented in this section. The main feature on which each world has been selected has been provided and the corresponding layers are highlighted for clarity.

	<b>Spes I</b>	<b>Spes II</b>	<b>Spes III</b>	<b>Spes IV</b>	<b>Gelo I</b>	<b>Gelo II</b>	<b>Aqva I</b>	<b>Aqva II</b>	<b>Aqva III</b>	<b>Aqva IV</b>	<b>Aqva V</b>	<b>Libra I</b>	<b>Libra II</b>	<b>Libra III</b>
<i>Feature</i>	<b>ESA 1</b>	<b>ESA 2</b>	<b>ESA 3</b>	<b>ESA 4</b>	<i>Max V</i>	<i>Max III</i>	<i>Max L1</i>	<i>Max L2</i>	<i>Min VI</i>	<i>200 VI</i>	<i>900 M</i>	<i>50 I<sub>h</sub></i>	<i>Max VI</i>	<i>800 C</i>
<i>Mass [e23 kg]</i>	1.4817	1.4819	1.4816	1.4818	1.4819	1.4816	1.4818	1.4816	1.4815	1.4818	1.4818	1.4817	1.4818	1.4817
<i>Mol Factor [-]</i>	0.3083	0.31	0.3127	0.3090	0.3078	0.3095	0.3099	0.3104	0.3077	0.3086	0.3100	0.3087	0.3107	0.3084
<i>Core Press. [GPa]</i>	10.58	10.09	8.07	9.33	9.76	9.10	9.91	9.86	9.59	11.71	9.43	10.77	10.78	8.62
<i>Core ρ [g/cm<sup>3</sup>]</i>	8.000	8.000	5.150	7.030	8.000	7.030	5.150	5.150	5.150	7.030	5.150	7.030	8.000	5.150
<i>Salinity [wt%]</i>	3	5	5	10	0	5	10	10	5	3	0	0	10	3
<i>Ice I<sub>h</sub> [km]</i>	125	100	75	100	150	150	75	25	150	50	75	<b>50</b>	25	100
<i>Ocean [km]</i>	250	220	270	240	30	20	<b>750</b>	<b>740</b>	620	570	560	400	370	380
<i>Ice III [km]</i>	0	0	0	0	70	<b>80</b>	0	0	0	0	0	0	0	0
<i>Ice V [km]</i>	40	70	50	40	<b>140</b>	120	0	0	0	0	0	0	0	0
<i>Ice VI [km]</i>	379	414	389	434	414	434	39	119	<b>4</b>	<b>194</b>	119	344	<b>459</b>	284
<i>Mantle [km]</i>	1210	1240	1170	1210	1270	1250	630	610	830	960	<b>900</b>	1080	1120	1070
<i>Core [km]</i>	630	590	680	610	560	580	1140	1140	1030	860	980	760	660	<b>800</b>

## 6.2. HETEROGENEOUS 3D MODELS

JUICE will provide measurements on Ganymede's gravitational potential field whilst in orbit. The variations of these measurements are due to internal density distributions within Ganymede. To effectively analyze the variations, it should be considered how these can be distinguished. To achieve this, the effects of the different possible internal density distributions on the gravitational potential field will be modeled. Then, the signal variations for individual anomalies and the different selected worlds can be analyzed. JUICE's instrument accuracy is also considered during these simulations.

Fourteen distinct 1D homogeneous interior models have been selected in Section 6.1.4. The variations introduced in Chapter 3 are now added to these models to observe the difference in gravitational potential field output. First, several anomalies are added to each of the fourteen worlds, described in Section 6.2.1. The degree variances (Section 4.2.3) and gravitational potential fields of these worlds are compared to observe how signals differ. Then, based on these results, several worlds will be considered in more detail to distinguish effects of individual anomalies. The effect of the individual anomalies and different layers will be inspected using degree variance in Section 6.2.2.

### 6.2.1. GLOBAL WORLDS

The gravitational signal power of the different worlds is compared to inspect which type of signals could be measured by JUICE. First fourteen full models have been considered, based on the homogeneous worlds provided in Section 6.1.4 and the following heterogeneous variations:

- Ganymede's topography that is based on a point control network (Section 3.1).
- A combined crustal model which consists of albedo thickness variations with a maximum variance of 20 km and isostatic Pratt compensation between 0 and 100% (Section 3.2).
- Internal boundary variations located between all other present layers with a maximum variance of 20 km (Section 3.3).
- Ten brine pockets that have a fixed location with a radius of 8 km in the models crust (Section 3.4).

Pratt compensation has been considered in the combined crustal model as the maximum Airy compensation percentage varies between the different worlds based on the crust and ocean layer thicknesses. This type of compensation will be considered when inspecting individual worlds in Section 6.2.2. The signal powers of the fourteen different worlds including all heterogeneous variations (with 0% Pratt compensation) are depicted in Figure 6.19. This has been simulated for spherical harmonics degree and order 2-48 (excluding  $C_{2,0}$ ) on a height of 500 kilometers above the model's surface.

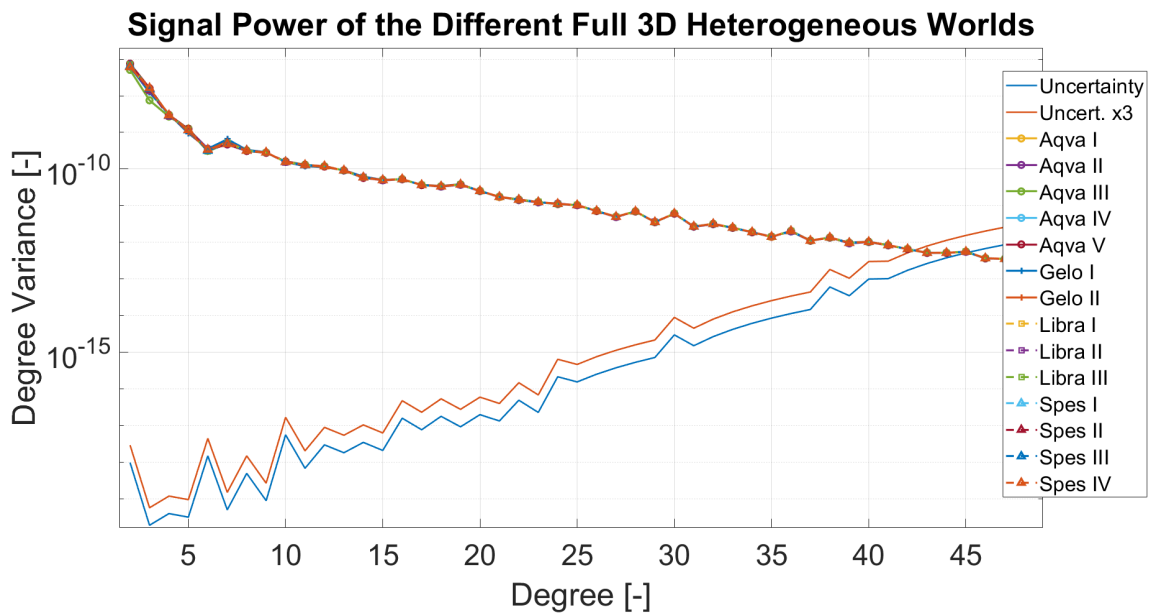


Figure 6.19: Degree variances of the 14 selected worlds with all heterogeneous anomalies included except isostatic compensation. Degree 2-48, 500 km above sphere. Uncertainties are based on JUICE's instrument performance [4].

The signals of the worlds almost coincide. For lower degrees these signals are large in comparison to the uncertainties. All signals decay over degree due to the wavelength of the signals which decreases. The gravitational potential field of one world (as these are similar), Spes I, is depicted in Figure 6.20.

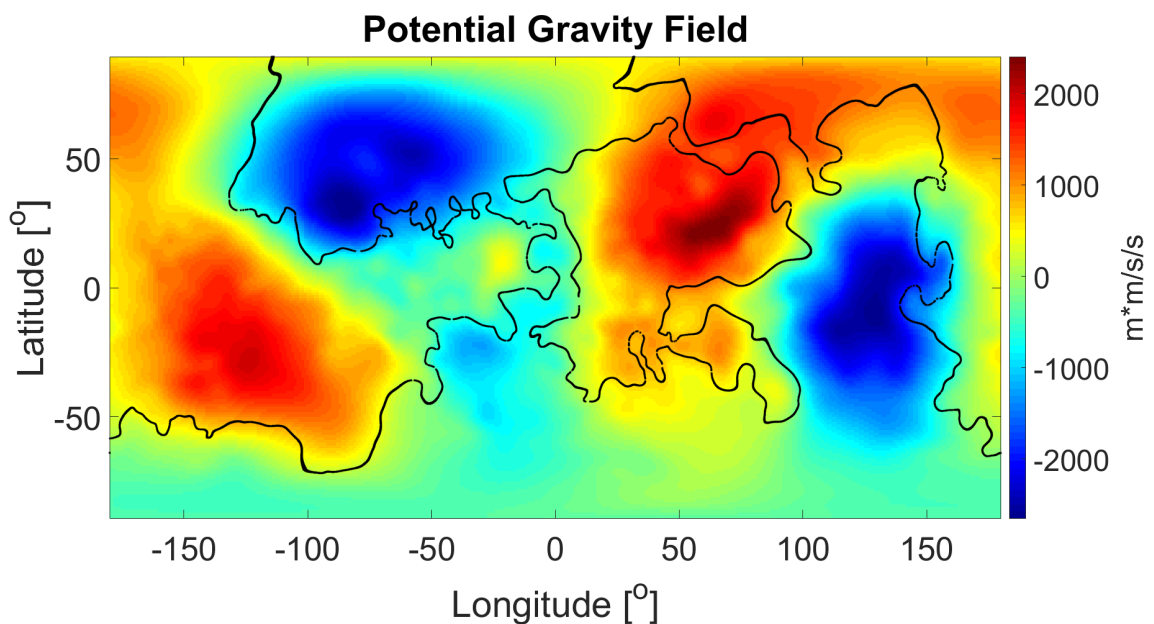


Figure 6.20: The gravitational potential field of Spes I including all heterogeneous anomalies except isostatic compensation. Degree 2-48 (no  $C_{2,0}$ ), 500 km above sphere.

Figure 6.20 shows that the signal is clearly dominated by the topography, since the outlines of Ganymede largely coincide with the signal. Topographic reduction (Section 4.2.1) will be applied to see how this influences the different signal powers. The Pratt compensation within the crustal models is increased to 50% (Section 3.2.2).

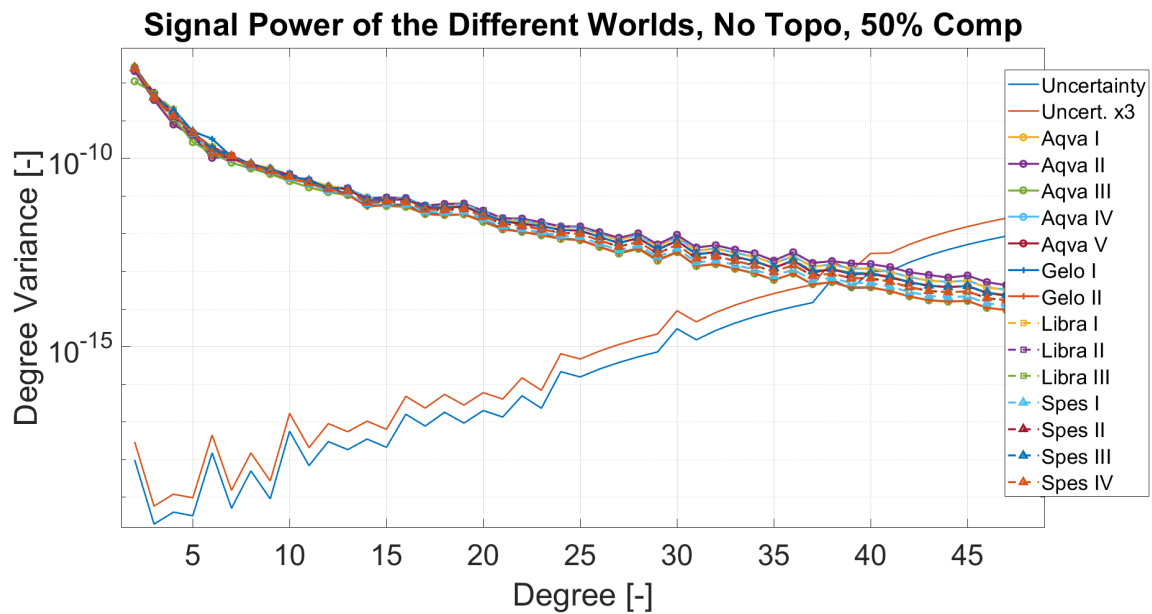


Figure 6.21: Degree variances of the 14 selected worlds with all heterogeneous anomalies included except the topography. 50% compensation, degree 2-48, 500 km above sphere. Uncertainties are based on JUICE's instrument performance [4].

The signals start to differ slightly for larger spherical harmonics degrees. These do however still follow the same global trends. Thus for Figure 6.23 the Pratt compensation within the crustal models will be set to 0%. A new gravitational potential field for Spes I is included in Figure 6.22.

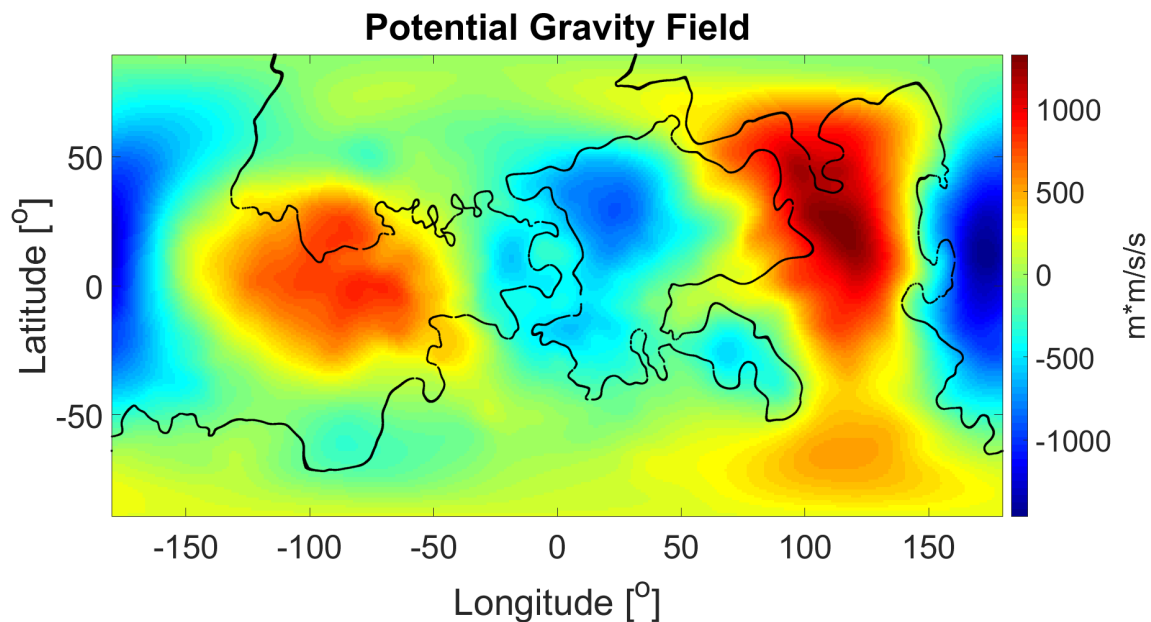


Figure 6.22: The gravitational potential field of Spes I including all heterogeneous anomalies except the topography. 50% compensation, degree 2-48 (no  $C_{2,0}$ ), 500 km above spheroid.

The values of the gravitational potential field variations have inverted due to the topographic reduction (Section 3.2). The Pratt compensation dominates this signal, which has inverse properties with respect to the topography. The power of the signal has decreased in size by  $\pm 1000 \text{ m}^2/\text{s}^2$ , which is approximately half of the topographic signal. Models still follow the same trend and thus the Pratt compensation in the crustal model will be set to 0%. Other percentages of compensation were considered but did not alter the results in any significant way. Therefore these are not included in this report.

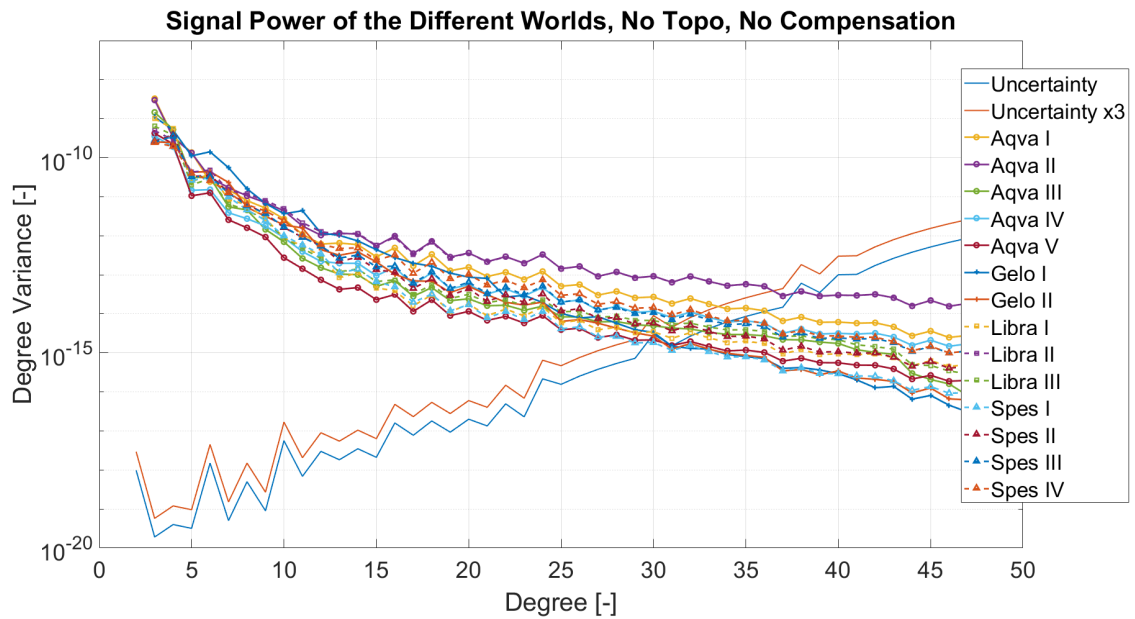


Figure 6.23: Degree variances of the 14 selected worlds with all heterogeneous anomalies included except the topography and isostatic compensation. Degree 2-48, 500 km above sphere. Uncertainties are based on JUICE's instrument performance [4].

Through topographic reduction and by excluding isostatic compensation, the crustal variations are based solely on albedo variations (Section 3.2), which are now the dominant component for most worlds. The signal power will thus be affected by two main components; the salinity of the ocean as this can increase the density gap between the crust and ocean and the thickness of the crust, which varies with depth. This behavior is observed in Figure 6.23 since Aqva II and Libra II have the highest signal powers. The worlds both have an ocean salinity of wt10% and a thin crust of 25 km thickness. This configuration results in a crustal variations signal that fully dominates the combined signal power and thus the signals of these two worlds are identical. Aqva I slightly stands out as it has a wt10% ocean, but a average crust thickness of 75 km. The other models with crust of 50 or 75 km all have salinity below wt5% and thus lose signal power due to the smaller density gap. There is one other world with a wt10% salinity ocean, Spes IV, but this model includes a crust of 100 km thickness. This correction only has a small impact on the gravitational potential field signal strength, as depicted in Figure 6.24.

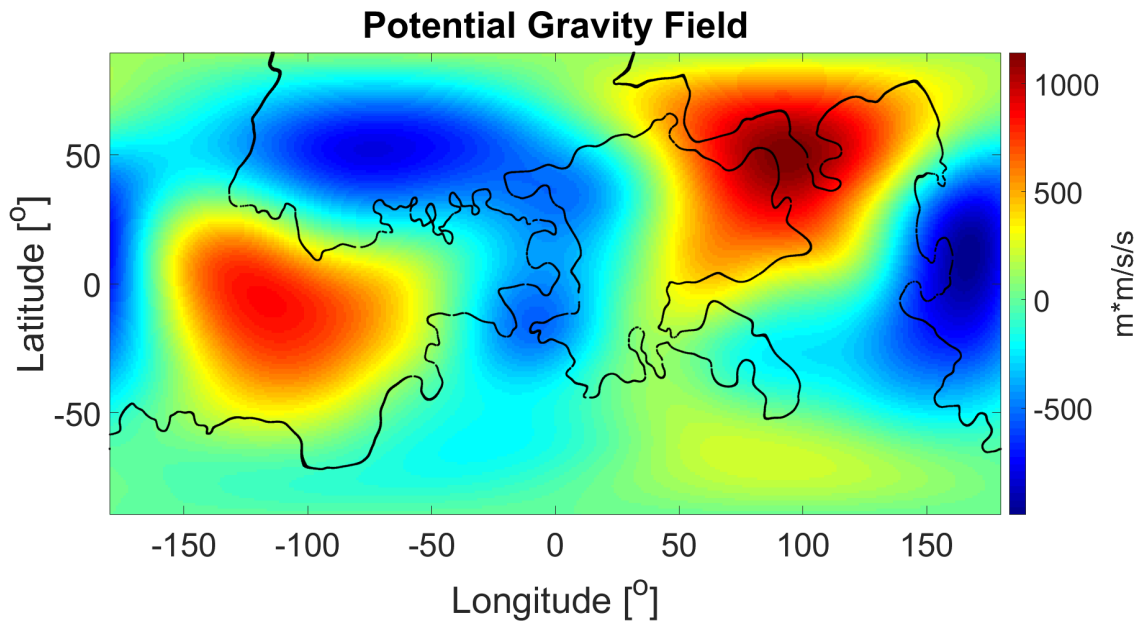


Figure 6.24: The gravitational potential field of Spes I including all heterogeneous anomalies except the topography and isostatic compensation. Degree 2-48 (no  $C_{2,0}$ ), 500 km above spheroid.

The gravitational potential field signal in Figure 6.24 has flipped again and it becomes clear that still several large entities dominate the signal for lower orders/degrees. As an extra step, the crust variations, which are based on a visible entity (Ganymede's albedo), will be corrected for. This results in Figure 6.25.

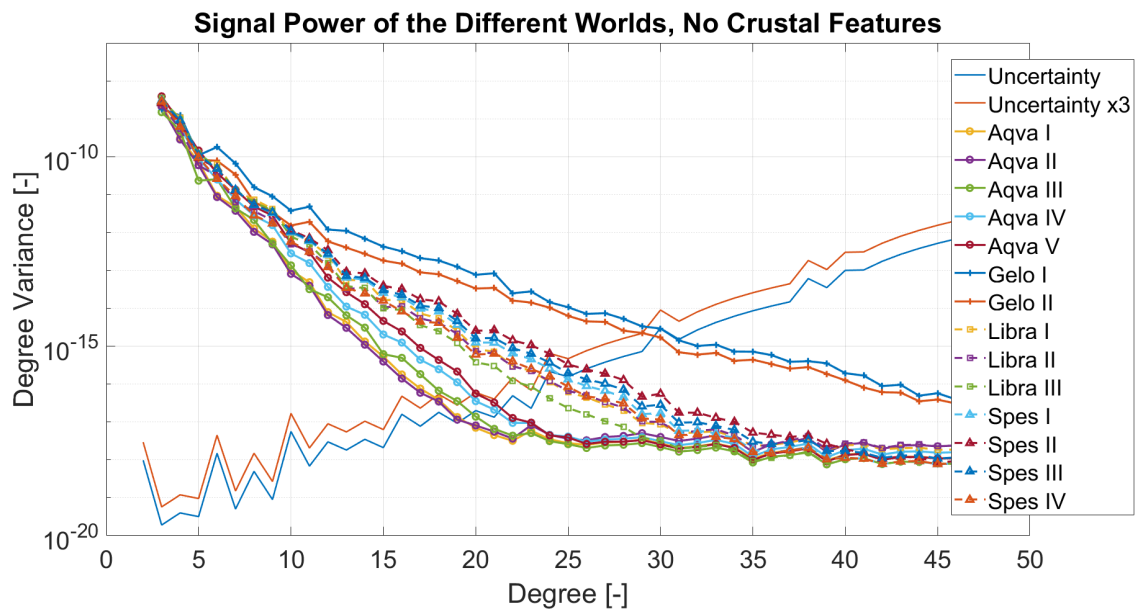


Figure 6.25: Degree variances of the 14 selected worlds with internal boundary variations and pockets included. Degree 2-48, 500 km above sphere. Uncertainties are based on JUICE's instrument performance [4].

Different gradients between three signal groups are observed. The icy Gelo worlds show the least signal decay over degree whereas the liquid Aqva worlds shows the largest decay, including a stagnation from degree 25 and upwards. The Libra and Spes worlds all follow a similar linear trend. It seems that signals stagnate due to the pockets which are included within the signals. This is checked by removing these entities, this results in Figure 6.26.

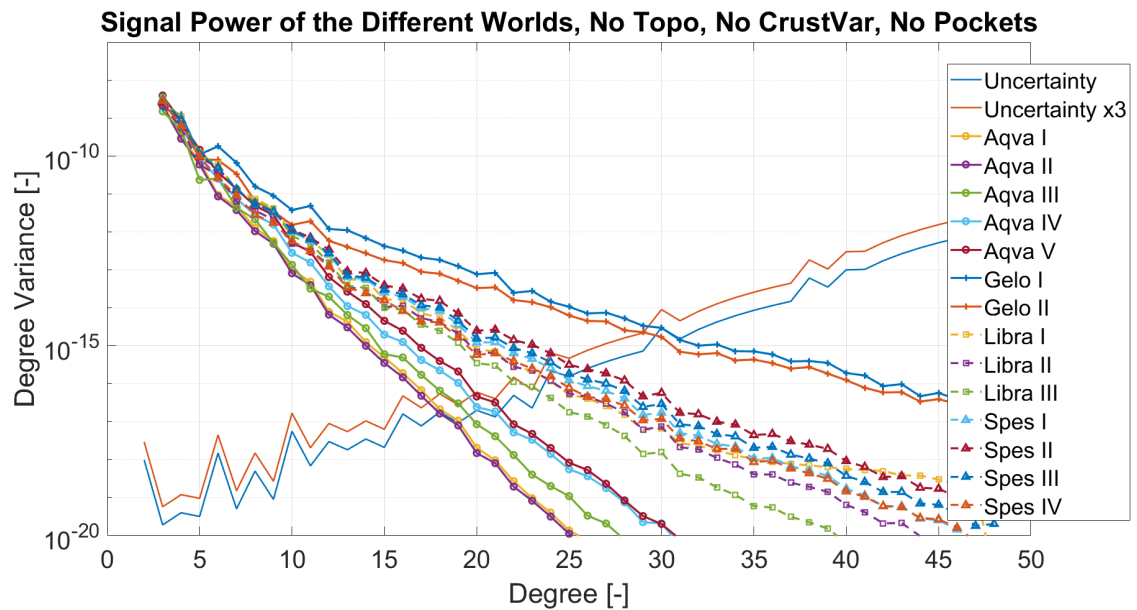


Figure 6.26: Degree variances of the 14 selected worlds with only the different internal boundary variations included. Degree 2-48, 500 km above sphere. Uncertainties are based on JUICE's instrument performance [4].

Pockets did induce the stagnating behavior and the signals simply follow the gradient of the dominant boundary layer in Figure 6.26. To obtain a better understanding on why the three types of signals from Figure 6.26 differ, one world from each of the three sets has been selected for further analysis; these are Spes I, Gelo I and Aqva II. Not all models have been considered due to time limitations as the simulations in Section 6.2.2 are time consuming. The impact on the final conclusions will be neglectable as the consistency of the degree variance signal within each signal group will be similar.

### 6.2.2. INDIVIDUAL ANOMALIES

During this section the individual effects of the different heterogeneous anomalies on the gravitational potential field signal will be considered. This is done using the three previously selected models, Spes I, Gelo I and Aqva II. The upcoming figures consist of colored regions, these represent variations within the different anomalies to depict their impact on the degree variance. The anomalies are varied as follows:

- Isostatic Pratt compensation between 0 and 100%.
- Isostatic Airy compensation between 0 and maximum % possible.
- Crust variations with a maximum value between 10 and 50 km (or maximum allowable for thin crusts).
- Internal boundary variations with a maximum value between 1 and 20 km.
- Ten brine pockets with a radius of 8 km in the models crust.

The regions are the area's between the two extreme values for each boundary, which are indicated with a dotted line. The signal power of an anomaly decreases when it's maximum variation becomes lower. In the case of isostasy the signal power gets lower for higher compensation amounts (as the topography is included).

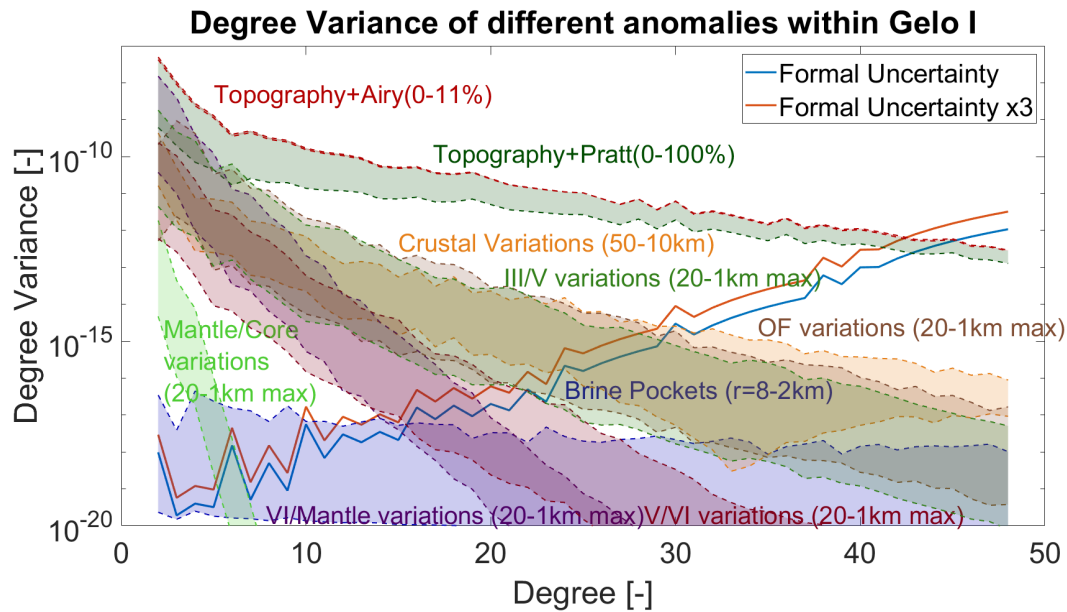


Figure 6.27: Signal power of all the different anomalies for Gelo I. Degree 2-48, 500 km above sphere. Uncertainties are based on JUICE's instrument performance [4].

The signal powers due to all the different individual heterogeneous variations within Gelo I are depicted in Figure 6.27. Only a small amount of Airy compensation is possible (11%) due to Gelo I's thin ocean. A lot of variations are included as Gelo I consists of all different ice phases and thus all boundary interactions.

The individual boundaries vary in gradients and signal strength. When a boundary is located deeper within the model, its signal power has a larger gradient. Longer wavelengths, at the lower degrees, are not dominated by crustal-variations. Therefore results are more sensitive for deeper boundaries at these degrees. If the density gap between two layers increases in size, the signal of that boundary will be more apparent. These density gaps were provided in Table 3.1. Both the mantle-core and VI-mantle boundaries have a large density difference. However, these layers are both located deep within the model. For lower degrees the power of these signals will be high with respect to their depth, but for increasing degrees these will decrease rapidly. The inverse is true for the OF (ocean floor) and III-V interfaces, these have a smaller decay due to their shallowness. Lower degree interface signals vary less as the ice layer interfaces consist of smaller density differences. Distinctions become clear for the higher degrees due to the different gradients of the signals.

Since the topography is located at the models surface, its signal power is large in Figure 6.27. Even when fully compensated by Pratt isostasy, its signal power remains multiple times larger than that of other signals.

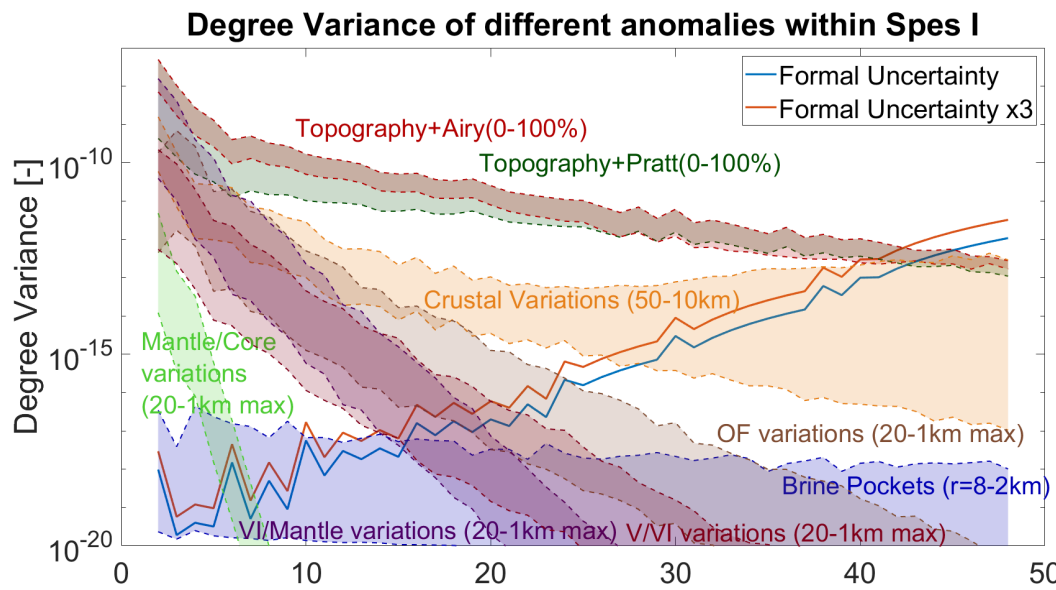


Figure 6.28: Signal power of all the different anomalies for Spes I. Degree 2-48, 500 km above sphere. Uncertainties are based on JUICE's instrument performance [4].

The signal powers of all anomalies within Spes I are provided in Figure 6.28. Airy compensation is possible up to 100% within this model and one less boundary interaction is present due to the lack of ice III. Both types of compensation are possible up to 100%. Airy compensation varies the bottom boundary of the crust and Pratt compensation the densities between two boundaries. The lower crust boundary is located further away from the surface than the density variations. Thus the topographic and Airy compensation signals will have a larger induced difference. This results in the Airy signal to remain larger for 100% compensation at lower degrees.

No ice III is present within Spes I and its ocean is located at a greater depth than the ocean of Gelo I. The gradient of the ocean signal therefore is larger as for Gelo I, resulting in a larger signal loss at higher degrees. The behavior due to the brine pockets between Figures 6.25 and 6.26 can now be explained. These figures show models which include all anomalies except for the topography and crustal variations. Brine pockets thus become the dominant signal around degree 33 for the Spes I model in Figure 6.25. This possibly results in the stagnating behavior of this signal, whereas this is not present in Gelo I due to its larger OF and III-V interface signal power.

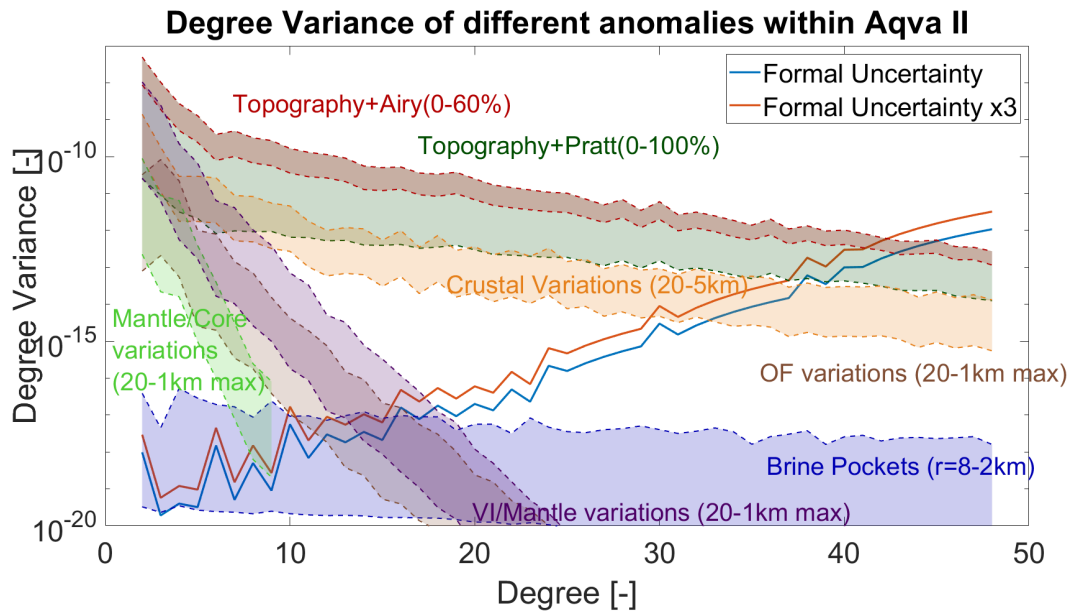


Figure 6.29: Signal power of all the different anomalies for Aqva II. Degree 2-48, 500 km above sphere. Uncertainties are based on JUICE's instrument performance [4].

Figure 6.29 depicts the variation in the different anomalies for Aqva II. Two boundary interactions are not included due to the lack of ice III and V within the model. Airy compensation is possible up to 60%. Pratt compensation has a wide range for this model. This is due to its thin crust of only 25 km, thus the density compensation will be located closer to the surface of the model. This reduces the height difference between the topographic and isostatic anomalies, decreasing the signal power for high compensation percentages.

For this model the VI-M (mantle) interface signal is larger as that of the OF interface. This is due to the structure of the model; both boundaries are located below the 740 km thick ocean and only 119 km of ice VI lies between the interfaces. But the VI-M has a larger density gap, thus its signal will be more distinguishable. The other two models host an OF boundary which is located less deep and thus will have a higher signal power. The Mantle-Core boundary has a higher signal strength for this model, due to a core size of 1140 km radius. The core of both other models is 500 km smaller and thus those Mantle-Core interface signals will lose power due to depth.

When this model is considered without the topography and crustal variations, the signal of the brine pockets will become dominant around degree 18. Since no shallow boundary interface are present due to the models thick ocean, the signal of the model will decay rapidly at lower degrees. This explains why some models in Figure 6.25 first show a large signal drop-off and then settle at a certain power.

### 6.2.3. RESULTS SYNOPSIS II

The fourteen selected models selected in Section 6.1 were combined with the heterogeneous variations provided below in Section 6.2.1:

- Ganymede's topography.
- A combined crustal model.
- Internal boundary interfaces with a maximum variance of 20km.
- Ten brine pockets with a radius of 8 km within the models crust.

Using the Global Spherical Harmonics Package, the fourteen 3D heterogeneous worlds were compared. Several dominant variations were removed to better understand the behavior between signals due to all anomalies. The Gelo worlds result in a high power signal, which linearly decreases over degree. Signal degradation is different for the Aqva worlds, these drop rapidly and stagnate around degree 25. Signals due to the Libra and Spes worlds have a slightly larger gradient as for the Gelo worlds, but do decrease constantly over degree.

From each of the three distinguished model sets in Figure 6.26, one world was selected for further investi-

gation. These are Gelo I, Spes I and Aqva II. Variations within individual anomalies were compared to observe the difference these induce in a model's signal power. Several relations were found and these will be discussed, together with all other results, in Chapter 7.

Current models of the gravitational potential field and the interior of Ganymede are still uncertain. A precise gravitational model of Ganymede could provide a lot of information about its interior. JUICE will obtain a model of Ganymede's gravitational potential field up to at least degree and order 15 [12]. The results of this thesis, which were given in Chapter 6, provide insight in how different possible internal density distributions of Ganymede influence the gravitational potential field of the moon. This chapter discusses these results and how these compare to interior models of Ganymede from other literature. The influence of JUICE is taken into account as it will perform a variance of measurements which can further restrict internal density models of Ganymede.

A collection of models was established during the 1D homogeneous modeling. These models consist of several layer correlations, which will be discussed in Section 7.1. The findings with respect to the degree variance signals will be discussed in Section 7.2.

## 7.1. HOMOGENEOUS 1D MODELS

The main correlation patterns between all layers are considered. These will be elaborated on using specific plots from Figure 6.4 and the figures found in Appendix C. The different layers and requirements will be considered to provide a full overview of which characteristics are correlated.

### 7.1.1. ICE $I_h$ LAYER CORRELATIONS

Next to the main interactions between layers, some plots are color-scaled based on the thickness of the ice  $I_h$  layer. Figures 7.1 and 7.2 have been taken from Figure 6.4.

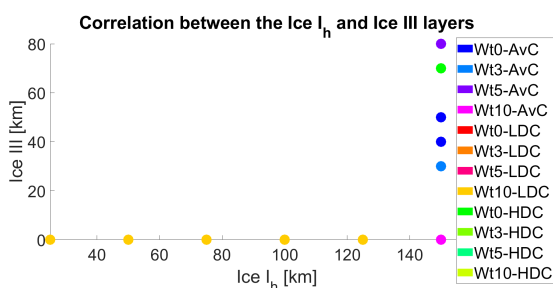


Figure 7.1: Correlation between the ice III and crust layers with the model set color-scale.

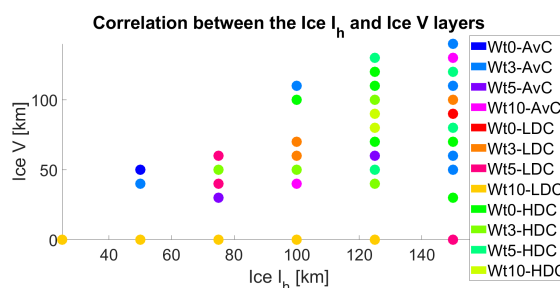


Figure 7.2: Correlation between the ice V and crust layers with the model set color-scale.

Figures like 7.1 and 7.2 depict the correlations between two layer thicknesses. One thickness range is located on the x-axis and the other on the y-axis. If both thicknesses are fully correlated, this would result in a diagonal collection of dots. This means that if one layer increases by 20 km, the other also increases by this value. No correlations are present when the dots are distributed evenly over the figure.

Figures 7.1 and 7.2 show that the ice III and ice V layers are related to the thickness of the models crust. Ice III is only present when the crust is at its thickest (150 km) and otherwise vanishes entirely. Larger layers of ice V are present for larger crust thicknesses. Hence when the crust becomes thicker, more types of ice can be present within the models interior. This is due to the thermoclines of water, which are again depicted in Figure 7.3.

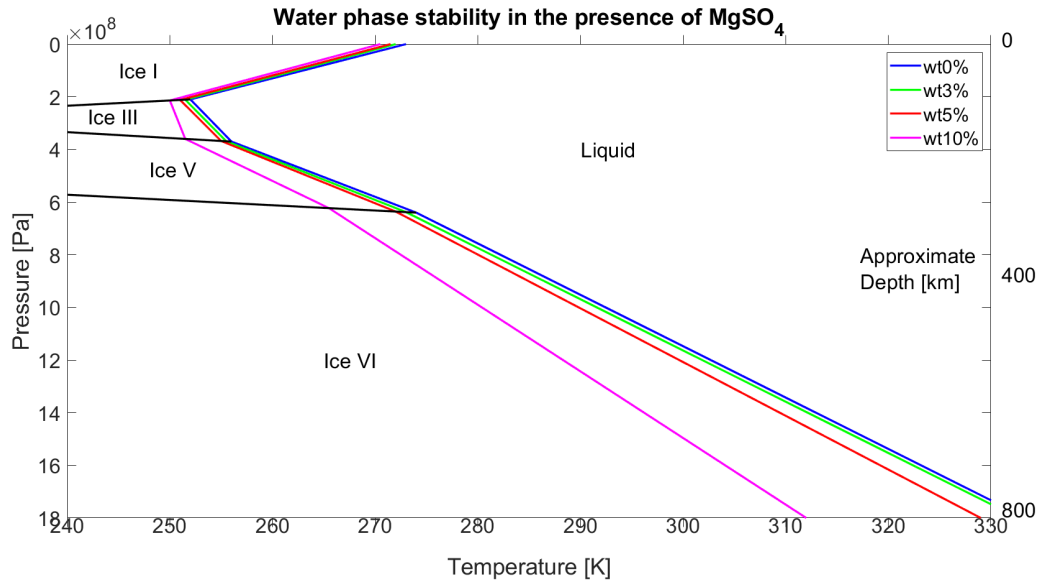


Figure 7.3: The used phase transitions for sweet and saline water [54].

Thick crusts will result in a relatively high pressure at the crust/ocean boundary, hence the boundary will be located downwards (and thus to the left) in Figure 7.3. This makes it possible for Ice III and V to exist as 1D-steady-state temperature profiles should be sub-adiabatic, with an exception for low pressures ( $<200$  MPa) [54] [22]. Due to this behavior no models with thicker crusts are included in the results, as pressures would increase even further resulting in ice III directly below the crust. These models do not include an ocean and have not been considered during this research (Section 2.1). The maximum crustal thickness within the simulated models corresponds with literature; ice  $I_h$  layers between 13 and 148 km thick are expected [54] [22].

Measurements of JUICE will improve the gravity field of Ganymede, without relying on the assumption of hydrostatic equilibrium [12]. This will result in  $J_2$  and  $C_{22}$  coefficients with an accuracy of three orders of magnitude smaller as current measurements [1]. The uncertainty of Ganymede's moment of inertia factor can greatly be improved using these measurements, resulting in stricter requirements for the modeling process. If JUICE provides knowledge on the internal heat processes within Ganymede, several assumptions from this thesis research should be reconsidered; 1D-steady-state temperature profiles then do not necessarily have to be sub-adiabatic and temperature jumps could be present within the thermal profiles of generated models. Internal heating processes will lead to higher local temperatures and thus more melting of ice within models. It could change the order at which layers occur, which now has been limited to the homogeneous order in which the water phases occur for increasing pressure [54].

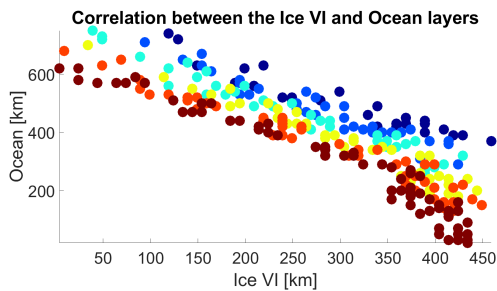


Figure 7.4: Correlation between the ice VI and ocean layers with an ice  $I_h$  color-scale.

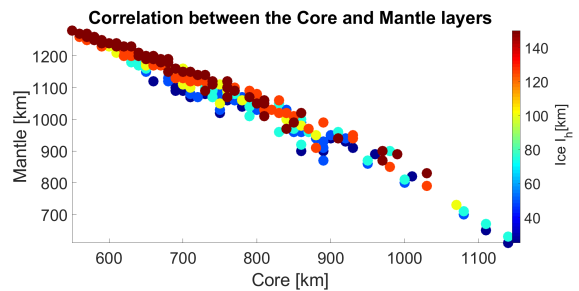


Figure 7.5: Correlation between the mantle and core layers with an ice  $I_h$  color-scale.

Figures 7.4 and 7.5 have been selected from Figure C.3. Figure 7.4 depicts that, for constant ice VI, the ocean layer becomes larger for a thinner crust. This is due to the thermoclines of water, a thin crust shall have less pressure at its bottom interface due to the smaller amount of mass above the interface. The models thermal profiles are assumed to be sub-adiabatic (Section 2.2.4) and adhere to Figure 7.3. Due to the location of the

phase interfaces in Figure 7.3, models with less pressure below their crust require a larger pressure increase within the ocean to reach the next ice phase. For constant density, the ocean should thus be thicker.

Figure 7.5 shows that the core of the models become smaller for thicker crusts. This is due to the constant MoI restriction; when the outer layers become less dense (crust has lowest density), the inner layers should also become less dense (core has largest density). The core and mantle are almost inversely proportional, this is again due to the MoI requirements of the models. Ganymede is highly differentiated and the densities of the mantle and core (Table 2.1) are significantly larger as those of other layers. The mantle and core layers are thus necessary to achieve this high differentiation and their thicknesses are therefore related.

Whilst in orbit, JUICE will carry out a detailed investigation of Ganymede's magnetic field [12]. This will provide important information on dynamo theories, which combined with thermal-evolution models, can tell more about the conditions required to maintain and generate dynamo activity [22]. This information can be used to narrow down on the core consistency and density. Since these aspects are related to core size, which is inversely proportional to mantle size, these measurement of JUICE could yield mantle and core thickness restrictions.

### 7.1.2. OCEAN LAYER CORRELATIONS

Some interactions are present between the ocean layer thickness and those of other layers.

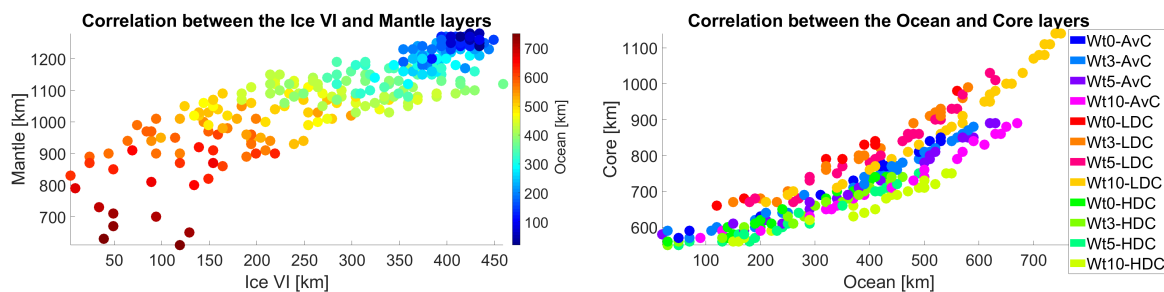


Figure 7.6: Correlation between the mantle and VI layers with an ocean color-scale. Figure 7.7: Correlation between the core and ocean layers with the model set color-scale.

Figure 7.6 has been taken from Figure C.4. Together with Figure 7.7 it shows that the ocean is thin for thick ice VI and mantle layers. Oceans become very thick for large, low density, cores and small ice VI/mantle layers. This is due to both the mass and the MoI requirements. The first allows the relatively low density core to obtain large sizes without exceeding Ganymede's mass. But since this core still has a high density with respect to the mantle and ice VI layers, it has to be compensated by an outer layer with a relatively high density (MoI). Saline oceans have a high density, comparable to that of ice III. But due to the thermoclines of water, which prevent ice III from occurring for crust thicknesses below 150 km and ocean thicknesses above 80 km, the saline ocean has to compensate for the low density core. This is a very specific combination which results in models with huge cores (see Aqva I + II). Saline oceans are able to produce electrical currents and can generate secondary magnetic and electric fields as a response to an external magnetic field [3] [54]. JUICE will constrain the electrical conductivity and extent of Ganymede's ocean through magnetometer measurements at multiple frequencies [12]. This could provide information on the salinity and thickness of Ganymede's internal ocean. Core radius can be restricted based on measured ocean salinity through the correlations given in Figure 7.7.

In previous research, the ocean thickness varies between 31-753 km thickness [54]. This is in agreement with the findings of this research, but certain models include a large core (>1000 km) radius and a small mantle (<800 km). When considering previously estimated models [54] [49], these are new findings. Since the thermal profile of the silicon mantle was not considered during this research, it could be that a thin mantle does not result in a high enough pressure such that liquid iron(-sulfide) occurs within Ganymede's core. This liquid core is required to generate Ganymede's magnetic field through dynamo action [41] [1]. However, the models which include the large cores all consist of wt10% oceans and cores of the highest mass percentage sulfide (with a density of  $5.150 \text{ g/cm}^3$ ). These cores should have lower melting temperatures [17] [54] [41] [3] [22]. A lower pressure is then required to transit to a liquid state, thus these models with smaller mantles

could be possible.

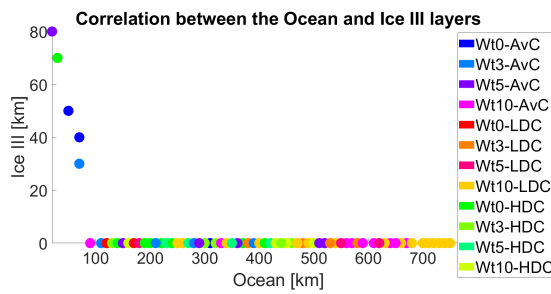


Figure 7.8: Correlation between the ice III and ocean layers with the model set color-scale.

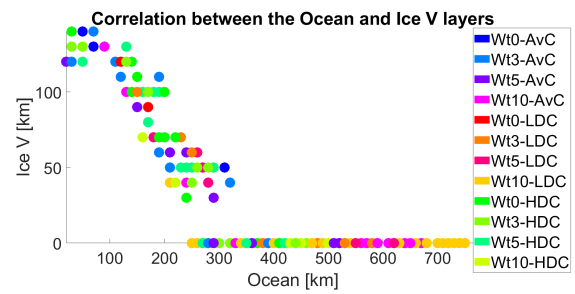


Figure 7.9: Correlation between the ice V and ocean layers with the model set color-scale.

Figures 7.7-7.9 result from Figure 6.4. Ice III and V layers are limited and become larger for thinner ocean layers. When considering the thermoclines of water in Figure 7.3, ice III and V only occur for thin oceans which result in a small pressure increase. Temperatures within the ocean should not rise significantly for these layers, especially ice III, to occur. Models from literature consist of ice III and V layers up to 52 and 155 km thickness respectively [22] [54]. These values are similar to models originating from this research, which can include up to 80 and 150 km layers for ice III and V. Ice III layers can thus be slightly thicker, but this is the case only for 2 models (Figure 7.8). Hence this could be to slight variances between the research density inputs and/or due to different layer combinations considered.

Since the ocean layer thickness is related to core size, the magnetic field measurements performed by JUICE, as discussed in Section 7.1.1, could provide limitations on Ganymede's internal ocean thickness. Furthermore, JUICE will determine variations of  $J_2$  and  $C_{22}$  over time, which is a result of a satellite's response to tidal forcing [12]. These tides are directly related to the existence and characteristics of a liquid layer within Ganymede's interior. Information about the crustal and liquid layers within Ganymede can be constrained through these measurements [12], further narrowing down possible interior models.

### 7.1.3. ICE III LAYER CORRELATIONS

Ice III only exists for thin oceans and thick cores, but it is restricted in several other ways.

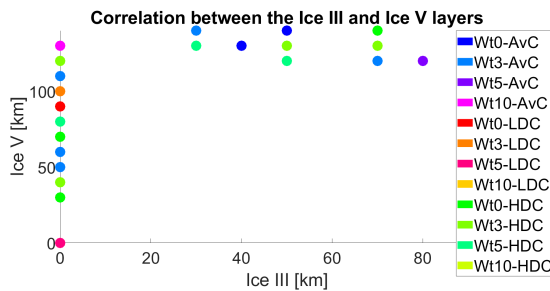


Figure 7.10: Correlation between the ice III and ice V layers with the model set color-scale.

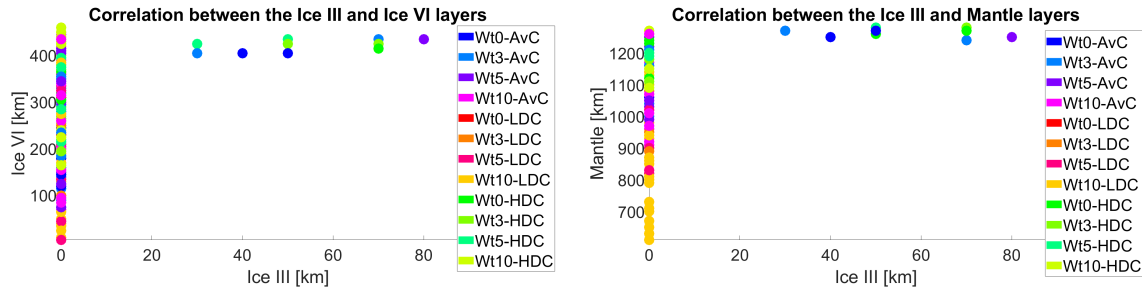


Figure 7.11: Correlation between the ice III and ice VI layers with the model set color-scale. Figure 7.12: Correlation between the ice III and mantle layers with the model set color-scale.

Figures 7.10-7.12 again are selected from Figure 6.4. It is depicted that the ice III layer can only exist for thick ice V, ice VI and mantle layers. Thus for small core sizes as this is inversely proportional to the mantle layer thickness. Therefore it can be concluded that ice III is only present within worlds that are to a great extent frozen (like Gelo I and II). This is purely due to the restrictions based on the thermoclines of water (Figure 7.3).

Models consisting of a low density core of iron-sulfide or with high salinity do not include ice III. Higher salinity results in more liquid water (Figure 7.3) and low density iron cores include larger oceans due to MoI restrictions (Section 7.1.2). Hence these factors both increase ocean thickness, which results in no ice III to be present (Figure 7.8). Ice III layers in previous models also melt entirely when ocean salinity increases [54]. Since the ice III layer is only present at small cores sizes, measurements from JUICE which constrain core size (Sections 7.1.1 and 7.1.2) could be used to distinguish ice III presence and thickness.

#### 7.1.4. RELATIONS WITH RESPECT TO THE ICE V, VI, MANTLE AND CORE LAYERS

The correlations which have not been considered with respect to the deeper interior layers (ice V, VI, mantle and core) are provided in this section.

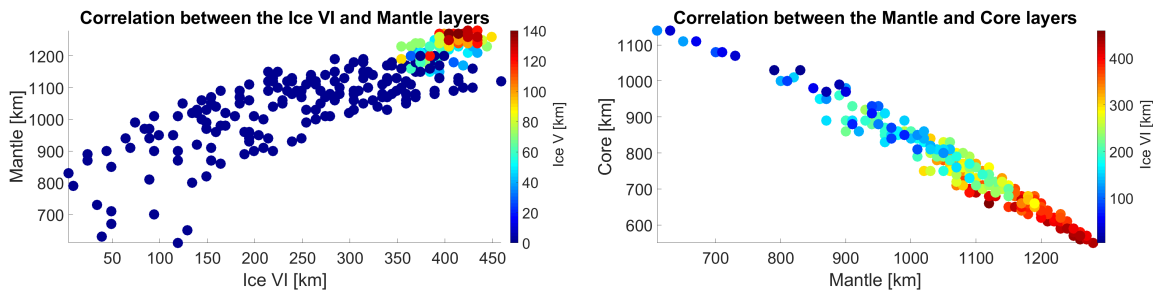


Figure 7.13: Correlation between the ice VI and mantle layers with an ice V color-scale. Figure 7.14: Correlation between the mantle and core layers with an ice VI color-scale.

From Figure 7.13 it can be concluded that if the thickness of ice V is large, the models mantle thickness is approximately 1250 km. Then through previously provided correlations, the core and ice VI layer thicknesses can be determined. Thick ice VI layers require a thick mantle and a thin core to be present within the model (Figure 7.14). This is again due to the MoI restrictions, as with a small core and thick mantle more high density pressure ices are able to be included in the model.

Previously determined models consist of ice VI layers varying between 100 and 447 km [22] [54]. Models determined during this thesis include ice VI layers between 4 and 450 km. Thus, for some models a thinner ice VI layer is present with respect to previous research. When considering Figure 7.1, these models all consist of thick ocean and thin mantle layers. Hence these low ice VI layers are related to the large core sizes discussed in Section 7.1.2.

The libration-amplitude, obliquity, pole-position and rotation-rate of Ganymede will be precisely measured by JUICE [12]. These characteristics will yield information on the deeper interior within Ganymede and its sub-surface ocean [42]. The models core, mantle, higher ice phases and ocean layer thicknesses could thus be further restricted by these measurements. Together with all the previously discussed correlations this could

greatly reduce possibilities for Ganymede's interior.

### 7.1.5. MAIN 1D HOMOGENEOUS MODEL FINDINGS

Several correlations between the different layers have been distinguished. Due to the requirements set on the generated models (Table 2.2), based on current knowledge about Ganymede, layers tend to intersperse. Models have been restricted by mass and moment of inertia factor, which physically means that the mass and its global distribution cannot vary in extreme ways. Due to the pressure and temperature restrictions when regarding the  $H_2O$  phase layers, high pressure ice phases (VI) tend to develop first before other, lower pressure, ice phases occur (V, and then III). This results in ice III to be a scarce occurrence, only present within the worlds with the largest amounts of ice and the thinnest oceans. A collection of correlations was determined, these have been summarized below:

- |  |  |
|--|--|
| 1. Ice $I_h \downarrow \rightarrow$ ice V $\downarrow$                             | 10. No ice VI $\rightarrow$ no ice V                                       |
| 2. If Ice VI=constant: ice $I_h \uparrow \longleftrightarrow$ liquid $\downarrow$  | 11. ice III $> 0 \rightarrow$ Ice $I_h = 150\text{km}$                     |
| 3. Mantle $\uparrow \propto$ core $\downarrow$                                     | 12. Ice III $> 0 \rightarrow$ ice V $> 120\text{km}$                       |
| 4. ice $I_h \uparrow \rightarrow$ core $\downarrow$                                | 13. Ice III $> 0 \rightarrow$ ice VI $> 400\text{km}$                      |
| 5. Liquid $\uparrow \longleftrightarrow$ mantle $\downarrow$ & ice VI $\downarrow$ | 14. Ice III $> 0 \rightarrow$ mantle $> 1240\text{km}$                     |
| 6. Liquid $\uparrow \longleftrightarrow$ core $\uparrow$                           | 15. Mantle $> 1200\text{km}$ & ice VI $> 340 \rightarrow$ ice V $\uparrow$ |
| 7. Liquid $\uparrow \longleftrightarrow$ ice III $\downarrow$                      | 16. Ice V $> 0 \rightarrow$ ice VI $> 350\text{km}$                        |
| 8. Liquid $\uparrow \longleftrightarrow$ ice V $\downarrow$                        | 17. Ice V $> 0 \rightarrow$ mantle $> 1160\text{km}$                       |
| 9. No ice V $\rightarrow$ no ice III   | 18. Core $> 1020\text{km} \rightarrow$ wt10% & FeS core                    |

Once JUICE performs its measurements in orbit around Ganymede, it can constrain several internal layer consistencies and thicknesses for the celestial body. The determined correlations from this thesis and measurements made by JUICE can then complement each other to find a better expectation of Ganymede's internal density distributions.

## 7.2. HETEROGENEOUS 3D MODELS

Several observations and occurrences within the simulated 3D anomalies should be discussed in more detail. These are elaborated on in this section, together with relations to previous literature and new information which JUICE could provide on these subjects. Also, the interesting features which stand out in Figures 6.19 - 6.29 are examined during this section. It is already apparent that, when several corrections can be applied, different worlds can be distinguished. It is identified which of the different anomalies cause these variations. Furthermore, it is inspected which signal components are measurable for the uncertainties within JUICE's instrumentation (Section 4.2.3).

### 7.2.1. GLOBAL WORLDS

The degree variance signal of the gravitational potential field were compared in Section 6.2.1. For convenience, Figures 6.19 and 6.26 have again been depicted as Figures 7.15 and 7.16.

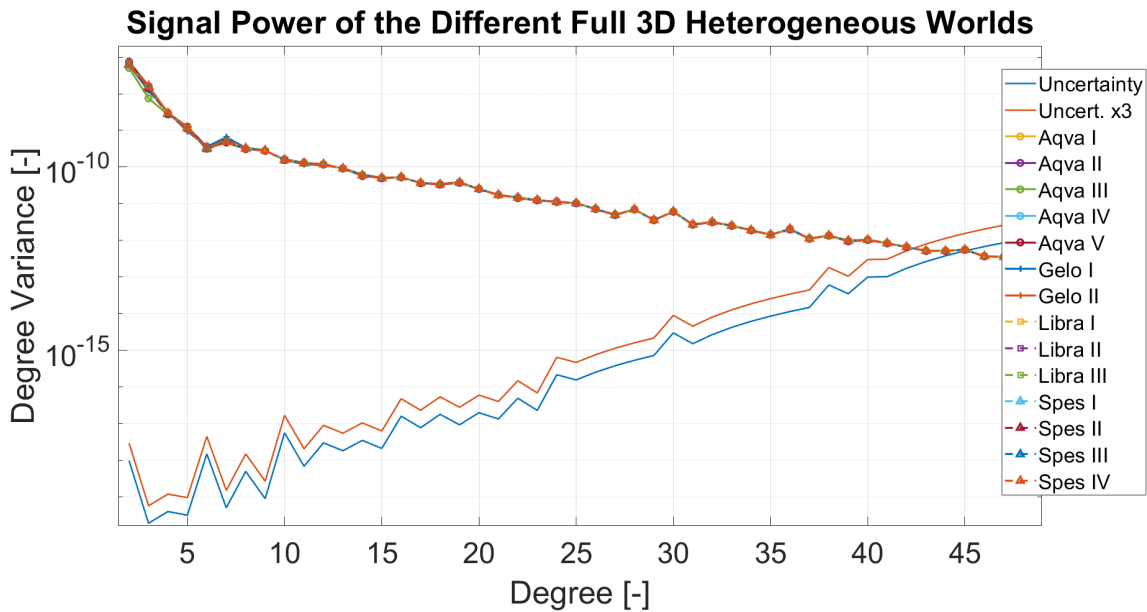


Figure 7.15: Degree variances of the 14 selected worlds with all heterogeneous anomalies included except isostatic compensation. Degree 2-48, 500 km above sphere. Uncertainties are based on JUICE's instrument performance [4].

The models in Figure 7.15 include a topography, crustal model, internal boundary variations and ten brine pockets. Since no variances between signal powers are observable, several of the anomalies induced on the models were corrected for. These are corrections that can be determined from measurements by JUICE, several important aspects of the removed anomalies will be discussed.

#### TOPOGRAPHY

JUICE will perform global high precision topographic measurements (10 cm resolution), which will provide references for local and global high-degree topography. By combining these shape measurements with gravity data, offsets between the centre of mass and the centre of figure can be determined [12]. This is a huge improvement on the current PCN model. This new topographic model can be used to increase the accuracy of the gravitational potential models resulting from this research. The main shape corrections, introduced in Section 4.2.1, will be improved as JUICE will measure time-varying tidal deformations (Section 7.1.2). These can be related to the equilibrium shape of a body [12].

Hence a precise topographic model can be generated from data resulting from JUICE. It will consist of both local and global topographic variations and thus the corrections applied in the theoretical approach based on Ganymede's topography will be applicable once JUICE is in orbit around Ganymede.

#### CRUSTAL VARIATION LIMITATIONS

JUICE has several scientific objectives regarding Ganymede's ice shell, these are listed below [12].

- Understand crustal behavior.
- Identify structural and stratigraphic patterns.
- Match the surface geology with subsurface features.
- Study the global tectonic setting and geological evolution.

A radar sounder will be used to perform measurements based on these objectives. These measurements can penetrate the subsurface and analyze it up to 9 km depth with a vertical resolution of several meters [12]. These measurements will be complemented by imaging spectroscopy in the UV to IR regions and the local and global high-degree topography. The results from these measurements can determine the amount of compensation within Ganymede's crust. The amount of Airy and Pratt compensation will therefore be further narrowed down. If JUICE achieves to measure the exact compensation within Ganymede's crust, this can be used to correct the degree variance results. If the compensation is corrected for, Ganymede's internal density structure can be determined. JUICE's data can verify if the albedo model of the crust (Section 3.2) is correct. If the darker and brighter area's at Ganymede's surface are not related to crustal thickness, which was assumed

[46] [47], this model should be reconsidered.

An implication for the isostatic compensation models is the maximum percentage which can be present within the models without unrealistic manipulation. The limited maximum roots due to Airy compensation were already discussed in Section 3.2.2 as these would result in model errors if not corrected for. Maximum Airy compensation varies between 11% (roots of  $\approx 25$  km) for models with a thin crust and up to 100% for models with a thick crust, dependent of ocean salinity. Ocean salinity increases the density gap between a models crust and ocean layers, reducing the required root size. For models including thick crusts, maximum root sizes vary between 50 km (wt10%) and 150 km (wt0%).

Pratt compensation has different limitations. Since this model varies the density of the crustal layer, it should be inspected if these densities still adhere to ice  $I_h$ . This behavior can escalate for models with small compensation depths, or thin crusts, which have larger density differences due to compensation. Model crust thicknesses vary between 25 and 150 km, exact ice density variations are hard to determine for Ganymede's crust as these could vary for several reasons: the presence of salt, the exact pressure profile of the crust and the behavior ice  $I_h$  in general under these specific circumstances.

Since the crust of Ganymede's interior models floats on its internal ocean [21] [2], it is improbable that the maximum ice density within the models crust exceeds  $0.997 \text{ g/cm}^3$ . Minimum natural ice densities are expected up to  $0.917 \text{ g/cm}^3$ <sup>1</sup>. To obtain a rough estimate on the impact of the Pratt compensation on density variations Equations 3.3 and 3.4 are rewritten for maximum compensation percentage in Equations 7.1 and 7.2 (where  $\rho_w = 0$ ).

$$\%_{max} = \left( \frac{\rho_u}{\rho_1} - 1 \right) \frac{D}{T_{max}} \cdot 100 \quad (7.1)$$

$$\%_{max} = \left( 1 - \frac{\rho_u}{\rho_d} \right) \frac{D}{T_{min}} \cdot 100 \quad (7.2)$$

Applying Equations 7.1 and 7.2 with the density ranges as discussed for crust layers of 25-150 km with  $\rho_u = 0.937 \text{ g/cm}^3$ , the results in Table 7.1 are obtained. Maximum Pratt compensation percentage is based on the minimum and maximum values of Ganymede's topography, represented by  $T_{min}$  and  $T_{max}$ , which are equal to -11.8960 and 9.2879 km respectively (Section 5.2.2).

Table 7.1: The maximum Pratt compensation percentages based on the different crust thicknesses of the generated models.

Crust Thickness [km]	Surplus Max %	Deficiency Max %
25	5.87	10.65
50	11.74	21.29
75	17.62	31.94
100	23.48	42.58
125	29.35	53.23
150	35.22	63.88

Table 7.1 shows that Pratt compensation will be limited by the models crust thickness. Especially for thinner crusts, only lower percentile compensations are possible such that the crust remains within a reasonable ice  $I_h$  density range. Maximum compensation percentages are smaller for the mass surpluses due to the lower density gap constraint ( $0.917\text{-}0.937 \text{ g/cm}^3$ ), this is thrice as large for mass deficits ( $0.937\text{-}0.997 \text{ g/cm}^3$ ). Even for thick crusts of 150 km 100% Pratt compensation is not possible, hence the results from this thesis for higher Pratt compensations seem unlikely to occur.

This is in line with previous literature, which has studied isostasy on other ice moons. On Europa, Airy isostasy cannot effectively support short-wavelength topographic bands and ridges [27]. These topographic elements are also present at Ganymede [46] [47]. Pratt compensation is only likely to occur on Enceladus when porosity variations, which are void spaces within the crust, are present [2].

Therefore if Airy and Pratt compensation are present at Ganymede, these will only occur in smaller percent-

<sup>1</sup>Ice densities: <https://hypertextbook.com/facts/2000/AlexDallas.shtml>, [cited 05-03-2019]

ages. This is due to the limited density gap between Ganymede's ocean and crust layers, together with the limited thickness of the crust. Since JUICE will perform both topographic and gravitational measurements, it will gain more insight in the amount of compensation present within Ganymede. Therefore these can be corrected for in the degree variance signals of the different models.

#### POCKET IMPLEMENTATION

JUICE's determinations on the time-dependent variations of  $J_2$  and  $C_{22}$  will be able to quantify mass anomalies, mass distributions, asymmetries and other non hydro-static contributions to Ganymede's gravitational potential field [12]. Therefore JUICE's measurements will provide more information about the amount, consistencies and sizes of pockets within Ganymede's crust.

The degree variance signals of the pockets resulting from this research were inspected in Figures 6.27 - 6.29. Due to their tiny size and the relatively small density gap (0.937-1.15) induced [55], pockets have a small, unmeasurable, signal power. Pockets currently cannot be varied over depth due to the minimal thickness of the model layers generated, which is 100 km. If this would be decreased to a scale convenient for pocket depth varying (5-10 km), simulation times would increase significantly. Since individual pocket signals are tiny in comparison to other anomaly signals, these were removed from the degree variance signal of the global models.

#### 7.2.2. INDIVIDUAL ANOMALIES

When the discussed anomalies in Section 7.2.1 are corrected for, the degree variance signals in Figure 7.15 reduce to the signals depicted in Figure 7.16.

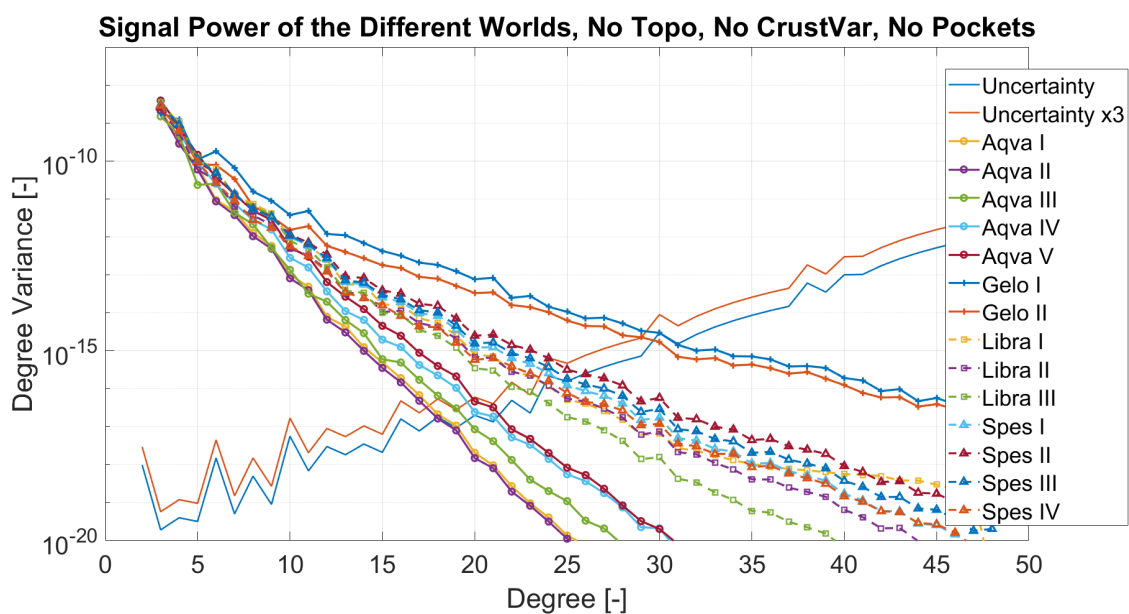


Figure 7.16: Degree variances of the 14 selected worlds with only the different internal boundary variations included. Degree 2-48, 500 km above sphere. Uncertainties are based on JUICE's instrument performance [4].

Figure 7.16 shows the degree variance signals of the 14 selected worlds without topography, crustal variations and pockets. Three types of worlds stand out in Figure 7.16, which seem to be separated by different gradients of degree. The selected worlds from each set, introduced in Section 6.2.1, will be inspected by separating all the individual elements of which the signals in Figure 7.16 consist. These are depicted in Figures 7.17 - 7.19.

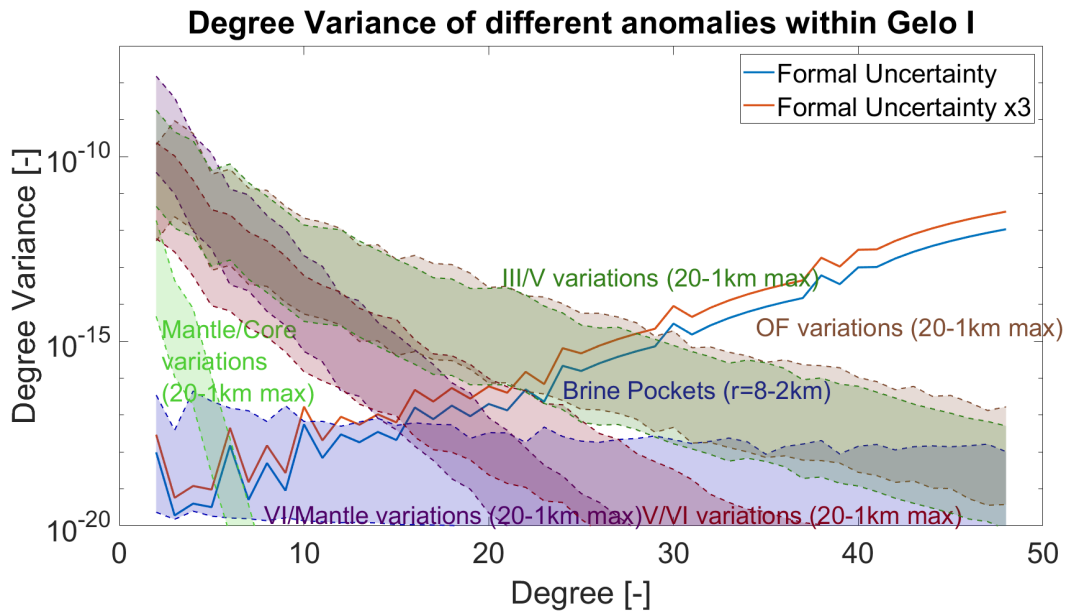


Figure 7.17: Signal power of boundary variations for Gelo I. Degree 2-48, 500 km above sphere. Uncertainties are based on JUICE's instrument performance [4].

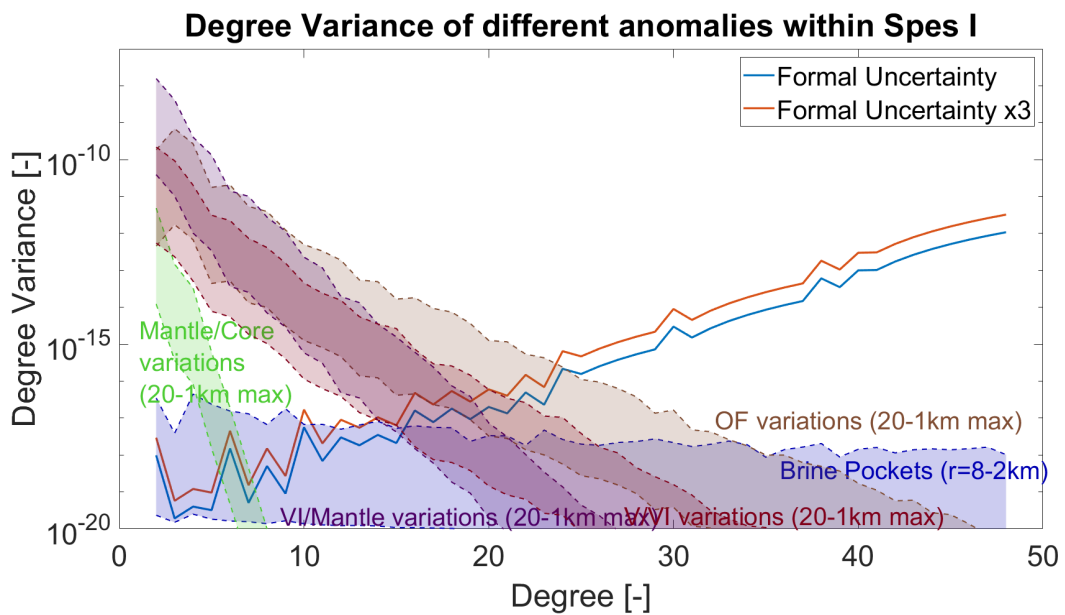


Figure 7.18: Signal power of boundary variations for Spes I. Degree 2-48, 500 km above sphere. Uncertainties are based on JUICE's instrument performance [4].

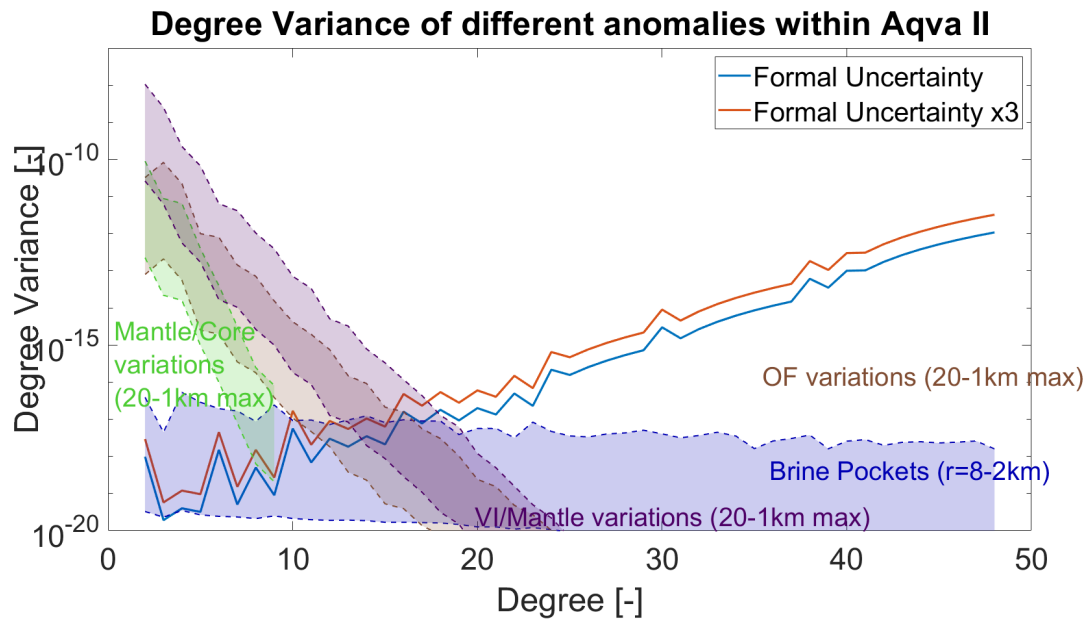


Figure 7.19: Signal power of boundary variations for Aqva II. Degree 2-48, 500 km above sphere. Uncertainties are based on JUICE's instrument performance [4].

Figures 7.17 - 7.19 show that the variance of signal powers in Figure 7.16 results from the difference in depth of certain layers within these models. Aqva II consists of several less layer interactions as Gelo I, since ice III and ice V are absent. Spes I is missing one boundary interaction due to the model's lack of ice III. Gelo I hosts several shallow boundary interactions, whereas Aqva II's interactions are hidden below a 740 kilometers thick ocean. Spes I's signal power lies in between the other selected signals due to its ocean of 250 km thickness and the presence of its ice V boundary.

JUICE's 3GM instrument will perform range-rate measurements to determine the spacecraft's radial position with respect to Ganymede [12]. These measurements will be used to determine the gravitational potential field of Ganymede (Section 1.2.3). The uncertainties of the 3GM instrument were discussed in Section 4.2.3 and are provided in all degree variance figures. The signal powers in Figures 7.16 - 7.19 are larger than the uncertainties up unto at least degree 20. These are distinguishable due to the different gradients within the signals and thus JUICE will be able to measure these variances. Therefore the degree variance signals resulting from this research can complement JUICE data to determine what is the most likely interior structure of Ganymede. This is an immense improvement on previous research, as currently only the  $J_2$  and  $C_{22}$  coefficients of Ganymede's potential field are determined [1]. These were a result of several fly-by's of the Galileo satellite and uncertainties within these coefficients can be decreased by an orbiter [15]. As JUICE will orbit Ganymede a large improvement within this data will be acquired [1] [18].

During Section 7.1.1 it became apparent that, using current knowledge of Ganymede, the ice crust cannot exceed a thickness of approximately 150 kilometers. Only models with an ice crust of 150 kilometers host ice III (Figure 7.1). Using Table 6.3 and Figure 7.16 it can be concluded that the gradient of the corrected gravitational potential signal almost solely depends on the thickness of the liquid layer within the model. For thick ocean layers the signal gradient becomes large (Aqva II, Figure 7.19), as all internal boundary interactions will be located beneath a huge mass of water. In models with thinner oceans (Gelo I, Figure 7.17), a larger variance of ice layers (ice III and V) is present. Ice III only exists in models with an ocean thickness of 70 kilometer or less (and vice-versa) and with a crust of 150 kilometer thickness. Therefore, the boundary interactions of possible ice III layers will result in a larger signal power for the model considered. This results in a smaller degree variance signal gradient for models with an ice III layer and a thin ocean layer. Worlds which include ice III should also consist of ice V (due to Figure 2.3 [54]), which is dependent on liquid layer thickness (Figure 7.9). Models containing ice V will have a lower signal gradient than worlds without it, which in turn have larger oceans. This is due to the same reasoning as for ice III, only to a lesser extent. Figure 7.16 shows this behavior, since the Spes worlds (with Ice V) are all located above the Libra worlds (No ice V) regarding signal power. It

can be observed in Figure 7.18 as the V-VI interface has a non-negligible impact on its signal power. The Spes worlds have a significantly less thick ocean as the Libra worlds, which is the logical consequence.

When JUICE has measured the degree variance signal resulting from Ganymede's gravitational potential field, its gradient can determine the size and presence of different internal layers within Ganymede. Through correlations provided in Section 7.1 and the degree variance signal powers in Figure 7.16, JUICE can determine various elements within Ganymede through its gravitational potential field measurements:

- The thickness of Ganymede's inner ocean layer.
- The presence of Ice III and V within Ganymede and their thicknesses.
- The size of Ganymede's core and mantle.

Hence through gravitational potential field measurements and the results of this thesis, JUICE can determine aspects of at least 5 internal layers within Ganymede. If specific variations within these layers appear to be present, even more layer thicknesses could be specified. If ice III is present, the crust should be at least 150 km thick (Figure 7.1). A large layer of ice V (>100 km) and a large mantle (>1200 km) will result in a large ice VI layer of 400-450 km thickness (Figure 7.13).

JUICE will perform several different measurements on Ganymede's interior and environment to specify internal density distributions [12]. These were discussed in more detail previously during this chapter and consist of magnetic field investigations, optical inspection, spectrometry, laser altimetry and radar measurements. Therefore the findings through the gravitational potential field measurements can be compared to those of other measurements. This can be used as a direct verification/validation of the different methods discussed and applied during this thesis research and by JUICE. If measurements result in different conclusions on Ganymede's internal layering, methods and assumptions should be reconsidered. In this way assumptions can be checked on validity. If it turns out that Ganymede's internal dynamics are active, then the assumption of hydrostatic equilibrium should be reevaluated. This will require significant modifications of the algorithm used during this thesis research, but would increase knowledge on Ganymede and its interior structure, resulting in the generation of higher accuracy models.

### 7.2.3. MAIN 3D HOMOGENEOUS MODEL FINDINGS

Using the Global Spherical Harmonics Package, the variations within the gravitational potential field of Ganymede due to different internal density distributions have been determined. The signal powers of several worlds including all anomalies were compared and it was observed that, if certain corrections to the models are possible, these can be distinguished through Ganymede's gravitational potential field. When considering the effect of the individual elements within the models, it was determined that the thickness of an inner ocean has a large impact on the size of the gravitational potential field signal power.

The gradient of the degree variance signal can be used to greatly narrow down the global variation of Ganymede's ocean layer thickness. This can in turn be utilized to converge on the possible inner structure of Ganymede as this layer is closely related to the present ice layer thicknesses, mantle layer thickness and core size. Once JUICE provides these measurements of Ganymede's gravitational potential field, one can greatly narrow down the possibilities of its internal structure. Conclusions resulting from other measurements of JUICE can be used to re-evaluate methods and assumptions considered during this research and by JUICE, further improving methods to determine Ganymede's interior structure.

## CONCLUSIONS

The conclusions resulting from this thesis research are presented in this chapter. It answers the research question and its sub-questions through the acquired knowledge. Implications determined during this research with relation to its results and the JUICE mission are discussed. The research question and its sub-questions are restated below:

### ***What can JUICE's gravitational potential field measurements provide about Ganymede's interior?***

1. What are possible 1D homogeneous interior models for Ganymede?
  - (a) *Which  $H_2O$  phases are present and how can JUICE distinguish these?*
  - (b) *In what way are individual layer thicknesses correlated with respect to each other?*
  - (c) *How can these correlations be used to better analyze JUICE's measurements?*
  - (d) *How are layer thicknesses restricted to known observations of Ganymede?*
  
2. What are possible 3D heterogeneous interior models for Ganymede?
  - (a) *Which heterogeneous variations are expected and measurable by JUICE?*
  - (b) *What degree of spherical harmonics is required to model these heterogeneous models?*
  
3. How is the gravitational potential field of Ganymede affected by the different heterogeneous models?
  - (a) *How do different 1D worlds affect variations within the gravitational potential field?*
  - (b) *How do local variations within a single homogeneous world affect the gravitational potential field?*
  - (c) *Is it possible to distinguish different worlds with the expected accuracy of JUICE?*

From 44 billion 1D homogeneous models generated during this research, only 260 adhered to current known characteristics of Ganymede. Certain elements and water phases are present in all models: a pure iron or iron-sulfide core, a silicon mantle, an ice VI layer together with an liquid ocean and an outer crust consisting of Ice  $I_h$ . Dependent on the exact layer thicknesses within a model, also intermediate ice phases, ice III and V, can be present. Layer correlations between the 260 models were analyzed and their implications on the thesis research are discussed in Section 8.1 to provide answers to questions 1a-1d. Based on the correlations between the layers of the models, fourteen models were selected for further research. These models are discussed in Section 8.2, which answers question 1.

Several anomalies are expected within Ganymede; topography, crustal variations related to surface albedo and/or isostasy, internal boundary interactions and pockets were considered. These anomalies will create local boundary and/or density variations within the selected homogeneous models, creating 3D heterogeneous models, which partly answers questions 2 and 2a. Simulations for spherical harmonics coefficients up to degree and order 48 were performed. It was found that several relations exist between gravitational potential field data and internal density distributions within Ganymede. If one can effectively correct gravitational potential field signals for measurable components within Ganymede's interior, discussed in Section 8.3, several sets of internal structures emerge. This section further answers question 2 and 2a. Distinguishable models showed that the presence of ice III, and to a lesser extent ice V, increase the gravitational signal power of a model. Taking into account the established limitations and correlations between layers, the gradient of the gravitational signal power over spherical harmonics degree can be directly related to the thickness of an interior ocean. When combined with the correlations found between internal layers during this research, one could even establish an accurate first order approximate of Ganymede's internal composition. Implications of these results are provided in Section 8.4, which answers questions 2a-b, 3 and 3a-c.

### 8.1. LAYER CORRELATIONS

These correlations are all based on the known radius, mass and moment of inertia factor of Ganymede. The internal (hydrostatic) pressure and (adiabatic) temperature profiles of Ganymede's interior were also considered together with the known thermoclines of water. The moment of inertia factor and thermocline requirements resulted in several important relations. These correlations are considered most important as these can relate all different internal layers within Ganymede and will be discussed in more detail below.

1. *The mantle and core sizes are inversely proportional.* Since these are the two layers with the highest densities considered, these will intersperse as the moment of inertia factor of models has to be constant. JUICE will carry out a detailed investigation of Ganymede's magnetic field, which will provide important information on its core size and consistency. These measurements can thus directly result in a mantle size through this correlation.
2. *The ice III and ice V layers are related to the thickness of the models crust.* Ice III is only present when the crust is at its thickest (150 km) and otherwise vanishes entirely. Larger layers of ice V are present for larger crust thicknesses. Hence when the crust becomes thicker, more types of ice can be present within the models interior. This is due to the thermoclines of water, thick crusts will result in a relatively high pressure at the crust/ocean boundary. This makes it possible for Ice III and V to occur as 1D-steady-state temperature profiles are assumed to be sub-adiabatic, with an exception for low pressures (<200 MPa). JUICE will provide knowledge on the internal heat processes within Ganymede, if these are present this assumption should be reconsidered. Internal heating processes will lead to higher local temperatures and thus more melting of ice within models. It could change the order at which layers occur, which now has been limited to the order in which water phases occur for increasing pressure.
3. *The model's crust, consisting of ice  $I_h$  increases in size for large mantles.* This correlation directly relates the measurable crust layer to the mantle and core sizes of Ganymede. It again results from the moment of inertia factor requirement. When the mantle increases in size, the core decreases in size. Since the mantle has a lower density than the core, the density of the outer layers should also decrease. The crust has the lowest density of all considered layers, explaining this behavior. This is an important finding since JUICE will provide measurements on the crust thickness of Ganymede, which can then be compared to these correlations if theories add up or should be reconsidered.
4. *Thicker and saline oceans result in larger, low density, cores.* This is due to both the mass and the MoI requirements. The first allows the relatively low density core to obtain large sizes without exceeding Ganymede's mass. But since this core still has a high density with respect to the mantle and ice VI layers (which become thin), it has to be compensated by an outer layer with a relatively high density (MoI restriction). Saline oceans have a high density, comparable to that of ice III. But due to the thermoclines of water, which prevent ice III from occurring for crust thicknesses below 150 km and ocean thicknesses above 80 km, the saline ocean has to compensate for the low density core. Saline oceans are able to produce electrical currents and can generate secondary magnetic and electric fields as a response to an external magnetic field. JUICE will constrain the electrical conductivity and extent of Ganymede's ocean through magnetometer measurements at multiple frequencies. This will provide information on the salinity and thickness of Ganymede's internal ocean. Core radius can then be restricted based on measured ocean salinity through this correlation.
5. *The thickness of the ocean is directly related to that of the ice III and V layers.* Ice V, and especially ice III, can only occur for relatively thin oceans as otherwise the pressure below the ocean becomes too large. Temperatures within the ocean should not rise significantly for these layers, especially ice III, to occur.
6. *Ice III/Ice V are only present for Ice VI layers over 400/350 km respectively.* Two correlations which relate the thickness of the ice VI layer to the presence of the other high pressure ice phases. These are purely restricted by the thermoclines of water.

### 8.2. SELECTED HOMOGENEOUS MODELS

Based on the established correlations between the layers of the models, fourteen models were selected to account for all possible layer variations within Ganymede. Even though all models vary with respect to interior, these can be split up into four different groups and were named accordingly. These are as follows:

- **Spes I-IV** - These are the models which lie within ESA's hypothetical range. Ice V is typically included and the ocean and crust layers are limited by Figure 1.9.
- **Gelo I-II** - Models which include ice III, V and VI, a set of frozen end-members based around correlations 2, 3, 5 and 6, discussed in Section 8.1. Thin oceans with a maximum thickness of 30 km, large mantles and small cores are included.
- **Aqva I-V** - These worlds all host oceans with a thickness of 560 km or larger. This can result in configurations consisting of large cores and small mantles. These liquid end-members are a direct result of correlation 4.
- **Libra I-III** - More 'balanced' worlds. Typically a mix between oceans of approximately 400 km and ice VI layers between 300 and 450 km. In contradiction to the Spes worlds, these models do not include ice V.

These fourteen selected models were used as the foundation for the generation of the 3D heterogeneous models.

### 8.3. ANOMALY LIMITATIONS

Some conclusions can be drawn with respect to several anomalies. These will be of use during the analysis of JUICE's data.

#### 8.3.1. ISOSTASY

Airy isostasy is limited within the models of Ganymede. The density difference between the ice  $I_h$  and ocean layers is relatively small, 0.937 and 0.997 g/cm<sup>3</sup> respectively. Therefore this theory will result in large variations of the bottom boundary of Ganymede's crust. Since the compensation cannot exceed the crust and ocean layer thicknesses, only low Airy compensation amounts are possible for a large amount of models. This resulted in maximum Airy compensation amounts of 11% ( $\approx$  25 km roots) for models with thin crusts. Only models with thicker crusts and saline oceans can include 100% Airy compensation ( $\approx$  80 km roots).

Pratt compensation has different limitations. Since this model varies the density of the crustal layer, it should be inspected if these densities still adhere to ice  $I_h$ . This behavior can escalate for models with small compensation depths, or thin crusts, which have larger density differences due to compensation. It was determined that maximum Pratt compensation is limited between 6% and 64% dependent on crust thickness. Therefore if Airy and Pratt compensation are present at Ganymede, these will only occur in smaller percentages. This is due to the limited density gap between Ganymede's ocean and crust layers, together with the limited thickness of the crust.

#### 8.3.2. POCKETS

Pockets currently cannot be varied over depth due to the minimal thickness of the model layers generated, which is 100 km. If this would be decreased to a scale convenient for pocket depth varying (5-10 km), simulation times would increase significantly. Individual pocket signals are tiny in comparison to other anomaly signals, thus these were removed from the degree variance signal of the global models. These anomalies are expected to be undetectable through JUICE's gravitational potential field measurements.

### 8.4. DEGREE VARIANCE FINDINGS

Through gravitational potential field simulations, three distinct types of degree variance signals were found between the fourteen worlds provided in Section 8.2. These three types of signals are distinguished by different degree variance gradients over degree. These become apparent for degree 14 and higher, where higher degrees results in larger differences between the signals. The icy Gelo worlds show the least signal decay over degree whereas the liquid Aqva worlds shows the largest decay. The Libra and Spes worlds all follow a similar linear trend. To obtain a better understanding on why these three types of signals differ, one world from each of the three sets has been selected for further analysis.

It was concluded that the gradient of the corrected gravitational potential signal almost solely depends on the thickness of the liquid layer within the model, since crust thicknesses are limited to 150 km. For thick

ocean layers the signal gradient becomes large, as all internal boundary interactions will be located beneath a huge mass of water. In models with thinner oceans, a larger variance of ice layers (ice III and V) is present. Ice III only exists in models with an ocean thickness of 70 kilometer or less (and vice-versa) and with a crust of 150 kilometer thickness. Therefore, the boundary interactions of possible ice III layers will result in a larger signal power for the model considered. This results in a smaller degree variance signal gradient for models with an ice III layer and a thin ocean layer. Models containing ice V will have a lower signal gradient than worlds without it due to same reasoning as for ice III. Since Ice V is related to the liquid layer, the ocean within these models will be larger than for models without ice V.

JUICE's 3GM instrument will perform range-rate measurements to determine the spacecraft's radial position with respect to Ganymede. These measurements will be used to determine the gravitational potential field of Ganymede. This is an immense improvement on previous research, as currently only the  $J_2$  and  $C_{22}$  coefficients of Ganymede's potential field are determined. When JUICE has measured the degree variance signal resulting from Ganymede's gravitational potential field, its gradient can determine the size and presence of different internal layers within Ganymede. Through correlations provided during this research and the degree variance signal powers, JUICE can determine the following elements within Ganymede solely through its gravitational potential field measurements:

- The thickness of Ganymede's inner ocean layer.
- The presence of Ice III and V within Ganymede and their thicknesses.
- The size of Ganymede's core and mantle.

Hence through gravitational potential field measurements and the results of this thesis, JUICE can determine aspects of at least 5 internal layers within Ganymede. If specific variations within these layers appear to be present, even more layer thicknesses could be specified. If ice III is present, the crust should be at least 150 km thick. A large layer of ice V (>100 km) and a large mantle (>1200 km) will result in a large ice VI layer of 400-450 km thickness.

## 8.5. CONCLUDING REMARKS

This thesis has resulted in several new findings when considering Ganymede's internal density distributions and its relations with respect to the bodies gravitational potential field. A multitude of correlations between layers was established and degree variance signals of different worlds could be distinguished. This knowledge can be used as a direct validation of the different methods discussed and applied during this thesis research and by JUICE. If results are similar, this will confirm that assumptions and methods used during this research are in line with Ganymede's internal dynamics. When measurements result in different conclusions on Ganymede's internal layering, methods and assumptions should be reconsidered. In this way assumptions can be checked on validity, leading to improved models of Ganymede. Both options will lead to new knowledge on Ganymede's internal structure and its relations on the moon's gravitational potential field. In conclusion, this results in the achievement of the research objective, which was stated as:

**Determining the effects of expected density variations within Ganymede's interior on its gravitational potential field, as observable by JUICE.**

Therefore these results, together with measurements performed by JUICE, will provide numerous new insights on Ganymede's frozen enigma.

## RECOMMENDATIONS

Several new topics for research have arisen through this work, these are listed below.

- *Consider dual sea's with different salinities*; NASA<sup>1</sup> has theories about a dual ocean within Ganymede. It could be an interesting addition to add models based on these expectations to the current determined set.
- *Consider different orders of layers*; if Ganymede's interior is no longer in hydrostatic equilibrium, the order of layers could be different. Therefore it is advised that these are considered during future research.
- *Consider internal dynamic processes*; for now it was assumed that no dynamic processes were present within Ganymede. It is however theoretically possible that these do affect Ganymede interior. The ocean could for example include currents.
- *Consider internal heat processes*; if internal heat processes are present within Ganymede, these could greatly affect the different phases of ice and water which are present within Ganymede's interior.
- *Consider mantle and core temperature profiles*; currently a lot is unknown about the isolating characteristics of Ganymede's mantle. As the mantle thickness varies quite a lot in the models resulting from the research, one could check which mantle/core boundaries result in liquid and solid cores. The core's composition should be taken into account. If the core of a model appears to be completely solid, it will not be able to generate Ganymede's magnetic field.
- *Consider varying densities over pressure*; layer densities have been assumed constant over pressure. In reality this is not true and densities will slightly increase with pressure. It could be wise to investigate the impact of this assumption.
- *Inspect pocket behavior*; The module which generates pockets now is not scalable over height. It is advised to evaluate it's functioning before drawing conclusions from it.

---

<sup>1</sup>Ganymede dual ocean's: <https://www.jpl.nasa.gov/news/news.php?release=2014-138> [cited 01-02-2019]



## BIBLIOGRAPHY

- [1] J. D. Anderson, E. L. Lau, W. L. Sjogren, G. Schubert, and W. B. Moore. Gravitational constraints on the internal structure of Ganymede. *Nature*, 384(6609):541–543, 1996. ISSN 00280836. doi: 10.1038/384541a0.
- [2] M. Beuthe, A. Rivoldini, and A. Trinh. Enceladus's and Dione's floating ice shells supported by minimum stress isostasy. *Geophysical Research Letters*, 43(19):10,088–10,096, 2016. ISSN 19448007. doi: 10.1002/2016GL070650.
- [3] M. T. Bland, A. P. Showman, and G. Tobie. The production of Ganymede's magnetic field. *Icarus*, 198(2): 384–399, 2008. ISSN 00191035. doi: 10.1016/j.icarus.2008.07.011. URL <http://dx.doi.org/10.1016/j.icarus.2008.07.011>.
- [4] P Cappuccio, M Di Benedetto, and G Cascioli. Report on JUICE 3GM gravity experiment performance. 12:3–4, 2018.
- [5] P. M. Cassen, R. T. Reynolds, and M. Field. Is there liquid water on Europa? *Geophysical Research Letters*, 6(9):731–734, 1979.
- [6] H.D Curtis. *Orbital Mechanics for Engineering Students*, volume 3. Elsevier, 2010. ISBN 9780080977478.
- [7] M. E. Davies, T. R. Colvin, J. Oberst, W. Zeitler, P. Schuster, G. Neukum, A. S. McEwen, C. B. Phillips, P. C. Thomas, J. Veverka, M. J S Belton, and G. Schubert. The Control Networks of the Galilean Satellites and Implications for Global Shape. *Icarus*, 135(1):372–376, 1998. ISSN 00191035. doi: 10.1006/icar.1998.5982.
- [8] M. B. Dines. Ganymede: Observations by Radar. *Science*, pages 6–8, 1975.
- [9] European Space Agency. JUICE's primary target: Ganymede, 2018. URL <http://sci.esa.int/juice/59905-juice-s-primary-target-ganymede/>.
- [10] European Space Agency. ESA JUICE Homepage, 2018. URL <http://sci.esa.int/juice/>.
- [11] European Space Agency. JUICE's mission summary, 2018. URL <http://sci.esa.int/juice/50067-mission-summary/>.
- [12] European Space Agency (ESA). JUpiter ICy moons Explorer Exploring the emergence of habitable worlds around gas giants. Definition Study Report. (September):128, 2014. doi: ESA/SRE(2014)1.
- [13] U. Fink, N. H. Dekkers, and H. P. Larson. Infrared Spectra of the Galilean Satellites of Jupiter. *Astrophysical Journal*, 179:155–159, 1973.
- [14] C.M.R. Fowler. *The Solid Earth: An Introduction to Global Geophysics*, volume 2. Cambridge University Press, 2005. ISBN 0521584094.
- [15] R. Greenberg. The icy Jovian satellites after the Galileo mission. *Reports on Progress in Physics*, 73(3), 2010. ISSN 00344885. doi: 10.1088/0034-4885/73/3/036801.
- [16] S. D. Guzewich, J. B. Abshire, M. D. Smith, H. Rrirs, X. Sun, B. M. Gentry, A. Yu, and G. R. Allan. Understanding Kaula's Rule for small bodies. *Lunar and Planetary Science Conference XLVII*, pages 46–47, 2016. ISSN 19453027. doi: 10.1038/ngeo2474.
- [17] S. A. Hauck, J. M. Aurnou, and A. J. Dombard. Sulfur's impact on core evolution and magnetic field generation on Ganymede. *Journal of Geophysical Research E: Planets*, 111(9):1–14, 2006. ISSN 01480227. doi: 10.1029/2005JE002557.

- [18] H. Hussmann, G. Choblet, V. Lainey, D. L. Matson, C. Sotin, G. Tobie, and T. Van Hoolst. Implications of rotation, orbital states, energy sources, and heat transport for internal processes in icy satellites. *Space Science Reviews*, 153(1-4):317–348, 2010. ISSN 00386308. doi: 10.1007/s11214-010-9636-0.
- [19] T. V. Johnson and T. R. McGetchin. Topography on satellite surfaces and the shape of asteroids. *Icarus*, 18(4):612–620, 1973. ISSN 10902643. doi: 10.1016/0019-1035(73)90064-X.
- [20] T.V. Johnson. *Albedo and spectral reflectivity of the Galilean satellites of Jupiter*. PhD thesis, California Institute of Technology, 1969.
- [21] R. L. Kirk and D. J. Stevenson. Thermal evolution of a differentiated Ganymede and implications for surface features. *Icarus*, 69(1):91–134, 1987. ISSN 10902643. doi: 10.1016/0019-1035(87)90009-1.
- [22] M. G. Kivelson, K. K. Khurana, and M. Volwerk. The Permanent and Inductive Magnetic Moments of Ganymede. *Icarus*, 157(2):507–522, 2002. ISSN 00191035. doi: 10.1006/icar.2002.6834. URL <http://linkinghub.elsevier.com/retrieve/pii/S001910350296834X>.
- [23] R. Klees. Representation of the gravitational potential in spherical harmonics. *Lecture Notes AE4-E03*, 0: 19–34, 2010.
- [24] J. S. Lewis. Satellites of the outer planets: Their physical and chemical nature. *Icarus*, 15(2):174–185, 1971. ISSN 10902643. doi: 10.1016/0019-1035(71)90072-8.
- [25] Luciano Iess. European Geosciences Union Jean Dominique Caasini Medal Lecture, 2017. URL <https://www.youtube.com/watch?v=bpC681-CKHo>.
- [26] O. Montenbruck and E. Gill. *Satellite Orbits, Models, Methods, Applications*, volume 4. Springer, 2012. ISBN 9783540672807.
- [27] F. Nimmo. Non-Newtonian topographic relaxation on Europa. *Icarus*, 168(1):205–208, 2004. ISSN 00191035. doi: 10.1016/j.icarus.2003.11.022.
- [28] F. Nimmo and R. T. Pappalardo. Role of 3D seismic for quantitative shallow hazard assessment in deep-water sediments. *Journal of Geophysical Research E: Planets*, 121:1378–1399, 2016. ISSN 1070-485X. doi: 10.1002/2016JE005081. Received.
- [29] R. Noomen. Orbital Mechanics lecture, 2015.
- [30] G. W. Ojakangas and D. J. Stevenson. Episodic volcanism of tidally heated satellites with application to Io. *Icarus*, 66(2):341–358, 1986. ISSN 10902643. doi: 10.1016/0019-1035(86)90163-6.
- [31] E. M. Parmentier and J. W. Head. Internal-Processes Affecting Surfaces of Low-Density Satellites - Ganymede and Callisto. *Journal of Geophysical Research*, 84(NB11):6263–6276, 1979.
- [32] M. Pauer, S. Musiol, and D. Breuer. Gravity signals on Europa from silicate shell density variations. *Journal of Geophysical Research E: Planets*, 115(12):1–13, 2010. ISSN 01480227. doi: 10.1029/2010JE003595.
- [33] S. J. Peale, P. Cassen, and Reynolds R. T. Melting of Io by Tidal Dissipation. *Science*, 203(March):892–895, 1979.
- [34] J. B. Pollack and R. T. Reynolds. Implications of Jupiter's early contraction history for the composition of the Galilean satellites. *Icarus*, 21(3):248–253, 1974. ISSN 10902643. doi: 10.1016/0019-1035(74)90040-2.
- [35] Richard H Rapp. Degree Variances of the Earth's Potential, Topography and its Isostatic Compensation. 56:84–94, 1982.
- [36] Moritz Rexer and Christian Hirt. Spectral analysis of the Earth's topographic potential via 2D-DFT: a new data-based degree variance model to degree 90,000. *Journal of Geodesy*, 89(9):887–909, 2015. ISSN 14321394. doi: 10.1007/s00190-015-0822-4.
- [37] R. T. Reynolds and P. M. Cassen. On the Internal Structure of the Major Satellites of the Outer Planets. *Geophysical Research Letters*, 6(2):121–124, 1979.

- [38] B. C. Root, P. Novák, D. Dirkx, M. Kaban, W. van der Wal, and L. L.A. Vermeersen. On a spectral method for forward gravity field modelling. *Journal of Geodynamics*, 97:22–30, 2015. ISSN 02643707. doi: 10.1016/j.jog.2016.02.008. URL <http://dx.doi.org/10.1016/j.jog.2016.02.008>.
- [39] J. Saur, S. Duling, L. Roth, X. Jia, D. F. Strobel, P. D. Feldman, U. R. Christensen, K. D. Retherford, M. A. McGrath, F. Musacchio, A. Wennmacher, F. M. Neubauer, S. Simon, and O. Hartkorn. The search for a subsurface ocean in Ganymede with Hubble Space Telescope observations of its auroral ovals. *Journal of Geophysical Research: Space Physics*, 120(3):1715–1737, 2015. ISSN 21699402. doi: 10.1002/2014JA020778.
- [40] G. Schubert, D. J. Stevenson, and K. Ellsworth. Internal structures of the Galilean satellites. *Icarus*, 47(1): 46–59, 1981. ISSN 10902643. doi: 10.1016/0019-1035(81)90090-7.
- [41] G. Schubert, K. Zhang, M. G. Kivelson, and J. D. Anderson. The magnetic field and internal structure of Ganymede. *Nature*, 384(6609):544–545, 1996. ISSN 00280836. doi: 10.1038/384544a0.
- [42] G. Schubert, H. Hussmann, V. Lainey, D. L. Matson, W. B. McKinnon, F. Sohl, C. Sotin, G. Tobie, D. Turrini, and T. Van Hoolst. *Evolution of icy satellites*, volume 153. 2010. ISBN 1121401096351. doi: 10.1007/s11214-010-9635-1.
- [43] Y. Shibazaki, E. Ohtani, H. Terasaki, R. Tateyama, T. Sakamaki, T. Tsuchiya, and K. Funakoshi. Effect of hydrogen on the melting temperature of FeS at high pressure: Implications for the core of Ganymede. *Earth and Planetary Science Letters*, 301(1-2):153–158, 2011. ISSN 0012821X. doi: 10.1016/j.epsl.2010.10.033. URL <http://dx.doi.org/10.1016/j.epsl.2010.10.033>.
- [44] A. P. Showman and R. Malhotra. The Galilean satellites. *Science*, 286(5437):77–84, 1999. ISSN 00368075. doi: 10.1126/science.286.5437.77.
- [45] A. P. Showman, D. J. Stevenson, and R. Malhotra. Coupled Orbital and Thermal Evolution of Ganymede. *Icarus*, 129(2):367–383, 1997. ISSN 00191035. doi: 10.1006/icar.1997.5778. URL <http://www.sciencedirect.com/science/article/B6WGF-45MFXSB-31/2/d11419dbef6ad0cac6f108a5bb0f8ca2>.
- [46] A. Smith, A. Soderblom, V. Johnson, P. Ingersoll, A. Collins, M. Shoemaker, G. E. Hunt, H. Masursky, M. H. Carr, M. E. Davies, A. F. Cook, J. Boyce, G. E. Danielson, T. Owen, C. Sagan, R. F. Beebe, J. Veverka, R. G. Strom, J. F. Mccauley, D. Morrison, G. A. Briggs, and V. E. Suomi. The Jupiter System Through the Eyes of Voyager 1. *Science*, 204(4396):951–957, 1979. ISSN 0036-8075. doi: 10.1126/science.204.4396.951.
- [47] B. A. Smith, L. A. Soderblom, R. F. Beebe, J. Boyce, G. A. Briggs, M. H. Carr, S. A. Collins, A. F. Cook, G. E. Danielson, M. E. Davies, G. E. Hunt, A. Ingersoll, T. V. Johnson, H. Masursky, J. Mccauley, D. Morrison, T. Owen, C. Sagan, E. M. Shoemaker, R. Strom, V. E. Suomi, and J. Veverka. The Galilean Satellites and Jupiter: Voyager 2 imaging science results. *Science*, 206(3):927–950, 1979.
- [48] T.A.B. Snijders. The Degree Variance: An Index of Graph Heterogeneity, 1981.
- [49] F. Sohl. Implications from Galileo Observations on the Interior Structure and Chemistry of the Galilean Satellites. *Icarus*, 157(1):104–119, 2002. ISSN 00191035. doi: 10.1006/icar.2002.6828. URL <http://linkinghub.elsevier.com/retrieve/doi/10.1006/icar.2002.6828>.
- [50] C. Sotin and G. Tobie. Internal structure and dynamics of the large icy satellites. *Comptes Rendus Physique*, 5(7):769–780, 2004. ISSN 16310705. doi: 10.1016/j.crhy.2004.08.001.
- [51] Beauchesne S. Sotin C., Grasset O. Thermodynamic properties of high pressure ice, Implications for the dynamics and internal structure of large icy satellites. *Solar System Ices*, 227:79–96, 1998.
- [52] Robin Thor. Mapping the thickness of the Martian elastic lithosphere using maximum likelihood estimation. 2016.
- [53] W van der Wal. Planetary Sciences I, Planetary Oceanography lecture, 2017.

- [54] S. Vance, M. Bouffard, M. Choukroun, and C. Sotin. Ganymede's internal structure including thermodynamics of magnesium sulfate oceans in contact with ice. *Planetary and Space Science*, 96:62–70, 2014. ISSN 00320633. doi: 10.1016/j.pss.2014.03.011. URL <http://dx.doi.org/10.1016/j.pss.2014.03.011>.
- [55] S. D. Vance, J. H. Roberts, and A. A. Ganse. Inverse Theory for Planning Gravity Investigations of Icy Moons. *46th Lunar and Planetary Science Conference*, page 3, 2015. doi: 10.1029/2006JE002729.7.
- [56] J.F. Ververka. *Photometric and polarimetric studies of minor planets and satellites*. PhD thesis, Harvard University, 1970.
- [57] M.A. Wieczorek. *Gravity and Topography of the Terrestrial Planets*, volume 10. Elsevier, 2015.
- [58] M.K. Zolotov and J. Kargel. On the chemical composition of Europa's icy shell ocean and underlying rocks. *Pappalardo, R.T., McKinnon, W.B., Khurana, K., Europa*, pages 431–458, 2009.
- [59] A. Zubarev, I. Nadezhdina, J. Oberst, H. Hussmann, and A. Stark. New Ganymede control point network and global shape model. *Planetary and Space Science*, 117:246–249, 2015. ISSN 00320633. doi: 10.1016/j.pss.2015.06.022. URL <http://dx.doi.org/10.1016/j.pss.2015.06.022>.

# A

## APPENDIX A - VANCE'S INTERIOR MODELS

wt%		K					
		250	252.5	255	260	265	270
0	$q_b$	-	-	4	5	8	18
	Ice Ih	-	-	134	104	70	32
	Liquid	-	-	119	239	375	506
	Ice III	-	-	0	0	0	0
	Ice V	-	-	142	55	0	0
	Ice VI	-	-	426	416	360	260
	$R_{mantle}$	-	-	1814	1820	1829	1836
	$R_{core}$	-	-	690	680	667	658
	S/Si	-	-	4.60	4.42	4.37	4.26
3	$q_b$	-	4	4	5	8	21
	Ice Ih	-	144	130	100	66	27
	Liquid	-	45	121	233	372	514
	Ice III	-	46	0	0	0	0
	Ice V	-	157	139	60	0	0
	Ice VI	-	434	438	434	387	282
	$R_{mantle}$	-	1807	1806	1807	1809	1811
	$R_{core}$	-	703	702	699	701	700
	S/Si	-	5.04	5.51	6.03	6.77	7.52
5	$q_b$	-	4	4	6	9	24
	Ice Ih	-	141	127	96	63	24
	Liquid	-	64	128	243	381	537
	Ice III	-	29	0	0	0	0
	Ice V	-	156	134	48	0	0
	Ice VI	-	441	446	448	394	278
	$R_{mantle}$	-	1803	1799	1798	1796	1795
	$R_{core}$	-	709	715	714	719	723
	S/Si	-	5.38	6.21	7.45	8.72	10.09
10	$q_b$	4	4	5	6	11	44
	Ice Ih	148	129	114	84	50	13
	Liquid	31	125	183	321	477	753
	Ice III	52	0	0	0	0	0
	Ice V	155	127	81	0	0	0
	Ice VI	447	465	475	460	348	130
	$R_{mantle}$	1801	1788	1781	1769	1759	1738
	$R_{core}$	713	730	741	759	772	799
	S/Si	5.57	7.73	9.18	12.30	15.84	21.67

Figure A.1: The results using the models from Vance et al [54]. Interiors are provided for varying mass fractions of salinity and bottom melting temperatures of the ice  $I_h$  layer (The temperatures between 250 and 270K are chosen as lower boundary conditions as these correspond to the phase diagram of ice I over the range of temperatures for a homogeneous solid mix of water which contains magnesium sulfate, see Figure 2.3. Zero values indicate that a layer is not present and dashed values indicate that salinity is too low to allow for the presence of a liquid layer.  $q_b$  is the heat flux used for the thermal profile in  $mW/m^2$  that corresponds to the equilibrium ice  $I_h$  thickness. S/Si is the Sulfur to Silicon mass fraction which is consistent with the interior structure.



# B

## APPENDIX B - SPHERICAL HARMONICS

To gain a better insight of the interior structure of a celestial object, in this case Ganymede, one can measure and observe the gravitational potential field of the body. When modeling this gravitational potential field, a mathematical method which can effectively determine the size, shape and variation of this field is required. Such a model should however be able to account for the fact that a celestial object will probably not be perfectly spherical and will have varying density distributions within its interior. This can be done using spherical harmonics, which may be used to represent functions defined on the surface of a sphere (just as a Fourier series uses sines and cosines to represent functions on a circle).

Section B.1 illustrates how an object in the sphere of influence of a perfect spherical body represented by a point mass is accelerated. Using the perfect sphere as a foundation, Section B.2 discusses how one can model for latitudinal variations with respect to the perfect sphere. Section B.3 expands the theory of Section B.2 by also including longitudinal variations and the chapter concludes with a discussion on the order/degree of the spherical harmonics model and what could be detected by using different order/degrees in section B.3.2.

### B.1. SPHERICAL BODIES

One can obtain spherical coordinates from Cartesian coordinates by applying Equations B.1 - B.5 which follow from Figure B.1.

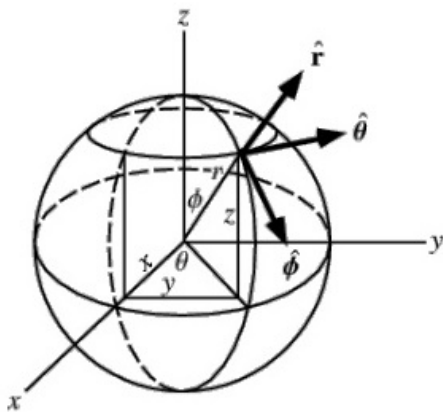


Figure B.1: Cartesian and spherical coordinate systems. <sup>1</sup>

Where  $r$  is the radial distance to the center of the reference frame,  $\theta$  is the azimuthal angle and  $\phi$  is the polar angle as presented in Figure B.1.

As a simple first order approximation, a celestial body of significant mass can be represented as a sphere of radius  $R$  with a symmetric mass distribution, then its gravitational potential field will also be spherically symmetric (acting as if all mass were concentrated at the center of the sphere). The gravitational potential energy per unit mass is then given by Equation B.6 [6].

$$V = -\frac{\mu}{r} \quad (\text{B.6})$$

<sup>1</sup>Cartesian to spherical coordinates: <https://www.slideshare.net/leingang/lesson-6-polar-cylindrical-and-spherical-coordinates>, [cited 17-12-2017]

Where  $\mu$  (the gravitational parameter) equals  $GM$ , with  $M$  being the sphere's mass,  $G$  the universal gravitational constant and  $r$  is the radial distance from the origin of the sphere to a point outside of the sphere. Note that  $r$  represents the magnitude of a position vector  $\mathbf{r}$ , as also depicted in Figure B.1. Equation B.7 shows this in formula form (with positions  $x$ ,  $y$ ,  $z$  and quaternions  $\mathbf{i}$ ,  $\mathbf{j}$ ,  $\mathbf{k}$ ).

$$\mathbf{r} = x\mathbf{i} + y\mathbf{j} + z\mathbf{k} \quad (\text{B.7})$$

The acceleration (in this case due to gravity) exerted on a unit mass placed at a distance  $\mathbf{r}$  from the source can be determined using Equation B.8.

$$\mathbf{a} = -\nabla V = \left( \frac{\partial}{\partial x}\mathbf{i} + \frac{\partial}{\partial y}\mathbf{j} + \frac{\partial}{\partial z}\mathbf{k} \right) V \quad (\text{B.8})$$

The value of this acceleration can be found by taking the corresponding derivatives using Equation B.6.

$$\mathbf{a} = \mu \left( \frac{\partial^{\frac{1}{r}}}{\partial x}\mathbf{i} + \frac{\partial^{\frac{1}{r}}}{\partial y}\mathbf{j} + \frac{\partial^{\frac{1}{r}}}{\partial z}\mathbf{k} \right) = \frac{\mu}{r^2} \left( \frac{\partial r}{\partial x}\mathbf{i} + \frac{\partial r}{\partial y}\mathbf{j} + \frac{\partial r}{\partial z}\mathbf{k} \right) \quad (\text{B.9})$$

Solve the three derivatives in Equation B.9 whilst keeping in mind Equations B.1 and B.7, this results in Equation B.10.

$$\mathbf{a} = -\mu \frac{\mathbf{r}}{r^3} \quad (\text{B.10})$$

Equation B.10 illustrates how an object in the sphere of influence of a perfect sphere (with its mass concentrated at its center) is accelerated due to the gravitational potential field of the sphere. This is the perfect scenario (also known as zeroth order harmonics), section B.2 will elaborate on zonal spherical harmonics, which are able to better represent the shape of the gravitational potential field varying over latitude and section B.3 will discuss the variation over both the latitude and longitude of the body.

## B.2. ZONAL SPHERICAL HARMONICS

Unfortunately most celestial objects are not perfect spheres. The shape of these bodies is influenced by several factors (more elaborately discussed in section B.3.2), which should be modeled for. This can be done using zonal spherical harmonics for latitude dependent factors. This section will elaborate on how this is done and gives an example of the most prominent deformation for most spinning celestial bodies as these are flattened.

### B.2.1. $J_2$ EFFECT, MAIN DISTORTION

First an example for such a distortion is introduced. Due to the spinning of celestial bodies, most of these represent oblate (in the case of Earth; flattened) spheroids. In this case the spin axis of the planet becomes the main axis of rotational symmetry of its gravitational field. Due to the equatorial bulge caused by centrifugal effects, the gravitational field also starts to vary with latitude (and thus not only radius). This is known as the so called  $J_2$  effect. This model of the gravitational potential is still dominated by the theory as discussed in section B.1, but now the contribution due to this flattening will be superimposed on this spherical model.

It is more convenient to use spherical coordinates. The  $z$ -axis of the associated Cartesian coordinate system then is the axis of rotational symmetry (as shown in Figure B.1). Furthermore  $\phi$  is the polar angle measured from the positive  $z$ -axis to the radial (Equation B.11) and  $\theta$  is the azimuth angle measured from the positive  $x$ -axis to the projection of the radial onto the  $xy$  plane.

$$\phi = \text{atan} \left( \frac{\sqrt{x^2 + y^2}}{z} \right) \quad (\text{B.11})$$

Zonal spherical harmonics are not dependent on the azimuth angle  $\theta$ , therefore the gravitational potential can now be determined using Equation B.12.

$$V(r, \phi) = -\frac{\mu}{r} + \Phi(r, \phi) \quad (\text{B.12})$$

Where  $\Phi$  in this case is the perturbation of the gravitational potential due to the planets oblateness. The zonal spherical harmonics can be represented by the infinite series given in Equation B.13 [6] [29].

$$V(r, \phi) = \frac{\mu}{r} \left( 1 - \sum_{n=2}^{\infty} J_n \left( \frac{R}{r} \right)^n P_n(\sin(\phi)) \right) \quad (\text{B.13})$$

$J_n$  are the Zonal Harmonic constants, which are dimensionless numbers that are not derived from mathematics but are determined by observing the motion of a celestial body (and thus are unique for each celestial body).  $R$  is the radius of the body,  $n$  is the degree considered and  $P_n$  are the Legendre polynomial functions, which can be determined using Rodrigues' formula (Equation B.14 [6] [29]) The summation starts at 2 instead of 1 because  $J_1 = 0$  due to the fact that the origin of the spherical coordinate system is the celestial objects center of mass.

$$P_n(x) = \frac{1}{-2^n n!} \frac{d^n}{dx^n} (1-x^2)^n \quad (\text{B.14})$$

It should be noted that  $x$  in this case does not represent the x-position of the affected body considered, but is a general argument (and will be replaced by the  $\sin(\phi)$  given in Equation B.13). For the  $J_2$  effect only (hence no spherical term;  $-\frac{\mu}{r}$ ), Equations B.13 and B.14 reduce to ( $n = 2$ ):

$$V_2(r, \phi) = \frac{\mu}{r} J_2 \left( \frac{R}{r} \right)^2 P_2(\sin(\phi)) \quad (\text{B.15}) \quad P_2(x) = -\frac{1}{2} + \frac{3}{2}x^2 \quad (\text{B.16})$$

Or combined:

$$V_2(r, \phi) = \mu J_2 R^2 r^{-3} \left( -\frac{1}{2} + \frac{3}{2} \sin^2(\phi) \right) \quad (\text{B.17})$$

Equation B.17 has been plotted in Figure B.2 [29]. Note that the gravitational potential is represented by  $U$  and that this plot is created using the Earth as dominant attractor. It clearly shows how the potential of an external body in the zone of influence of a gravitational field is affected by the flattening of this dominating body. Another important factor to note is that the values do not vary over longitude, just as expected.

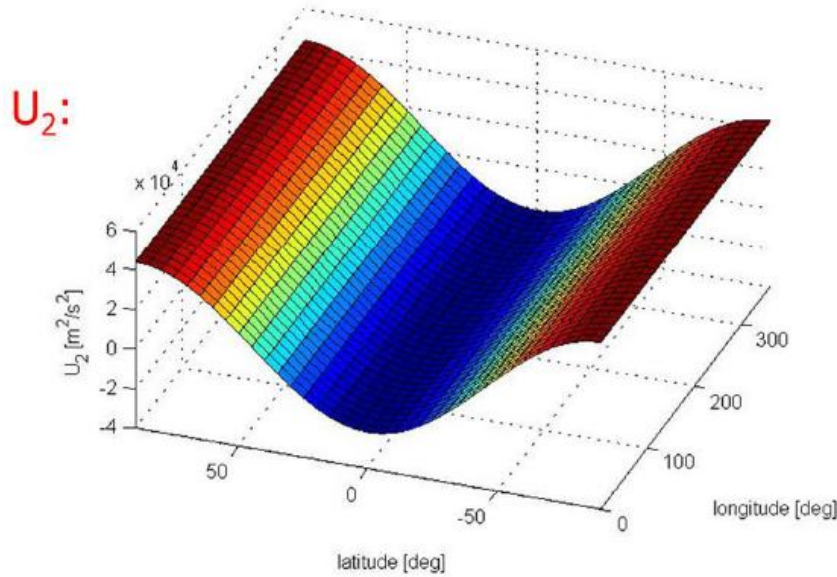


Figure B.2: The gravitational potential due to the  $J_2$  effect as function of latitude and longitude [29].

### B.2.2. HIGHER ORDER ZONAL TERMS

As already discussed, the flattening of a celestial body is the main zonal influence on the gravitational field of attraction. However, several smaller influences exist such as mountains, lakes (and thus basins), high and dense subsurface mass concentrations or hollow caves. Figure B.4 depicts the first six degrees of zonal harmonics. The white parts represent minima, whereas the grey area's represent maxima. It can be clearly

observed that the zonal harmonics follow a vertical wavy pattern, which especially becomes clear for higher order terms.

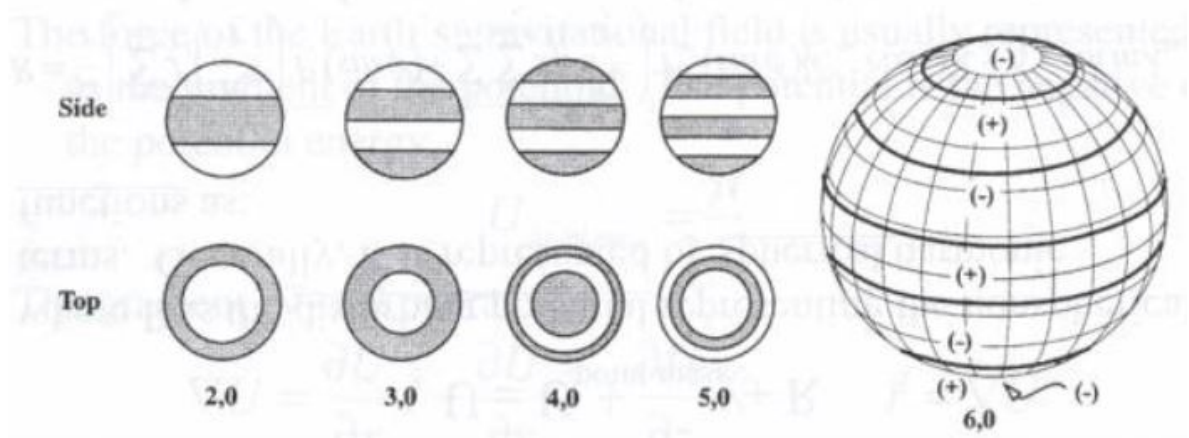


Figure B.3: First six degrees of zonal harmonics.<sup>2</sup>

### B.3. SECTORAL AND TESSERAL SPHERICAL HARMONICS

For sectoral and tesseral harmonics also terms are considered which vary as a function of longitude. This introduces new components to Equation B.13 which will contribute for these terms. The equation now does rely not only a degree (as for the zonal terms), but also an order (represented by  $m$ ), which represents the longitudinal varying component. Note that the zonal harmonics have an order of 0; thus the terms due to the  $J_2$  effect could also be written as  $J_{2,0}$ .

Sectoral harmonics are a special type of tesseral harmonics for which the degree and order are equal ( $n = m$ ). Equation B.18 provides the combined function which includes all spherical harmonic terms [29], this equation is also known as the classical description of the gravity field potential for a celestial body.

$$V(r, \phi) = \frac{\mu}{r} \left( 1 - \sum_{n=2}^{\infty} J_n \left( \frac{R}{r} \right)^n P_n(\sin(\phi)) + \sum_{n=2}^{\infty} \sum_{m=1}^{\infty} \left( \frac{R}{r} \right)^n P_{n,m}(\sin(\phi)) [C_{n,m} \cos(m\lambda) + S_{n,m} \sin(m\lambda)] \right) \quad (\text{B.18})$$

Or when rearranging the summations, one obtains Equation B.19

$$V(r, \phi) = \frac{\mu}{r} \left( \sum_{n=0}^{\infty} \sum_{m=0}^{\infty} \left( \frac{R}{r} \right)^n P_{n,m}(\sin(\phi)) [C_{n,m} \cos(m\lambda) + S_{n,m} \sin(m\lambda)] \right) \quad (\text{B.19})$$

Where  $C_{n,m}$  and  $S_{n,m}$  are the Tesseral and Sectoral Harmonic coefficients which describe the dependence on the internal mass distribution of the celestial body considered, given in Equations B.20 and B.21 [26].

$$C_{nm} = \frac{2 - \delta_{0m}}{M} \frac{(n-m)!}{(n+m)!} \int \left( \frac{s}{R} \right) P_{nm}(\sin(\phi')) \cos(m\lambda') \rho(\mathbf{s}) d^3\mathbf{s} \quad (\text{B.20})$$

$$S_{nm} = \frac{2 - \delta_{0m}}{M} \frac{(n-m)!}{(n+m)!} \int \left( \frac{s}{R} \right) P_{nm}(\sin(\phi')) \sin(m\lambda') \rho(\mathbf{s}) d^3\mathbf{s} \quad (\text{B.21})$$

Where  $\rho(\mathbf{s})$  represents the density as function of position,  $s$  the position,  $M$  the Mass of the celestial object and  $\delta_{0m}$  represents the Kronecker symbol.  $P_{nm}$  is the associated Legendre function which can be determined using Equation B.22 [26].

$$P_{n,m}(x) = (1-x^2)^{\frac{m}{2}} \frac{d^m P_n(x)}{dx^m} \quad (\text{B.22})$$

<sup>2</sup>First six degrees of zonal harmonics: [http://ccar.colorado.edu/asen5050/projects/projects\\_2002/fehring/gf.html](http://ccar.colorado.edu/asen5050/projects/projects_2002/fehring/gf.html), [cited 20-12-2017]

Hence it is clear that the associated Legendre functions rely on the Legendre polynomials [26]. The first five degrees of sectoral harmonics ( $n = m = 1, 2, 3, 4$  and  $5$ ) can be found in Figure B.4. It is also clear that the model now follows a wavy pattern in the horizontal direction.

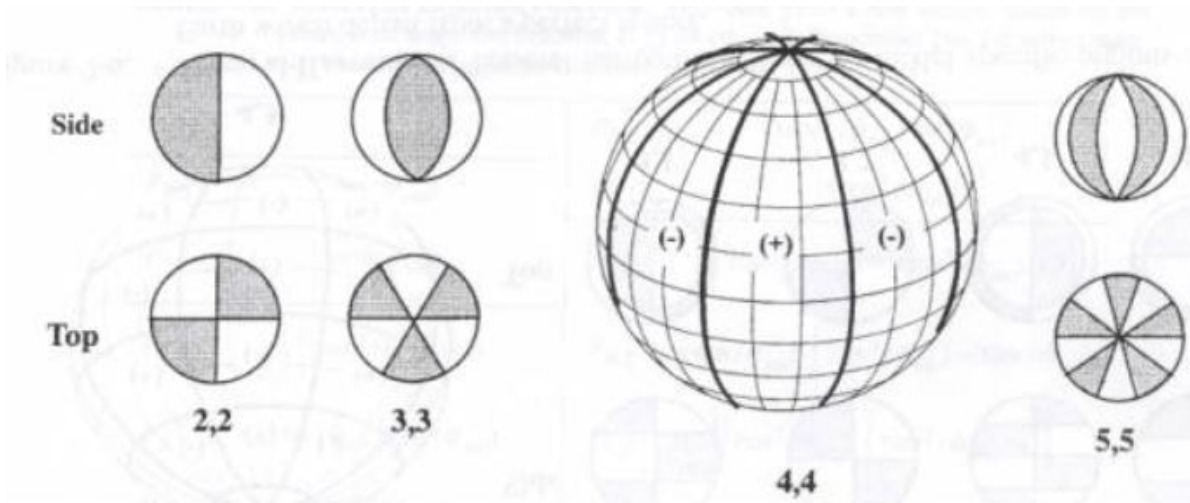


Figure B.4: First five degrees of sectoral harmonics. <sup>3</sup>

Finally, Figure B.5 depicts five different tesseral harmonic terms. Note that the first number is the degree ( $n$ ) and the second the order ( $m$ ). It can be clearly observed that now the harmonics vary with both longitude and latitude and will be able to provide an accurate representation of a celestial bodies gravitational field. It should be noted that for most spinning celestial bodies the  $J_2$  effect is by far the most dominant factor (for Earth 1000x larger than higher order terms). It can also be observed that a grid is formed on the sphere, consisting of dents and peaks. Thus is this way, especially with higher order harmonics, the gravitational potential field due to more specific/local density variations can be determined.

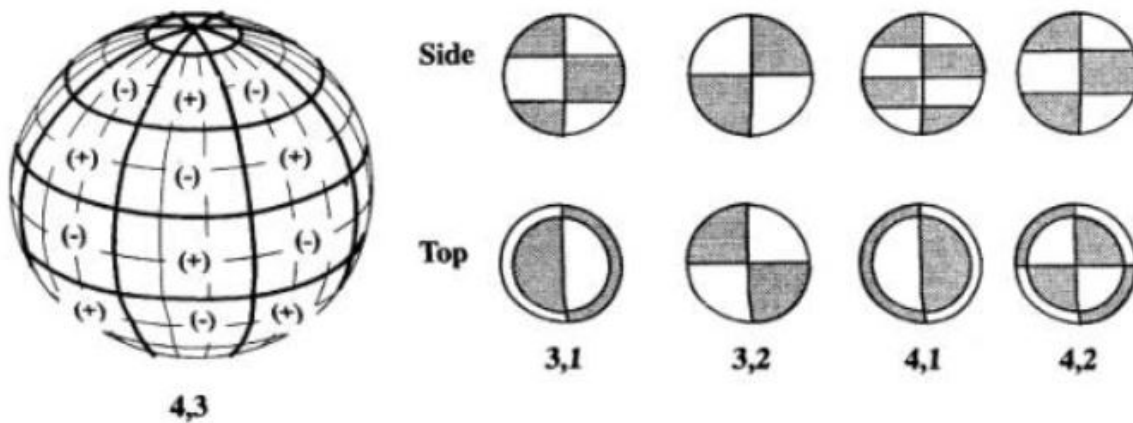


Figure B.5: Some tesseral harmonics. <sup>4</sup>

Finally, an overview and summary of the different coefficients and their influence on the spherical model can be found in Figure B.6 [23]. It also clearly distinguishes the different types of coefficients and illustrates the 5th order harmonics on the included spheres for zonal, tesseral and sectoral harmonics.

<sup>3</sup>First five orders of sectoral harmonics: [http://ccar.colorado.edu/asen5050/projects/projects\\_2002/fehring/gf.html](http://ccar.colorado.edu/asen5050/projects/projects_2002/fehring/gf.html), [cited 21-12-2017]

<sup>4</sup>Some tesseral harmonics: [http://ccar.colorado.edu/asen5050/projects/projects\\_2002/fehring/gf.html](http://ccar.colorado.edu/asen5050/projects/projects_2002/fehring/gf.html), [cited 21-12-2017]

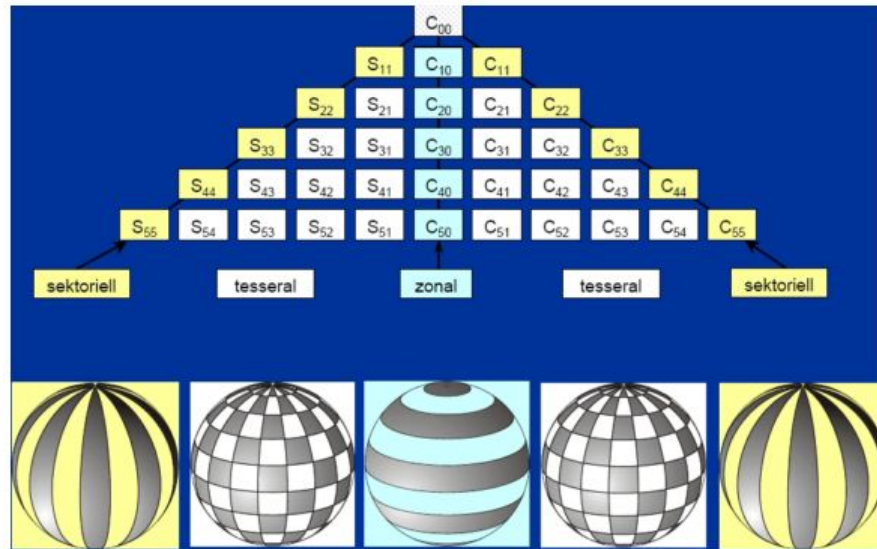


Figure B.6: An overview of the different harmonics, their influence on the gravitational potential field model and the corresponding coefficients. The  $S$  coefficients are used for negative orders and the  $C$  coefficients for positive orders [23].

### B.3.1. NORMALIZING THE GEOPOTENTIAL COEFFICIENTS

Even for small models, the  $C_{nm}$  and  $S_{nm}$  coefficients can already span several orders of magnitude. Therefore it is convenient to normalize these coefficients using Equation B.23 [26].

$$\begin{cases} \bar{C}_{nm} \\ \bar{S}_{nm} \end{cases} = \sqrt{\frac{(n+m)!}{(2-\delta_{0m})(2n+1)(n-m)!}} \begin{cases} C_{nm} \\ S_{nm} \end{cases} \quad (\text{B.23})$$

Where  $\bar{C}_{nm}$  and  $\bar{S}_{nm}$  are the normalized coefficients. In contrast to the original coefficients, these coefficients are convenient to work with as their magnitudes are more uniform. The size of these normalized coefficients is approximately given by the empirical Kaula rule [16] [26], given by Equation B.24.

$$\bar{C}_{nm}, \bar{S}_{nm} \approx \frac{K}{n^2} \quad (\text{B.24})$$

Where  $K$  is a constant that depends on the celestial body considered and is equal to  $10^{-5}$  for Earth. Now the acceleration due to Earth's gravitational potential can be rewritten using these normalized geopotential coefficients.

$$\ddot{r}_{geo} = \nabla V = \nabla \frac{\mu}{r} \left( \sum_{n=0}^{\infty} \sum_{m=0}^{\infty} \left( \frac{R}{r} \right)^n \bar{P}_{n,m}(\sin(\phi)) [\bar{C}_{n,m} \cos(m\lambda) + \bar{S}_{n,m} \sin(m\lambda)] \right) \quad (\text{B.25})$$

Equation B.25 provides the acceleration in terms of the normalized coefficients.

### B.3.2. MODELING DENSITY VARIATIONS

The order and degree of a spherical harmonics model will have an effect on the precision of the model and its ability to predict certain aspects of the gravitational potential field of a celestial body. As has been illustrated in section B.2.1, the lower order harmonics are able to provide a lot of information about the global structure of the body such as internal layering and/or global deformations such as the flattening of the body due to spinning. When considering higher order harmonics, the models will be able to detect more local/specific boundary and density variations.

**C**

**APPENDIX C - FULL CORRELATION  
FIGURES**

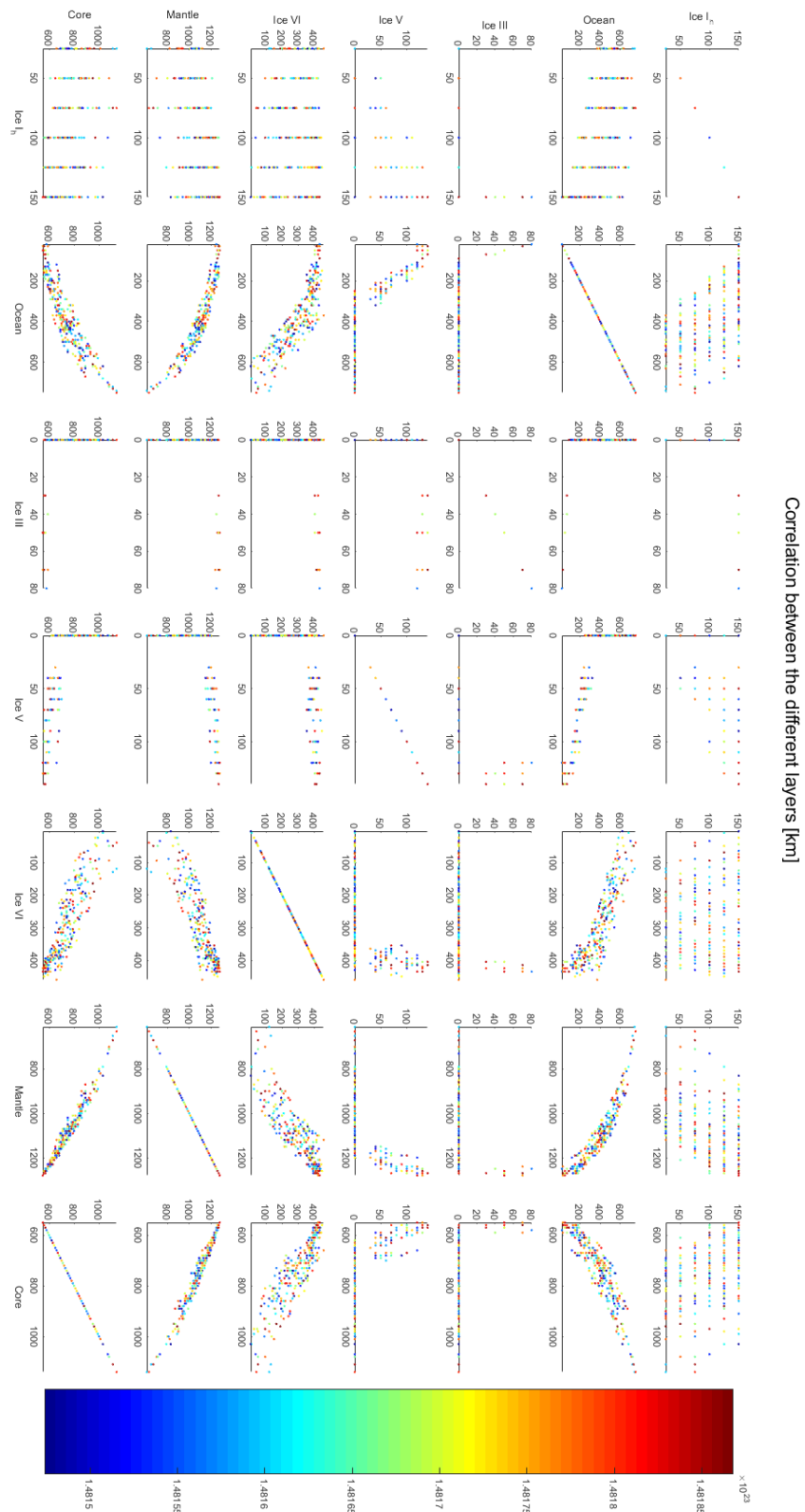


Figure C.1: The correlation between the different layers of the models that passed all requirements, colors scaled with respect to the models mass [kg].

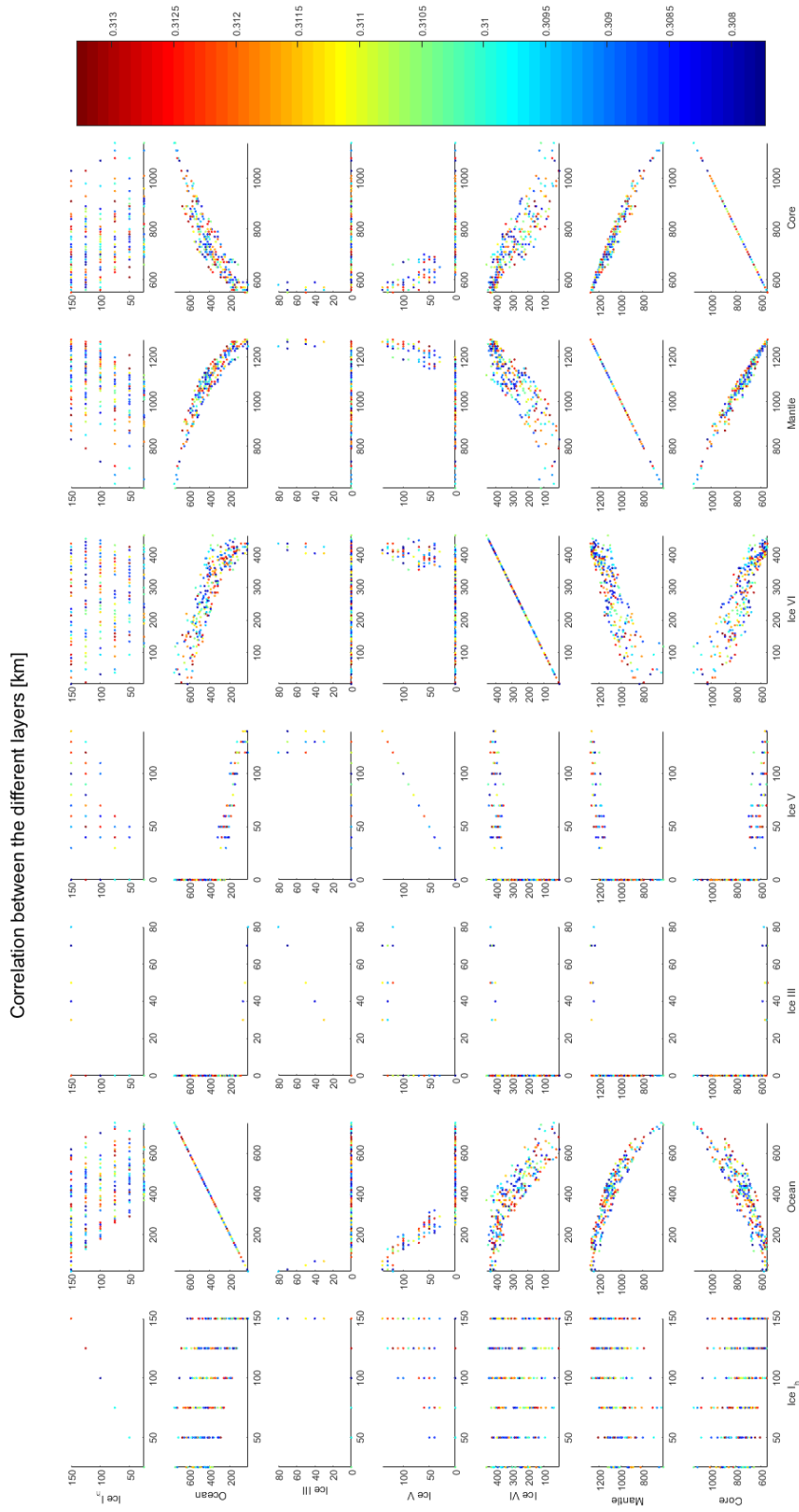


Figure C.2: The correlation between the different layers of the models that passed all requirements, colors scaled with respect to the models moment of inertia factor [-].

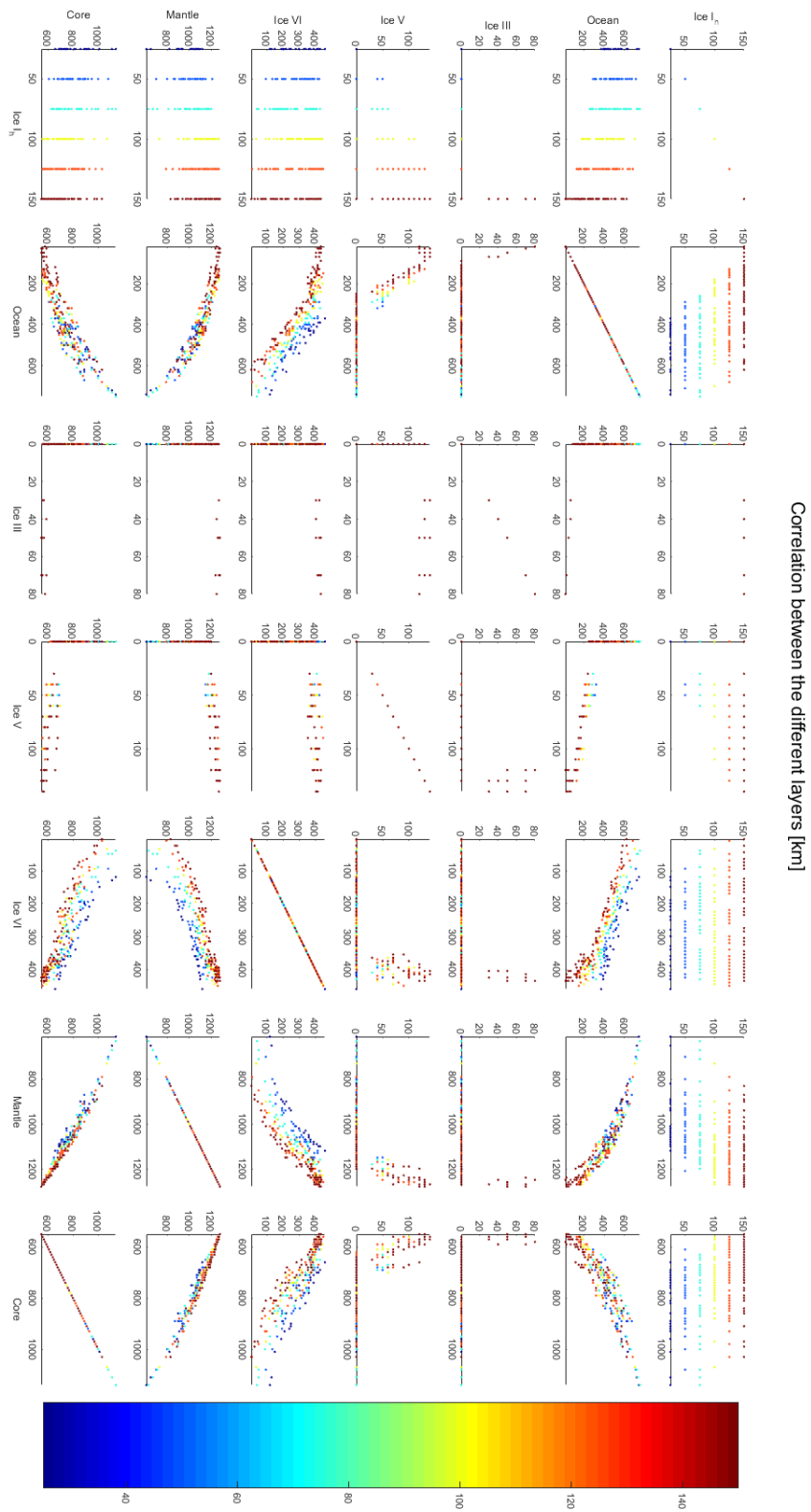


Figure C.3: The correlation between the different layers of the models that passed all requirements, colors scaled with respect to the ice  $I_h$  layer thickness [km].

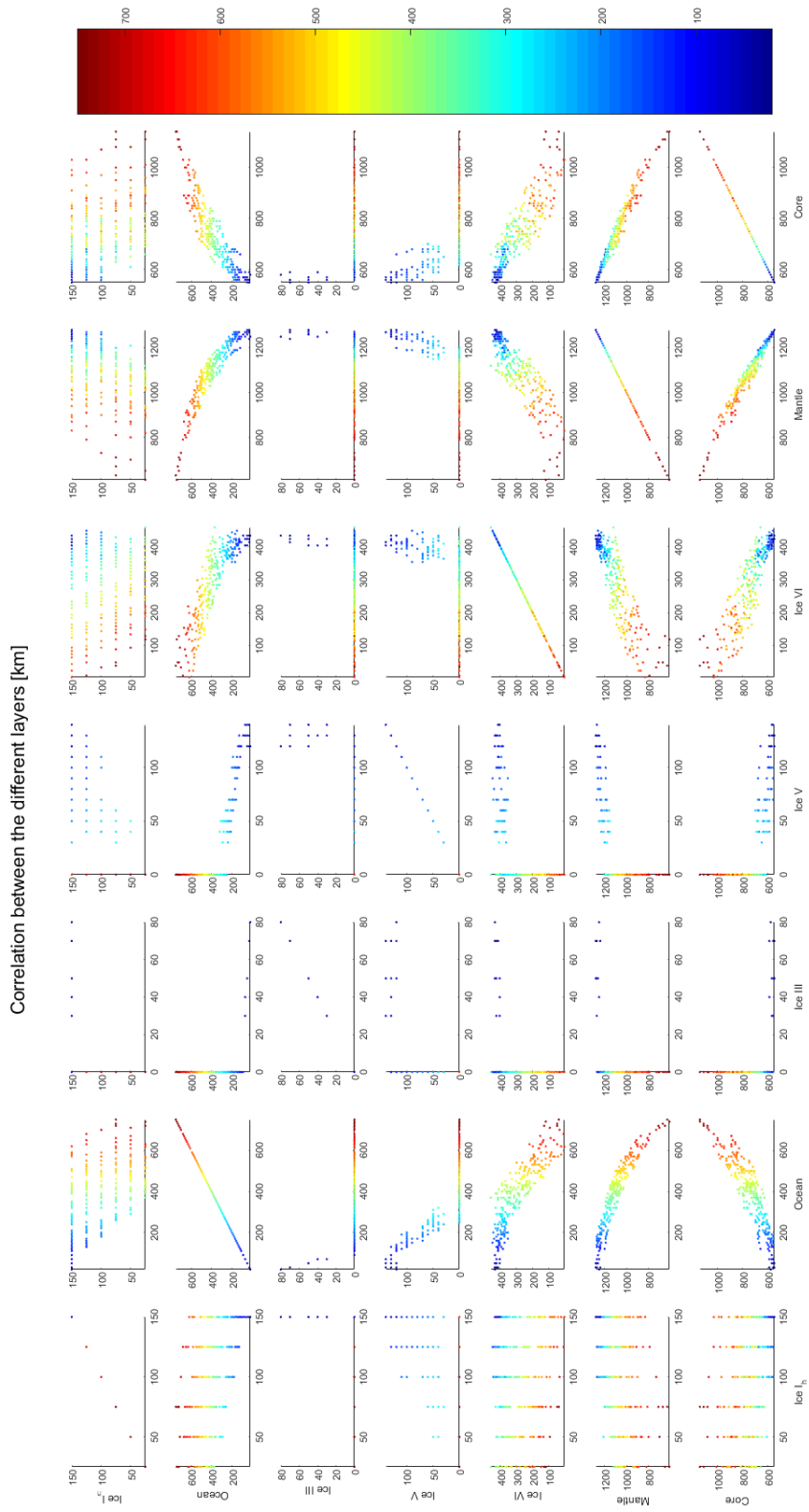


Figure C.4: The correlation between the different layers of the models that passed all requirements, colors scaled with respect to the Ocean layer thickness [km].

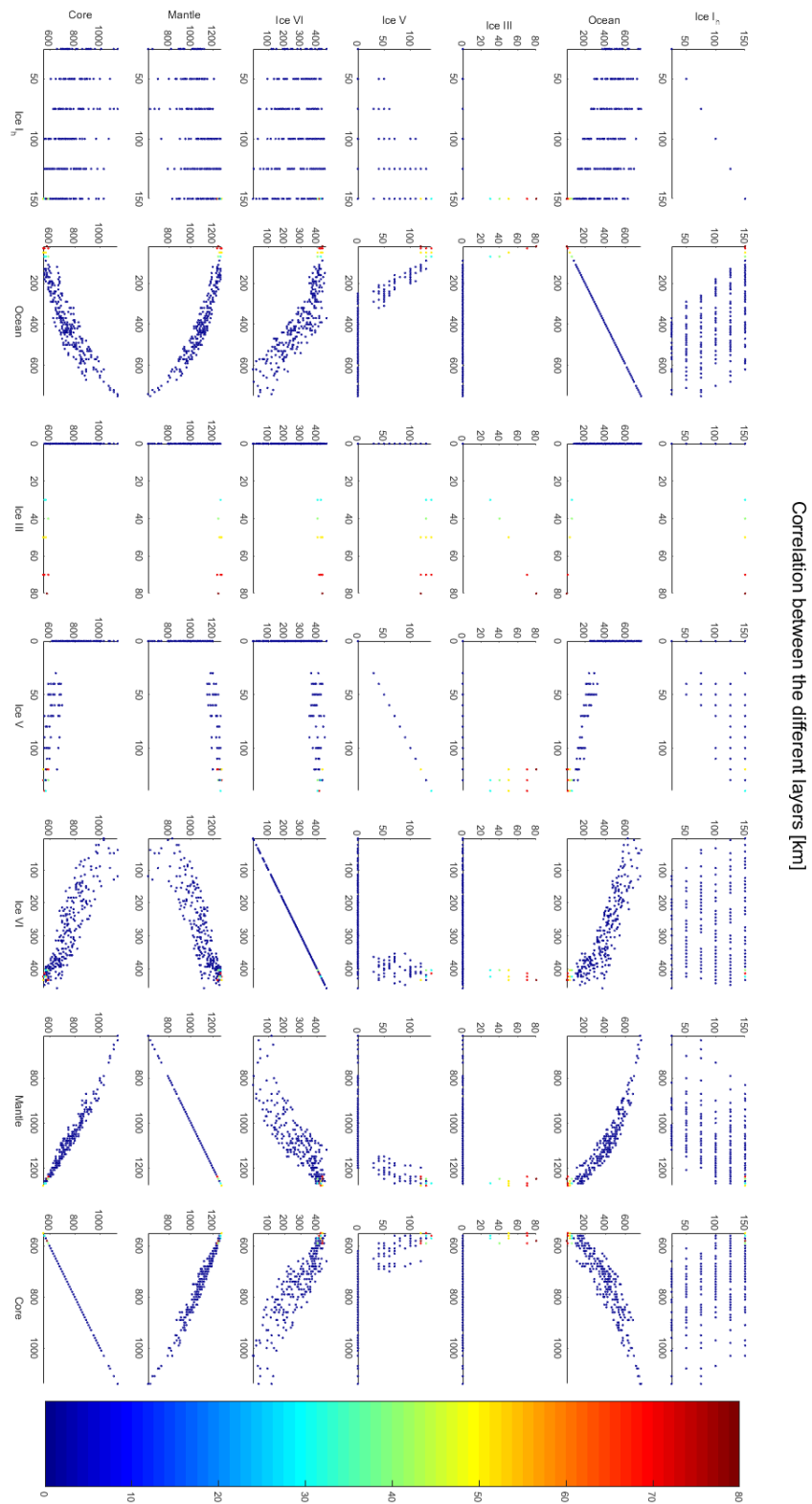


Figure C.5: The correlation between the different layers of the models that passed all requirements, colors scaled with respect to the ice III layer thickness [km].

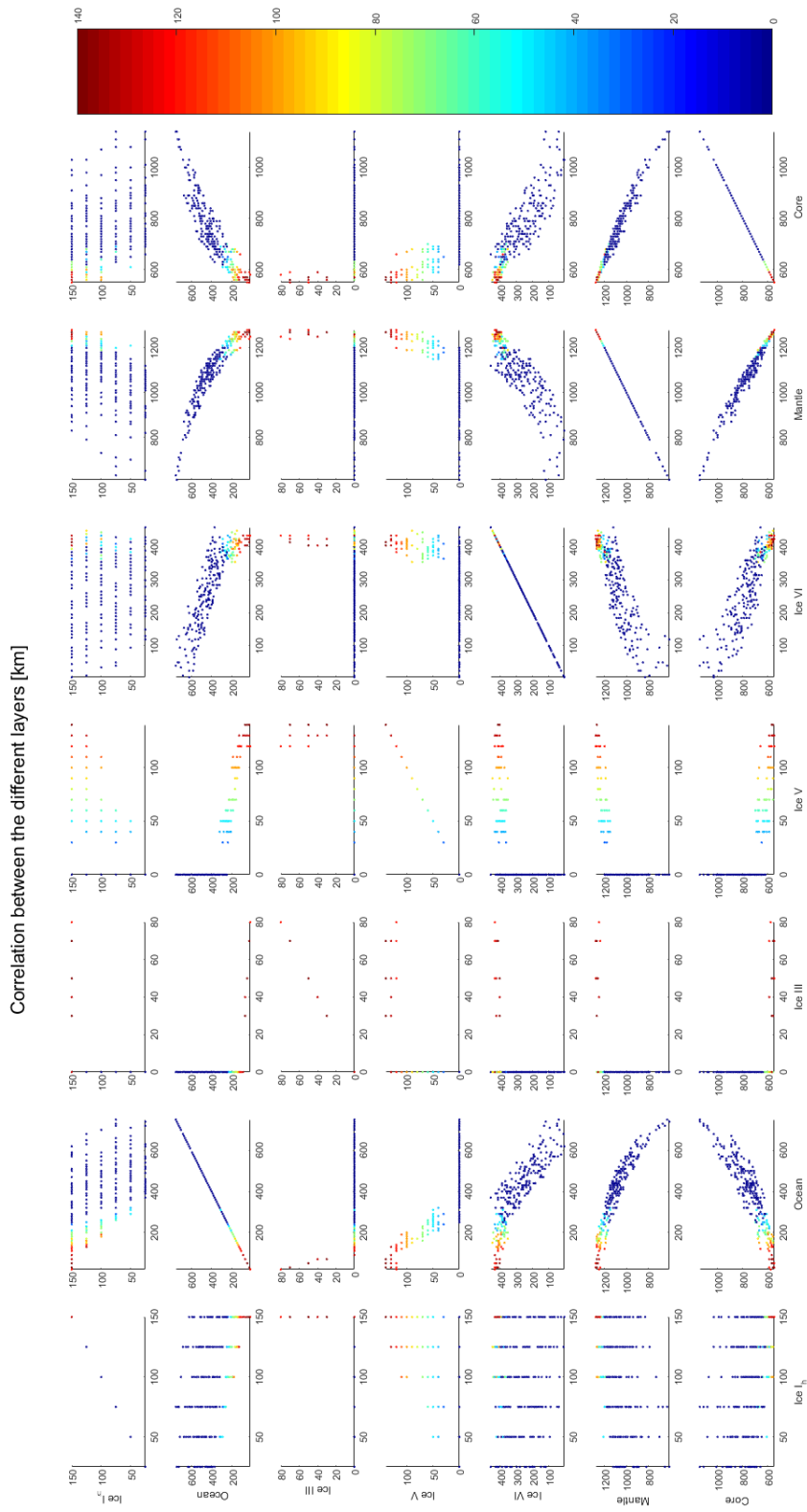


Figure C.6: The correlation between the different layers of the models that passed all requirements, colors scaled with respect to the ice V layer thickness [km].

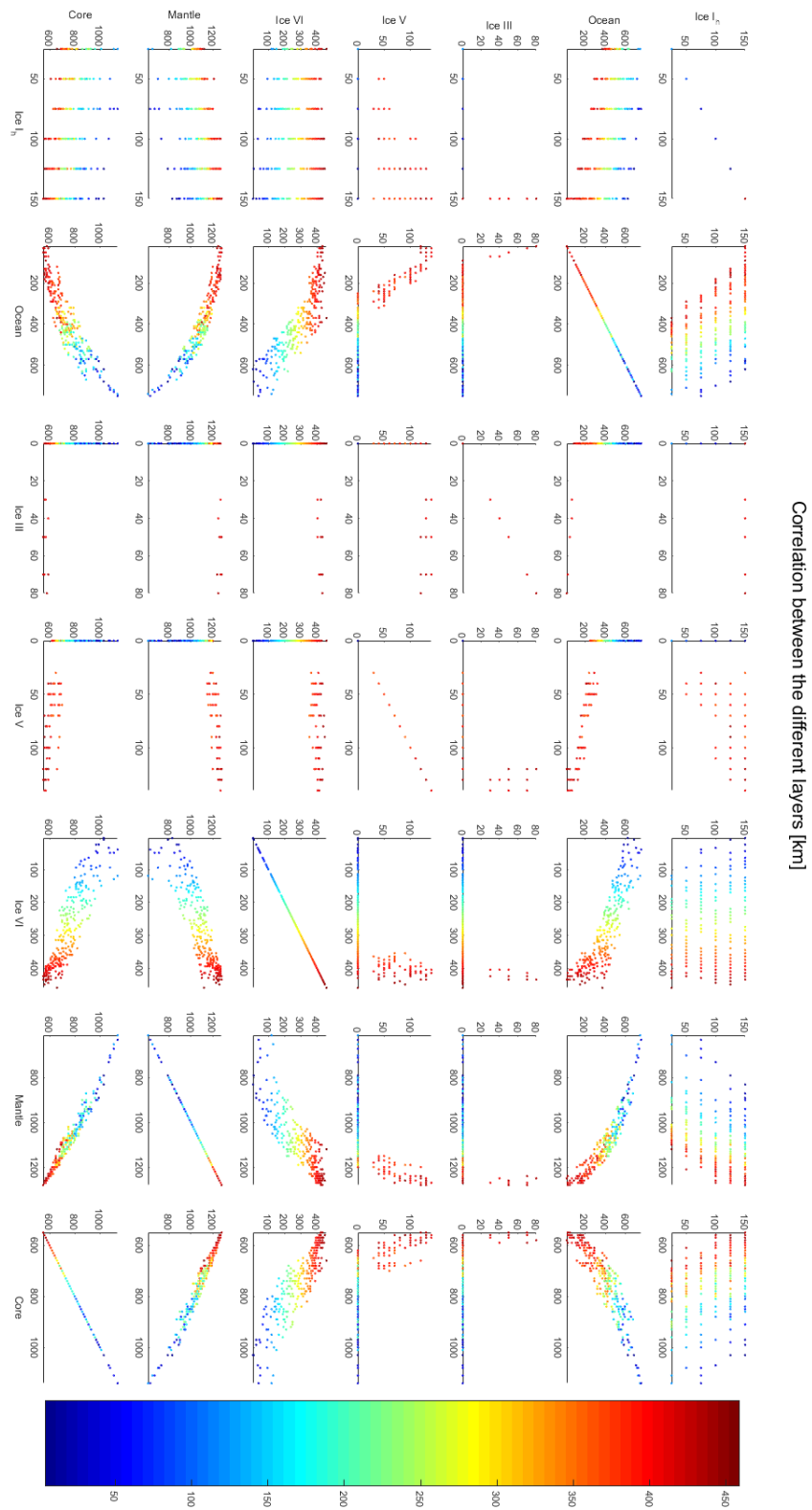


Figure C.7: The correlation between the different layers of the models that passed all requirements, colors scaled with respect to the ice VI layer thickness [km].

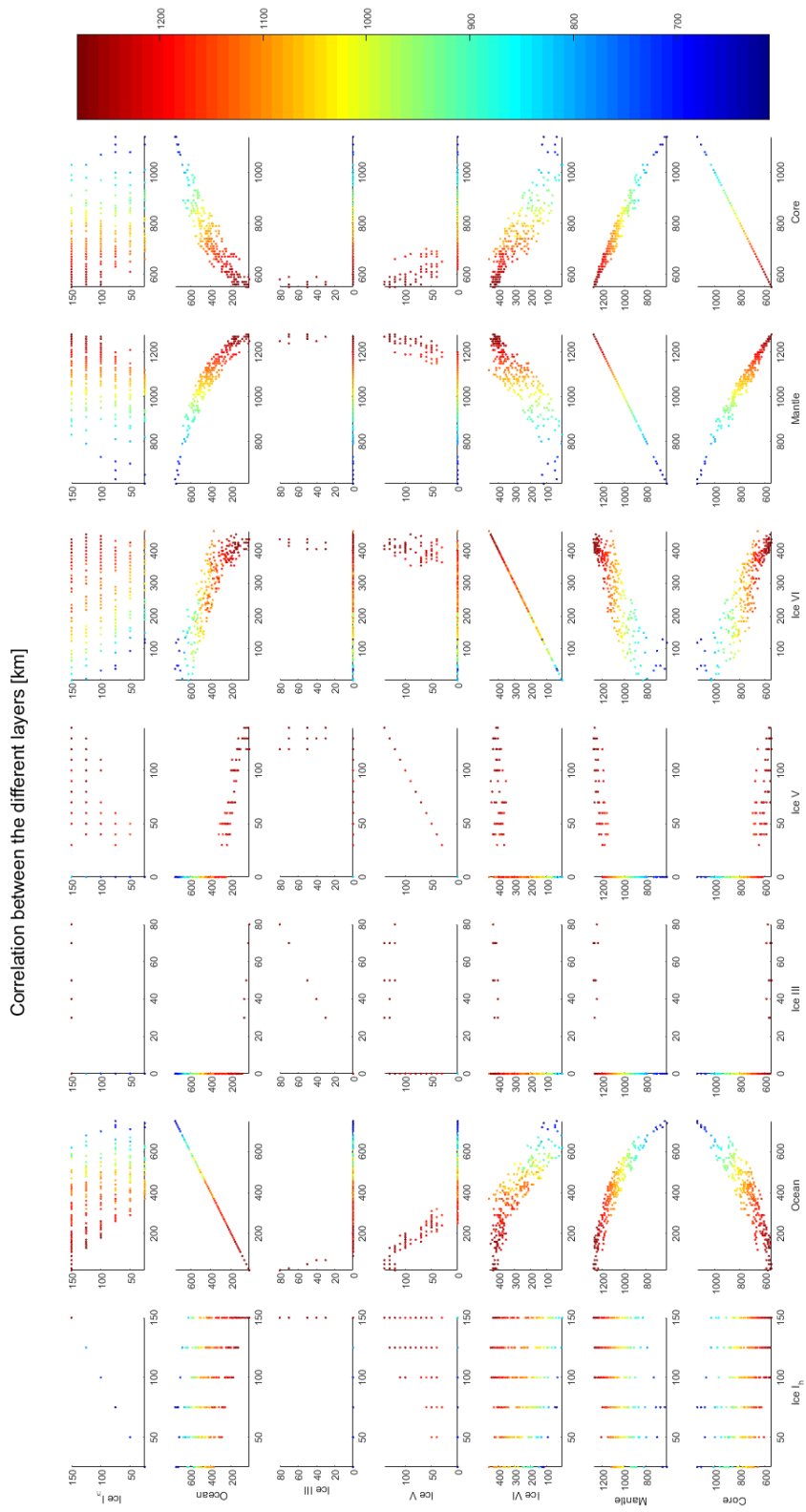


Figure C-8: The correlation between the different layers of the models that passed all requirements, colors scaled with respect to the mantle thickness [km].

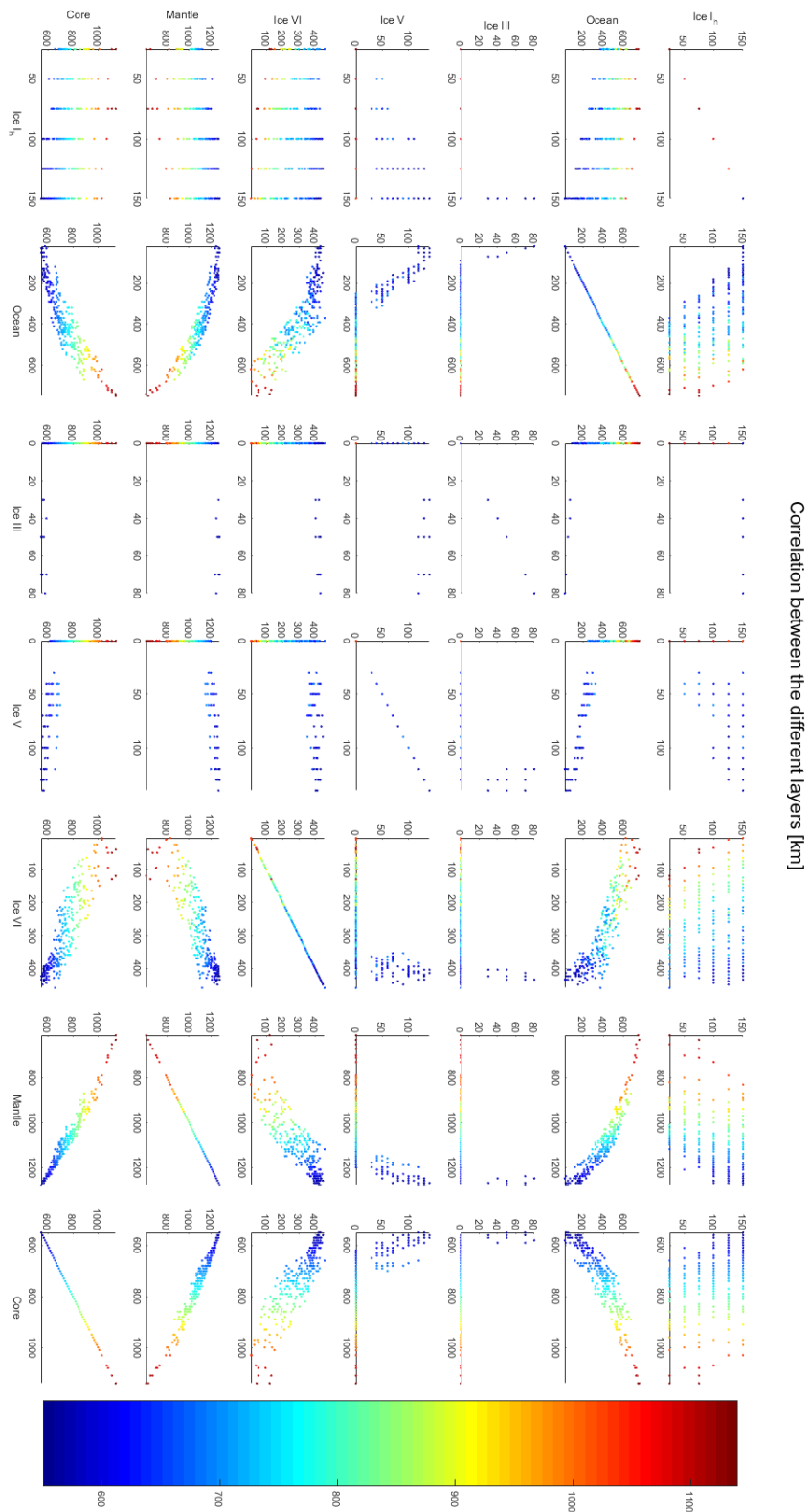


Figure C.9: The correlation between the different layers of the models that passed all requirements, colors scaled with respect to core thickness [km].

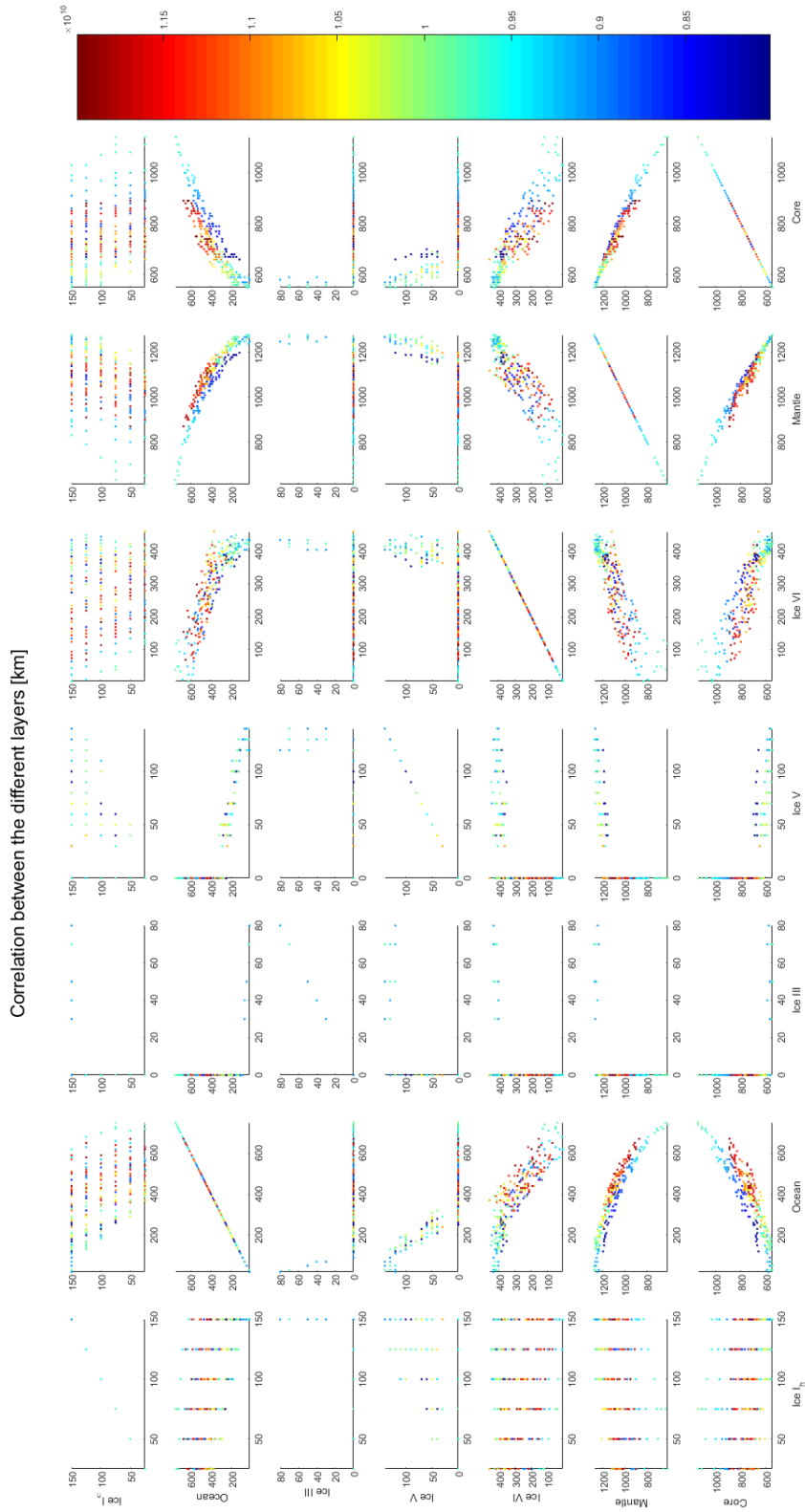


Figure C.10: The correlation between the different layers of the models that passed all requirements, colors scaled with respect to the models core pressure [Pa].